Methane Isotope Studies with Cavity Ring-Down Spectroscopy

Shaoyue Yang
Tai'an, Shandong, P.R.China

B.S., University of Science and Technology of China, 2009
M.A., University of Virginia, 2011

A Dissertation presented to the Graduate Faculty
of the University of Virginia in Candidacy for the Degree of
Doctor of Philosophy

Department of Physics

University of Virginia
05/2015

Abstract

Cavity ring-down spectroscopy (CRDS), as a highly sensitive optical spectroscopic method, has been widely used during the past three decades. This idea is to use cavity decay time to extract the information of single pass transmission or reflectivity of the optical resonator. Because of its immunity to intensity fluctuation, high sensitivity and high repetition rate, CRDS have been practiced in various field including trace gas detection, radical studies, chemical reaction kinetics, combustion research, photo dissociation dynamics, atmospheric and environmental studies, deposited nanoparticles, etc.

Distributed feedback (DFB) semiconductor laser diodes are used in our CRDS setup. There are two different ways to tune DFB lasers - temperature and current tuning. A new design of temperature controller with more evenly wavenumber stepsize is introduced. Also, a feedback loop from absorption peak is used for stabilizing laser frequency. When using the optimum modulation amplitude as well as appropriate PID parameters, the laser jitter decreases by over 20 times.

Three DFB near-IR lasers are used to measure the line strengths of CH_3D ro-vibrational transitions ($2\nu_4$) in the wavenumber regions of 6017.5 – 6031.5 cm^{-1} and 6046.5 – 6070.0 cm^{-1} using continuous-wave (cw) CRDS. The N_2, O_2 and CO_2 pressure-broadening and pressure-shift coefficients of CH_3D are also measured.

As one of the most important hydrocarbon prototype molecules, CH_3D's $2\nu_4$ overtone band are analyzed using different methods including combination differences, temperature dependence and double resonance. The fundamentals of theoretical spectrum analysis, including group theory, rotational spectra of symmetric top molecules,

vibrational transition types, Herzberg's character table, irreducible representation, and selection rules are also covered.

At last, we describe and test a novel cell for CW-CRDS. The cell is monolithic and maintains a rigid alignment of the two cavity mirrors. Two high-resolution and high-force PZTs are used to sweep the length of the cell by elastic deformation of the 2.86 cm outer diameter stainless steel tube that makes up the body of the cell. The performance of the cell is demonstrated by using it to detect the absorption spectrum of methane (CH_4) at the wavenumber regions of around 6051.8 – 6057.7 cm^{-1}.

Acknowledgements

I still remember the days before I made up my mind to pursue PhD in a different country. Back then I emailed a previous graduate student Haifeng Huang, who soon kindly introduced me to Professor Kevin Lehmann. That was when I finally decided to collect my courage and come to UVa. Now more than 6 years has passed, and I have always been feeling so grateful and lucky to have Kevin as my research advisor. He is my academic father. Kevin is always so kind and patient to my slow research progress, and his brilliant innovations and profound knowledge gave me the best experience that any student can ask for. Without his help, I would never be able to finish what I have completed today.

I would like to thank Professor Bob Jones and Professor Bellave Shivaram for their constant help through the years of my PhD studies. Even during the early stage of my research when I had setback and failures, they still encouraged me and gave me tons of helpful suggestions and that's one of the few important reasons why I could continue and finish the work.

I would also like to thank Professor Brooks Pate and Professor Cass Sackett, who gave me useful advices in previous years and also kindly agreed to help me with my thesis and defense examination in spite of my last minute request.

There are many other people that I want to express my gratitude to. I'd like to thank all my labmates, especially Yongxin Tang, Mausumi Goswami, Vitali Stsiapura, Vincent Kan, and Robert Fehnel. They were always there whenever I needed help, suggestions or new ideas. I want to thank our department staff, Dawn Shifflett, Tammie Shifflett, Beth Guyton, Helen McLaughlin, and David Wimer. I would never forget their smiles and

warm greetings. Also I want to thank all my amazing friends that I met in Charlottesville, especially Moran Chen, Caixia Bu, Kejia Li, Dien Nguyen, and Lichao Zhang. They helped me through ups and downs and gave me the best friendship possible.

Finally I want to thank my parents, Shouxiang Yang and Cuifen Zhang. They were always supportive and open minded. Without their love, support and understanding, I cannot even imagine that one day I would have been able to live in a different country and complete my Phd study. I hope they are and will always be proud of me.

Best wishes for all these wonderful people who showed up in my life and made it so much better. Now I'm about to start a new journey and I hope all the best for them.

Contents

Chapter 1 Cavity Ring-down Absorption Spectroscopy

1.1 Introduction

Spectroscopy is the study focused on the interaction between matters and radiative energy. Historically the concept of spectroscopy came from the phenomenon of visible lights' dispersion through a prism. Later this concept was expanded to the interaction related with other radiative energy sources as well. Spectroscopic data is usually represented by a spectrum, often plotted as a function of radiative wavelength or frequency.

The basic principle behind all absorption spectroscopy methods is the same: measuring the intensity of light after it's transmitted through a certain sample. Beer's law can be simply written as:

$$I(\lambda, x) = I_0(\lambda)e^{-\alpha(\lambda)x} \qquad (1)$$

Where λ is the wavelength, α is absorption coefficient, and x is the distance that light travels within the sample. Spectrometers, for example Fourier transform infrared spectrometers (FTIR), usually use multi-pass cells to improve sensitivity, whose length can be up to hundreds of meters. However, the spectral resolution is quite limited (usually > 0.001 cm^{-1}) and sometimes impossible to separate lines that are too close to each other.

Cavity ring-down spectroscopy (CRDS), as a highly sensitive optical spectroscopic method, has been widely used during the past three decades. It is difficult to date the first documented theoretical or experimental demonstration about absorption spectroscopy using a high finesse optical cavity. In the early applications of optical

cavities with flat mirrors [5,6], which later developed into the Fabry-Perot etalon, the possibilities of using these cavities for high resolution atomic spectra were explored. The exponential decay time behavior of optical cavity in equation (1) was reported by Kastler [7] in 1974. And later in the early 1980s the coating technologies improved significantly, allowing high reflectivity mirrors, also known as super mirrors, to be utilized in optical cavity spectroscopy.

Later in the effort of charactering high reflectivity mirrors, the method called cw-based cavity attenuated phase shift (CAPS) was developed by Herbelin et al. in the 1980s [1]. This idea is to use cavity decay time to extract the information of single pass transmission or reflectivity of the optical resonator. The original experiment of CAPS measured the lifetime of a photon in high finesse optical cavities in the visible and near-infrared region, and then the reflectivity of resonator's mirror can be calculated with known distance between mirrors.

The simplified CAPS experimental setup is shown in Figure 1. The cw laser beam was modulated by frequency *f* and then coupled into the high finesse cavity consists of mirrors M_1 and M_2, and after exiting, the phase shift is α. The relationship between reflectivity and phase shift would be [2]:

$$\tan\alpha = \frac{4\pi L f\left[R_1(1-A)^2 R_2\right]}{c\left[1-R_1(1-A)^2 R_2\right]} \qquad (2)$$

Where L is the distance between M_1 and M_2, R_1 and R_2 are reflectivities of M_1 and M_2, A is molecular absorption (assuming that A « 1; if cavity is vacuumed, then A is 0). The phase shift α can be determined by using the two channel lock-in. With this

experimental setup, Herbelin et al. [1] were able to measure mirror reflectivity with a precision between 50 to 5000 parts per million (ppm) [2].

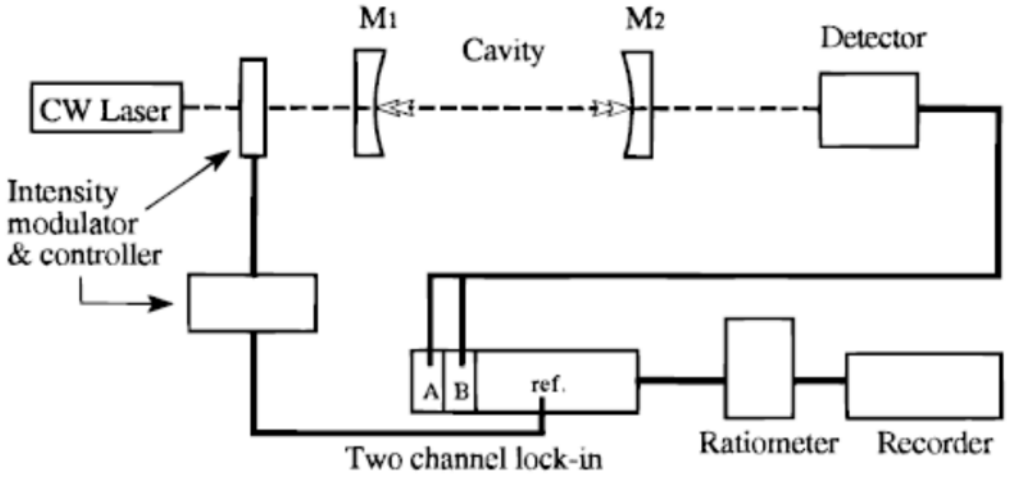

Figure 1: Cavity attenuated phase shift (CAPS) experimental diagram [1,2]. The continuous wave (cw) laser is modulated and then coupled into the optical resonator with two high reflectivity mirrors M_1 and M_2. The phase shift measured after the exit mirror can be used to calculate mirror reflectivity.

Soon later, in 1983, Anderson et al. [3] made another major progress by measuring the photon lifetime directly through monitoring the exponential decay waveform of the intracavity light intensity with a rapidly switched cw laser, shown in Figure 2 [2,3]. The cw laser beam is coupled into the cavity, and when the intracavity power (monitored by the fast detector after exit) reached a certain threshold, the Pockels cell rapidly switched off the laser injection, and the fast detector after the exit mirror registered the transient response, also known as 'ring-down', of the optical cavity. Ideally the cavity decays exponentially and ring-down time is affected by mirror reflectivity:

$$I(t) = I_0 e^{-t/\tau} \tag{3}$$

$$\tau = \frac{L}{c}\left(\frac{\sqrt{R_1 R_2}}{1-\sqrt{R_1 R_2}}\right) \qquad (4)$$

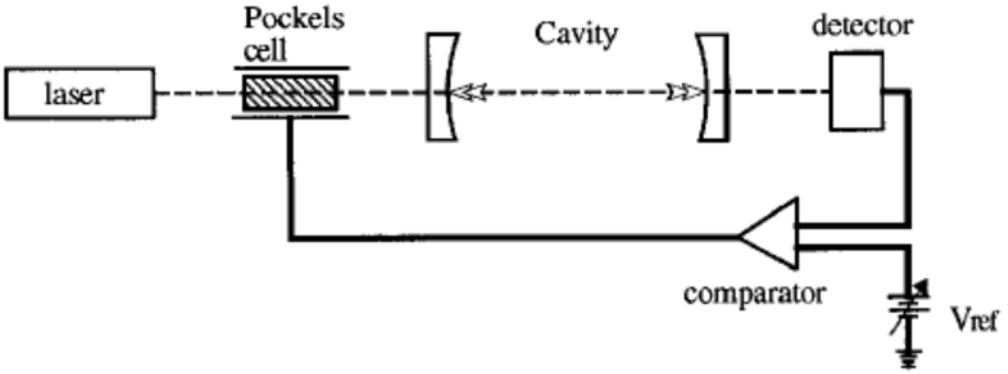

Figure 2: Experimental setup of Anderson et al. [3]. The cw laser beam is quickly shut off with a Pockels cell. Then they measured the intensity decay instead of phase shift.

Anderson et al. [3] reported a sensitivity of about 5ppm per pass, which is over an order of magnitude higher than previous CAPS experiment. They can achieve a higher level of sensitivity because ring-down time can be measured at nanosecond precision. However, this setup also requires triggering at the threshold and therefore limited by the dynamic mode matching between cw laser beam and optical resonator.

To overcome the problems by these two previous techniques, O'Keefe and Deacon [14] reported using pulse laser to excite the optical cavities, and therefore the rapid switch for cw lasers or threshold trigger were no longer the issues. Soon, Grand et al. [15-17] explored the possibility of using cw lasers modulated by Acousto-optic modulators (AOM) and cavity length scanned by attaching one or both mirrors to piezo transducers (PZT). Both of these techniques will be discussed in more details later.

During the following few decades, extensive work on cavity ring-down technique has been carried out for various purposes. More reviews about cavity ring-down spectroscopy can be found in [2,8-13,59,65-74].

1.2 Basic cavity ring-down spectroscopy setup

As mentioned before, the first real CRDS setup was realized with the use of pulsed laser by O'Keefe and Deacon [14], and the pulsed laser based CRDS is also very easy to be understood, so we'll discuss the basics from pulsed CRDS experiments. The typical experimental setup is shown in Figure 3. The pulsed laser beam is coupled into the optical resonator with two high reflectivity mirrors. When choosing cavity length L and mirrors' radius of curvatures R_1 and R_2, their values have to be such that the resonator is stable, which means:

$$0 \le \left(1 - \frac{L}{R_1}\right)\left(1 - \frac{L}{R_2}\right) \le 1 \qquad (5)$$

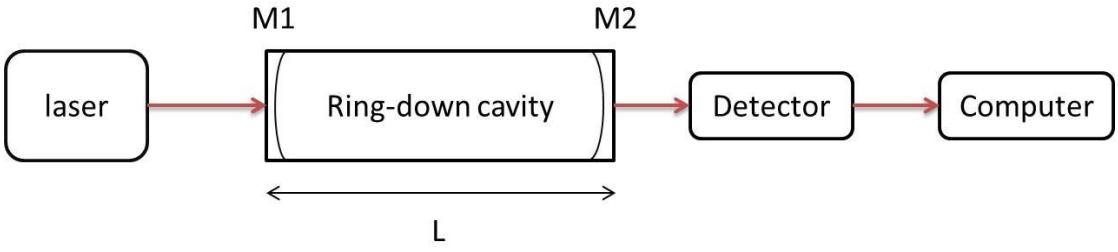

Figure 3: Typical experimental setup for pulsed CRDS. The sample is contained in a cavity with two ends sealed by concave or flat super mirrors M_1 and M_2. The fast detector picks up the ring-down curve and computer would fit the curve to get corresponding decay time.

Typically only a very small amount of light (a few ppm) enters the cavity, and the rest was reflected by mirror M_1. The light intensity transmitted through the second mirror M_2 is monitored by the detector, as it's directly proportional to the number of photons remained inside the cavity. Since both mirrors have high reflectivity (close to unit), photons may experience hundreds to thousands of round trips inside the cavity before transmitted again. The intensity change is shown in Figure 4.

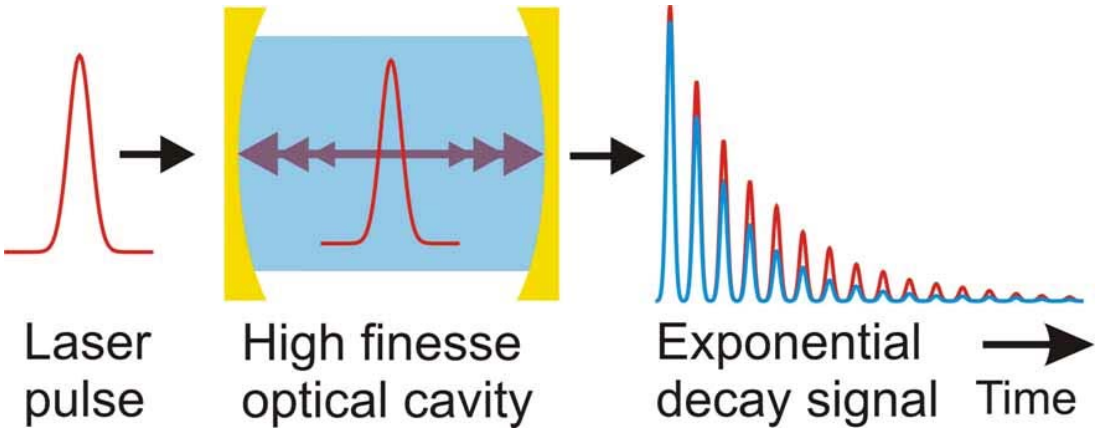

Figure 4: Pulsed CRDS laser intensity change with time. A small amount of laser pulse entered the cavity, and the peaks of transmitted energy after the cavity follow an exponential decay shape. When there is no absorbing species inside the cavity, the decay (in red) has a longer time constant, where the loss comes mostly from scattering and limited reflection. When there is one or more absorbing gas inside the cavity, the decay curve (in blue) drops faster, suggesting that extra loss from molecular absorption.

From Beer's law in Equation (1), we can easily get the light intensity change after n times of round trip is:

$$I(t) = I_0\left[R_1 R_2 \exp(-\alpha \cdot 2L)\right]^n \qquad (6)$$

Where R_1 and R_2 are mirror reflectivities, and L is the cavity length. And Equation (6)

can also be easily written as:

$$I(t) = I_0 \exp\left(-\frac{t}{\tau}\right) \tag{7}$$

Where $t = \frac{2L}{c}n$ and $\tau = \frac{L}{c(-\ln(R_1R_2)/2 + \alpha L)} \approx \frac{L}{c(1-\sqrt{R_1R_2} + \alpha L)}$, since both R_1 and R_2 are close to unity.

There are different ways to extract decay constant τ from the detector signal, and the most common method is to do a least-square fit to the transient light intensity decay. The absorption spectrum can then be generated by plotting decay rate $k = 1/\tau$ vs. frequency. Since the empty cavity decay rate reflects mirror losses, the difference between decay rates of empty cavity (τ_0) and cavity filled with absorbing gas (τ) yields the information about sample absorption. Therefore:

$$\alpha(\nu) = \frac{1}{c}\left(\frac{1}{\tau} - \frac{1}{\tau_0}\right) \tag{8}$$

And absorption cross section would be:

$$\sigma(\upsilon) = \alpha(\upsilon)/N \tag{9}$$

Where N is the number density of the absorbing molecule.

1.3 Applications

1.3.1 Pulsed cavity ring-down spectroscopy (P-CRDS)

The pulsed CRDS was firstly applied by O'Keefe and Deacon [14] and the basic experimental setup has been discussed in the previous section.

Because of its relatively simple setup, broad tuning range, and relatively high

sensitivity, P-CRDS has been widely used during the past three decades in different fields, including high sensitivity trace gas detection [18,19], methyl radical detection [20,21,23], chemical reaction kinetics [22], combustion research [24-30], photo dissociation dynamics [31-33], atmospheric and environmental studies [34-39], deposited nanoparticles [40-42], etc.

In the previous section, the simple description about P-CRDS is also called ‘photon bullet model’, which means it views photons only as particles and ignored the wave perspective. In fact, the interference of light inside the cavity should also be considered. Because the optical resonators of CRDS always use high reflectivity super mirrors and thus have very high finesse, only a very narrow bandwidth of light (a few kHz) can be in resonance with the cavity. The modes in resonance with the cavity have different longitudinal nodes, separated by $c/2L$ in frequency, and their transverse modes can be noted as TEM_{nm} modes, where n is number of radical nodes while m is number of angular nodes.

When a laser pulse enters the cavity, each excited mode of the cavity will decay at its own rate and also they would interfere with each other. Although higher order transverse modes can be reduced by ‘mode matching’, which means that the input beam (typically considered as in Gaussian shape) is carefully shaped such that it matches the TEM_{00} modes of the cavity, in reality, there are always some transverse mode beating left. The mode beating would result in the inconsistency of the position and shape where the laser beam hits the mirrors per pass. Also, for higher order modes, since their decay rate is different from TEM_{00} mode, the detected decay rate from CRDS would be instable because of the existence of higher order modes. More

detailed discussion can be found in the work of Huang et al. [48-50].

Although P-CRDS has the advantages of simple setup and broad tuning range, its disadvantages like low energy coupling efficiency, low repetition rate (a few Hz) and mode beating noise mentioned above all put limits on further improvement in sensitivity.

1.3.2 Continuous-wave cavity ring-down spectroscopy (CW-CRDS)

To solve the difficulties for P-CRDS, cw lasers were brought back to CRDS, when Grand et al. [15-17] demonstrated the experiments using PZT to adjust cavity length, in order to achieve mode matching between the frequency stabilized cw laser and optical cavity. The typical experimental setup for CW-CRDS is shown in Figure 5. The first demonstration of narrow band CW-CRDS was presented by Romanini et al. [43-45]. In their experiments, the cw laser was modulated by acousto-optic modulator (AOM), which also serves as the beam on/off switch, and then mode matched with the optical cavity. In order to achieve resonance between laser beam and cavity, one of the super mirrors was attached to PZT and cavity length can therefore be scanned over one free spectral range. When tuning the laser wavelength, the PZT voltage should also change accordingly in order to remain resonant.

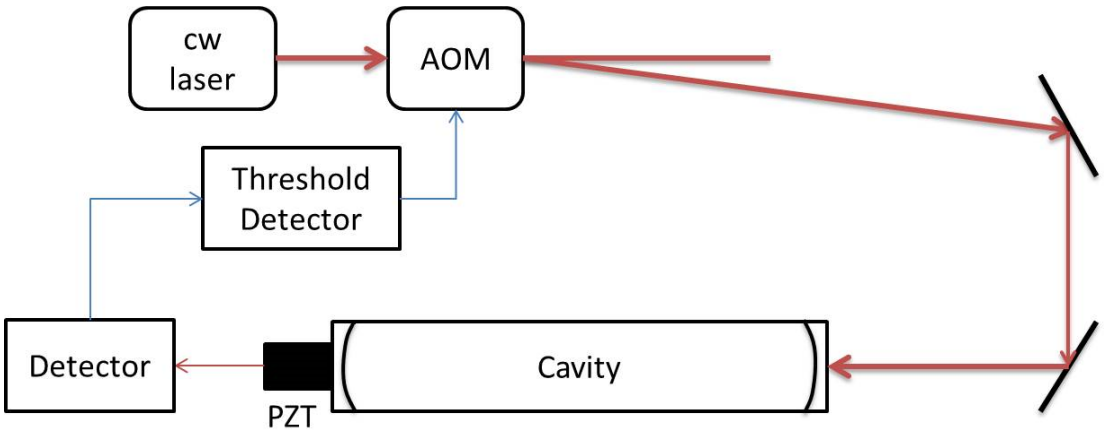

Figure 5: Typical experimental setup of CW-CRDS.

The main difference between P-CRDS and CW-CRDS is that cw laser needs a fast light switch and threshold monitor. As for light switch, other than using AOM as modulator, various other approaches have also been applied, for example, switching off laser current supply [46], or using semiconductor optical amplifier (SOA) instead of AOM as light switch [47,51].

In CW-CRDS, the same problem with mode beating can be greatly reduced by adding an aperture inside the cavity, mentioned in the work of Huang et al. [48-50]. In their work, the aperture loss for TEM_{00} mode is negligible, while higher order modes experienced much higher loss from the aperture. Since cw lasers can have narrower bandwidth (a few MHz), the excitation of higher order modes can also be significantly reduced, as compared with pulsed lasers. Also defects on lens may cause higher order modes as well [48, 53-54]. There are other sources that would introduce noise to CRDS, such as any kind of light feedback outside the cavity reflecting back and interfering with intracavity light [52]. Therefore wedged optics were often employed in order to eliminate the backwards reflection into the cavity.

Because of the high sensitivity, high repetition rate (since each ring-down event occurs on the millisecond scale), and immunity to laser intensity variation, CW-CRDS has been widely used in trace gas detection, and chapter 3 uses this technology to explore stable isotopic measurements of Methane. Various light sources have also been introduced into CW-CRDS, such as external cavity diode laser [55], optical feedback stabilized diode laser [56], distributed feedback (DFB) diode laser [57], quantum cascade laser [58], etc. The next chapter mainly discusses the employment of DFB diode lasers in CW-CRDS. They have narrow linewidth, low cost and are widely used in telecommunication industry at near infrared region.

1.3.3 A few of other approaches of CRDS

In late 1990s, another scheme without determining ring-down time, known as cavity enhanced absorption spectroscopy (CEAS), was implemented [60-62]. Here it's worth mentioning that CEAS can be used as a broad name for all absorption spectroscopic methods with high finesse cavity. Here we use its narrow definition [60-62], which refers to a particular CRDS scheme. The experimental setup for CEAS, shown in Figure 6, is very similar to CW-CRDS. The main difference is that CEAS doesn't have a shutter for cw lasers; instead, the cw laser scans through the cavity modes and the time averaged cavity transmission is measured by detector. CEAS typically has simpler setup than CW-CRDS, however, usually at the expense of higher noise. Also, to determine the absolute absorbance of the sample from the change in the mean optical transmission of the cavity, the empty cavity decay time must be known which often requires the ability to do a traditional CRDS measurement.

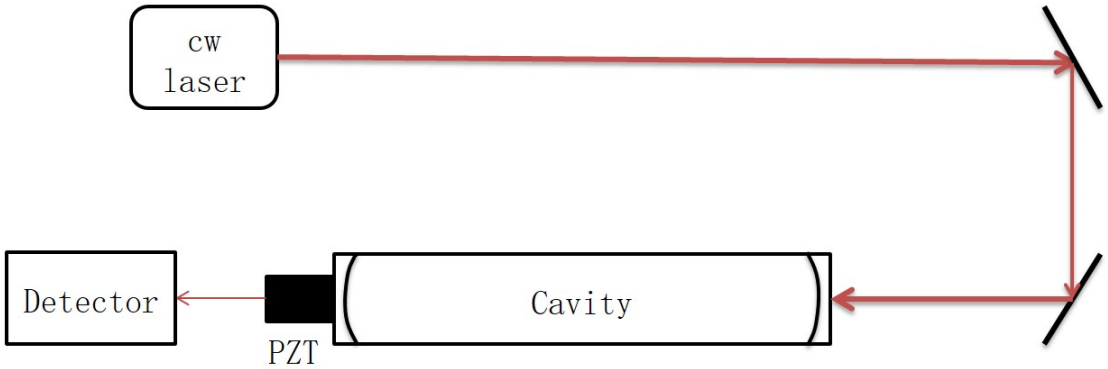

Figure 6: Typical experimental setup for CEAS.

At about the same time, Ye et al. [63] introduced another scheme called Noise-Immune Cavity-Enhanced Optical Heterodyne Molecular Spectroscopy (NICE-OHMS). They used a super narrow linewidth laser (less than 1 kHz) and lock the laser to one of the cavity modes. They used high frequency phase modulation to generate laser sidebands at exactly the free spectral range (FSR) of the cavity. Since the beats from carrier frequency and its two sidebands can be precisely cancelled, any small intracavity absorption leads to a substantial change in heterodyne signal, therefore, NICE-OHMS improves shot noise by several order of magnitude. However, the setup is technically challenging, and the shot noise improvement was mostly because of the super narrow linewidth laser. Also, NICE-OHMS is not as useful for broad spectral lines since their two frequencies differ by two cavity FSRs, which are typically only a few hundred MHz apart.

While all the schemes mentioned before used narrow band lasers, Engeln and Meijer [64] demonstrated broadband Fourier transform (FT) P-CRDS with the linewidth of 400 cm^{-1}. They recorded the interferograms at different spots on ring-down events with a time resolved Michelson interferometer. The broadband CRDS can take the whole spectrum all at once while keeping high sensitivity like narrowband CRDS.

Different light sources were later implemented in broadband CRDS, for example, supercontinuum generation [75] and frequency comb [76]. More progress in broadband CRDS works can be found in [77-83].

1.4 Summary

In this chapter we first gave a brief introduction about CRDS, and then discussed more about fundamentals of CRDS. Later we described two of the most common CRDS schemes, P-CRDS and CW-CRDS, along with brief information about several other CRDS developments. As we can see, CRDS has developed significantly during the past three decades. Because of its immunity to intensity fluctuation, high sensitivity and high repetition rate, CRDS have been practiced in various field including trace gas detection, radical studies, chemical reaction kinetics, combustion research, photo dissociation dynamics, atmospheric and environmental studies, deposited nanoparticles [40-42], etc.

1.5 The outline of thesis

Chapter 2 will discuss two different ways to tune DFB semiconductor diode lasers. The temperature tuning can serve as a course tuning. A temperature variation from -10 to 65 ^{o}C corresponds to about 14 cm^{-1} change in wavenumber. A new design of temperature controller is introduced using almost the same thermistor and analog voltage controller. Previously the coefficient of temperature tuning at 45 ^{o}C was about -42.9 ^{o}C/V, while only -4.3 ^{o}C/V near 3 ^{o}C, which means the laser wavenumber step corresponding to one bit change of the Digital/Analog controlling the laser temperature varies from 0.00016 cm^{-1} (4.8 MHz) at temperature T = 3 ^{o}C, to 0.00161 cm^{-1} (48.3 MHz) at T = 40 ^{o}C, compared with 0.009 cm^{-1} (270 MHz) Doppler width

(HWHM). With the new design, the temperature tuning coefficient is much more even throughout the entire temperature region, with -14.2 ^{o}C/V near 3 ^{o}C and -9.7 ^{o}C/V near 45 ^{o}C. This results in a laser frequency step per D/A bit of 16.0 MHz at 3 ^{o}C and 10.9 MHz at 45 ^{o}C. The frequency-current dependence is also discussed in this chapter. When laser current increased from 20 mA to 100 mA, the laser chip shifts about 2 ^{o}C (while holding the thermistor attached to the laser at constant temperature), which equals to about -0.5 cm^{-1} change in frequency. At last, the design of frequency modulation and PID feedback loop is introduced, and when using the optimum modulation amplitude as well as appropriate PID parameters from Tyreus-Luyben method, the laser jitter decreases significantly. Over a time period of 300 seconds, the DFB diode laser frequency drifts have a standard deviation of 4.37 MHz (of averages over 1/60 sec) when there is no feedback applied. This value decreases to only about 0.18 MHz when applying PID parameters from Tyreus-Luyben method.

Chapter 3 introduces using three DFB near-IR lasers to measure the line strengths of CH_3D ro-vibrational transitions ($2\nu_4$) in the wavenumber regions of 6017.5 – 6031.5 cm^{-1} and 6046.5 – 6070.0 cm^{-1} by CW-CRDS. In the wavenumber interval of 6017.5 – 6031.5 cm^{-1}, the strongest peak is located at 6024.697 cm^{-1}, which has a line strength of 1.24×10^{-25} cm/molecule, considering the natural abundance of CH_3D (0.0616 %). In the 6046.5 – 6060.0 cm^{-1} interval, the strongest peak is located at 6055.178 cm^{-1}, which has a line strength of 9.31×10^{-26} cm/molecule. In the 6060.5 – 6070.0 cm^{-1} interval, the strongest peak is located at 6066.538 cm^{-1}, with strength 2.27×10^{-25} cm/molecule. By using the small step size of the laser wavenumber scan, we are able to measure the foreign pressure-broadening and the pressure-shift effects on CH_3D absorption lines. The N_2, O_2 and CO_2 pressure-broadening coefficients of

CH_3D are 0.064(1), 0.060(1) and 0.061(5) cm^{-1}/atm respectively, at the wavenumber of 6017.941 cm^{-1}; and 0.051(1), 0.052(1) and 0.046(2) cm^{-1}/atm respectively, at the wavenumber of 6064.286 cm^{-1}. The N_2 and O_2 pressure-broadening coefficients of CH_3D are 0.065(2) and 0.060(1) cm^{-1}/atm, respectively, at the wavenumber of 6066.538 cm^{-1}. The N_2, O_2 and CO_2 pressure-shift coefficients of CH_3D at the wavenumber of 6032.443 cm^{-1} are -0.012(1), -0.012(1) and -0.013(1) cm^{-1}/atm, respectively. These coefficients are needed for the precise determination of the concentration of CH_3D and thus methane isotopic ratio when present as a trace component in these gases.

Chapter 4 explains our CRDS analysis and double resonance of methane isotopomer CH_3D in near infra-red region. As one of the most important hydrocarbon prototype molecules, CH_3D's overtone band in the near infrared region has not been well studied. This chapter covers the fundamentals of theoretical spectrum analysis, including group theory, rotational spectra of symmetric top molecules, vibrational transition types, Herzberg's character table, irreducible representation, selection rules, etc. Various methods were used to help identifying transitions in previous CW-CRDS experiment result of CH_3D from previous chapter. Symmetric top molecules' Hamiltonian diagonal terms for the ground state, perpendicular state and parallel state are simulated by the publically available software package Pgopher. Combination differences are used to find possible pairs of transitions starting from adjacent ground state rotational levels and ending in same excited states. Also we introduce our temperature controlled spectrum setup for estimating lower state energy and rotational quanta prediction from temperature dependence, which proves to be working well for lower J levels for CH_4. At last, we set up a double resonance system, using two lasers

to excite transitions from the same ground state, to provide strong proof for the lower state quanta.

Chapter 5 describes and tests a novel cell for CW-CRDS. The cell is monolithic and maintains a rigid alignment of the two cavity mirrors. Two high-resolution and high-force PZTs are used to sweep the length of the cell by elastic deformation of the 2.86 cm outer diameter stainless steel tube that makes up the body of the cell. The cavity length is scanned more than 1/2 wavelength of the near-IR light used, which ensures that at least one TEM_{00} mode of the cavity will pass through resonance with the laser. This allows the use of a frequency-locked-laser cw-CRDS technique, which increases the precision of the measurements compared to the alternative of sweeping the laser more than one FSR of the cavity. The performance of the cell is demonstrated by using it to detect the absorption spectrum of methane (CH_4) at the wavenumber regions of around 6051.8 – 6057.7 cm^{-1}.

Bibliography

[1] J. M. Herbelin, J. A. McKay, M. A. Kwok, R. H. Ueunten, D. S. Urevig, D. J. Spencer and D. J. Benard, Appl. Opt., 19(1), 144 (1980).

[2] J. J. Scherer, J. B. Paul, A. O'Keefe, and R. J. Saykally, Chemical Reviews 97, 25 (1997).

[3] D. Z. Anderson, J. C. Frisch, and C. S. Masser, Appl. Opt., 23(8), 1238 (1984).

[4] P. Connes, J. Phys. Radium 19(3), 262 (1958).

[5] D.A. Jackson, Proc. R. Soc. A, Math. Phys. Eng. Sci. 263(1314), 289 (1961).

[6] D.A. Jackson. Proc. R. Soc. London, Ser. A, 263, 289 (1961).

[7] A. Kastler. Nouv. Rev. d'Optique, 5, 133 (1974).

[8] K. Busch and M. Busch, eds., Cavity Ringdown Spectroscopy - An Ultratrace Absorption Measurement Technique, vol. 720 of ACS Symposium Series (American Chemical Society, Washington, D.C., 1999).

[9] M. D. Wheeler, S. M. Newman, A. J. Orr-Ewing, and M. N. R. Ashfold, Journal of the Chemical Society-Faraday Transactions 94, 337 (1998).

[10] G. Berden, R. Peeters, and G. Meijer, International Reviews in Physical Chemistry 19, 565 (2000).

[11] M. Mazurenka, A. J. Orr-Ewing, R. Peverall, and G. A. D. Ritchie, Annual Reports on the Progress of Chemistry, Section C 101, 100 (2005).

[12] C. Vallance, New Journal of Chemistry 29, 867 (2005).

[13] B. A. Paldus and A. A. Kachanov, Canadian Journal of Physics 83, 975 (2005).

[14] A. O'Keefe and D. A. G. Deacon Rev. Sci. Instrum. , 59 (12), 2544 (1988).

[15] Y. Le Grand and A. Le Floch, Applied Optics 27, 4925 (1988).

[16] Y. Le Grand and A. Le Floch, Applied Optics 29, 1244 (1990).

[17] Y. Le Grand, J. P. Tache, and A. Le Floch, Journal of the Optical Society of

America B-Optical Physics 7, 1251 (1990).

[18] A. O'Keefe and O. Lee, American Laboratory 21, 19 (1989).

[19] R. T. Jongma, M. G. H. Boogaarts, I. Holleman, and G. Meijer, Review of Scientific Instruments 66, 2821 (1995).

[20] P. Zalicki, Y. Ma, R. N. Zare, E. H. Wahl, J. R. Dadamio, T. G. Owano, and C. H. Kruger, Chemical Physics Letters 234, 269 (1995).

[21] P. Zalicki, Y. Ma, R. N. Zare, E. H. Wahl, T. G. Owano, and C. H. Kruger, Applied Physics Letters 67, 144 (1995).

[22] T. Yu and M. C. Lin, Journal of the American Chemical Society 115, 4371 (1993).

[23] J. J. Scherer, K. W. Aniolek, N. P. Cernansky, and D. J. Rakestraw, Journal of Chemical Physics 107, 6196 (1997).

[24] G. Meijer, M. G. H. Boogaarts, R. T. Jongma, D. H. Parker, and A. M.Wodtke, Chemical Physics Letters 217, 112 (1994).

[25] R. Evertsen, R. L. Stolk, and J. J. Ter Meulen, Combustion Science and Technology 149, 19 (1999).

[26] R. Evertsen, J. A. Van Oijen, R. T. E. Hermanns, L. P. H. De Goey, and J. J. Ter Meulen, Combustion and Flame 132, 34 (2003).

[27] R. Evertsen, J. A. van Oijen, R. T. E. Hermanns, L. P. H. de Goey, and J. J. ter Meulen, Combustion and Flame 135, 57 (2003).

[28] R. L. Vander Wal and T. M. Ticich, Applied Optics 38, 1444 (1999).

[29] C. Schoemascker-Moreau, E. Therssen, M. X., J. F. Pauwels, and P. Desgroux, Applied Physics B 78, 485 (2004).

[30] S. Cheskis, Progress in Energy and Combustion Science 25, 233 (1999).

[31] M. D. Wheeler, A. J. OrrEwing, and M. N. R. Ashfold, Journal of Chemical Physics 107, 7591 (1997).

[32] M. D. Wheeler, A. J. OrrEwing, M. N. R. Ashfold, and T. Ishiwata, Chemical Physics Letters 268, 421 (1997).

[33] F. Ito and T. Nakanaga, Journal of Chemical Physics 119, 5527 (2003).

[34] A. D. Sappey, E. S. Hill, T. Settersten, and M. A. Linne, Optics Letters 23, 954 (1998).

[35] J. E. Thompson, B. W. Smith, and J. D. Winefordner, Analytical Chemistry 74, 1962 (2002).

[36] J. E. Thompson, H. D. Nasajpour, B. W. Smith, and J. D. Winefordner, Aerosol Science and Technology 37, 221 (2003).

[37] D. B. Atkinson, Analyst 128, 117 (2003).

[38] S. S. Brown, Chemical Reviews 103, 5219 (2003).

[39] K. C. Clemitshaw, Critical Reviews in Environmental Science and Technology 34, 1 (2004).

[40] J. M. Antonietti, M. Michalski, U. Heiz, H. Jones, K. H. Lim, N. Rosch, A. Del Vitto, and G. Pacchioni, Physical Review Letters 94, 213402 (2005).

[41] A. Del Vitto, G. Pacchioni, K. H. Lim, N. Rosch, J. M. Antonietti, M. Michalski, U. Heiz, and H. Jones, Journal of Physical Chemistry B 109, 19876 (2005).

[42] S. Gilb, K. Hartl, A. Kartouzian, U. Peter, J.and Heiz, H. G. Boyen, and P. Ziemann, The European Physical Journal D 45, 501 (2007).

[43] D. Romanini, A. A. Kachanov, N. Sadeghi, and F. Stoeckel, Chemical Physics Letters 264, 316 (1997).

[44] D. Romanini, J. Gambogi, and K. K. Lehmann, “Cavity ring-down spectroscopy with cw diode laser excitation”, (1995). Talk RH06 in 50th International Symposium of Molecular Spectroscopy, Columbus OH.

[45] K. K. Lehmann, “Ring-down cavity spectroscopy cell using continuous wave excitation for trace species detection”, (1996). Patent number 5528040.

[46] B. A. Paldus and R. N. Zare, “Swept continuous wave cavity ring-down spectroscopy”, (2002). US Pat. 6466322.

[47] H. Huang, and K. K. Lehmann, Chemical Physics Letters, 463(1), 246-250 (2008).

[48] H. Huang, and K. K. Lehmann, Optics express, 15(14), 8745-8759 (2007).

[49] H. Huang and K. K. Lehmann, Applied optics, 49(8), 1378-1387 (2010).

[50] H. Huang and K. K. Lehmann, Applied optics, 47(21), 3817-3827 (2008).

[51] H. Huang and K. K. Lehmann, Applied Physics B, 94(2), 355-366 (2009).

[52] D. Romanini, K. K. Lehmann, J. Chem. Phys., 99, 6287 (1993).

[53] A. E. Siegman, Lasers, University Science Books; Mill Valley, CA (1986).

[54] K. K. Lehmann, D. Romanini, J. Chem. Phys., 105, 10263–10277 (1996).

[55] D. Romanini, A. A. Kachanov, and F. Stoeckel, Chemical Physics Letters 270, 538 (1997).

[56] B. A. Paldus, J. S. Harris, J. Martin, J. Xie, and R. N. Zare, Journal of Applied Physics 82, 3199 (1997).

[57] M. Mazurenka, A. J. Orr-Ewing, R. Peverall, and G. A. D. Ritchie, Annual Reports on the Progress of Chemistry, Section C 101, 100 (2005).

[58] B. A. Paldus, C. C. Harb, T. G. Spence, R. N. Zare, C. Gmachl, F. Capasso, D. L. Sivco, J. N. Baillargeon, A. L. Hutchinson, and A. Y. Cho, Optics Letters 25, 666 (2000).

[59] D. Romanini, I. Ventrillard, G. Méjean, J. Morville and E. Kerstel, Introduction to cavity enhanced absorption spectroscopy. In Cavity-Enhanced Spectroscopy and Sensing (pp. 1-60). Springer Berlin Heidelberg (2014).

[60] R. Engeln, G. Berden, R. Peeters and G. Meijer, Rev. Sci. Instrum., 69, 3763−3769 (1998).

[61] A. O'Keefe, J. J. Scherer and J. B. Paul, Chem. Phys.Lett., 307, 343−349 (1999).

[62] R. Peeters, G. Berden, A. Apituley and G. Meijer, Appl. Phys. B, 71, 231−236 (2000).

[63] J. Ye, L.S. Ma and J.L. Hall, J. Opt. Soc. Am. B **15**(1), 6 (1998).

[64] R. Engeln and G. Meijer, Review of Scientific Instruments 67, 2708 (1996).

[65] J.J. Scherer, J.B. Paul, A. O'Keefe, R.J. Saykally, Chem. Rev. 97, 25 (1997).

[66] M.D. Wheeler, S.M. Newman, A.J. Orr-Ewing, M.N.R. Ashfold, J. Chem. Soc. Faraday Trans. 94(3), 337 (1998).

[67] G. Berden, P. Peeters, G. Meijer, Int. Rev. Phys. Chem. 19(4), 565 (2000).

[68] G. Berden, G. Meijer,W. Ubachs, in Experimental Methods in the Physical Sciences, vol. 40 (Elsevier, Amsterdam, 2003), pp. 47–82.

[69] B.A. Paldus, A.A. Kachanov, Can. J. Phys. 83(10), 975 (2005).

[70] M.I. Mazurenka, A.J. Orr-Ewing, R. Peverall, G.A.D. Ritchie, Annu. Rep. Prog. Chem., Sect. C, Phys. Chem. 101, 100 (2005).

[71] C. Vallance, New J. Chem. 29(7), 867 (2005).

[72] K.W. Busch, M.A. Busch, Cavity-Ringdown Spectroscopy (American Chemical Society, Washington, 1999), pp. i–vii.

[73] R.D. van Zee, J.P. Looney (eds.), Experimental Methods in the Physical Sciences, vol. 40 (Academic Press, New York, 2003), pp. 1–323.

[74] G. Berden, R. Engeln, Cavity Ring-Down Spectroscopy: Techniques and Applications (Wiley-Blackwell, West Sussex, 2009)

[75] R. R. Alfano, ed., The Supercontinuum Laser Source (Springer, 2006), 2nd ed.

[76] J. Ye, H. Schnatz, and L. W. Hollberg, IEEE Journal of Selected Topics in Quantum Electronics 9, 1041 (2003).

[77] M. J. Thorpe, D. D. Hudson, K. D. Moll, J. Lasri, and J. Ye, Optics Letters 32, 307 (2007).

[78] P. Johnston and K. K. Lehmann, Optics Express 16, 15013 (2008).

[79] K. K. Lehmann and P. Rabinowitz, “High-finesse optical resonator for cavity ring-down spectroscopy based upon Brewster’s angle prism retroreflectors”, (1999). US Pat. 5973864.

[80] T. Gherman and D. Romanini, Optics Express 10, 1033 (2002).

[81] M. J. Thorpe, K. D. Moll, R. J. Jones, B. Safdi, and J. Ye, Science 311, 1595 (2006).

[82] M. J. Thorpe, D. Balslev-Clausen, M. S. Kirchner, and J. Ye, Optics Express 16, 2387 (2008).

[83] J. M. Langridge, Optics Express 16, 10178 (2008).

Chapter 2 DFB semiconductor diode laser tuning and stabilization

Two different ways to tune DFB semiconductor diode lasers are discussed in this chapter. Temperature tuning, monitored by a thermistor bound to the laser chip, can serve as a course tuning element. The temperature variation from -10 to 65 ^{o}C corresponds to about -14 cm^{-1} change in the wavenumber of the laser output. A new design of temperature controller was introduced using the same thermistor and analog voltage controller. Previously the temperature tuning coefficient at 45 ^{o}C is about -42.9 ^{o}C/V, while only -4.3 ^{o}C/V near 3 ^{o}C, which means the laser wavenumber step corresponding to one bit change of the Digital/Analog unit controlling the laser temperature varies from 0.00016 cm^{-1} (4.8 MHz) at temperature T = 3 ^{o}C, to 0.00161 cm^{-1} (48.3 MHz) at T = 40 ^{o}C, comparing with 0.009 cm^{-1} (270 MHz) Doppler width (HWHM). With the new design, the varying coefficient is much more even throughout the entire temperature region, with -14.2 ^{o}C/V near 3 ^{o}C and -9.7 ^{o}C/V near 45 ^{o}C. The frequency-current dependence is also discussed in this chapter. When laser current increases from 20 mA to 100 mA at constant thermistor temperature, the laser chip shifts about -2 ^{o}C, which results in about -0.5 cm^{-1} change in wavenumber. At last, the design of a frequency modulation and PID feedback loop is demonstrated, and when using the optimum modulation amplitude as well as appropriate PID parameters from Tyreus-Luyben method, the laser jitter decreases significantly. Over a time period of 300 seconds, the DFB diode laser frequency drifts have a standard deviation of 4.37 MHz when there is no feedback applied. This value decreases to only about 0.18 MHz when applying optimum PID feedback parameters.

2.1 Introduction

A standard Fabry Perot (FP) laser consists of an optical gain medium and two mirrors on the output facets of the laser, forming a FP cavity to provide optical feedback [1]. The problem with standard FP lasers is that they generate many wavelengths over a broad spectral region with too great a linewidth for many applications, such as telecommunications [2], spectroscopic sensing [3], terahertz waves [4], infra-red countermeasures [5], quantum key cryptography [6], atomic clock state preparation [7-8], frequency doubling [9], and photodynamic therapy [10].

As one of the first few single frequency lasers, the first demonstration of the basic concepts of Distributed feedback (DFB) laser diodes were found in a certificate by Soviet inventors Alferov et al [18] in 1971. In this certificate, they described two ideas [19] that were later used by DFBs and distributed Bragg reflectors (DBRs): the grating for diffraction is formed on the surface of waveguide layer instead of in the bulk; the interaction between diffraction grating and waveguide modes provides both the distributed feedback and the well collimated radiation at the output.

DFB laser diode, which consists of Bragg grating structure within the semiconductor as resonator, is one of the solutions for generating narrow linewidth. Unlike using discrete mirrors, which would result in either multiple longitudinal modes being excited simultaneously or mode hopping among different longitudinal modes, the grating in DFB laser diode only reflects narrow bandwidth and thus operates in a single longitudinal and transverse mode. Therefore, the emission of a DFB laser usually has precise wavelength with a narrow linewidth, which can be smaller or on

the order of a few MHz [11-17]. A picture of a DFB laser diode used in our work is shown in Figure 1.

Figure 1. Picture of DFB laser diode. Model number: NEL model NLK 1556STG, 15mW output power, 14 pin butterfly, +/-1nm accuracy, PANDA-PMF fiber, FC/Angled PC connector.

As mentioned above, because of its design of using a Bragg grating as the laser cavity, only a very narrow linewidth, whose wavelength usually equals to the period of Bragg grating, can get amplified within DFB laser diodes. Also, the absence of critical opto-mechanical components, for example discrete mirrors compared with traditional laser cavity, results in less noise from mechanical vibrations. By fine temperature and current control, high long-term stability and reliability can be easily achieved.

DFB lasers are very sensitive to temperature change [20-23], which is used as an effective way for tuning and will be described later. Also, DFB lasers are extremely sensitive to reflections reentering the cavity [24-30], so usually there will be an

isolator to minimize reflection interference effect. Another disadvantage is that the laser output power is usually not very big, and conditions like laser current and temperature variation usually would cause significant power fluctuation. Therefore precise temperature control, power control and optical isolation are all required.

Because of the narrow linewidth and precise wavelength tuning, DFB lasers have been widely used in absorption spectroscopy [31-33], gas monitoring [34,40-41], trace gas analysis [35-39], molecular and atomic spectroscopy [42-43], etc. They are also commonly used in various laser cooling techniques, including Doppler cooling, magneto optical trapping, atomic fountains, and optical dipole traps.

2.2 Temperature tuning

As mentioned in the first part, the grating acts as both light reflecting and wavelength selective element. The refractive index of grating material changes with temperature because of thermal expansion. (The DFB diodes in our CRDs experiments are NEL UL band CW DFB lasers near 1600nm, with specifications of: 10 or 15mW output power, 14 pin butterfly type, +/-1nm accuracy, PANDA-PMF fiber, FC/Angled PC connector. The wavenumber of DFB laser diode output beam varies about -0.25 cm^{-1}/ ^{o}C, with a small nonlinear dependence. The temperature controllers are Wavelength Electronics HTC1500 and HTC3000, which provide linear temperature stability of less than 1 mK.) Usually we operate the DFB lasers to work between 3 to 45 C^{o}. If lower than $3C^{o}$, the temperature controller gets significantly noisier, and high temperature might also damage the diode. One thing that needs to be emphasized is that the DFB laser diodes we use (NTT Electronics Corporation, model NLK1U5EAAA) are vacuum sealed. If they have open cases, one should never use

the diode below the water vapor dew point temperature, which would cause unrepairable damage to the diode.

From Steinhart equation, the resistance of a semiconductor thermistor is

$$\frac{1}{T} = C_1 + C_2 \ln(R) + C_3 [\ln(R)]^2 \quad (1)$$

where $C_1 = 1.1292E\text{-}3$, $C_2 = 2.3411E\text{-}4$, $C_3 = 8.7755E\text{-}8$ from the NEL lasers specifications and T is in Kelvin.

The laser chip is mounted on a Thermoelectric cooling (TEC) plate and the laser temperature is controlled by the current passing through this TEC. The traditional temperature controllers pass the output of a precision constant current source through the laser thermistor and adjust the voltage across the thermistor while maintaining constant current. For a thermistor current of $I=100\ \mu A$, the temperature versus voltage (U) across the thermistor is:

$$\frac{1}{T} = C_1 + C_2 \ln\left(\frac{U}{I}\right) + C_3 \left[\ln\left(\frac{U}{I}\right)\right]^2 \quad (2)$$

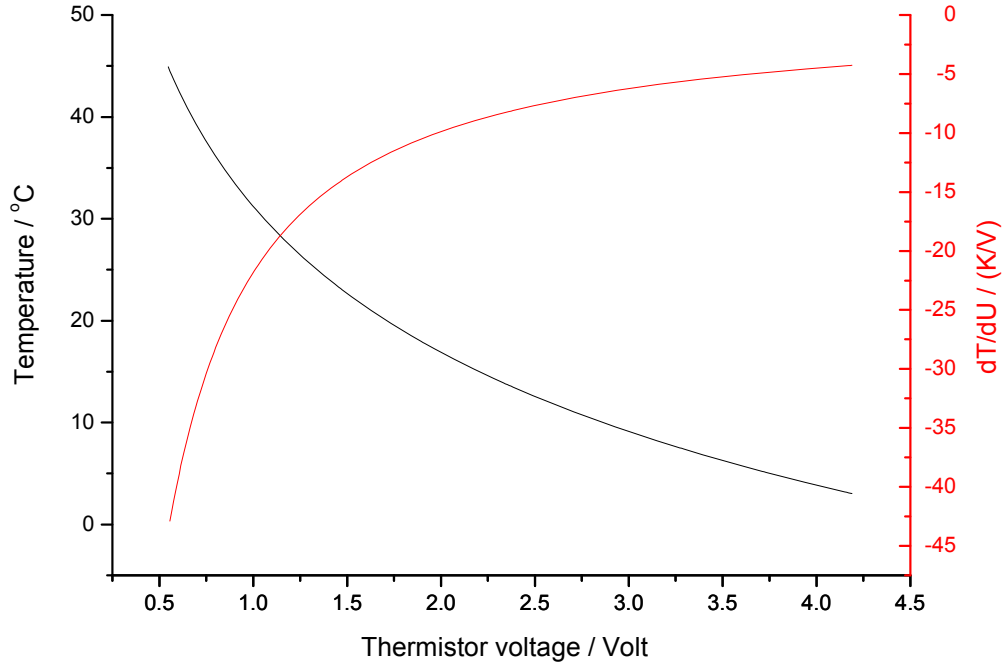

Figure 2. DFB diode laser temperature dependence on thermistor voltage in black curve and temperature variation coefficient in red. The change at high temperature end is significantly faster than that at low temperature end, when varying the same amount of voltage applied to thermistor. The varying coefficient at 45 ºC is about -42.9 ºC/V, while only -4.3 ºC/V near 3 ºC.

From equation 2, it is obvious that there is a non-linear dependence of voltage U versus temperature T. *U* is controlled by a 16bit D/A convertor (Measurement Computing USB3103) with an output that can vary between 0 to 10V, with a single bit step size of $10V/2^{16} = 0.15mV$. The laser wavenumber step corresponding to this one bit change of the D/A controlling the laser temperature varied from 0.00016 cm^{-1} (4.8 MHz) at temperature T = 3 ºC, to 0.00161 cm^{-1} (48.3 MHz) at T = 45 ºC, due to the nonlinear temperature dependence of the thermistor incorporated in the laser. These are comparible to the 0.009 cm^{-1} (270 MHz) Doppler width (HWHM) of the methane lines in the NIR.

In order to solve the nonlinear temperature varying step size problem, our new design is to use a voltage divider. Instead of using constant current mode, we put the thermistor R in series with fixed resistor R', and R and R' are driven by a fixed voltage source U'. Both R' and U' have very low temperature coefficients. By varying the voltage U across thermistor R (whose value determines the temperature), we have

$$\frac{1}{T} = C_1 + C_2 \ln\left(\frac{U \cdot R'}{U'-U}\right) + C_3\left[\ln\left(\frac{U \cdot R'}{U'-U}\right)\right]^2 \qquad (3)$$

where $R' = 7.26\ k\Omega$, $U' = 10\ V$.

In this case, the smallest R in our temperature range from -10 to 65 degrees is about 70% of the largest value, as shown in figure 3. This results in a laser frequency step per D/A bit of 16.0 MHz at 3 ^{o}C and 10.9 MHz at 45 ^{o}C, which allows good sampling of Doppler limited peaks throughout the scan range. The more constant tuning rate also allows for better optimization of the temperature controller feedback parameters. We also expand the temperature tuning region (previously 3 to 45 ^{o}C and significant noise increase below 3 ^{o}C). With this new design, in the larger temperature region, -10 to 65 ^{o}C, no obvious noise increase is observed at low or high temperature region

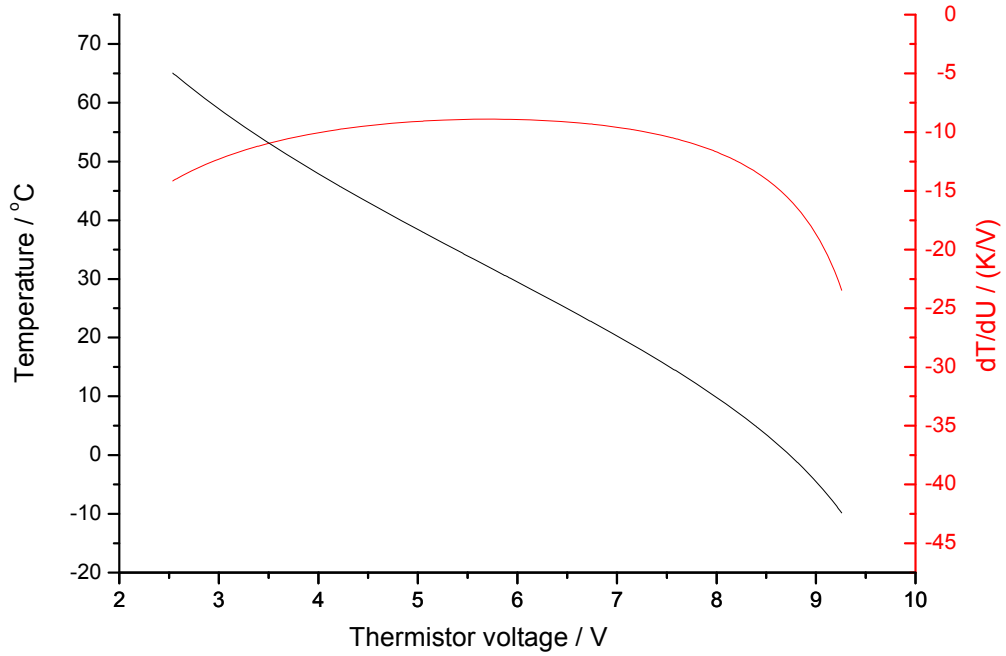

Figure 3. DFB diode laser temperature dependence on thermistor voltage when using the voltage divider design. The temperature-voltage varying coefficient are not too different throughout the whole region. The varying coefficient is -14.2 ºC/V near 3 ºC, -9.7 ºC/V near 45 ºC.

A typical CRDS spectrum that results from a laser temperature sweep with our setup is shown in figure 4.

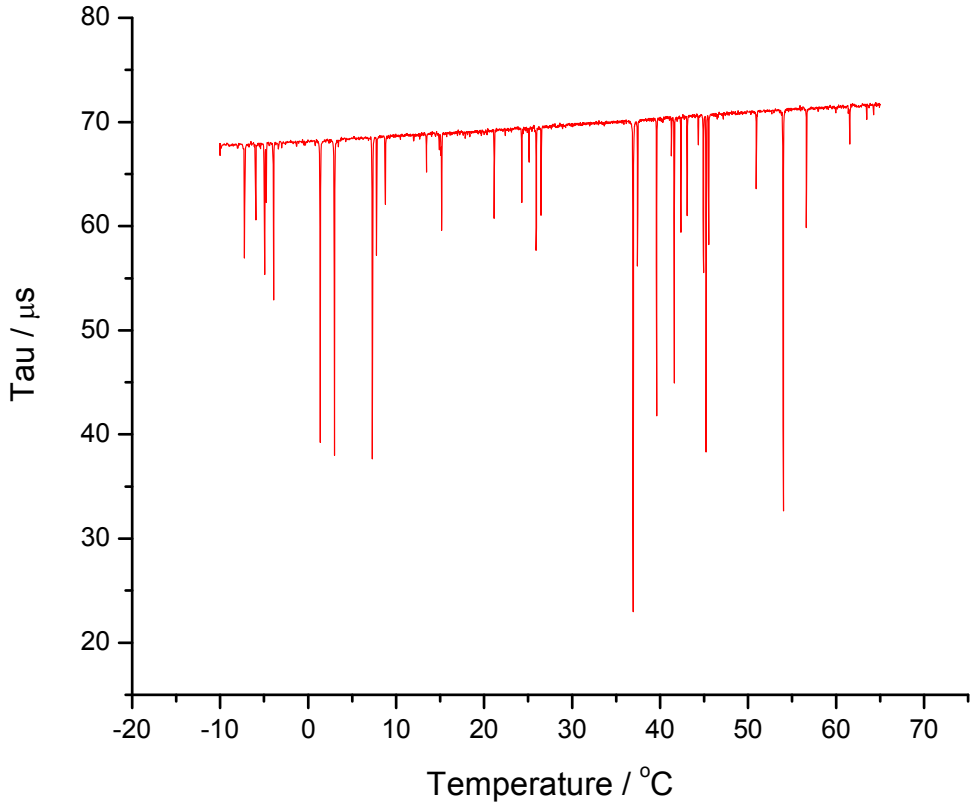

Figure 4. Typical CRDS absorption spectrum when varying DFB laser diode temperature. There were 5 parts per million (ppm) CH_4 in the cavity in ~8 torr N_2 gas, and the temperature varying from -10 to 65 °C corresponds to about 14 cm^{-1} change in wavenumber.

As mentioned before, the laser frequency is not linearly proportional to temperature, so additional calibration needs to be done after using a nonlinear model to convert x axis from DFB laser diode temperature into optical frequency. The easiest and relatively accurate way to calibrate is by comparing the CH_4 absorption peaks against those provided in HITRAN data base [49].

Figure 5 shows the nonlinear correction. The curve joining those points in the graph provides the nonlinear calibration for wavenumber. If keeping other settings the same, the same curve can be repeated when running temperature scan for the same laser diode. The calibrated wavenumbers are within 0.001 cm^{-1} accuracy.

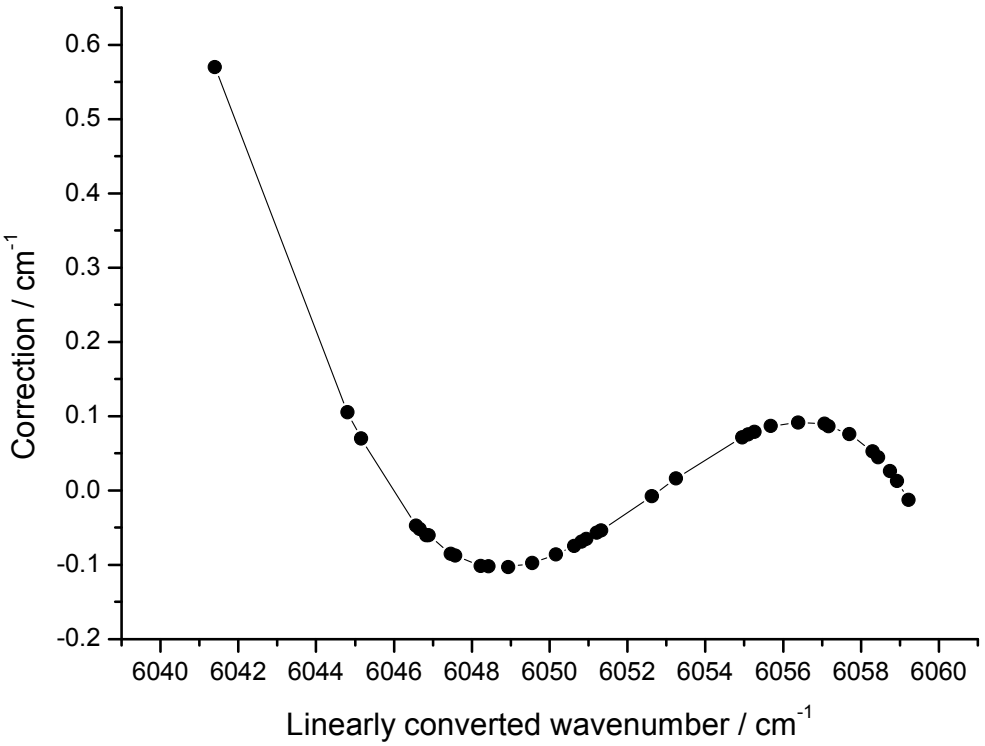

Figure 5. Wavenumber calibration for linear diode temperature conversion. Here the x-axis is wavenumber from linear conversion from DFB laser diode's temperature, the y-axis is the difference when comparing corresponding absorption peaks (the dots in the graph) against those reported in HITRAN database.

2.3 Current tuning

As mentioned before, the current provided to DFB laser controls not only the output power of the diode beam, but also the light frequency. The frequency shifts by

different current value are relatively small compared to temperature tuning, thus it can serve as a fine tuning method for laser frequency.

To get a straightforward view of how much the laser frequency can shift for temperature and current tuning, Figure 6 gives the comparison of temperature tuning when using different current settings for laser power supply, shown as different colors in the graph. The dips on the curve are absorption peaks of CH_3D, the most abundant isotope of CH_4 in the sample used.

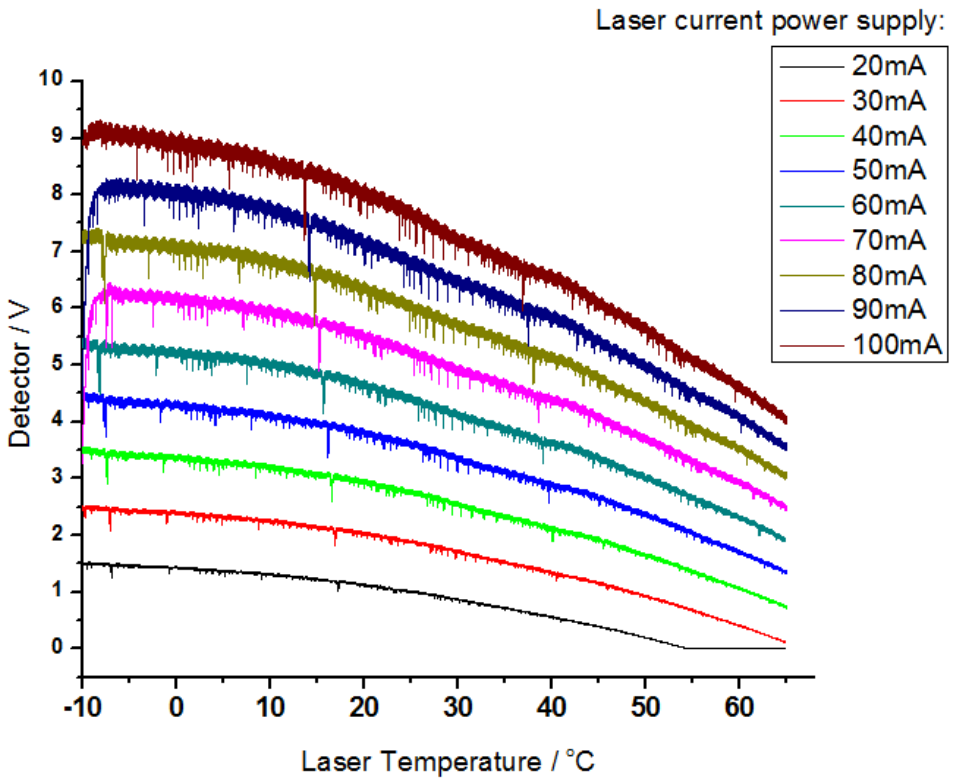

Figure 6. Detector voltage of single pass cell (filled with 8torr 98% CH_3D) at different laser driver current. The current supply (ILX Lightwave ultra low noise current source LDX-3620) can provide constant current 0-200 mA range with less than 100 nA rms noise in battery mode.

It is easy to tell that not only the overall beam power increased proportionally to current increasing from 20 mA to 100 mA, but also the corresponding peaks shifted to lower temperature, which corresponds to larger wavenumber/frequency. For example, one relative strong absorption peak was at about 17 ^{o}C when laser was running at 20 mA, and the same peak showed up at about 15 ^{o}C when the current increased to 100 mA. In other words, the laser shifted for about 2 ^{o}C, which equals to about 0.5 cm^{-1} change in frequency, when current changed for 80 mA. This is primary a thermal effect. At high current modulation frequencies, the current tuning rate drops, reaching a value about one order of magnitude smaller that arises from changes in carrier density inside the laser cavity.

Considering that we usually operate the DFB laser diodes between 50 mA to 100 mA, the maximum frequency tuning we can achieve by varying current is about 0.3 cm^{-1}. Therefore the current tuning can serve as a fine tuning for laser temperature, and also, as a variable for feedback to stabilize laser frequency, which will be discussed in details later.

2.4 Frequency modulation and electronic feedback locking

Normally the DFB lasers in our experiments have a peak-to-peak frequency stability of about 10 MHz in the period of a few seconds, caused by the temperature stability of 1 mK by Wavelength electronics HTC1500 1.5 Amp low profile OEM temperature controllers; and from our previous experiments [44], the frequency drifts about 20 MHz over a time period of 4 hours, which is probably caused by a temperature change of the laser diode by about 0.015 K.

For cavity ring down experiments, the absorption cross sections σ are directly related to the difference of ring-down time with and without absorption species $k(\upsilon)$, as in equation 4. In other words, the improvement in frequency stability can reduce errors in absorption cross section.

$$\sigma(\nu) = \frac{\Delta k(\nu)}{N \cdot c} \tag{4}$$

where N is number density of absorbing gas, and c is speed of light.

What's more, better laser beam frequency stability will also improve cavity transmission by equation 5. The smaller frequency jitter Δν is, the larger the cavity transmission T_c is:

$$T_c = \frac{T^2}{(1-R)^2} \cdot \frac{1}{1 + 2\pi\tau \cdot \Delta\nu} \tag{5}$$

where T is cavity transmission, R is reflectivity, τ is ring down time.

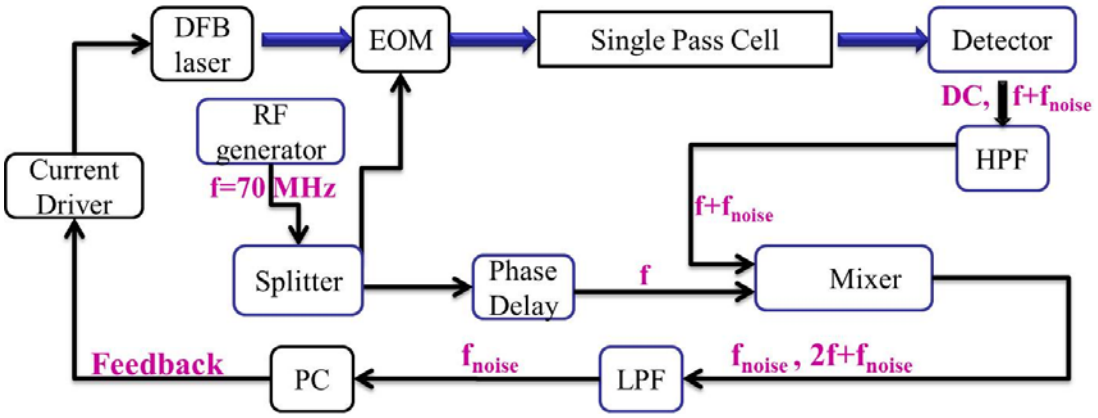

Figure 7. Experimental setup for frequency stabilization of DFB laser diode. RF generator, radio frequency generator; LPF, low pass filter; HPF, high pass filter; EOM, electro-optic modulator.

Our experimental setup for stabilizing laser frequency is shown in figure 7. We use single pass cell absorption as reference to lock the laser beam near the center of the absorption peak. The signal generator (IntraAction ME-70 355nm RF Modular Driver Signal Processor) produces 70 MHz signal. After splitter, part of the signal is sent to an EOM (Sumitomo Osaka Cement co ltd. 10GHz Phase modulator) to modulate DFB laser diode beam. The modulated laser beam then goes through a single pass cell filled with desired gas, 8 torr 98% CH_3D in our experiment, and transmitted light intensity is picked up by detector. After filtering out the DC part of the signal by HPF, the high frequency part of the detector signal is used as signal input (RF) of mixer (Mini circuit coaxial frequency mixer, 0.5 – 500 MHz, 15542 ZAD-1 0 9817). Another input, local oscillator, is from signal generator after phase delay (Tennelec Delay Nim Bin Module, Model TC 412A). The low frequency part of the mixer output is then used as the feedback signal, picked up by analog-digital IO device (Measurement Computing 1608FS), and sent to computer program. The computer

then applies corresponding correction (by digital-analog IO device Measurement Computing 3103) to current supply of laser diode.

If assuming that the modulating signal is a single tone sinusoid

$$m(t) = \alpha \cos(\nu_{\text{mod}} t) \tag{6}$$

where ν_{mod} is the modulation frequency. And it is easy to get

$$a(t) = \int_{-\infty}^{t} m(\tau) d\tau = \frac{\alpha}{\nu_{\text{mod}}} \sin(\nu_{\text{mod}} t) \tag{7}$$

Then the FM signal can be expressed as

$$\varphi_{FM} = e^{(j\nu t + j\beta \sin(\nu_{\text{mod}} t))} \tag{8}$$

where ν is the carrier frequency.

The frequency deviation ratio, also called modulation index, is $\beta = \frac{k_f \alpha}{\nu_{\text{mod}}}$.

The exponential term $e^{j\beta \sin(\nu_{\text{mod}} t)}$ can be expanded in Fourier series

$$e^{\beta \sin(\nu_{\text{mod}} t)} = \sum_{n=-\infty}^{+\infty} C_n e^{jn \sin(\nu_{\text{mod}} t)} \tag{9}$$

where $C_n = \frac{\nu_{\text{mod}}}{2\pi} \int_{-\pi/\nu_{\text{mod}}}^{\pi/\nu_{\text{mod}}} e^{j\beta \sin(\nu_{\text{mod}} t) - jn\nu_{\text{mod}} t} dt$ (10)

We can then substitute the above integral by the n[th] order Bessel function $J_n(\beta)$ of the first kind:

$$\varphi_{FM}(\nu) = \sum_{n=-\infty}^{+\infty} J_n(\beta) e^{(j\nu t + jn\nu_{\mathrm{mod}} t)} \tag{11}$$

The 1f signal would be (neglecting normalization constants)

$$\chi_{FM}(\nu) = -\sum_{n=0}^{5+floor(\beta)} \left[J_n(\beta) \cdot J_{n+1}(\beta) \cdot \left(e^{-[\nu-(n+1)\nu_{\mathrm{mod}}]^2} + e^{-[\nu-n\nu_{\mathrm{mod}}]^2} - e^{-[\nu+n\nu_{\mathrm{mod}}]^2} - e^{-[\nu+(n+1)\nu_{\mathrm{mod}}]^2} \right) \right] \tag{12}$$

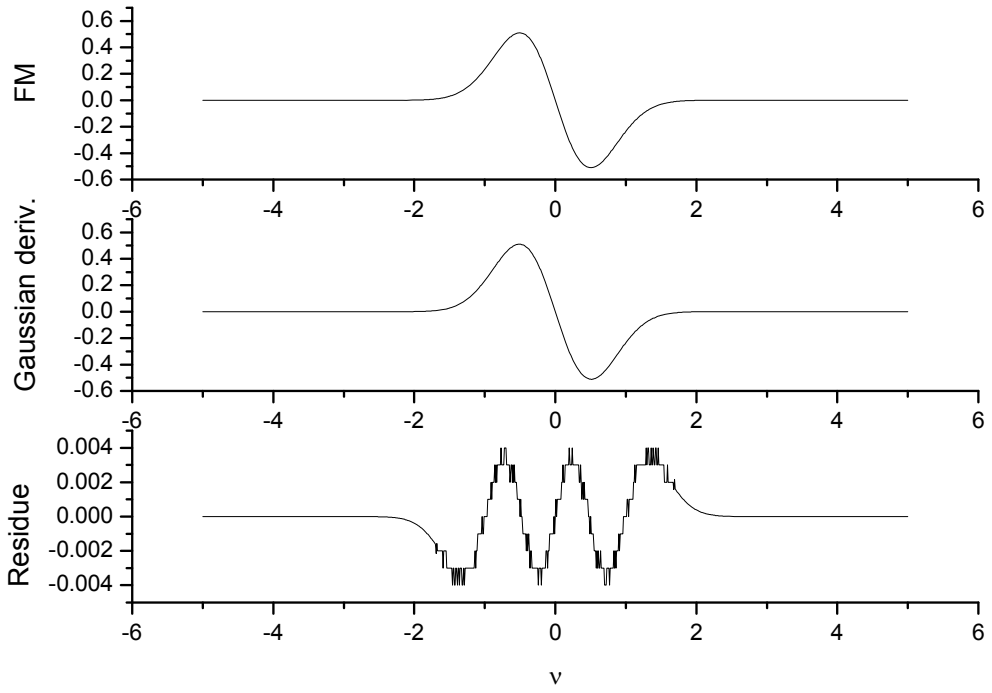

Figure 8. Numerical simulation for fitting FM 1f signal. The x-axis is relative frequency to the center (unit remains to be determined according to different Doppler width of absorption peak in real experiments). The curve on the top is from FM 1f calculation from equation 12. The second curve is from fitting the FM curve to the expression of Gaussian function's first order derivative, $A\left(-\frac{2\nu}{\gamma}\right)e^{-\frac{\nu^2}{\gamma}}$, where A, ν and γ are variables. The bottom curve is the difference between FM calculation and Gaussian derivative fitting.

For simplicity, for a Gaussian absorption line, this 1f signal can be approximately fitted to the form of first order derivative of Gaussian function, which is $A\left(-\frac{2\nu}{\gamma}\right)e^{-\frac{\nu^2}{\gamma}}$. The numerical simulation of Gaussian derivative showed less than 1% difference from equation (12), shown in figure 8.

The reason we use frequency modulation instead of direct absorption is that the sign of FM feedback signal is different for positive and negative frequency drift from the center of peak. Plus it usually comes with a better signal to noise ratio.

Figure 9 is one of the experimental FM 1f signal (from the mixer output), when tuning the laser diode temperature. The absorption peaks were from CH_3D. And as mentioned before, there is peak-to-peak amplitude change as well as frequency drift when laser current varies.

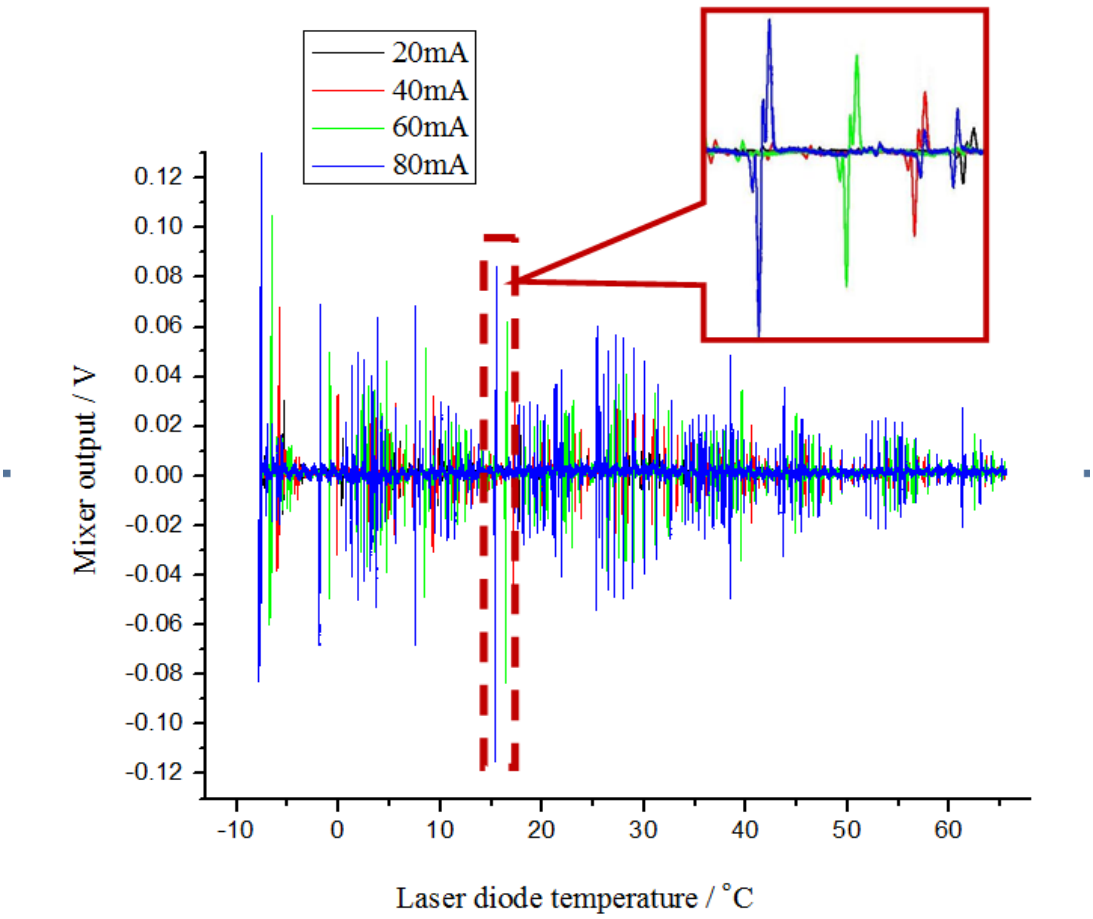

Figure 9. Example of experimental FM 1f signal.

In normal conditions, the DFB diode laser drifts within 20MHz. This is narrower compared to the few hundred MHz frequency region corresponding to the part of FM curve near the absorption peak center, where $\nu=\nu_0$, and approximately linear. The linear slope near absorption center is what we want to get the feedback signal from.

When increasing the modulation amplitude, which is the carrier level of the signal generator, first the peak-to-peak of FM curve increases while the center slope remains about the same. After modulation reaches a certain value, the peak-to-peak value would remain the same while the center slope begins to drop. The optimal modulation index is therefore right before the center slope reaches the maximum value, since it's

also where the peak-to-peak value for 1f FM signal gets maximum. Figure 10 is taken near CH_3D absorption peak at 6055.178cm^{-1}. The frequency variance is about 0 to +/- 1.5GHz. The slope near $v=v_0$ is about 0.78 V/GHz.

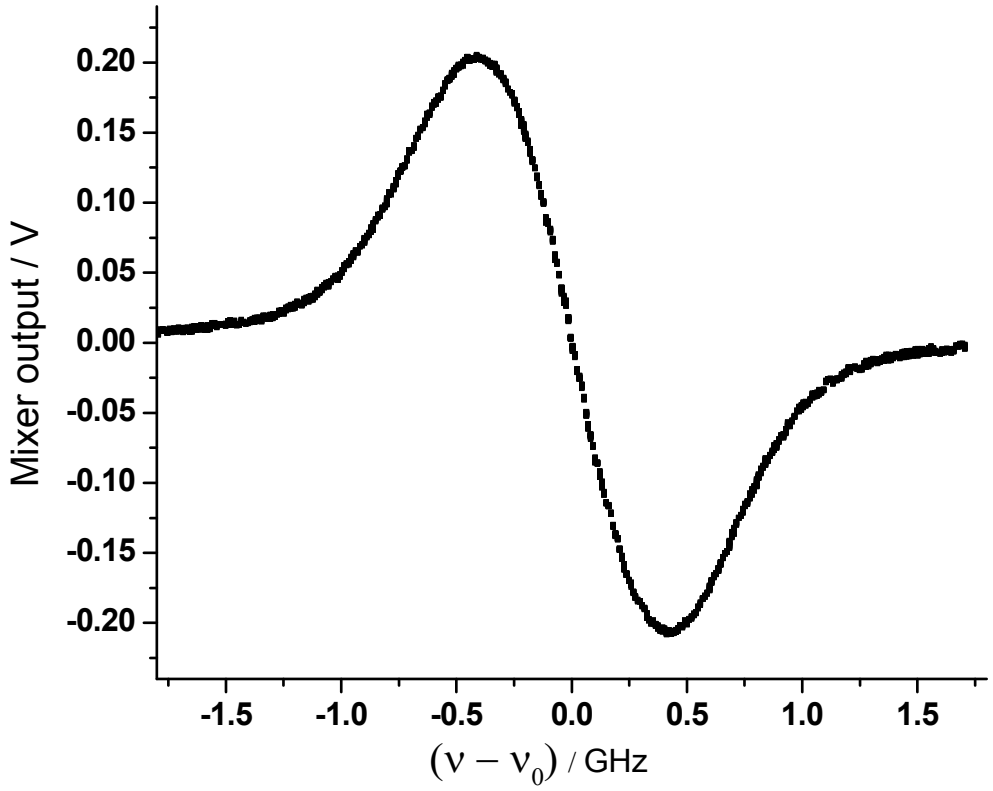

Figure 10. Feedback slope when using the optimal modulation index. The x-axis is frequency difference from the center of this absorption peak. The y-axis is mixer output. The slope near $v=v_0$ is about 0.78 V/GHz.

In order to eliminate 60 Hz and harmonics pick-up noise efficiently, the easiest way is to digitize the feedback signal at high frequency (several hundred kHz) and then average it over periods of 1/60 seconds. When converting mixer output signal into feedback signal, we created a computer program of numerical proportional-integral-derivative controller (PID controller). This program is able to control the proportional,

the integral and derivative values, denoted P, I, and D, as well as overall gain and digitizing time intervals. As we find, by using different PID parameters, the laser stability differs drastically. Figure 11 shows that when just applying proportional gain, e.g. *I=0* and *D=0*, when proportional gain increases at first, the laser gets more stable, and after a certain point, the laser begins to oscillate significantly.

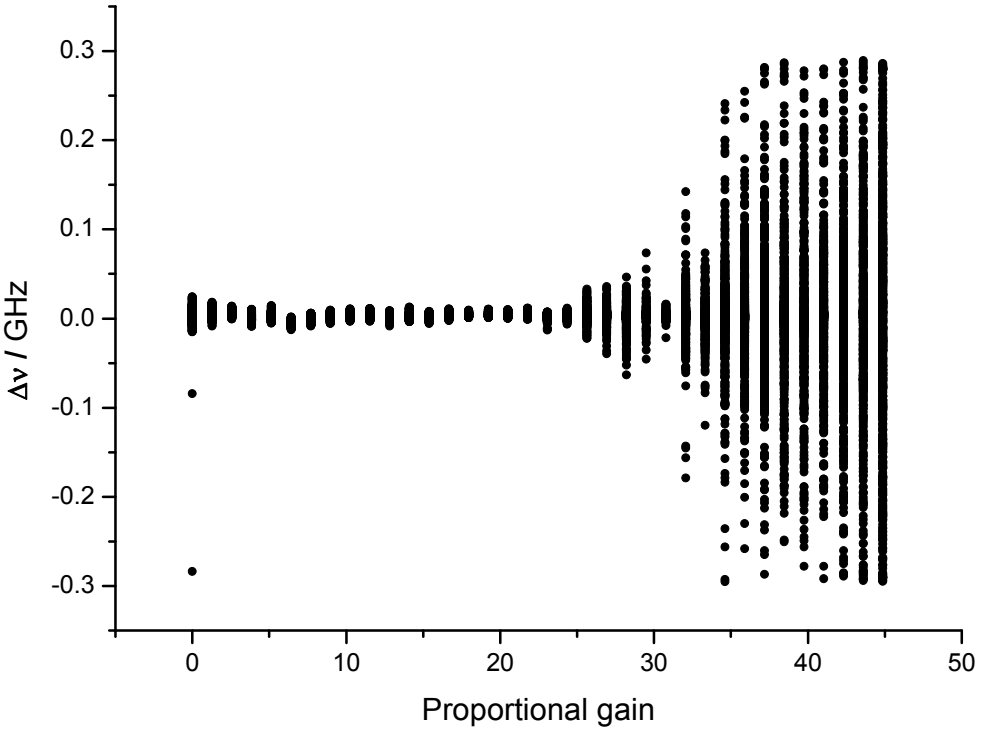

Figure 11. DFB diode laser stability changes according to different proportional gain. DFB laser is near CH_3D absorption peak at 6055.178cm^{-1}. The y-axis is frequency drift from the center of absorption peak. At each gain setting, 2000 real-time diode laser frequencies are collected over a time period of seconds.

When taking *I* and *D* parameters into consideration, the optimum parameters become more complicated to determine. We adopt two popular PID parameter settings,

Ziegler-Nichols tuning rule [45, 47-48] and Tyreus-Luyben tuning rule [46]. The results are shown in Figure 12 and Table 1. It is very obvious that when using parameters from Tyreus-Luyben method, the laser is significantly more stable than under other feedback parameters. Compared with the result when no feedback is applied, the laser jitter is over 20 times smaller.

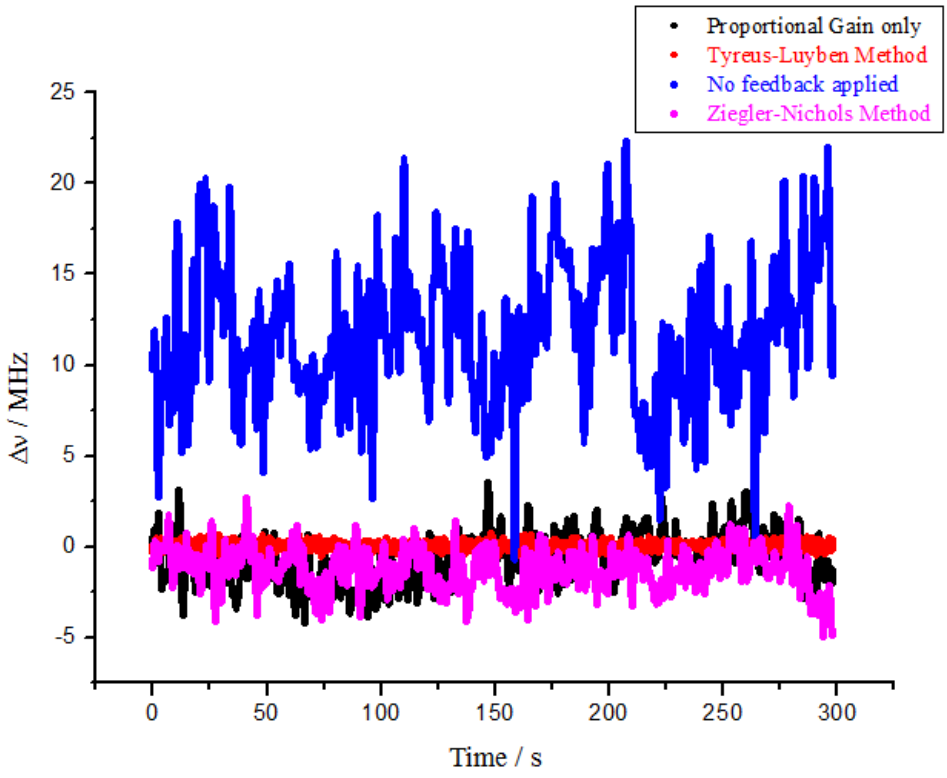

Figure 11. DFB diode laser frequency jitters under different PID feedback parameters. All the measurements are taken over a time period of 300 seconds. The blue points are taken when there is no feedback applied, black when only applying proportional gain, purple when using Ziegler-Nichols tuning rule, and red using Tyreus-Luyben method.

Table 1. Comparison of DFB laser jitters when free running and under different PID feedback controllers. The average column is mean value of frequency drift away from the center the peak. These deviations are for averages over 1/60 sec.

PID parameters	Average / MHz	Standard Deviation / MHz
No feedback applied	12.75845	4.3672
Proportional feedback only	-1.46707	1.25413
Ziegler-Nichols Method	-0.77357	1.44293
Tyreus-Luyben Method	-0.00046	0.18393

2.5 Conclusion

We discussed tuning DFB semiconductor diode lasers by temperature and current in details. The temperature tuning can serve as a course tuning. The temperature varying from -10 to 65 ^{o}C corresponds to about 15 cm^{-1} change in wavenumber. With the new design, the varying coefficient is much more linear throughout the entire temperature region. Also, with frequency modulation and PID feedback loop, and using the optimum modulation amplitude as well as appropriate PID parameters from Tyreus-Luyben method, the DFB laser jitter decreases significantly. Over a time period of 300 seconds, the DFB diode laser frequency drifts have a standard deviation of 4.37MHz when there is no feedback applied. This value decreases to only about 0.18 MHz when applying Tyreus-Luyben method.

Bibliography

[1] A. E. Siegman, Lasers p.2. , University Science Books (1986).

[2] T. Garlington, J. Babbitt and G. Long, Analysis of Free Space Optics as a Transmission Technology, WP No. AMSEL-IE-TS-05001 (1986).

[3] M. N. Fiddler, I. Begashaw, M. A. Mickens, M. S. Collingwood, Z. Assefa, and S. Bililign, Laser Spectroscopy for Atmospheric and Environmental Sensing Sensors 9, 10447-10512 (2009).

[4] G. Scalari, C. Walther, M. Fischer, R. Terazzi, H. Beere,D. Ritchie, and J. Faist, Laser & Photonics Review 3: 45–66 (2009).

[5] D. H. Pollock, J. S. Accetta, and D. L. Shumaker, The Infrared & Electro-Optical Systems Handbook, Countermeasure Systems, Volume 7 (1993).

[6] C. H. Bennett and G. Brassard, In Proceedings of IEEE International Conference on Computers, Systems and Signal Processing, volume 175, page 8 (1984).

[7] Udem, T. et al, Phys. Rev. Lett. 86, 4996–4999 (2001).

[8] Chou, C. W., Hume, D. B., Koelemeij, J. C. J., Wineland, D. J. & Rosenband, T., Phys. Rev. Lett. 104, 070802 (2010).

[9] P. A. Franken et al., Phys. Rev. Lett. 7 (4), 118 (1961).

[10] D. Fukumura, R. K. Jain, Dennis E.J., and G.J. Dolmans, Nature Reviews Cancer 3, 380-387 (2003).

[11] H. Kogelnik and C. V. Shank, J. Appl. Phys. 43 (5), 2327 (1972).

[12] A. Yariv, IEEE J. Quantum Electron. QE-9, 919 (1973).

[13] H. W. Yen et al., Opt. Commun. 9, 35 (1973).

[14] K. H. Ylä-Jarkko and A. B. Grudinin, IEEE Photon. Technol. Lett. 15 (2), 191 (2003).

[15] B. K. Das et al., Opt. Lett. 29 (2), 165 (2004).

[16] K. Sato, IEEE J. Lightwave Technol. 23 (11), 3790 ().

[17] A. Schülzgen et al., Opt. Lett. 33 (6), 614 (2008).

[18] Zh. I. Alferov, V. M. Andreev, R. F. Kazarinov, E. L. Portno, and R. A. Suris, Inventor's Certificate No. 392875 [in Russian], Application No.1677436, priority as of July 19 (1971).

[19] Zh. I. Alferov, The history and future of semiconductor heterostructures, Semiconductors 32 (1) (1998).

[20] M. Nakamura, K. Aiki, J. Umeda and A. Yariv, Appl. Phys. Lett. 27, 403 (1975)

[21] K. Aiki1, M. Nakamura, J. Umeda, A. Yariv, A. Katzir and H. W. Yen, Appl. Phys. Lett. 27, 145 (1975)

[22] Kagi, N., Oyobe, A., and Nakamura, K., J. Lightwave Technology. VOL. 9, NO. 2 (1991)

[23] Yariv, Amnon and Nakamura, Michiharu, IEEE J. Quantum Electronics, VOL. QE-13, NO. 4 (1977)

[24] J. T. Kringlebotn, W. H. Loh and R. I. Laming, Opt. Letters, Vol. 21, pp. 1869-1871 (1996)

[25] K. P. Koo and Wanser, A. D. Kersey, Electron. Lett., Vol 31, pp. 1180-1182 (1995)

[26] J. T. Kringlebotn, Optical fiber distributed feedback laser (distributed feedback laser used as sensor), US Patent 5 844 927, UK Patent 2 299 203, NO Patent 302 441, Optoplan As (1996)

[27] K. Petermann, IEEE J. of Sel. Topics in Q. El., Vol. 1, pp. 480-487 (1995)

[28] K. H. Wanser, Electron. Lett., Vol. 28, pp. 53-54 (1992)

[29] S. Knudsen, Dr.ing. thesis, Norwegian Univ. of Sci. and Tech. NTNU (1996)

[30] G. A. Ball, G. Hull-Allen, C. Holton, and W. W. Morey, Electron. Lett., Vol. 29, pp. 1623-1625 (1993)

[31] Namjou, K.; Roller, C.B.; Reich, T.E.; Jeffers, J.D.; McMillen, G.L.; McCann, P.J.; Camp, M.A., Applied Physics B, 85, 427-435 (2006)

[32] Kim, S.H., Meas. Sci. Technol. (2003)

[33] Allen, M.G., Meas. Sci. Technol., 9, 545-562 (1998)

[34] Werle, P., Spectrochim. Acta. A., 54, 197-236 (1998)

[35] Dahnke, H., Stry, S., and von Basum, G., In Laser in Environmental and Life Science, 1st ed.; Hering, P., Lay, J.P., Stry, S., Eds.; Springer-Verlag: New York, NY, USA; Volume 1, pp. 283-295 (2004)

[36] Werle, P., In Laser in Environmental and Life Science, 1st Ed.; Hering, P., Lay, J.P., Stry, S., Eds.; Springer-Verlag: New York, NY, USA; Volume 1, pp. 223-243 (2004)

[37] Kosterev, A.A.; Tittel, F.K.; Serebryakov, D.V., Rev. Sci. Instrum., 76, 043105 (2005)

[38] Ebert, V.; Hemberger, R.; Meinenburg, W.; Wolfrum, J. In-situ gas analysis with infrared lasers. Ber. Bunsenges. Phys. Chem., 97, 1527-1534 (1993)

[39] Kosterev, A.; Wysocki, G.; Bakhirkin Y.; So S.; Lewicki, R.; Fraser, M.; Tittel, F.; Curl, R.F., Appl. Phys. B 2008, 90, 165-176.

[40] Kelleter, J. Fire-Gas Monitoring Inside Large Industrial Buildings—"Fire-Laser". AUBE '09 14th International Conference on Automatic Fire Detection, Duisburg, Germany (2009)

[41] Fehér, M.; Jiang, Y.; Maier, J.P., Appl. Opt., 33, 1655-1658 (1994)

[42] Ricci, L.; Weidemueller, M.; Esslinger, T.; Hemmerich, A.; Zimmermann, C.; Vuletic, V.; Koenig, W.; Haensch, T.W. , Opt. Commun., 117, 541-549 (1995)

[43] Hildebrandt, L.; Knispel, R.; Stry, S.; Sacher, R.J.; Schael, F., Appl. Opt., 52, 1457-1464. (1998)

[44] Huang, H. and Lehmann, K. K., Applied Optics, Vol. 49, No. 8 (2010)

[45] J. G. Ziegler and N. B. Nichols, Trans. ASME, Vol. 64 (1942)

[46] Luyben, W. and Luyben, M. Essentials of Process Control. McGraw-Hill, New York, 1997.

[47] T. R. Kurfess, Getting in tune with Ziegler-Nichols, Control Engineering magazine, issue, p. 28, (2007).

[48] Karl J. Åström & Tore Hägglund, Automatic Tuning of PID Controllers, Chapter 52, The Control Handbook, IEEE/CRC Press (1995).

[49] P.G.J. Irwin, S.B. Calcutt, F.W. Taylor, and A.L. Weir, J. Geophys. Research 101:26,137-26,154 (1996).

Chapter 3 Measurements of CH_3D Line Strengths, Foreign Pressure-Broadening and Pressure-Shift at near-IR region

Three DFB near-IR lasers are used to measure the line strengths of CH_3D ro-vibrational transitions ($2\nu_4$) in the wavenumber regions of 6017.5 – 6031.5 cm^{-1} and 6046.5 – 6070.0 cm^{-1} using continuous-wave cavity ring-down spectroscopy (cw-CRDS). In the wavenumber interval of 6017.5 – 6031.5 cm^{-1}, the strongest peak is located at 6024.697 cm^{-1}, which has a line strength of 1.24×10^{-25} cm/molecule, considering the natural abundance of CH_3D (0.0616 %). In the 6046.5 – 6060.0 cm^{-1} interval, the strongest peak is located at 6055.178 cm^{-1}, which has a line strength of 9.31×10^{-26} cm/molecule. In the 6060.5 – 6070.0 cm^{-1} interval, the strongest peak is located at 6066.538 cm^{-1}, which gives 2.27×10^{-25} cm/molecule. By using the small step size of the laser wavenumber scan, we are able to measure the foreign pressure-broadening and the pressure-shift effects on CH_3D absorption lines. The N_2, O_2 and CO_2 pressure-broadening coefficients of CH_3D are 0.064(1), 0.060(1) and 0.061(5) cm^{-1}/atm respectively at the wavenumber of 6017.941 cm^{-1}; 0.051(1), 0.052(1) and 0.046(2) cm^{-1}/atm, respectively at the wavenumber of 6064.286 cm^{-1}. The N_2 and O_2 pressure-broadening coefficients of CH_3D are 0.065(2) and 0.060(1) cm^{-1}/atm respectively at the wavenumber of 6066.538 cm^{-1}. The N_2, O_2 and CO_2 pressure-shift coefficients of CH_3D at the wavenumber of 6032.443 cm^{-1} are -0.012(1), -0.012(1) and -0.013(1) cm^{-1}/atm, respectively.

3.1 Introduction

Methane is an important greenhouse gas in the Earth's atmosphere. Although its concentration is much less than CO_2, its greenhouse forcing effect per molecule is 21 -

25 times larger than CO_2 in promoting global warming over a 100-year period [1-3]. Its concentration on Earth has increased from ~ 700 to ~ 1800 ppb since the year 1750 [4-5], while it has stayed nearly constant since 1998 [6]. Methane in the atmosphere has a lifetime of about 9 - 10 years [1, 4], and its primary removal process is the reaction with hydroxyl radicals [7], ultimately producing carbon dioxide and water. Methane also affects the degradation of the ozone layer in the stratosphere and in the troposphere [7]. It was recently reported that the methane-outgassing rate from Earth's oceans is greater than previously thought [8]. Recent studies provided new insights into the microorganisms that inhabit methane-rich sediments, and raised new questions regarding reaction mechanisms [9]. CH_3D, the subject of this paper, has been monitored in the Earth's atmosphere by ATMOS [10-11]

Methane, including the CH_3D isotopomer, has also been found in other locations both within and outside the solar system, including Mars [12-14], Jupiter [15], Saturn [15-17], Uranus [18-20], comets [21-22], and the extrasolar planet HD 189733b [23]. It is particularly well studied on Titan (Saturn's largest moon) because of the rich hydrocarbon chemistry on that body [24-31]. It is believed to have been created by abiotic processes, with the possible exceptions of Mars [12-14] and Titan (Saturn's largest moon) [32-34]. On Mars, the atmosphere contains an average of 10 ppb methane [35-36]. In 2009, NASA scientists announced that Mars often vents methane into the atmosphere in summer in some specific areas [12]. Methane is photodissociated by deep-UV solar radiation [12, 36-37]. The calculated photochemical lifetime of CH_4 on Mars is between 250 and 430 years [36], but the observed rate of variation is sufficiently fast that other destruction mechanisms appear to dominate. It has been speculated that Martian methane bursts might be of gas produced by subsurface biological activity [12,

37-39]. Titan's atmosphere contains 1.6 % methane and thousands of methane lakes have been detected [32]. In its upper atmosphere, methane is converted into more complex molecules including acetylene, a process that also produces molecular hydrogen [32]. There is evidence that acetylene and hydrogen are recycled into methane again near the surface [40]. This suggests the possible presence of an unfamiliar form of methanogenic life [13-14]. The ratios of different methane isotopes might provide constraints on methane's formation and destruction chemistries [41]. For example, Titan's atmosphere is enriched in deuterium by a factor of more than 3 relative to that reported for Jupiter and Saturn atmospheres [42-43].

Detection of trace species continues to be an important application of optical spectroscopic techniques. Cavity ring-down spectroscopy (CRDS) [44] realizes long effective path-lengths, on the order of 100 km, therefore it has been extensively used for the detection of low concentration species in recent decades. Since CRDS records the decay rate of the intracavity light after the excitation laser being turned off, laser intensity fluctuations do not affect the measurement of absorption spectra. Each ring-down event takes no more than a few milliseconds, so CRDS can have a relatively high detection rate. Compared with pulsed-laser CRDS, continuous-wave CRDS provides higher spectral resolution [45-47]. More importantly, stable excitation of only the TEM_{00} modes of the cavity, which is only possible when the excitation laser has a bandwidth much narrower than the free spectral range (FSR) of the cavity, leads to more stable cavity decay rates and thus higher sensitivity of the method. In the IR region, particularly at low pressure, the width of an individual ro-vibrational transition is comparable to the FSR of cavities of convenient length, and then cw excitation of the

cavity is important for the accuracy of the experimentally determined spectrum or the molecular concentrations deduced from it [48].

The eventual goal of this project is to quantify the ratios of the three principle isotopic forms of methane, $^{12}CH_4$ (which will be simplified as CH_4 in this paper), $^{13}CH_4$ and CH_3D, ideally without the need of pre-concentration. The terrestrial natural abundances of these isotopes are 98.8 %, 1.11 %, and 0.0616 %, respectively, using the standard natural atomic abundances [49-50]. Considering the current mean atmospheric molar density of CH_4 is around 1800 ppb, the detection limitation of CH_3D must be better than 1.1 ppb to detect this species and about 2-3 orders of magnitude higher to be useful for characterizing isotopic abundances. Our existing cavity ring-down spectrometer, working in the 1.65 mm spectral region, was demonstrated to have a 3σ methane detection limit of 29 pptv [51] and we are confident that further improvements are possible, particularly by reducing the laser linewidth, and by locking the laser and cavity to increase the optical coupling efficiency and ring-down event rate. We focus on the first C-H overtone spectral region, because the lasers, detectors, and mirrors are all less expensive and have higher performance for building a trace detector than mid-IR component. These factors offset, at least to a considerable degree, the reduced absorption cross section of the overtone transitions in the near-IR compared to the fundamental bands in the mid-IR. For example, Webster and Mahaffy recently described a mid-IR instrument for detection of isotopic abundances of methane [41] and this instrument had a 1σ detection limit of 300 pptv. In order to quantify the ratio of different isotopes, it is necessary to know their line strengths. There were several studies on the absolute CH_3D intensities [52-59]. In the most current version of HITRAN (2008) [49], the line strength of CH_3D absorption in some regions are

included, but no information is available in the near-IR region that we are interested in, except for the $3\nu_2$ (C-D stretch second overtone) in the 6300-6510 cm^{-1} region [49]. In this work, we report the absolute line strengths of CH_3D transitions in the wavenumber regions of 6017.5 – 6031.5 cm^{-1} and 6046.5 – 6070.0 cm^{-1} (mainly rotational lines in the $2\nu_4$ overtone bands) for first time. The strongest lines in those regions are stronger than those of the $3\nu_2$ band and thus they are more favorable for trace detection. The N_2, O_2, and CO_2 pressure-broadening coefficients were also measured for transitions at 6017.941, 6064.286 and 6066.538 cm^{-1}. The pressure-shift coefficients were measured at 6032.443 cm^{-1}.

The spectroscopy literature of methane, and even its CH_3D isotopomer, is considerable. In the mid-IR region, recent studies of CH_3D include [60-64]. There is also a rich literature on the overtone spectral regions of CH_3D, including those in [65-72]. The comprehensive study of the overtone spectrum reported by Ulenikov *et al*. [73], the methane line list compiled by Campargue *et al*. [29], the study of the 1.58 μm region by Wang *et al*. [54], and the prior study of this spectral region using FTIR spectroscopy by Deng *et al*. [74], are particularly relevant for our work. There are also numerous studies of the pressure broadening and pressure shift of lines of CH_3D, but those are in other spectral regions [75-85].

3.2 Experimental

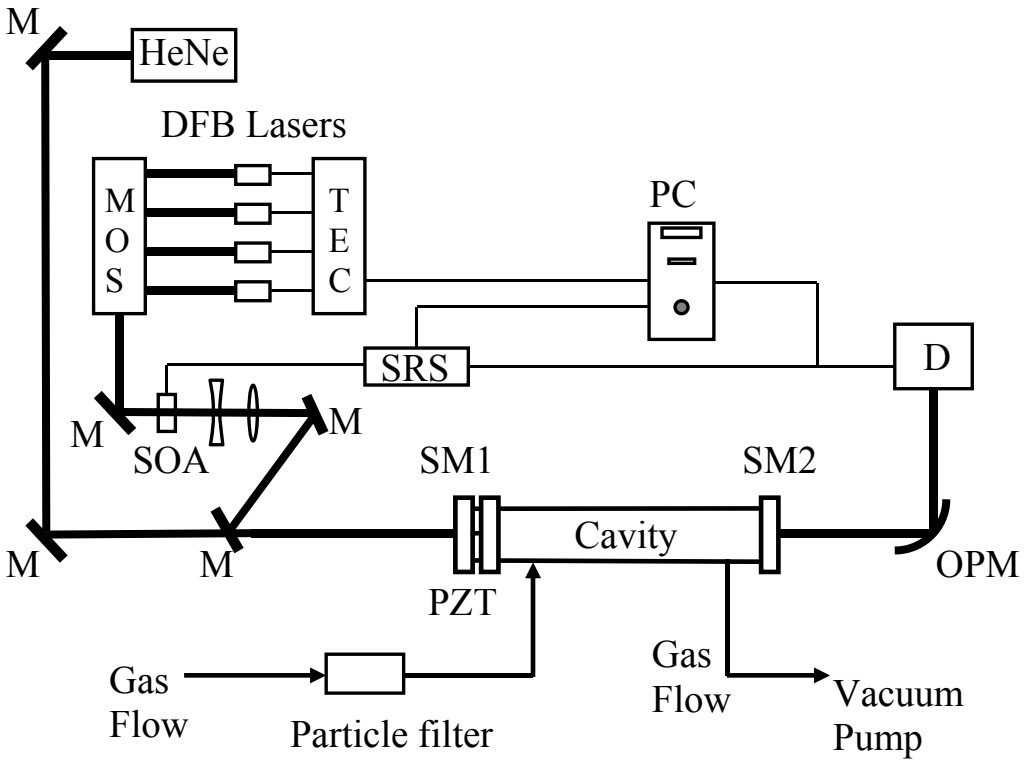

Figure 1 The experimental setup. PZT: piezoelectric transducer. SOA: semiconductor optical amplifier (COVEGA, model BOA5690). MOS: multiple-channel optical switch (Agiltron, model LBPM-41011B333). TEC: temperature controller. SRS: digital delay/pulse generator (Stanford Research System, model DG535). SM: super mirrors (Advanced Thin Films). OPM: off-axis parabolic mirror (Edmond Optics). D: InGaAs detector/amplifier (Tiger Optics).

The experimental setup has been presented elsewhere [46-47, 55]. In Figure 1, each laser's temperature (by wavelength electronics HTC1500 1.5 Amp low profile OEM temperature controllers) and current (by Newport LDX-3200 Series Precision Laser Diode Drivers) can be controlled individually, in order to change its wavelength. The four lasers are then combined into the system by a 4×1 multi-channel optical switch.

After a fiber beam splitter, part of the laser beam would go through the semi-conductor optical amplifier (SOA), which serves as a shut-off for continuous wave laser beam, and then the laser beam is carefully coupled into the cavity. He-Ne laser was used to help with the alignment. The cavity has two super mirrors; one of them is attached to PZT which can slightly change the length of the cavity. When the laser is on resonance with the cavity, and when the detector after the cavity would get a signal higher than threshold, the pulse generator would be triggered and send the pulse to shut down SOA. Then the data acquisition device (Measurement Computing PCI-DAS6000 series 12-bit multifunction board) picks up the intensity changing of transmitted light. And the computer would use exponential fitting to get the decay time.

The major change of our setup from previous presentation is that four distributed feedback (DFB) lasers will eventually be used for the measurements of three methane isotopes and the baseline. In this work, three lasers (NTT Electronics Corporation, model NLK1U5EAAA), with room temperature wavelengths around 1650.1, 1652.0 and 1660.8 nm respectively, were used to quantify the spectroscopic properties of CH_3D. Each laser module was independently driven by an ultra-low noise current source (ILX Lightwave, model 3620). The laser temperature was stabilized by using a temperature controller (Wavelength Electronics, models HTC1500 or HTC3000) controlled by a 16-bit D/A board (Measurement Computing, model USB-3103). The laser wavenumber step corresponding to one bit change of the D/A controlling the laser temperature varied from 0.00046 cm^{-1} (14 MHz) at temperature T = 3 ^oC, to 0.0033 cm^{-1} (99 MHz) at T = 40 ^oC, due to the nonlinear temperature dependence of the thermistor incorporated in the laser. These can be compared with 0.009 cm^{-1} (270 MHz) Doppler width (*HWHM*). The typical wavenumber step was between 1 and 8 times the minimum

value. No significant peak intensity difference was observed when different step sizes were employed. When we measured the pressure-broadening and pressure-shift coefficients, we used the minimum step sizes. The cavity and the signal collection were the same as previous reports [46-47, 55].

All the measurements were conducted at room temperature, 294(2) K. The pressure was monitored using several pressure gauges, including capacitance manometers (MKS-Baratron models 127AA-01000B, 0 – 1000 Torr, and 627B12TDC2B, 0 – 100 Torr), and Bourdons gauges (Pennwalt, models FA160, 0 – 20 or 0 – 400 Torr). The 1000 Torr Baratron gauge was calibrated against the local atmospheric pressure, as reported by the National Weather Service. Its linearity was tested by successive dilution of a fixed volume into another of ~ 80% of its volume, followed by pumping this secondary volume. The other gauges were calibrated against the 1000 Torr gauge. We estimate the remaining systematic errors in our pressure measurements to be within 2 % of the reading.

During the CRDS measurements, CH_3D samples were diluted twice in order to reach a suitable number density, which introduced an additional source of uncertainty. A single-pass 42.5 cm long cell filled with pure CH_3D, or $^{13}CH_4$, was used to determine the absorption strength of the strongest lines from transmission *vs.* wavenumber scans, using Beer's law. These lines were then used to calibrate the CH_3D concentrations in the CRDS cell, allowing quantitative determination of the absorption strength of the weaker lines. An Indium Gallium Arsenide (InGaAs) detector (Thorlabs, model PDA10CF) was used to measure the intensity of light transmitted through the single-

path cell. We also used this absorption cell to provide stable laser frequency values for the pressure-shift measurements.

CH_3D (98 % reported purity) and $^{13}CH_4$ (99 % reported purity) lecture bottles were purchased from ISOTEC. N_2, O_2, CO_2 and CH_4 (5.01 ppm in N_2) cylinders were purchased from GT&S/Praxair.

3.3 Results and Discussion

CH_3D, in high purity N_2 gas, was introduced into the cavity with a total pressure around 8.3 Torr. The CH_3D number densities varied between (0.5-2.0) $\times$ 10^{14} molecule/cm^3. The absorption spectra of CH_3D in different wavenumber regions were measured by using three DFB lasers. Four or five laser temperature scans were performed at each wavenumber region. Depending on the ring-down trigger rate during the experiments, sometimes one sample mixture covered the full wavenumber region of one laser, while sometimes several mixtures were used. Figure 2 shows a typical absorption spectrum of CH_3D measured using CRDS. The manufacturer specified laser frequency *vs.* temperature tuning coefficient of the laser wavenumber was -12.5 GHz/^{o}C, *i.e.* -0.417 $cm^{-1}/^oC$. In this work, the wavelength/wavenumber of each laser was independently obtained by using the absorption lines of CH_4, H_2O and CO_2, which have been well studied and tabulated in HITRAN [49]. The observed temperature coefficients for our lasers are -0.422(1) $cm^{-1}/^oC$ (6017.5 – 6031.5 cm^{-1} laser), -0.431(1) $cm^{-1}/^oC$ (6046.5 – 6060.0 cm^{-1} laser), and -0.427(1) $cm^{-1}/^oC$ (6060.5 – 6070.0 cm^{-1} laser) respectively.

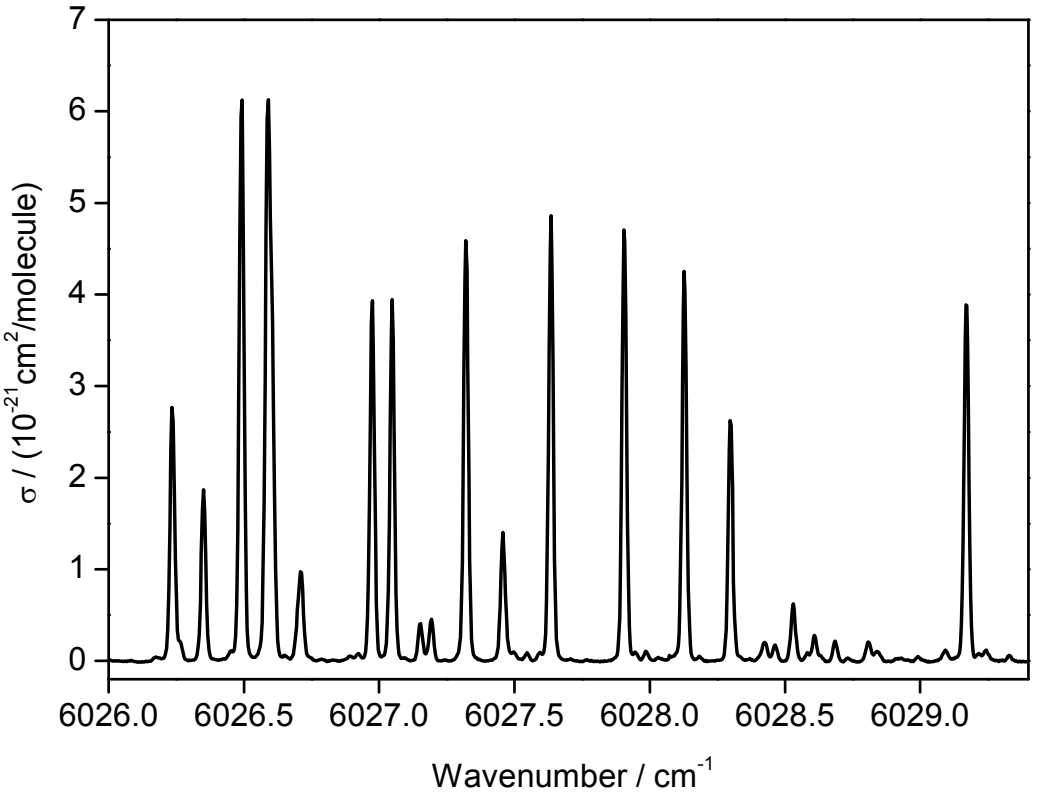

Figure 2 Cavity ring-down spectroscopy of CH_3D in ~ 8.3 Torr N_2 buffer gas. The CH_3D number density was 5.2×10^{13} molecule/cm^3.

The absorption cross sections were calculated using equation 1:

$$\sigma(\nu)=\frac{\Delta k(\nu)}{N\times c} \qquad (1)$$

where σ(ν) is the absorption cross-section at the wavenumber studied, *N* is the number density of the molecules in the cavity, and *c* is the light speed. $\Delta k(\nu)$, the increase in cavity decay rate caused by the sample, is defined by:

$$\Delta k(\nu)=\frac{1}{\tau(\nu)}-\frac{1}{\tau_0} \qquad (2)$$

where τ(ν) and τ_0 are the ring-down decay lifetimes with and without the sample respectively. In principle, τ_0 might drift slightly with the change of the laser

wavenumber and other experimental parameters, such as the temperature, and the ambient and the intra-cavity pressure [51], but it was assumed to be constant during each scan in this work.

The line strengths were obtained from the corresponding peak absorption cross sections, using a Voigt lineshape model and the number density determined from the strongest CH_3D peak at 6066.538 cm^{-1}. The line strength of CH_3D line at 6066.538 cm^{-1} (2.27×10^{-25} cm/molecule) was obtained by using a single-path cell filled with 8.3 Torr pure CH_3D and fitting the cell absorption spectrum with a Voigt lineshape function. The reproducibility of the line strength determined from the single-path absorption cell measurements was better than 1 %. This does not include the systematic bias introduced by errors in our pressure gauges and uncertainty in the gas temperature.

The difference between the pressure-broadening effects from CH_3D itself and from N_2 foreign gas needs to be considered. In the ring-down cavity, the number density of CH_3D was very small and the mixing ratios were smaller than 0.077 %, so the nitrogen broadening effect dominated. In the single-path absorption cell, the CH_3D self-broadening effect dominated. We calculated the air broadening effect and self-broadening effect on several lines of CH_4 and $^{13}CH_4$, using the Voigt function and the broadening coefficients listed in HITRAN. At 8 Torr, Doppler broadening (HWHM 0.009 cm^{-1}) dominated over pressure-broadening (HWHM of ~ 0.001 cm^{-1}). The air and self pressure-broadening coefficients (see below) affect the line strength by less than 3 %.

In calculation of absolute absorption cross sections, we assumed the CH_3D purity to be 98%, as claimed by the manufacturer. If this number is in error, all of our line strengths will change by a constant factor. The concentration of CH_4 in the CH_3D lecture bottle was checked several times and found to be 1.7(4)%. No obvious $^{13}CH_4$ absorption features were found when we measured the line strength of CH_3D. Other impurities from the lecture bottle, other than H_2O and CO_2, were not examined. The doubly substituted $^{13}CH_3D$ [86], along with CH_2D_2 [87] and other isotopologues [73], might have effects on our results. Among those, the effects from $^{13}CH_3D$ might be the largest. Unfortunately, neither $^{13}CH_3D$ commercial products nor literature spectra at low pressure were available. As an additional test, we measured line strengths of $^{13}CH_4$ transitions in this wavelength region, using $^{13}CH_4$ lecture bottle purchased from the same vendor as CH_3D bottle and these line strengths were found to agree within 1% with values tabulated in HITRAN.

In order to improve the wavenumber accuracy of the CH_3D lines we report in this work, we have matched our lines against those determined from High Resolution FTIR spectra [73-74]. Quack and coauthors reported the absorption spectrum of CH_3D at 80K and ~ 2 Torr with the nominal instrumental resolution of 0.0027 to 0.0048 cm^{-1} [73]. The absolute wavenumber accuracy of unblended of favorable intensity was claimed to be better than 10^{-4} cm^{-1}. The assignments of the absorption lines, along with the observed peak positions, were listed as supplementary materials of Ref. 40. These authors listed no fits nor gave spectroscopic constants for the $2\nu_4$ bands, except band origins. Deng *et al* [74] gave spectroscopic constants and term values for the ro-vibrational states of the A and E symmetry $2\nu_4$ bands. These authors provided us with a transmission *vs.* wavenumber file for an FTIR absorption spectrum of a CH_3D sample

at room temperature, 76.7 Torr pressure, 105 m absorption path length and an unapodized resolution of 0.01 cm^{-1}. This spectrum contained numerous CH_4 lines, and our comparison of these against HITRAN revealed an overall shift of 0.003 cm^{-1} [49, 88]. We have used the lines found in common between our two CH_3D spectra, and spline interpolation, to improve the calibration of our spectrum. We believe the wavenumber accuracy of the isolated lines we observed is 0.003 cm^{-1} or better. The difference for lines in common between our measured wavenumbers and those listed in ref [73] was about +0.008 cm^{-1}.

Table 1 Line strengths of CH_3D in the 6017.5 – 6031.5 cm^{-1} wavenumber region, and the possible quantum numbers of the perpendicular band $2\nu_4(E)$ transitions along with their calculated absorption positions and intensities (see text). Not all the CH_3D lines were assigned. Reported line strengths correspond to cm per methane molecule, assuming a CH_3D isotopic fraction of 6.1575×10^{-4}. The reproducibility of the line strengths was better than 1%. Transitions with star (*) belong to the parallel band $2\nu_4(A_1)$, whose absorption positions and intensities were not simulated.

Measured ν (cm^{-1})	Measured *S* (10^{-26} cm/molecule)	Calculated ν (cm^{-1})	Calculated Intensity (a.u.)	Transition Assignment
6017.590	0.506			
6017.706	2.74	6017.684	0.680	$^{P}Q_1(10)$
6017.941	0.887	6017.767	0.633	$^{R}Q_0(14)$
6018.098	0.553			
6018.235	3.40	6018.229	2.195	$^{P}Q_1(9)$
6018.279	0.644			
6018.322	0.541			
6018.488	3.87	6018.586	0.990	$^{R}Q_0(13)$
6018.731	4.24	6018.730	2.673	$^{P}Q_1(8)$
6018.811	6.98	--	--	$^{Q}R_0(4)$ *
6018.858	6.34	--	--	$^{Q}R_1(4)$ *
6019.053	4.85	--	--	$^{Q}R_2(4)$ *
6019.184	5.02	6019.185	3.099	$^{P}Q_1(7)$

6019.376	2.69	6019.380	2.98	$^{R}Q_{0}(12)$
6019.537	0.559			
6019.588	5.26	6019.589	3.406	$^{P}Q_{1}(6)$
6019.795	1.80			
6019.939	5.48	6019.942	3.531	$^{P}Q_{1}(5)$
6020.067	1.87			
6020.146	3.30	6020.114	2.13	$^{Q}R_{3}(4)$
6020.236	5.29	6020.240	3.421	$^{P}Q_{1}(4)$
6020.474	4.74	6020.481	3.046	$^{P}Q_{1}(3)$
6020.654	3.75	6020.663	2.407	$^{P}Q_{1}(2)$
6020.779	2.51	6020.785	1.544	$^{P}Q_{1}(1)$
6020.811	4.67	6020.817	5.851	$^{R}Q_{0}(10)$
6021.456	6.34	6021.472	7.672	$^{R}Q_{0}(9)$
6021.711	1.37			
6022.065	8.18	6022.077	9.590	$^{R}Q_{0}(8)$
6022.253	0.555			
6022.619	9.62	6022.627	11.39	$^{R}Q_{0}(7)$
6023.011	1.11			
6023.115	11.2	6023.117	12.80	$^{R}Q_{0}(6)$
6023.381	0.597			
6023.452	0.870			
6023.546	11.4	6023.545	13.54	$^{R}Q_{0}(5)$
6023.909	11.5	6023.907	13.34	$^{R}Q_{0}(4)$
6024.138	0.563			
6024.201	10. 5	6024.201	12.04	$^{R}Q_{0}(3)$

6024.318	0.611			
6024.422	8.46	6024.425	9.61	$^{R}Q_{0}(2)$
6024.470	0.799			
6024.490	0.463			
6024.570	5.44	6024.572	6.218	$^{R}Q_{0}(1)$
6024.697	12.4			
6025.329	0.983			
6025.356	0.699			
6025.419	1.20			
6025.917	4.75			
6025.943	2.12			
6026.473	2.20	--	--	$^{Q}R_{0}(5)$ *
6026.572	7.23	--	--	$^{Q}R_{1}(5)$ *
6026.689	7.28	--	--	$^{Q}R_{4}(5)$ *
6026.953	1.15	6026.957	2.459	$^{R}Q_{1}(7)$
6027.026	4.71	--	--	$^{Q}R_{2}(5)$ *
6027.129	4.72			
6027.170	0.504			
6027.298	0.537	6027.307	4.17	$^{R}Q_{1}(6)$
6027.433	5.22			
6027.610	1.61	6027.616	4.47	$^{R}Q_{1}(5)$
6027.879	5.52	6027.881	4.32	$^{R}Q_{1}(4)$
6028.100	5.37	6028.103	3.66	$^{R}Q_{1}(3)$
6028.269	4.82	6028.262	2.36	$^{R}Q_{1}(2)$
6028.497	2.99			

6029.134	0.703			
6029.581	4.32			
6029.652	0.448			
6029.788	1.72			
6029.849	0.624			
6029.873	2.27			
6030.052	0.631	6030.080	0.833	$^{R}Q_2(9)$
6030.139	0.548			
6030.235	3.08			
6030.275	0.694			
6030.489	1.51			
6030.581	0.486			
6030.634	0.712	--	--	$^{R}Q_2(8)$
6030.828	1.93	6030.832	2.409	$^{R}Q_2(7)$
6031.047	4.97			
6031.093	0.733	6031.159	2.618	$^{R}Q_2(6)$
6031.148	5.14			

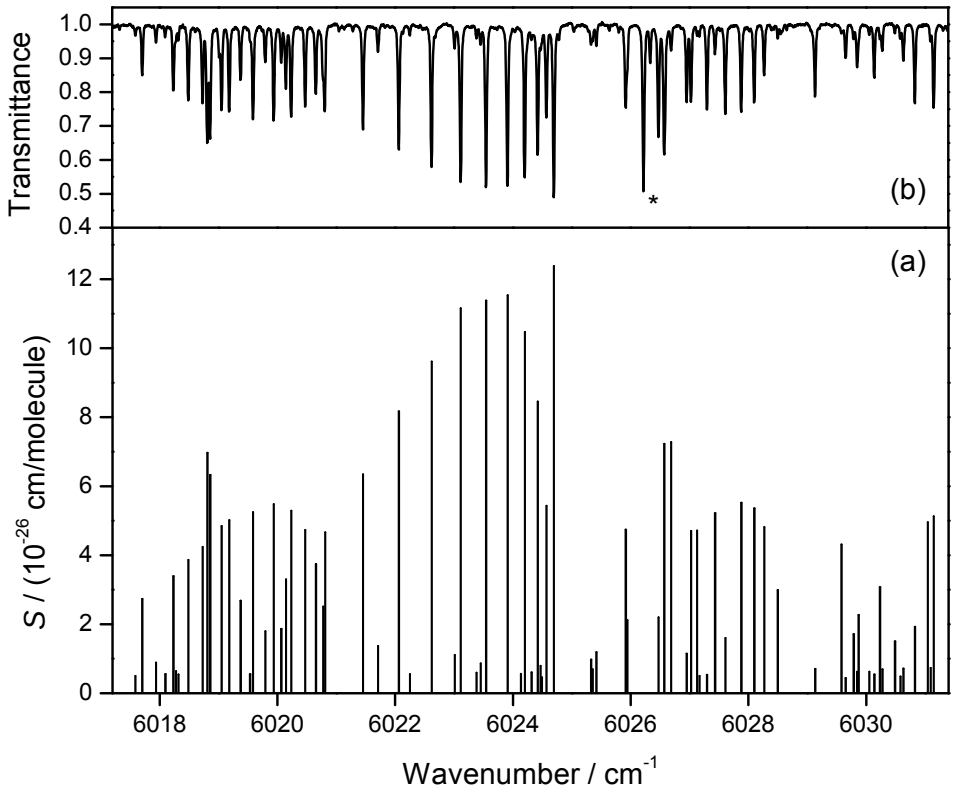

Figure 3 (a) Line strengths of CH_3D in the wavelength range of 6017.5 – 6031.5 cm^{-1}. The total pressure in the cavity was around 8.3 Torr. The CH_3D number densities varied between 0.5-2.0 $\times 10^{14}$ molecule/cm^3. (b) CH_3D absorption spectrum from Ref [74]. The total pressure was claimed to be 10227 Pa (*i.e.* 76.7 Torr). A CH_4 absorption line is marked with an asterisk.

The line strengths of CH_3D lines larger than 4.5×10^{-27} cm/molecule in the 6017.5 – 6031.5 cm^{-1} wavenumber region are shown in Figure 3 (a) and Table 1. The literature CH_3D absorption spectrum [74] is also shown in Figure 3 (b). Using the CH_3D lower state and upper state parameters given in [73-74, 89-90], we simulated the spectra using the P-Gopher program [91]. Using the constants listed in [74], we were not able to simulate the spectrum successfully, so we used P-Gopher to refit the $2\nu_4$(E) spectrum.

It was found that the $^{R}R_3$ branch is strongly perturbed. Removing these lines, we could fit the remaining lines with a mean absolute error of ~0.02 cm^{-1}, with residuals largest for the higher J, K lines. Our assignments are similar to these given in Ref. [73], but some of the Q-branches differ in numbering by one. The P-gopher log file that has the assignments and fit results is in supplementary material. Table 1 also lists quantum numbers for assigned lines of the perpendicular band $2\nu_4(E)$, along with their calculated absorption positions and intensities. The calculated intensities in Table 1 are those predicted by P-Gopher, scaled to reproduce the intensity of the $^{R}R_3(3)$ transition, 6066.538 cm^{-1}, which is the strongest in our observed spectrum. The intensities are badly predicted by the simulation, suggesting strong perturbations of the upper state.

As show in Figure 3, our CH_3D spectrum agrees well with the previous FTIR spectrum but we have improved resolution (due to the lower pressure and higher sensitivity), as well as reduced levels of impurities, particularly CH_4. It should be noted that the peak at ~ 6026.23 cm^{-1} as shown in Figure 2 is a mixture of CH_3D and CH_4. Since we cannot resolve these two components, we did not list the line strength of this specific CH_3D line in Figure 3 (a) and Table 1. The strongest line in this interval is at 6024.697 cm^{-1} and has a line strength of 1.24×10^{-25} cm/molecule, accounting for the natural abundance of CH_3D of 6.1575×10^{-4}, as assumed in the HITRAN database [49] and elsewhere [50].

Table 2 Line strengths of CH_3D in the 6046.5 – 6060.0 cm^{-1} wavenumber region, along with the possible assignments.

Measured ν (cm^{-1})	Measured *S* (10^{-26} cm/molecule)	Calculated ν (cm^{-1})	Calculated Intensity (a.u.)	Transition Assignment
6046.606	2.99	6046.580	1.158	$^{R}Q_6(7)$
6046.641	2.33			
6046.709	2.96	--	--	$^{R}Q_6(9)$
6046.884	4.67			
6047.076	2.35			
6047.434	0.824	6047.428	0.307	$^{P}R_2(3)$
6047.540	4.47			
6047.657	6.42	--	--	$^{R}R_0(2)$
6047.850	1.60			
6048.333	4.90			
6048.530	4.11			
6049.031	2.57			
6049.348	0.987			
6049.403	0.617			
6049.645	4.63			
6050.136	1.45			
6050.241	3.64			
6050.510	0.612			
6050.663	0.855			
6050.694	2.51			

6050.882	1.05	--	--	$^{R}Q_{7}(9)$
6051.005	1.01	6051.005	0.844	$^{P}R_{3}(4)$
6051.262	2.93	6051.267	0.607	$^{P}R_{1}(3)$
6051.304	2.14			
6051.375	6.17	6051.372	1.61	$^{R}R_{1}(2)$
6051.523	0.845			
6051.882	0.501			
6052.479	0.631			
6052.628	1.41			
6052.760	0.723			
6053.666	0.703			
6053.947	0.783			
6054.362	0.646			
6054.695	1.33			
6054.873	1.16	6054.874	0.421	$^{P}R_{2}(4)$
6055.021	3.63			
6055.178	9.31	6055.168	2.43	$^{R}R_{2}(2)$
6055.239	7.44	6055.249	4.30	$^{R}R_{0}(3)$
6055.274	0.543			
6055.594	4.17			
6055.626	4.12			
6056.293	3.65			
6056.969	2.86			
6057.118	0.726			
6057.443	0.627			

6057.616	4.25			
6058.212	1.48			
6058.245	5.20			
6058.390	1.35	6058.390	1.068	$^{P}R_3(5)$
6058.634	1.41			
6058.713	2.14	6058.716	0.682	$^{P}R_1(4)$
6058.906	6.30	6058.908	1.64	$^{R}R_1(3)$
6059.229	1.91			

Table 3 Line strengths of CH_3D in the 6060.5 – 6070.0 cm^{-1} wavenumber region, along with the possible assignments.

Measured ν (cm^{-1})	Measured *S* (10^{-26} cm/molecule)	Calculated ν (cm^{-1})	Calculated Intensity (a.u.)	Transition Assignment
6060.893	0.896			
6061.166	0.691	6061.172	0.282	$^{P}R_6(7)$
6061.280	1.26			
6061.516	0.822			
6061.552	2.57			
6062.257	1.36	6062.259	0.9628	$^{P}R_2(5)$
6062.719	8.39	6062.718	4.413	$^{R}R_2(3)$
6062.780	7.36	6062.791	8.896	$^{R}R_0(4)$
6062.840	0.610			
6062.865	0.552			

6062.950	3.10			
6063.064	1.78			
6063.351	0.656			
6063.535	3.14			
6063.558	0.908			
6063.652	3.03			
6064.286	2.45			
6064.536	0.521			
6064.692	0.501			
6065.717	1.34	6065.717	2.676	$^{P}R_{3}(6)$
6065.882	2.20			
6065.908	0.795			
6065.991	0.806			
6066.103	1.97	6066.105	1.379	$^{P}R_{1}(5)$
6066.384	6.11	6066.391	3.203	$^{R}R_{1}(4)$
6066.538	22.7	6066.535	22.7	$^{R}R_{3}(3)$
6066.583	1.19			
6066.751	0.760			
6066.998	0.740			
6068.762	0.490	6068.405	0.384	$^{P}R_{6}(8)$
6069.092	0.492	6069.093	0.230	$^{P}R_{4}(7)$
6069.263	3.94			
6069.429	0.507			
6069.587	1.18	6069.586	0.9813	$^{P}R_{2}(6)$

The line strengths of CH_3D in the 6046.5 – 6060.0 cm^{-1} wavenumber region are shown in Table 2. The strongest line in this interval is at 6055.178 cm^{-1} and its line strength is 9.31×10^{-26} cm/molecule. Both the absorption positions and the relative intensities agree well between our measurements and the literature. The line at ~ 6047.853 cm^{-1} (literature value) included the absorption from both H_2O and CH_3D. Our CRDS measurement was able to resolve them. The line strength of this CH_3D line is included in Table 2 (6047.850 cm^{-1}). The referenced H_2O peak position is 6047.790 cm^{-1}. The line strengths of CH_3D in the 6060.5 – 6070.0 cm^{-1} wavenumber region are shown in Table 3. The strongest line in this region is located at 6066.538 cm^{-1} and has a line strength of 3.69×10^{-22} cm per CH_3D molecule, which corresponds to 2.27×10^{-25} cm per methane molecule. This is the strongest line found in the wavenumber regions we studied, but it is only about 1/3 – ¼ the strength on of the strongest lines of CH_4 (1.278×10^{-21} cm/molecule at 6057.086 cm^{-1}), and $^{13}CH_4$ (1.42×10^{-21} cm per $^{13}CH_4$ at 6029.106 cm^{-1}) [49, 92-93]. Both CH_4 and $^{13}CH_4$ are spherical tops, which, except for the lowest J transitions, have several closely spaced absorption lines, due to tensor splitting that arises from centrifugal distortion, that blend together at atmospheric pressure and increase the cross section. CH_3D is a symmetric top. The strongest lines in this region of the CH_3D spectrum are from a perpendicular band, which has widely separated lines for different K values. The result is that the integrated line strength of CH_3D is more dispersed in frequency than for its spherical top isotopic variants. It should be mentioned that we only assigned the transition lines belonging to the perpendicular band $2\nu_4(E)$ along with some parallel band $2\nu_4(A_1)$ lines. Many absorption lines reported in this work are not presently assigned.

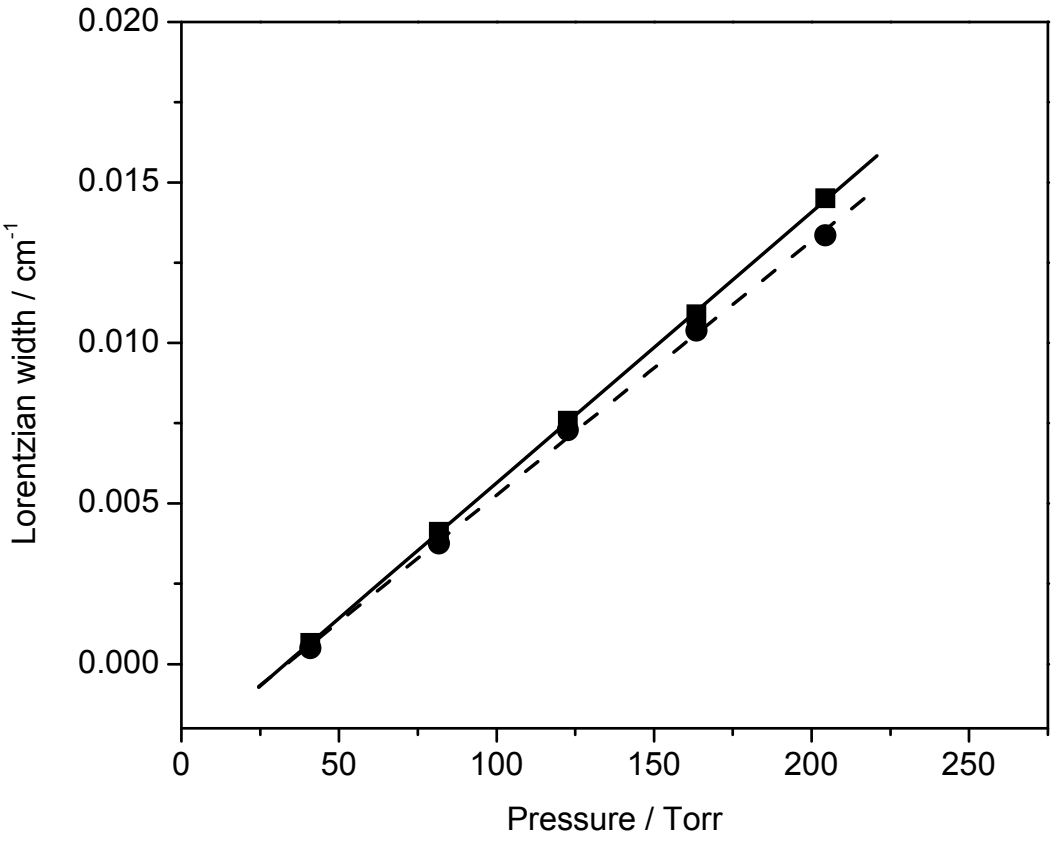

Figure 4 The N_2 (square and solid line) and O_2 (circle and dash line) pressure-broadening coefficients (*HWHM*) of the CH_3D absorption line at 6017.941 cm^{-1}. The scattering symbols are measurements and the lines are linear fits. The slope of the linear fit is defined as pressure-broadening coefficient.

The N_2, O_2, and CO_2 pressure-broadening coefficients of CH_3D were measured for the line at 6017.941 cm^{-1}. The pressure of N_2 and O_2 varied between 40 and 200 Torr. The pressure of CO_2 varied only 10 and 50 Torr because the interference of CO_2 is large at higher pressure. A Voigt lineshape model was used to simulate the absorption spectrum of CH_3D. The Doppler contribution to the Voigt lineshape was fixed at the calculated

value. A linear regression of the Lorentzian width *vs.* foreign gas pressure gave the pressure-broadening coefficient. The N_2 and O_2 pressure-broadening effect is presented in Figure 4. Laser frequency jitter (~ 20 MHz peak-to-peak in times intervals of ~ 1 sec) is not accounted for in our lineshape model, so we did not force the linear fits to go through (0, 0) as shown in Figure 4. The zero pressure intercept of the linear fits is -0.0028 and -0.0027 cm^{-1}, respectively. The N_2, O_2 and CO_2 pressure-broadening coefficients (*HWHM*) of this specific CH_3D line are 0.064(1), 0.060(1) and 0.061(5) cm^{-1}/atm, respectively. Here, the errors quoted are from the linear fits only (1σ). By using the above numbers, the air pressure-broadening coefficient is calculated to be 0.063(1) cm^{-1}/atm. For the spectral line at 6064.286 cm^{-1}, the N_2, O_2 and CO_2 pressure-broadening coefficients of CH_3D are 0.051(1), 0.052(1) and 0.046(2) cm^{-1}/atm, respectively. The pressures of N_2 and O_2 employed were between 8 and 260 Torr. The pressure of CO_2 employed was between 8 and 90 Torr. For this line, the CO_2 broadening coefficient is ~ 10 % smaller than N_2 and O_2, which is different from what we expected, given the fact that CO_2 has larger molecular quadrupole moment. A previous study of the pressure-broadening of a four line cluster of transitions of CH_4 at 6057.1 cm^{-1} reported room temperature pressure-broadening coefficients of 0.0744 and 0.0515 cm^{-1}/atm for CO_2 and N_2 respectively [94]. For the line at 6066.538 cm^{-1} and in the total pressure range of 8 – 250 Torr, the N_2 and O_2 pressure-broadening coefficients are 0.065(2) and 0.060(1) cm^{-1}/atm, respectively. CO_2 effect was not measured at this wavenumber because of strong CO_2 absorption. Our result of the pressure-broadening coefficients is presented in Table 4.

Table 4 Pressure-broadening coefficients (γ) of CH_3D at selected wavenumbers. Numbers in parentheses are from the linear fit only (1σ).

ν (cm^{-1})	γ_{N2} (cm^{-1}/atm)	γ_{O2} (cm^{-1}/atm)	γ_{CO2} (cm^{-1}/atm)
6017.941	0.064(1)	0.060(1)	0.061(5)
6064.286	0.051(1)	0.052(1)	0.046(2)
6066.538	0.065(2)	0.060(1)	

As a check, we measured the N_2 and O_2 broadening coefficients of CH_4 at 6026.225 cm^{-1}, which gave 0.0661(6) and 0.0602(9) cm^{-1}/atm, respectively. The corresponding air broadening coefficient by using these measured values is 0.0649(7) cm^{-1}/atm. In HITRAN 2008, this CH_4 absorption line has an air-broadening coefficient of 0.0634 cm^{-1}/atm, which is 2.3 % and 2σ smaller than our measured value. Our CH_3D results also fell within the range of the reported pressure-broadening coefficients of other CH_3D absorption lines [49, 85, 95]. For example, nearby CH_3D absorption lines (6300 – 6510 cm^{-1}) listed in HITRAN have air pressure-broadening coefficients between 0.0366 and 0.0729 cm^{-1} [49]. The CH_3D ν_2 band in the wavenumber region of 2066-2238 cm^{-1} has transitions with O_2 broadening coefficients from 0.0153 to 0.0645 cm^{-1}/atm at 296 K [95]. The ν_6 band has transitions with air broadening coefficients between 0.016 and 0.077 cm^{-1}/atm [85].

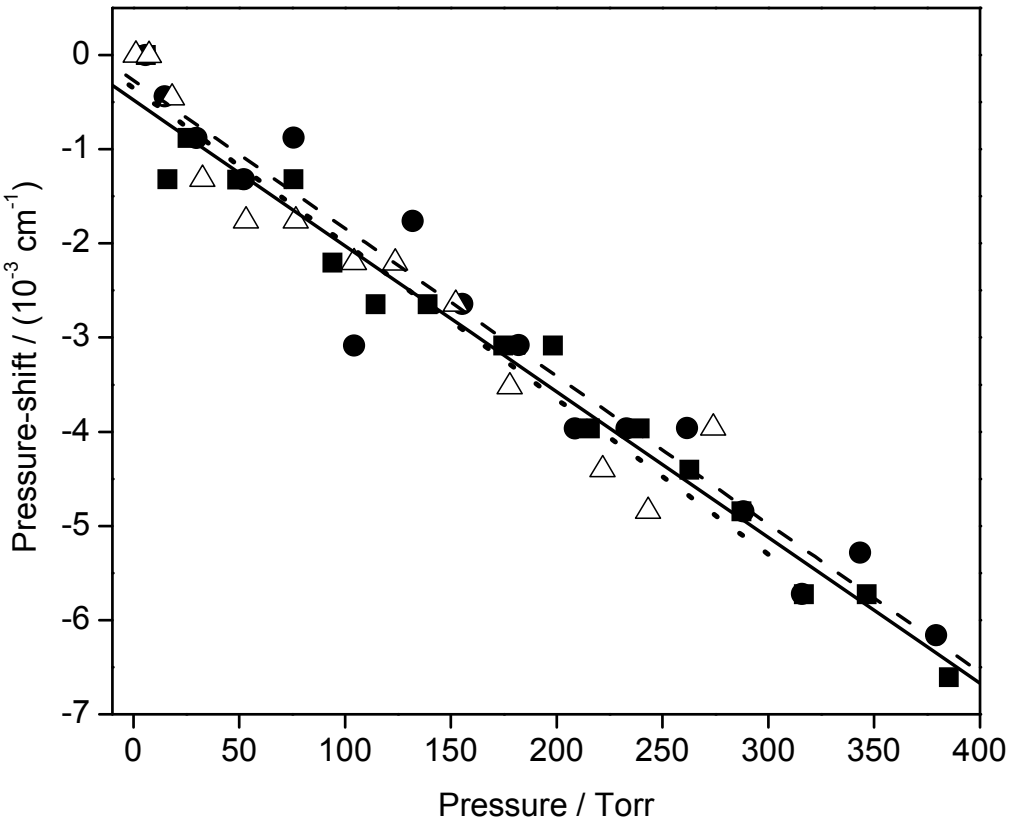

Figure 5 The N_2 (square and solid line), O_2 (circle and dash line), and CO_2 (triangle and dotted line) pressure dependence of the CH_3D absorption peak at ~ 6032.443 cm^{-1}. The scattering symbols are measurements and the lines are linear fits. The slope of the linear fit is defined as pressure-shift coefficient.

The N_2, O_2, and CO_2 pressure-shift coefficients of CH_3D were also measured at 6032.443 cm^{-1}. Since the pressure-shift coefficient is relatively small, the frequency drift of the laser itself has to be considered. The single-path absorption cell filled with ~ 8 Torr CH_3D was used to correct the laser wavenumber. The total pressure in the cavity for CRDS measurements varied between ~ 1 and 380 Torr, as shown in Figure 5. Here, the pressure range of CO_2 was much higher than that used in the measurements

of pressure-broadening coefficients. We did not measure the full absorption spectra when the CO_2 pressure-shift coefficient was being examined. The partial absorption spectra with and without CH_3D were measured separately. The subtracted spectra were used to find the CH_3D peak position. At each pressure, the peak position measured using CRDS was subtracted from that measured using the single-path absorption cell. As shown in Figure 5, the CH_3D peak position moved to lower wavenumber (red-shift) with the increasing pressure. Considering the pressure difference between the single-path cell and the cavity, along with other systematic errors, we did not force the linear fits to go through (0,0). The N_2, O_2, and CO_2 pressure-shift coefficients of the CH_3D absorption line at 6032.443 cm^{-1} are -0.012(1), -0.012(1), and -0.013(1) cm^{-1}/atm, respectively. The confidence intervals come from the linear fits. The air pressure-shift coefficients of nearby CH_4 lines are between -0.006 and -0.015 cm^{-1}/atm according to HITRAN 2008 [49]. Our results of CH_3D fell within this range. On the other hand, the O_2 pressure-shift coefficients of CH_3D ν_2 transitions were between -0.0017 and -0.0068 cm^{-1}/atm [95], which were significantly lower than our measurements. But the air pressure-shift coefficients of CH_3D ν_6 band transitions were between -0.012 and +0.008 cm^{-1}/atm and were mainly negative [85].

With the line strengths, pressure-broadening and pressure-shift coefficients, the literature CH_3D absorption spectrum [74] between 6021 and 6025 cm^{-1} was simulated using a Voigt lineshape. During the simulation, we used our measured line strengths with fixed the pressure-broadening coefficient at 0.064 cm^{-1}/atm and the pressure-shift coefficient at -0.012 cm^{-1}/atm. Since the pressure employed in the literature was not very high (76.7 Torr), the change of the pressure-broadening and pressure-shift coefficient with transition would only have small effect on the spectrum. The

simulation results are shown in Figure 6. The experimental conditions in the literature were not clearly described, so the simulation shown in Figure 6 is only quasi-quantitative. The major residual might be on account of the instrumental broadening.

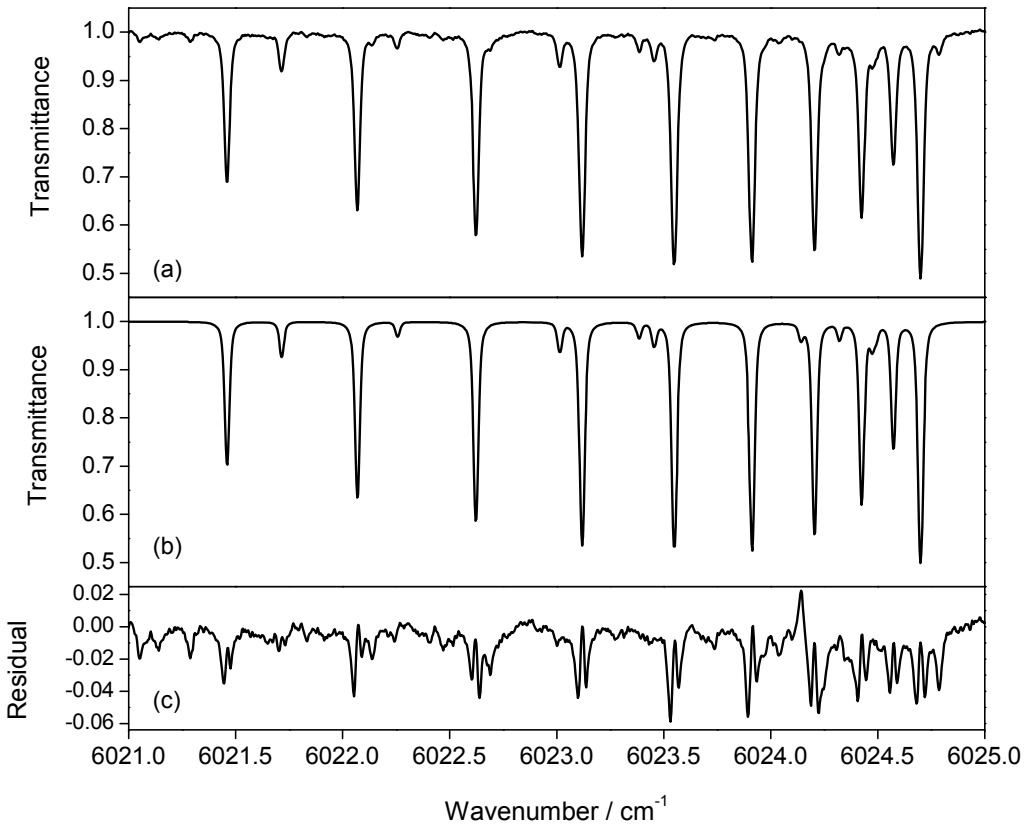

Figure 6 Simulation of the literature spectrum [74] using our measured line strengths, and average pressure-broadening and pressure-shift coefficients. (a) The simulation. (b) The literature. (d) The residual (literature - simulation).

3.4 Conclusions

The line strengths of CH_3D in near-IR wavelength regions are measured by cw-CRDS method. The lines with line strengths higher than 4.5×10^{-27} cm per methane molecule

are listed in this paper. The strongest transition in the studied wavenumber regions is located at 6066.538 cm^{-1}, which has an integrated line strength of 2.27×10^{-25} cm/molecule. CH_3D in this region indicates different absorption feature from both CH_4 and $^{13}CH_4$. There are more relatively strong lines of CH_3D than that of CH_4 and $^{13}CH_4$ falling in this wavenumber region, as can be expected due to the different rotational structures for the vibrational bands of a spherical top and the perpendicular bands of a symmetric top. Both CH_4 and $^{13}CH_4$ centrifugal distortion split clusters of lines separated by $2B(1 - \zeta)$, which is equal to ~ 10 cm^{-1}, while CH_3D has multiple overlapping sub-branches. In consequence, the absolute line strengths of the most intense CH_3D lines are weaker than those of CH_4 and $^{13}CH_4$. The foreign pressure-broadening coefficients of CH_3D were quantified for several transitions. At the wavenumber of 6017.941 cm^{-1}, N_2, O_2 and CO_2 have very similar pressure-broadening coefficients. At 6064.286 cm^{-1}, the CO_2 broadening coefficient is ~ 10 % smaller than those of N_2 and O_2. For the CH_3D absorption line at the wavenumber of 6032.443 cm^{-1}, N_2, O_2 and CO_2 have very similar pressure-shift coefficients on CH_3D. Our motivation for this work was to provide data for detection of trace levels of CH_3D. For that purpose, one only needs the assignment of the strongest, most isolated lines. In future work, we hope to assign the presently unassigned transitions in this region.

Bibliography

[1] D. T. Shindell, G. Faluvegi, D. M. Koch, G. A. Schmidt, N. Unger, S. E. Bauer, Science 326 (2009) 716-718.

[2] S. Solomon, Intergovernmental Panel on Climate Change Working Group 1 Science (2007), Climate Change 2007: the physical science basis, Cambridge University Press, Cambridge, 2007

[3] O. Boucher, P. Friedlingstein, B. Collins, K.P. Shine, Environ. Res. Lett. 4 (2009) doi:10.1088/1748-9326/4/4/044007

[4] J. Lelieveld, P.J. Crutzen, F.J. Dentener, Tellus B 50 (1998) 128-150.

[5] E. J. Dlugokencky, K. A. Masarie, P. M. Lang, P. P. Tans, Nature 393 (1998) 447-450.

[6] E. J. Dlugokencky, L. Bruhwiler, J. W. C. White, L. K. Emmons, P. C. Novelli, S. A. Montzka, K. A. Masarie, P. M. Lang, A. M. Crotwell1, J. B. Miller, L.V. Gatti, Geophys. Res. Lett. 36 (2009) L18803.

[7] P. J. Crutzen, Nature 350 (1991) 380-381.

[8] N. Shakhova, I. Semiletov, A. Salyuk, V. Yusupov, D. Kosmach, O. Gustafsson, Science 327 (2010) 1246-1250.

[9] M. Alperin, T. Hoehler, Science 329 (2010) 288-289.

[10] W Irion, E. J. Moyer, M. R. Gunson, C. P. Rinsland, Y. L. Yung, H. A. Michelsen, R. J. Salawitch, A. Y. Chang, M. J. Newchurch, M. M. Abbas, M. C. Abrams, and R. Zanders, Geophysical Research Letters 23 (1996) 2381-2384.

[11] C. P. Rinsland, M. R. Gunson, J. C. Foster, R. A. Toth, C. B. Farmer, and R. Zander, Journal of Geophysical Research-Atmospheres 96 (1991) 1057-1068.

[12] M. J. Mumma, G. L. Villanueva, R. E. Novak, T. Hewagama, B. P. Bonev, M. A. DiSanti, A. M. Mandell, M.D. Smith, Science 323 (2009) 1041-1045.

[13] R. E. Novak, M. J. Mumma, G. L. Villanueva**,** Planetary and Space Sci. 59 (2011) 163-168.

[14] V. Formisano, S. Atreya, T. Encrenaz, N. Ignatiev, M. Giuranna, Science 306 (2004) 1758-1761.

[15] E. Lellouch, B. Bezard, T. Fouchet, H. Feuchtgruber, T. Encrenaz, and T. de Graauw, Astronomy and Astrophysics 370 (2001) 610-622.

[16] J. H. Kim, S. J. Kim, T. R. Geballe, S. S. Kim, and L. R. Brown, Icarus 185 (2006) 476-486.

[17] L. A. Sromovsky, P. M. Fry, V. Boudon, A. Campargue, and A. Nikitin, Icarus. 218 (2012) 1-23.

[18] M. Burgdorf, G. Orton, J. van Cleve, V. Meadows, and J. Houck. Icarus 184 (2006) 634-637.

[19] B. Bezard, C. A. Nixon, I. Kleiner, and D. E. Jennings. Icarus 191 (2007) 397-400.

[20] P. G. J. Irwin, C. de Bergh, R. Courtin, B. Bezard, N. A. Teanby, G. R. Davis, L. N. Fletcher, G. S. Orton, S. B. Calcutt, D. Tice, and J. Hurley, Icarus 220 (2012) 369-382.

[21]. H. Kawakita and J. Watanabe, Astrophysical Journal 582 (2003) 534-539.

[22] H. Kawakita, J. I. Watanabe, R. Furusho, T. Fuse, and D. C. Boice, Astrophysical Journal 623 (2005) L49-L52.

[23] S. Redfield, Nature 463 (2010) 617-618.

[24] C. de Bergh, R. Courtin, B. Bezard, A. Coustenis, E. Lellouch, M. Hirtzig, P. Rannou, P. Drossart, A. Campargue, S. Kassi, L. Wang, V. Boudon, A. Nikitin, and V. Tyuterev, Planetary and Space Science 61 (2012) 85-98.

[25] K. H. Baines, T. W. Momary, B. J. Buratti, D. L. Matson, R. M. Nelson, P. Drossart, B. Sicardy, V. Formisano, G. Bellucci, A. Coradini, C. Griffith, R. H. Brown, J. P.

Bibring, Y. Langevin, F. Capaccioni, P. Cerroni, R. N. Clark, M. Combes, D. P. Cruikshank, R. Jaumann, T. B. McCord, V. Mennella, P. D. Nicholson, and C. Sotin, Earth Moon and Planets 96 (2005) 119-147.

[26] A. Coustenis, A. Salama, B. Schulz, S. Ott, E. Lellouch, T. Encrenaz, D. Gautier, and H. Feuchtgruber, Icarus 161 (2003) 383-403.

[27] S. J. Kim, T. R. Geballe, K. S. Noll, and R. Courtin, Icarus 173 (2005) 522-532.

[28] C. A. Griffith, L. Doose, M. G. Tomasko, P. F. Penteado, and C. See, Icarus 218 (2012) 975-988.

[29] A. Campargue, L. Wang, D. Mondelain, S. Kassi, B. Bezard, E. Lellouch, A. Coustenis, C. de Bergh, M. Hirtzig, and P. Drossart. Icarus 219 (2012) 110-128.

[30] T. R. Geballe, S. J. Kim, K. S. Noll, and C. A. Griffith, Astrophysical Journal 583 (2003) L39-L42.

[31] C. A. Nixon, B. Temelso, S. Vinatier, N. A. Teanby, B. Bezard, R. K. Achterberg, K. E. Mandt, C. D. Sherrill, P. G. J. Irwin, D. E. Jennings, P. N. Romani, A. Coustenis, and F. M. Flasar, Astrophysical Journal 749 (2012) 159.

[32] H. B. Niemann, S. K. Atreya, S. J. Bauer, G. R. Carignan, J. E. Demick, R. L. Frost, D. Gautier, J. A. Haberman, D. N. Harpold, D. M. Hunten, G. Israel, J. I. Lunine, W. T. Kasprzak, T. C. Owen, M. Paulkovich, F. Raulin, E. Raaen, S.H. Way, Nature 438 (2005) 779-784.

[33] J. I. Lunine, S. K. Atreya, Nature Geosci. 1 (2008) 159-164.

[34] A. Negrao, M. Hirtzig, A. Coustenis, E. Gendron, P. Drossart, P. Rannou, M. Combes, V. Boudon, J. Geophys. Res. 112 (2007) E02S92.

[35] A. Bar-Nun, V. Dimitrov, Icarus 188 (2007) 543-545.

[36] V.A. Krasnopolsky, J.P. Maillard, T.C. Owen, Icarus 172 (2004) 537-547.

[37] F. Lefevre, F. Forget, Nature 460 (2009) 720-723.

[38] M. E. Summers, B. J. Lieb, E. Chapman, Y. L. Yung, Geophys. Res. Lett. 29 (2002) 2171, doi: 10.1029/2002GL015377.

[39] D. H. Mordaunt, I. R. Lambert, G. P. Morley, M. N. R. Ashfold, R. N. Dixon, C.M. Western, L. Schnieder, K.H. Welge, J. Chem. Phys. 98, (1993) 2054-2065.

[40] C. P. McKay, H. D. Smith, Icarus 178, (2005) 274-276.

[41] C. R. Webster, P. R. Mahaffy**,** Planetary and Space Sci. 59 (2011) 271-283.

[42] C. A. Nixon, R. K. Achterberg, S. Vinatier, B. Bézard, A. Coustenis, P. G. J. Irwin, N. A. Teanby, R. de Kok, P. N. Romani, D. E. Jennings, G. L. Bjoraker, F. M. Flasar, Icarus 195 (2008) 778–791.

[43] J. P. Pinto, J. I. Lunine, S. J. Kim, Y. L. Yung, Nature 319 (1986) 388-390.

[44] A. O'Keefe; D. A. G. Deacon, Rev. Sci. Instru. 59 (1988) 2544-2551.

[45] D. Romanini, A. A. Kachanov, N. Sadeghi, F. Stoeckel, Chem. Phys. Lett. 264 (1997) 316-322.

[46] H. Huang, K. K. Lehmann, Chem. Phys. Lett. 463 (2008) 246-250.

[47] H. Huang, K. K. Lehmann, Optics Express 15 (2007) 8745-8759.

[48] K. K. Lehmann, D. Romanini, J. Chem. Phys. 105 (1996) 10263-10277.

[49] L. S. Rothman, I. E. Gordon, A. Barbe, D. C. Benner, P. F. Bernath, M. Birk, V. Boudon, L. R. Brown, A. Campargue, J. P. Champion, K. Chance, L. H. Coudert, V. Dana, V. M. Devi, S. Fally, J. M. Flaud, R. R. Gamache, A. Goldman, D. Jacquemart, I. Kleiner, N. Lacome, W. J. Lafferty, J. Y. Mandin, S. T. Massie, S. N. Mikhailenko, C. E. Miller, N. Moazzen-Ahmadi, O. V. Naumenko, A. V. Nikitin, J. Orphal, V. I. Perevalov, A. Perrin, A. Predoi-Cross, C. P. Rinsland, M. Rotger, M. Simeckova, M. A. H. Smith, K. Sung, S. A. Tashkun, J. Tennyson, R. A. Toth, A. C. Vandaele, J. Vander Auwera, J. Quan. Spec. Rad. Trans. 110 (2009) 533-572.

[50] P. De Bievre, N. E. Holden, I. L. Barnes, J. Phys. Chem. Ref. Data 13 (1984) 809-891.

[51] H. Huang, K. K. Lehmann, Appl. Optics 49 (2010) 1378-1387.

[52] L. R. Brown, A. Nikitin, D. C. Benner, V. M. Devi, M. A. H. Smith, L. Fejard, J. P. Champion, V. G. Tyuterev, R. L. Sams, J. Mol. Structure 695–696 (2004) 181-188.

[53] A.V. Nikitin, J. P. Champion, L. R. Brown, J. Mol. Spectrosc. 240 (2006) 14–25.

[54] L. Wang, S. Kassi, A.W. Liu, S.M. Hu, A. Campargue, J. Mol. Spectrosc. 261 (2010) 41-52.

[55] K. K. Lehmann, H. Huang, Optimal signal processing in cavity ring-down spectroscopy, Frontiers of Molecular Spectroscopy, Elsevier, Amsterdam, 2009, pp. 632-658.

[56] C. B. Suarez, Spectroscopy Letters 28 (1995) 429-439.

[57] C. Boussin, B. L. Lutz, C. De Bergh, A. Hamdouni, Journal of Quantitative Spectroscopy & Radiative Transfer 60 (1998) 501-514.

[58] L. R. Brown, D. C. Benner, J. P. Champion, V. M. Devi, L. Fejard, R. R. Gamache, T. Gabard, J. C. Hilico, B. Lavorel, M. Loete, G. C. Mellau, A. Nikitin, A. S. Pine, A. Predoi-Cross, C. P. Rinsland, O. Robert, R. L. Sams, M. A. H Smith, S. A. Tashkun, and V. G. Tyuterev, Journal of Quantitative Spectroscopy & Radiative Transfer 82 (2003) 219-238.

[59] L. R. Brown, A. Nikitin, D. C. Benner, V. M. Devi, M. A. H. Smith, L. Fejard, J. P. Champion, V. G. Tyuterev, and R. L. Sams, Journal of Molecular Structure 695 (2004) 181-188.

[60] A. Nikitin, J. P. Champion, V. G. Tyuterev and L. R. Brown, Journal of Molecular Spectroscopy 184 (1997) 120-128.

[61] O. N. Ulenikov, G. A. Onopenko, N. E. Tyabaeva, J. Schroderus, and S. Alanko, Journal of Molecular Spectroscopy 200 (2000) 1-15.

[62] O. N. Ulenikov, G. A. Onopenko, N. E. Tyabaeva, R. Anttila, S. Alanko, and J. Schroderus, Journal of Molecular Spectroscopy 201 (2000) 9-17.

[63] A. Nikitin, L. R. Brown, L. Fejard, J. P. Charnpion, and V. G. Tyuterev, Journal of Molecular Spectroscopy 216 (2002) 225-251.

[64] A. Nikitin, J. P. Champion, V. G. Tyuterev, L. R. Brown, G. Mellau, and M. Lock, Journal of Molecular Structure 517 (2000) 1-24.

[65] D. Mondelain, S. Kassi, L. Wang, and A. Campargue, Physical Chemistry Chemical Physics 13 (2011) 7985-7996.

[66] Y. Perez-Delgado, E. K. Lewis, C. J. Moehnke, M. C. Salazar, A. J. Hernandez, and C. E. Manzanares, Molecular Physics 107 (2009) 1367-1377.

[67] Y. Lu, D. Mondelain, S. Kassi, and A. Campargue, Journal of Quantitative Spectroscopy & Radiative Transfer 112 (2011) 2683-2697.

[68] A. Campargue, O. Leshchishina, L. Wang, D. Mondelain, S. Kassi, and A. V. Nikitin. Journal of Quantitative Spectroscopy & Radiative Transfer 113 (2012) 1855-1873.

[69] L. Wang, D. Mondelain, S. Kassi, and A. Campargue, Journal of Quantitative Spectroscopy & Radiative Transfer 113 (2012) 47-57.

[70] A. V. Nikitin, L. R. Brown, K. Sung, M. Rey, V. G. Tyuterev, M. A. H. Smith, and A. W. Mantz, Journal of Quantitative Spectroscopy & Radiative Transfer 114 (2013) 1-12.

[71] Z. Lin, K. Boraas and J. P. Reilly, Journal of Molecular Spectroscopy 179 (1995) 266-278.

[72] A. Campargue and D. Permogorov, Chemical Physics 182 (1994) 281-290.

[73] O. N. Ulenikov, E. S. Bekhtereva, S. Albert, S. Bauerecker, H. Hollenstein, M. Quack, Mol. Phys. 108 (2010) 1209-1240.

[74] K. Deng, X. G. Wang, H. Lin, D. Wang, Q. S. Zhu, Mol. Phys. 97 (1999) 787-795. The full spectrum was sent to us by private communication.

[75]. C. B. Suarez, C. Chackerian, and F. Valero, Spectroscopy Letters 26 (1993) 1523-1527.

[76] C. Boussin, B. L. Lutz, A. Hamdouni, and C. de Bergh, Journal of Quantitative Spectroscopy & Radiative Transfer 63 (1999) 49-84.

[77] M. Devi, D. C. Benner, M. A. H. Smith, and C. P. Rinsland, Journal of Quantitative Spectroscopy & Radiative Transfer 68 (2001)135-161.

[78] V. M. Devi, D. C. Benner, L. R. Brown, M. A. H. Smith, C. P. Rinsland, R. L. Sams, and S. W. Sharpe, Journal of Quantitative Spectroscopy & Radiative Transfer 15 (2002) 139-191.

[79] V. M. Devi, D. C. Benner, M. A. H. Smith, C. P. Rinsland, and L. R. Brown, Journal of Quantitative Spectroscopy & Radiative Transfer 73 (2002) 603-640.

[80] V. M. Devi, D. C. Benner, M. A. H. Smith, C. P. Rinsland, and L. R. Brown, Journal of Quantitative Spectroscopy & Radiative Transfer 74 (2002) 1-41.

[81] A. Predoi-Cross, K. Hambrook, M. Brawley-Tremblay, J. P. Bouanich, V. M. Devi, D. C. Benner, and L. R. Brown, Journal of Molecular Spectroscopy 234 (2005) 53-74.

[82] A. Predoi-Cross, K. Hambrook, M. Brawley-Tremblay, J. P. Bouanich, and M. A. H. Smith, Journal of Molecular Spectroscopy 235 (2006) 35-53.

[83] A. Predoi-Cross, S. Brawley-Tremblay, C. Povey, and M. A. H. Smith, Canadian Journal of Physics 85 (2007) 199-218.

[84] V. M. Devi, D. C. Benner, M. A. H. Smith, C. P. Rinsland, and L. R. Brown, Journal of Molecular Structure 517 (2000) 455-475.

[85] V. M. Devi, D. C. Benner, M. A. H. Smith, C. P. Rinsland, J. Quan. Spec. Rad. Trans. 68 (2001) 1-41.

[86] M. S. Ma, S. Wu, Y. C. Tang, Geochimica Cosmochimica Acta 72 (2008) 5446-5456.

[87] O. N. Ulenikov, E. S. Bekhtereva, S. Albert, S. Bauerecker, H. Hollenstein, M. Quack, J. Phys. Chem. A 113 (2009) 2218–2231.

[88] J. S. Margolis, Appl. Optics 27 (1988) 4038-4051.

[89] O.N. Ulenikov, G. A. Onopenko, N. E. Tyabaeva, J. Schroderus, S. Alanko, J. Mol. Spectrosc. 193 (1999) 249-259.

[90] G. Tarrago, M. Delaveau, L. Fusina, G. Guelachvili, J. Mol. Spectrosc. 126 (1987) 149-158.

[91] PGOPHER, a Program for Simulating Rotational Structure, C. M. Western, University of Bristol, http://pgopher.chm.bris.ac.uk

[92] A.V. Nikitin, O. M. Lyulin, S. N. Mikhailenko, V. I. Perevalov, N. N. Filippov, I. M. Grigoriev, I. Morino, T. Yokota, R. Kumazawa, T. Watanabe, J. Quan. Spec. Rad. Trans. 111 (2010) 2211-2224.

[93] A. Campargue, L. Wang, A.W. Liu, S.M. Hu, S. Kassi, Chem. Phys. 373 (2010) 203-210.

[94] M. Gharavi, S.G. Buckley, J. Mol. Spectrosc. 229 (2005) 78-88.

[95] A. Predoi-Cross, K. Hambrook, S. Brawley-Tremblay, J. P. Bouanich, V. M. Devi, M. A. H. Smith, J. Mol. Spectrosc. 236 (2006) 75-90.

Chapter 4 CRDS spectrum analysis and double resonance of methane isotopomer CH_3D in near infra-red region

As one of the most important hydrocarbon prototype molecules, CH_3D's overtone band in near infrared region has not been well studied. This chapter covers the fundamentals of theoretical spectrum analysis, including group theory, rotational spectra of symmetric top molecules, vibrational transition types, Herzberg's character table, irreducible representation, selection rules, etc. Various methods were used to help identifying transitions in the CRDS spectrum of CH_3D from previous chapter. Symmetric top molecules' Hamiltonian diagonal terms for the ground states, perpendicular state and parallel state were simulated by software Pgopher. Combination differences were used to find possible pairs of transitions starting from adjacent ground state and ending in same excited states. Also, we introduced our temperature controlled spectrum setup for ground state energy estimate and rotational quanta prediction from temperature dependence, and proven to be working well for lower J levels for CH_4. At last, we set up a double resonance system, using two lasers to excite transitions from the same ground state, to provide strong proof for the lower state quanta.

4.1 Introduction

Methane is a colorless, odorless gas with a wide distribution in nature and also the principal component of natural gas. The combustion of natural gas is widely used for heating and for generating electric power [1-4]. Compared with other fuels, methane produces less carbon dioxide when generating the same amount of heat [5-9], and it's also more environmental friendly, since no other pollution gases are generated during

this process. During the past decade, natural gas accounted for about 1/5 of the total energy consumption worldwide [10], and about 1/3 in the United States [11]. Also, on a molecule-for-molecule basis, methane is 86 times stronger as a greenhouse gas than carbon dioxide [12-19]. The surface levels of methane in earth's atmosphere varies from 1.6 to 1.84 parts per million.

A new landmark study by Harvard [20] found that the U.S. Environmental Protection Agency's (EPA) inventory of greenhouse gases is undercounting total U.S. methane emissions by roughly 50 percent. Results show that current inventories from the US Environmental Protection Agency (EPA) and the Emissions Database for Global Atmospheric Research underestimate methane emissions nationally by a factor of ~1.5 and ~1.7, respectively. This drastic undercounting is because the EPA does not currently have an effective and efficient means to measure methane from atmospheric samples, and instead they rely on many assumptions and biased self-reporting of voluntary emission reduction efforts by extraction companies. The estimates of missing methane are based on direct sampling of the atmosphere. Therefore, if there is a convenient way to measure atmospheric methane level directly, it would help fix the EPA's underestimation problem.

On earth, methane is emitted from a variety of both human-related and natural sources [21-26]. About two-thirds of methane emissions can be traced to human activities such as fossil-fuel extraction, rice paddies, landfills and cattle. Natural sources of methane include wetlands, gas hydrates, permafrost, termites, oceans, freshwater bodies, non-wetland soils, and other sources such as wildfires. Since different sources generates different ratios of methane isotopes [27-30], if there is a means to measure

the size and isotopic compositions of a certain sample, it would be feasible to determine what type of resources it comes from. With this idea in mind, our experiment in chapter 2 utilizes a CRDS method to measure atmospheric methane levels (on the order of a few part per million) and its isotopes that would directly help fix EPA's under-estimation and provide clues for the sources.

As one of the most important hydrocarbon prototype molecules, methane also has been studied extensively in various aspects like chemical bonding theory [31, 32], symmetrical molecule rotational dynamics [33], potential hypersurfaces structure [34-39], etc. As for isotopomers, spherical top $^{12}CH_4$ and $^{13}CH_4$ has been well studied for their rovibrational spectra and dynamics, with most of their spectrum information available in HITRAN database. As the second most abundant isotopomer of methane, symmetric top CH_3D's spectrum has been reported in the near infrared region in previous work [40, 41] and also discussed in previous chapter.

This chapter focuses on our approaches for analyzing CH_3D spectrum, for both the CRDS spectrum in our previous paper [41] and an FTIR spectrum [42]. The methods we use include spectrum simulation, combination differences calculation, temperature dependence and double resonance.

4.2 Experimental

In our previous work [41], three DFB near-IR lasers were used to measure the line strengths of CH_3D ro-vibrational transitions ($2\nu_4$) in the wavenumber regions of 6017.5 – 6031.5 cm^{-1} and 6046.5 – 6070.0 cm^{-1} using continuous-wave cavity ring-down spectroscopy (cw-CRDS). CH_3D in high purity N_2 gas was introduced into the

cavity with a total pressure around 8.3 Torr. The molecule number densities varied between (0.5-2.0) × 10^{14} molecule/cm^3. Details of our CRDS experimental setup were discussed in previous chapter.

The Fourier transform infrared spectrum (FTIR) [42] we compared against our CRDS spectrum was recorded at room temperature on a spectrometer with 105 m path length multi pass cell. The gas pressure was 10227 Pa and 1000 scans were co-added in total. They reported the unapodized resolution is 0.01 cm^{-1}. Our spectrum was very similar to this FTIR result, while there is an overall shift of 0.003 cm^{-1}. Also our spectrum has removed absorption lines from CH_4, H_2O and CO_2, which were still listed in this FTIR spectrum.

Also in this chapter, more transitions were assigned and several assignments were corrected, compared with those reported in our paper [41].

4.3 Theoretical background [40, 41-43]

Group Theory is the mathematical application of symmetry to an object to obtain knowledge of its physical properties. It is widely used to label and classify the energy levels of molecules and can qualitatively predict possible transitions between those levels. There are five types of symmetric operations: reflection $\hat{\sigma}$ (with subscripts v, h and d standing for vertical, horizontal and dihedral relative to principal axis), rotation $\hat{C}_n$ (rotates 2π/n clockwise), rotation-reflection $\hat{S}_n$, inversion $\hat{i}$ (inverting all atoms through a point), and identity $\hat{E}$ (do nothing). If molecule's atoms are symmetric, e.g. the center of mass of a molecule remains unchanged under certain symmetry

operations, they are called point groups. Conventionally, for molecules like CH_3D, who remains the same after $\hat{C}_3$ and has 3 symmetry plane $\hat{\sigma}_v$, they are noted as C_{3v}.

Symmetrical tops, which include all C_{3v} molecules, are those when two of their rotational axes have the same moment inertia and that of the third axis different. If the third rotational axis has a greater moment than the other two, the molecule is called an oblate symmetrical top; and if smaller, it's called prolate symmetrical top. CH_3D is a prolate symmetric top.

When considering the pure rotational spectra of symmetric tops, the energy-level expression is

$$F(J,K) = BJ(J+1) + (A-B)K^2 - D_J\left[J(J+1)\right]^2 - D_K K^4 - D_{JK}J(J+1)K^2 \quad (1)$$

where the first two terms are from solving Schrodinger equation of a rigid rotor using symmetric top wavefunctions, and the last three terms are because of centrifugal distortion when the molecule rotates. The parameters A is rotational constant about symmetry axis; B is rotational constant perpendicular to symmetry axis; D_J, D_K and D_{JK} are related to quartic centrifugal distortions.

The pure rotational spectra of symmetric tops have simple selection rules: $\Delta J = \pm 1$, $\Delta M = 0, \pm 1$ and $\Delta K = 0$. Here J is rotational quantum number, M is J's projection along laboratory fixed axis, and K is projection along the symmetry axis of molecule coordinate system.

Molecules vibrate and rotate at the same time, forming vibration-rotation spectra. For various types of infrared transitions, the fundamental transition refers to vibrational

quantum number $\nu = 1 \leftarrow 0$, and any transitions with lower state $\nu \neq 0$ are called hot bands. The transition $\nu = 2 \leftarrow 0$ is called the first overtone, $\nu = 3 \leftarrow 0$ the second overtone, and so on. It is worth mentioning that, the notations of vibrational modes are divided into symmetry species of the point group and the order for labeling follows Herzberg's character tables [45]. For example [44], for spherical tops like CH_4, ν_1 is symmetrical C-H stretching, ν_2 doubly degenerate deformation, ν_3 triply degenerate stretching, and ν_4 triply degenerate deformtion. For CH_3D, ν_1 is CH_3 s-stretching, ν_2 C-D stretching, ν_3 CH_3 s-deforming, ν_4 CH_3 d-stretching, ν_5 CH_3 d-deforming, ν_6 CH_3 rock [44], shown in figure 1.

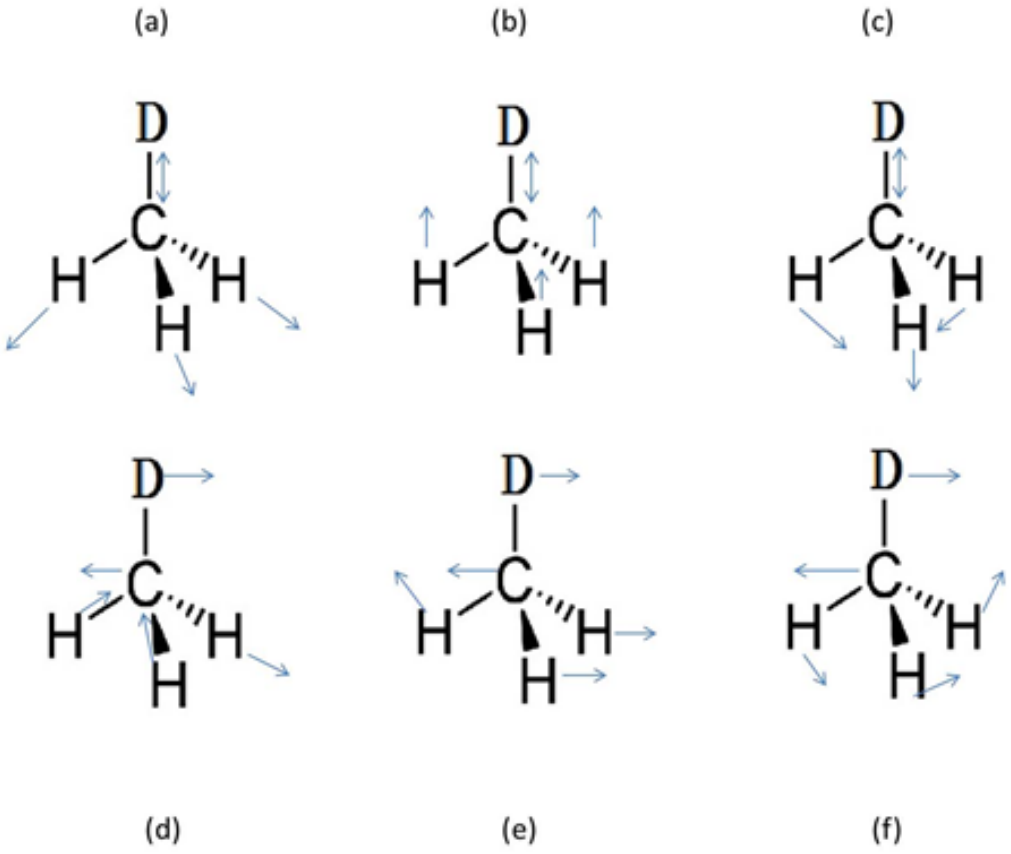

Figure 1. Vibrational modes of CH_3D with only one of each degenerate mode displayed. (a) ν_1 CH_3 s-stretching. (b) ν_2 C-D stretching. (c) ν_3 CH_3 s-deforming, or

called bending mode (umbrella mode). (d) ν_4 CH_3 d-stretching, or antisymmetric C-H stretch. (d) ν_5 CH_3 d-deforming, or antisymmetric bend. (f) ν_6 CH_3 rock.

It is useful to have characters of the irreducible representation of the point groups. The character table for C_{3v} molecules like CH_3D is

Table 1. Character table for C_{3v} point group [43]

C_{3v}	$\hat{E}$	$2\hat{C}_3$	$3\hat{\sigma}_v$
A_1	1	1	1
A_2	1	1	-1
E	2	-1	0

The first row of Table 1 is symmetry operations mentioned before. There are 6 operations that would keep the group 'the same': do nothing $\hat{E}$; two rotations, 120°clockwise $\hat{C}_3^+$ and counterclockwise $\hat{C}_3^-$; And three plane-reflections $\hat{\sigma}_v$. Therefore C_{3v} group order is 6. The first column lists the Mulliken symbols [46] for the irreducible representations of the group, where one-dimensional symmetric irreducible representation is labeled as A (labelled as A_1 when +1 under principle rotation and +1 under reflection; A_2 when +1 under rotation but -1 under reflection; if -1 under rotation, they are labeled as B_1, B_2 respectively.), two-dimensional symmetric irreducible representation as E (it's unrelated to the operator $\hat{E}$). Note that these A and B are not the spectroscopic parameters mentioned in equation (1). Normal modes of vibration and total vibrational wavefunctions transform under the symmetry operations as irreducible representations and can be labeled by which

representation they transform as. It is conventional to label normal modes with lower case letters and wavefunctions with upper case letters.

For molecules with no net spin or orbital angular momentum, for example, diatomic molecules, the selection rules are rotational selection rules $\Delta J = \pm 1$ and vibrational selection rules $\Delta \nu = \pm 1$ that come from Harmonic oscillation approximation. The transitions with $\Delta J = +1$ are called R branch, and those with $\Delta J = -1$ belong to P branch. For molecules with non-zero spin or angular momentum, selection rules for one-photon and electric-dipole-allowed transitions are $\Delta J = 0, \pm 1$, where $\Delta J = 0$ transitions are called Q branch. There are transitions, like Raman transitions, that have different selection rules and ΔJ. When ignoring the effect of centrifugal distortions, the line positions for R and P branch are:

$$\nu_R\left(\nu', J+1 \leftarrow \nu'', J\right) = \nu 0 + (B' + B'')(J+1) + (B' - B'')(J+1)^2 \quad (2)$$

$$\nu_P\left(\nu', J-1 \leftarrow \nu'', J\right) = \nu 0 - (B' + B'')J + (B' - B'')J^2 \quad (3)$$

Here B is the rotational constant perpendicular to symmetry axis. The upper state is marked by prime symbol (′) and lower state by double prime symbol (″).

As for linear molecules, the transitions in symmetric tops can have transition dipole moments parallel to the symmetric axis, and those are of the $A_1 - A_1$ type; or if perpendicular to the axis, they are of $E - A_1$ type. The $A_1 - A_1$ type parallel selection rules are $\Delta J = \pm 1$ for $K' = 0 \leftarrow K'' = 0$, and $\Delta J = 0, \pm 1$ for $K \neq 0$. The perpendicular $E - A_1$ type transitions of symmetric top require the addition of Coriolis term to the Hamiltonian operator, similar to equation (5) on next page. The presence of Coriolis interaction makes the energy-level structure of an E state more

complicated. The perpendicular E – A_1 type selection rules are $\Delta J = 0,\pm 1$ and $\Delta K = \pm 1$.

If two transitions share a common upper or lower level, the difference between these two transitions is called combination difference. These differences are useful because they depend only on the upper or lower state spectroscopic constants. In later part of this chapter the combination differences will be used to help analyzing CH_3D spectrum.

4.4 Analysis of the experimental data

4.4.1 Pgopher simulation

We used PGOPHER software to simulate two stretching bands, parallel band $2\nu_4(A_1)$ and perpendicular band $2\nu_4(E)$. The diagonal terms for the ground state of CH_3D symmetric top are [42]

$$H = \left\langle J,K\left|\frac{H}{hc}\right|J,K\right\rangle = \nu + (A-B)K^2 + BJ(J+1) - D_J J^2(J+1)^2$$
$$- D_{JK}J(J+1)K^2 - D_K K^4 + H_J J^3(J+1)^3$$
$$+ H_{JK}J^2(J+1)^2K^2 + H_{KJ}J(J+1)K^4 + H_K K^6 \qquad (4)$$

The parameters A, B are rotational constant about and perpendicular to symmetry axis, respectively; D_J, D_{JK}, D_K are quartic centrifugal distortion parameters; H_J, H_{JK}, H_{KJ}, and H_K are sextic centrifugal distortion parameters.

The expression for A_1 state is the same as above, with different parameters.

The expression for *E* state is:

$$H = \left\langle J,K\left|\frac{H}{hc}\right|J,K\right\rangle = \nu + (A-B)K^2 + BJ(J+1) - D_J J^2(J+1)^2$$
$$- D_{JK}J(J+1)K^2 - D_K K^4 + H_J J^3(J+1)^3$$
$$+ H_{JK}J^2(J+1)^2K^2 + H_{KJ}J(J+1)K^4 + H_K K^6$$
$$+ [-2A\xi + \eta_J J(J+1) + \eta_K k^2]kl \qquad (5)$$

where *l*=+/-*1, K*=|*k*|. *J* is total angular momentum quantum number, *l* is vibrational angular momentum quantum number, *K* is projection of *J* along molecular symmetric axis.

For the *K=1* in $2\nu_4(E)$ band, there is so called *l*-type splitting. The higher order terms should be used [47]:

$$\left\langle l=+1,J,k+2\left|(H_{22}+H_{24})/hc\right|l=-1,J,k\right\rangle = -\frac{1}{2}\left[q_{eff} + q_{eff}^{K}K^2\right]F(J,k)F(J,k+1) \qquad (6)$$

where $F(J,k) = \left[J(J+1) - k(k+1)\right]^{1/2}$.

PGOPHER [48] is convenient software for simulating rotational, vibrational and electronic structure of spectra. The comparison of our CRDS result, FTIR [42] and Pgopher simulation are shown in Figure 2 (only parts shown here). And the simulation parameters used are listed in Table 2. We found that some of the parameters are very different from literature [42], which cannot be used to reproduce a simulation that agrees well with experimental results.

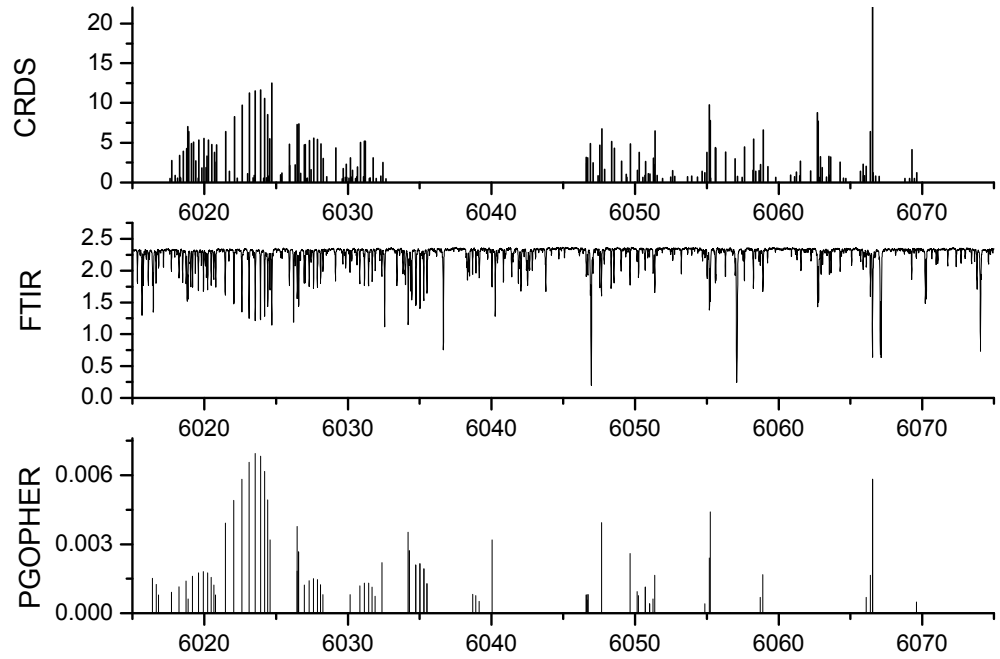

Figure 2. Comparison of CRDS spectrum, FTIR and Pgopher simulation in the region of 6015 – 6075 cm^{-1}. The gap in CRDS is the regions not covered by our DFB lasers. The FTIR is not pure CH_3D spectrum (there are CH_4, H_2O and CO_2 lines as well). The simulation of $2\nu_4(A_1)$ and $2\nu_4(E)$ agrees well with experimental results, with most assigned peaks within +/-0.004 cm^{-1} away from corresponding experimental results, while there are still many lines (possibly from other vibrational bands) that cannot be assigned.

Table 2. Vibration-rotational parameters for simulating $2\nu_4(A_1)$ and $2\nu_4(E)$ overtone bands (unit cm^{-1})

Parameter	Ground state [49]	$\langle 2\nu_4(A_1)\|2\nu_4(A_1)\rangle$	$\langle 2\nu_4(E)\|2\nu_4(E)\rangle$
v	-	5980.404(8)	6022.203(4)
A	5.250821	5.242(1)	5.2134(7)
B	3.880195	3.862(1)	3.8506(3)
$D_J/10^{-5}$	5.2614	-1.5(4) ×10	4.8(7)
$D_{JK}/10^{-4}$	1.26287	-1.6(2)×10	2.6(2)
$D_K/10^{-4}$	-0.78844	3.4(2)×10	-2.3(3)
$H_J/10^{-9}$	1.394	-	$1.0(5)\times10^2$
$H_{JK}/10^{-8}$	1.146	-	$3.9(2)\times10^2$
$H_{KJ}/10^{-9}$	-6.58	-	$3.9(4)\times10^2$
$H_K/10^{-9}$	-1.05	-	$-2.9(4)\times10^3$
$A\zeta$	-	-	-0.1021(1)
$\eta_J/10^{-3}$	-	-	1.26(2)
$\eta_K/10^{-3}$	-	-	1.20(5)
$q_{eff}/10^{-2}$	-	-	-1.59(2)
$q_{eff}^K/10^{-3}$	-	-	-
$\sigma/10^{-3}$	-	-	-

Note: The parameters for ground state were determined from ground state combination differences [54]. The parameters for A and E band were determined from fitting experimental spectrum.

4.4.2 Combination differences

Though the rovibrational parameters of most overtone bands of CH_3D are yet determined from experiments, the ground state parameters have been well studies. If there are two transitions from different ground states both go to the same overtone band state, their energy difference can be easily determined from equation (4).

For example, for transitions $J', K' \leftarrow J'', K''$ and $J', K' \leftarrow J''+1, K''$, their difference is

$$H(J''+1, K'') - H(J'', K'') = 2B(J+1) - 4D_J(J+1)^3 - 2D_{JK}(J+1)K^2 + 4H_{JK}(J+1)^3K^2 + 2H_{KJ}(J+1)K^4 \quad (7)$$

Most of the identified transitions from Pgopher simulation agree with combination differences in the above formula. We are able to match more transitions by using identified transitions and combination differences. Some exceptions for *K=1* transitions happen because those transitions do not go to the same upper state because of *l* splitting. What's more, since the experimental results' resolution is around 0.001 cm^{-1}, other than the first two terms and some of the higher K transitions, most of the terms in equation (7) are negligible, which sometimes results in disability to distinguish combination differences with same *J* and different *K*.

Other than frequency spacing calculation from equation (7), the relative intensities of combination differences can also be predicted. The line intensities in the bands of symmetric top molecules are proportional to the product:

$$CA_{JK}\nu g_{JK}e^{-F(J,K)hc/KT} \quad (8)$$

where C is a constant who is independent of K and J, but depending on the vibrational transition. g_{JK} and $F(J,K)$ are statistical weight and term value of the lower state. A_{JK} (and noted as f later) is proportional to the square of the transition moment ($R_{xf}^2 + R_{yf}^2 + R_{zf}^2$) summed over all orientations of J, which is also called the Hönl-London factors. They directly indicate how the total intensity of a transition is distributed among the branches, i.e. the relative intensity found in the R-, P- and Q-branch. These are derived assuming a separation of vibration and rotation, which only approximately holds when there are interactions between different vibrational bands.

The Honl-London factors for the Q-branch ($J'= J$) are:

$$f(J,K|J,K) = \frac{(2J+1)K^2}{J(J+1)} \tag{9}$$

$$f(J,K+1|J,K) = \frac{(J+1+K)(J-K)(2J+1)}{4J(J+1)} \tag{10}$$

$$f(J,K-1|J,K) = \frac{(J+1-K)(J+K)(2J+1)}{4J(J+1)} \tag{11}$$

For the P-branch ($J'= J-1$):

$$f(J-1,K|J,K) = \frac{(J+K)(J-K)}{J} \tag{12}$$

$$f(J-1,K+1|J,K) = \frac{(J-1-K)(J-K)}{4J} \tag{13}$$

$$f(J-1,K-1|J,K) = \frac{(J-1+K)(J+K)}{4J} \tag{14}$$

And for the R-branch ($J'= J+1$):

$$f(J+1,K|J,K)=\frac{(J+1+K)(J+1-K)}{J+1} \tag{15}$$

$$f(J+1,K+1|J,K)=\frac{(J+2+K)(J+1+K)}{4(J+1)} \tag{16}$$

$$f(J+1,K-1|J,K)=\frac{(J+2-K)(J+1-K)}{4(J+1)} \tag{17}$$

4.4.3 Temperature dependence

If only considering rotational energy, the relative integrated intensity of each rotational line should have a temperature dependence of

$$C(2J+1)e^{-E/KT}T^{-3/2} \tag{18}$$

where C is a constant, E is state energy and T is temperature. The $T^{-3/2}$ part comes from the inverse of the rotational partition function in the high temperature limit. (When calculating the rotational partition function, the numerator is the degeneracy of this rotational state and the denominator is the sum of all states' degeneracies, which yields a $T^{3/2}$ dependence.) Since all excited vibrational states are weakly excited ($E>>KT$), the methane spectrum should be dominated by the rotational partition function.

If we have the intensities of the same absorption line at two different temperatures T_1 and T_2, the ratio of their intensities would be

$$\frac{I_1}{I_2}=\exp\left[-\frac{E}{K}\left(\frac{1}{T_1}-\frac{1}{T_2}\right)\right]\cdot\left(\frac{T_2}{T_1}\right)^{\frac{3}{2}} \tag{19}$$

Therefore the energy would be

$$E = \frac{\ln\left(\frac{I_1}{I_2}\right) + \frac{3}{2}\ln\left(\frac{T_2}{T_1}\right)}{\frac{1}{T_2} - \frac{1}{T_1}} \tag{20}$$

In the meanwhile, from equation (4), for lower *J* levels, the majority of energy are from the term *E=BJ(J+1)*. Therefore after getting the transition energy from equation (20), one can easily estimate the corresponding J value:

$$J = \frac{1}{2}\left(\sqrt{1 + 4\frac{E}{B}} - 1\right) \tag{21}$$

In order to get the absorption spectrum under two different temperatures, for example, room temperature and liquid nitrogen temperature, we designed a temperature-controlled single-pass cell, shown in figure 3. The laser we used to get CH_3D absorption spectrum under different temperature was New Focus 6331 tunable diode laser, which covers the wavelength region of 1645 – 1686 nm.

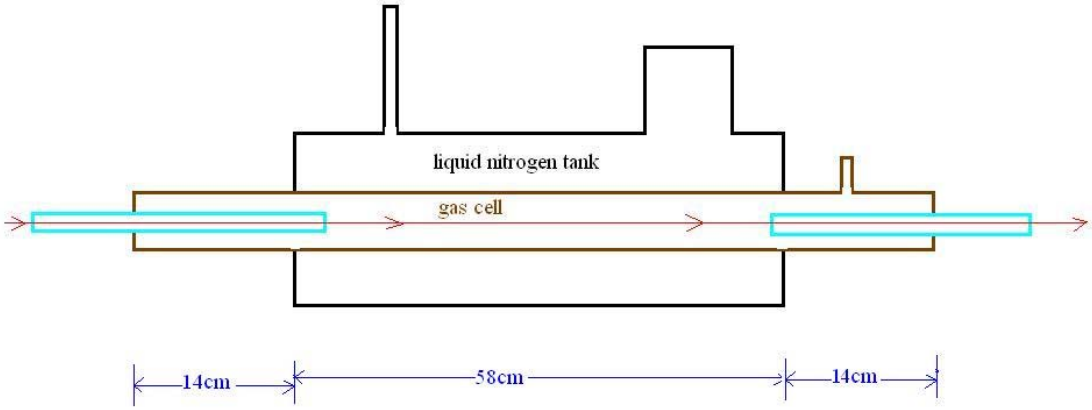

Figure 3. Temperature-controlled single-pass cell. The two blue tubes are vacuumed and sealed glass tubes, with flat windows on both ends. They are inserted into the cell such that the laser beam would only reach sample gas within temperature controlled region. The gas cell is surrounded by a tank which can be filled with liquid nitrogen.

In order to see how estimated J values from equation (21) agree with real J value, we took the direct absorption spectrum of CH_4 Q branch under room temperature and liquid nitrogen temperature, shown in Figure 4. Each peaks' integrated value are proportional to line intensities I_1 or I_2 in equations (19-20). Then experimentally predicted energy can be calculated from equation (21). The comparison between experimentally predicted state energy and $E=BJ(J+1)$ approximation is shown in Figure 5. The energies do not differ much for lower J levels. Therefore energy temperature dependence can serve as an effective way to estimate the rotational quantum number J but there is ambiguity for the very lowest J values. The estimate also fails for $J > 6$. These levels have very small absorption at 77K and the remaining absorption is likely strongly influenced by some residual warm gas in the laser path, as well as errors in the extraction of integrated intensity of weak lines. This situation

could be improved by taking a spectrum at an intermediate temperature, say near 200 K, but we presently are not set up to take such spectra.

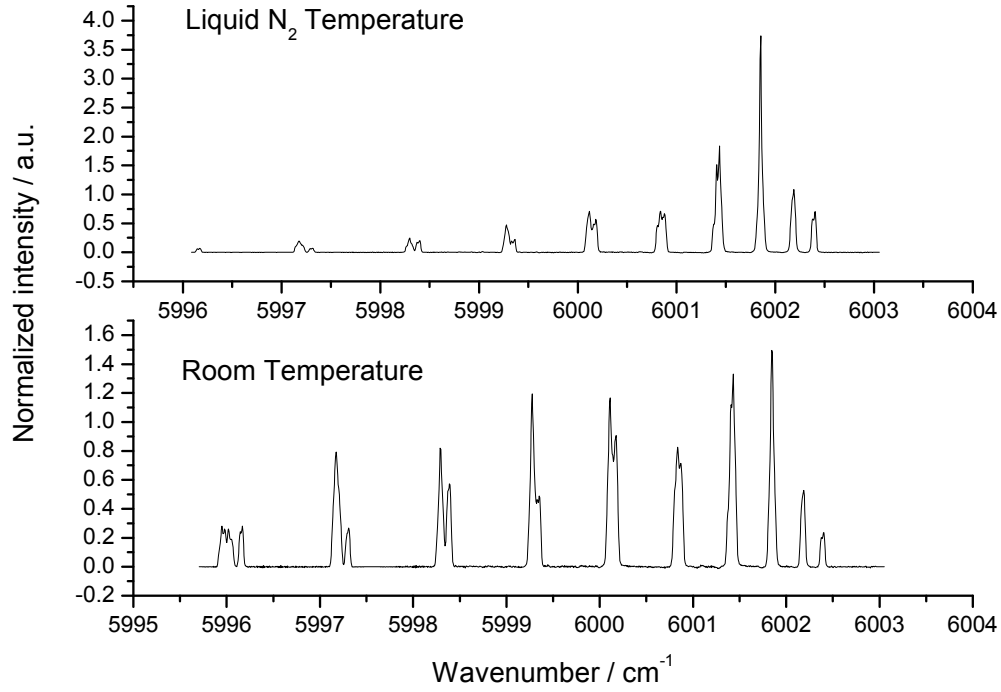

Figure 4. Normalized direct absorption spectrum of CH_4 Q-branch near 6000 cm^{-1}. Compared with those under room temperature 293K, under liquid nitrogen temperature 77K, the low *J* lines got stronger and high *J* lines got weaker, as expected.

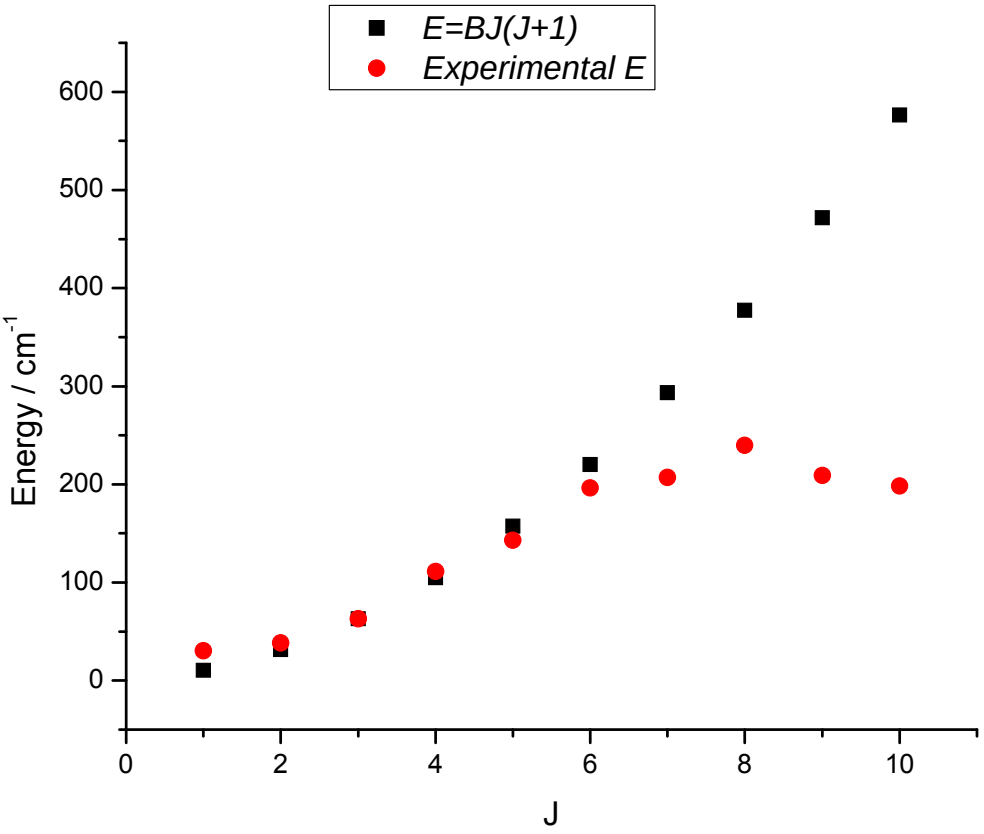

Figure 5. Comparison of state energy from experimental temperature dependence and rotational energy approximation. We can see that for lower *J* (less than 6) they agree well with each other, and for *J* higher than 8 they start to differ significantly. This is probably because for higher *J*, the energy contributed from vibrations is getting too big to be neglected and it may follow different temperature dependence.

We then fill the temperature-controlled single-pass cell with 15.5 torr CH_3D. (The reason we don't choose higher pressure is because the vapor pressure of CH_3D around liquid nitrogen temperature is about 10-15 torr.) After calibrating pressure change under liquid nitrogen temperature, the calculated energy is listed in appendix of CH_3D near infra-red spectrum.

4.4.4 Double resonance

Double resonance means exciting one resonant transition while simultaneously monitoring a different transition. In our setup, we used a pump laser (Aculight Argos Model 2400 CW OPO 3200 – 3900 nm) to excite fundamental transition, and then monitor all the first overtone band (mostly $2\nu_4$) that is accessible with our probe NIR lasers (New Focus 6331 tunable diode laser 1645 – 1686 nm and various NEL DFB diodes). The experimental setup is shown in Figure 6. The two laser beams counter propagate through the single pass cell filled with CH_3D, and are combined and separated by 60° prisms. The OPO's frequency is locked onto a CH_3D fundamental transition, by using wavemeter as well as a 150MHz etalon reference. The pump laser beam is mechanically chopped at a frequency of 2.7 kHz and near-IR detector signal is sent into Stanford Research Systems SR510 lock-in amplifier. The reference for the lock-in derives from the mechanical chopper. There is an additional single pass cell filled with higher pressure mixture of CH_4, $^{13}CH_4$ and CH_3D to help with NIR wavelength calibration, which is not shown in this figure.

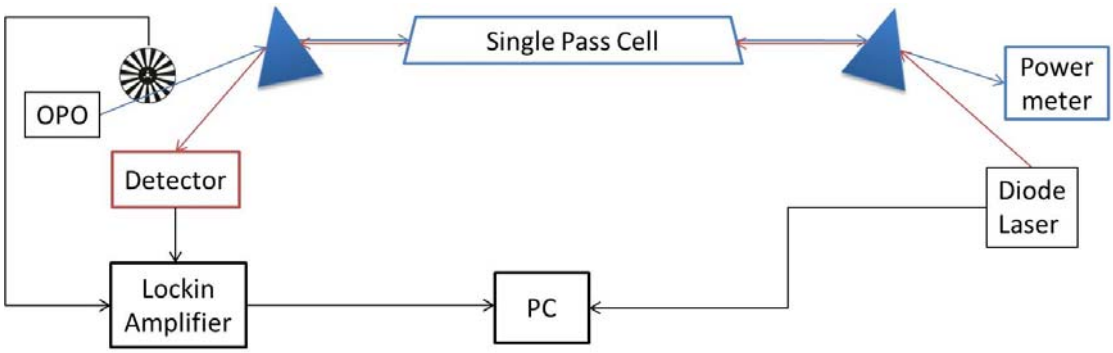

Figure 6. Experimental setup for double resonance. The OPO beam is chopped at 2.7 kHz, then combined with and later separated from diode laser beam by prisms. The single pass cell is filled with 300 mtorr CH_3D. The pressure is chosen to have strongest double resonance peaks. The two beams travel in opposite directions within the single pass cell. The lock-in amplifier is used to pick up CH_4 or CH_3D absorbing signal of diode laser. The pump laser is locked onto the desired fundamental transition absorption peak, and the probe laser is scanned throughout the entire region. The OPO locking system is not shown in the graph.

We first test this system on two known transitions of CH_4, and the result is shown in Figure 7 and 8, where Figure 7 is coarsely temperature tuning and 8 finely current tuning. As expected, the OPO excited fundamental transition ‘burns a hole’ in the diode laser excited first overtone band transition.

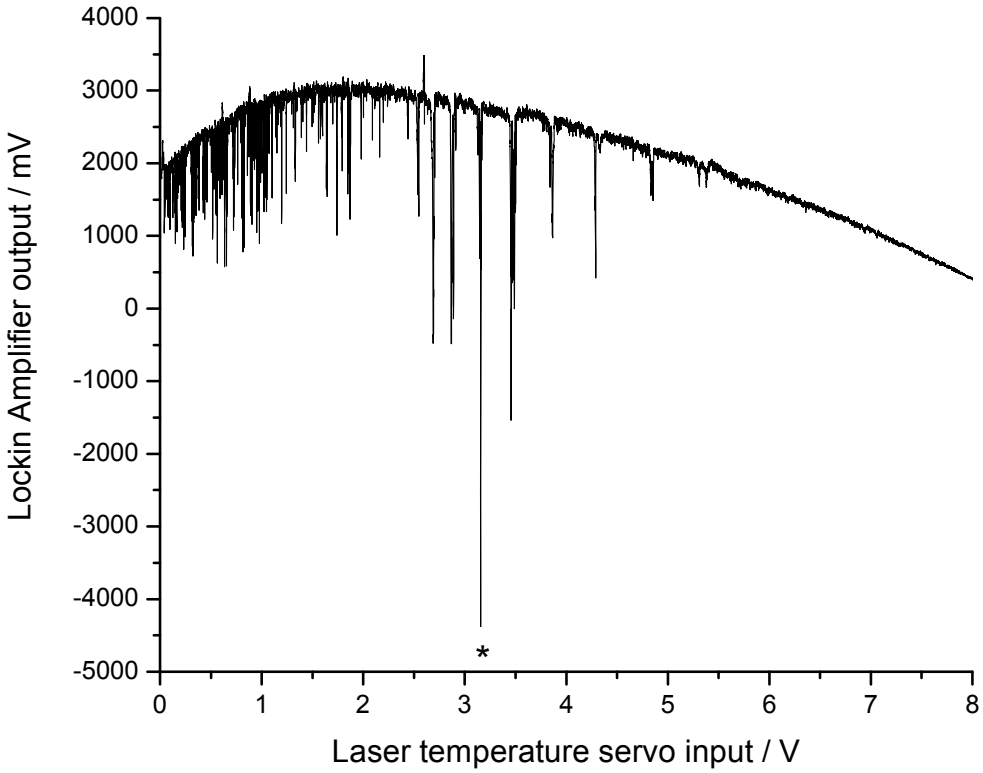

Figure 7. Locking amplifier output shows there is a double resonance peak, marked with star. This is the first overtone band of CH_4 near 6000 cm^{-1} Q branch, taken by DFB laser diode #927690. The pump laser is locked on the transition whose lower state is from ground state *J"=3*. The double resonance peak is Q(3).

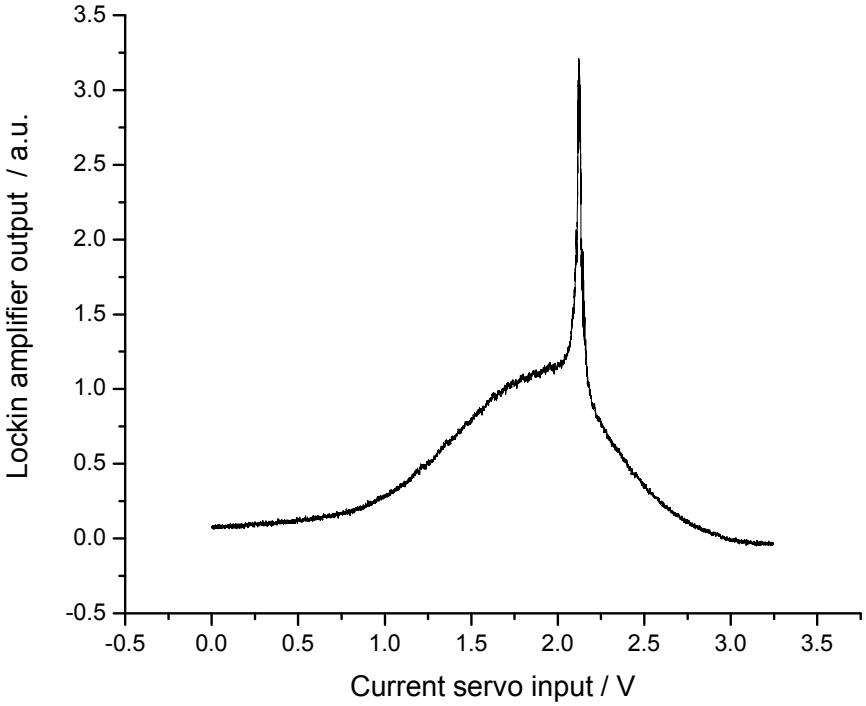

Figure 8. Double resonance signal of CH_4 transitions after normalization. OPO is locked at a fundamental transition of CH_4 at 3057.68cm^{-1} *(R(3))*. And this is the fine tuning (power supply current scan) through this first overtone peak of CH_4 at 6004.293 cm^{-1} *(Q(3))* by DFB laser diode #927690. The temperature of DFB laser was set at 19.5 ^oC, and power supply current at 23.6 mA. And x axis is varying the current servo input voltage in order to finely tune laser frequency. The asymmetric structure is because OPO beam is not locked exactly at the center of the fundamental transition. When locked exactly in the center, the sharp spike would be in the center of the broader peak.

The procedure of finding CH_3D double resonance peaks is similar to the one of CH_4, and the only difference is that the ground state of two beams should have same *J* and *K*. Since the fundamental transitions of CH_3D near 3μm have been well studied in HITRAN database, and then finding the ground state *J* and *K* value would be strong

proof for the unassigned overtone transitions near 1.6μm. All the results are listed in appendix.

In our double resonance experiment of CH_4 and CH_3D, there are four different features we observed: broad (Doppler limited) and sharp (pressure broadening and laser jitter limited) of negative (reduced absorption) and positive (increased absorption) going phases. All four different features are shown in Figure 9 (a) and (b).

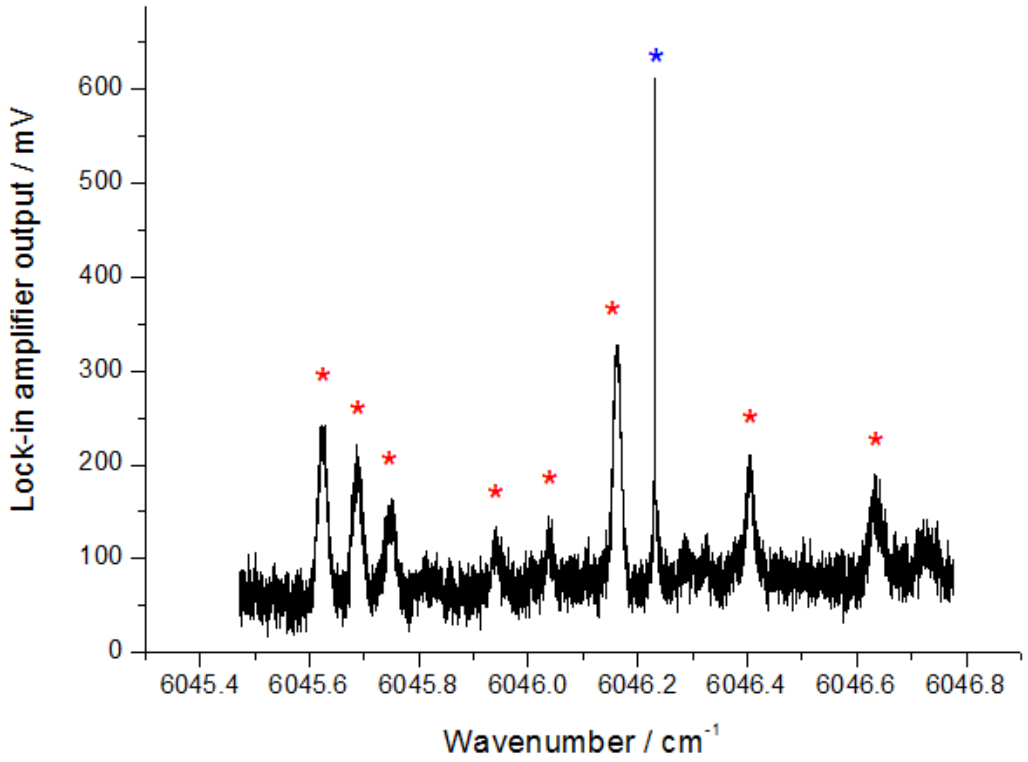

Figure 9 (a). Broad and sharp positive going features of double resonance. The double resonance single pass cell is filled with ~1torr pure CH_4. The pump laser OPO is locked at 3028.726 cm^{-1} which is *R(0) v=1←0* transition for CH_4. For the sharp positive going peak (marked with blue star), the probe laser excites molecules *v=3←1*.

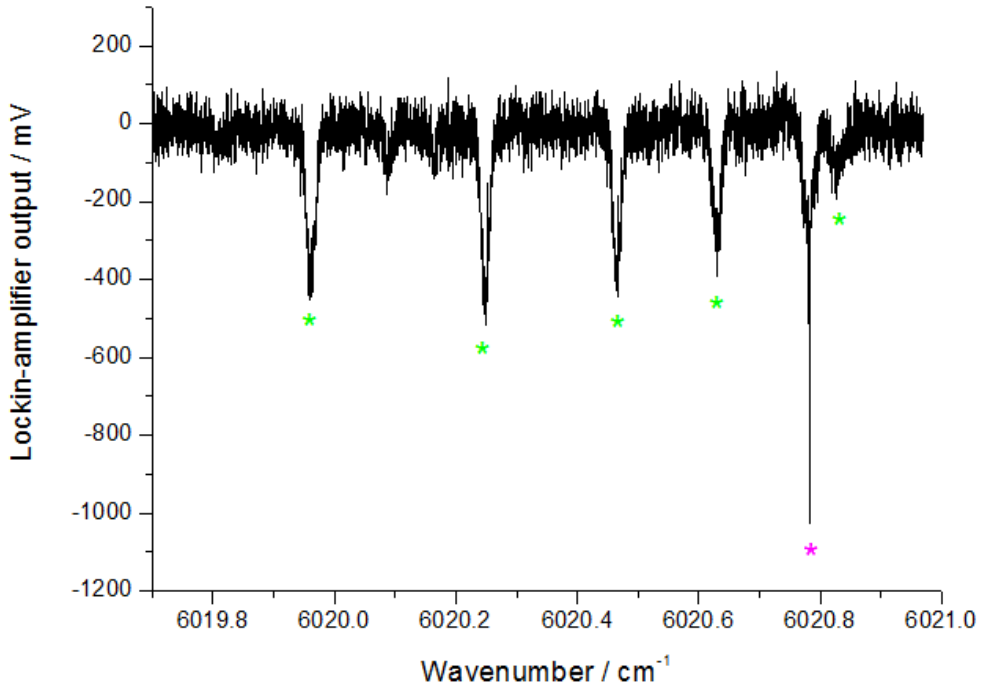

Figure 9 (b). Broad and sharp negative going features of double resonance. The double resonance single pass cell is filled with ~300 mtorr pure CH_3D. The pump laser OPO is locked at 3034.688 cm^{-1} which is $^{R}R_1(1)$ *v=1←0* transition for CH_3D, corresponding to the sharp negative going peak (marked with purple star). All the broad negative peaks (marked with green star and also including the one overlapped with sharp peak) correspond the probe laser excites molecules *v=2←0*.

The Doppler broadened negative going features are at the probe wavenumbers of the *v=2←0* absorption peaks. They are found to have a phase delay of ~-70° relative to the chopped pump laser light, while the sharp peaks' relative phase delay varies with different pump laser transitions. One might expect that the heating of the methane gas by the pump laser will result in an increase in temperature and thus a decrease in the absorption intensity of the lower J lines but an increase in intensity of the higher J lines. However, we observe an approximately uniform fractional depletion in the strength of transitions from the ground vibrational state. We would also expect that

for low J transitions, we should see an increase in absorption of the wings of the lines due the larger Doppler broadening at high temperature, and again, this is not observed. We believe these observations reflect the fact that the pump laser is primarily raising the vibrational temperature of the gas but having very little effect on the rotational and translational temperatures. Previous measurements of relaxation of methane found the collisional rotation-translation (RT) relaxation rate is ~20 $\mu s^{-1}Torr^{-1}$ [51], and thus very fast compared to our pump laser modulation frequency 2.7 kHz. Though the rate for vibrational relaxation is slower, about an order of magnitude slower than that for rotational relaxation [52], but still fast compared to our modulation frequency. However, the decay of vibration energy into a combination of rotational and translational excitation for methane is known to be very slow, only ~0.25 $\mu s^{-1}Torr^{-1}$ [53], comparable to our modulation rate at our optimal sample pressure range of ~0.2-1 *torr* and also the time required for molecules initially in the center of the cell to diffuse to the walls which is expected to also cause vibrational relaxation. For each methane molecule pumped to the $2\nu_3$ state, we can anticipate V-V relation to produce four molecules in the lowest bending state.

The sharp negative features almost always overlap with broad negative features, indicating that the probe laser and the pump laser are exciting molecules from the same lower state; in other words, the probe laser excites *v=2←0* and the pump laser *v=1←0*, with the same lower rotational state in common in both transitions (V type double resonance). As the pump laser has a linewidth of ~1 MHz, the initially pumped molecules have a narrowly selected velocity in the direction of the propagation of the pump laser. This results in a sub-Doppler transition for the probe with an expected width about twice that the pump laser. Power broadening of the pump laser, pump and

probe laser jitter, and pressure broadening (including from elastic collisions) all contribute to broadening this sub-Doppler feature, which we observe to have a typical width of 10 MHz (HWHM).

The sharp positive features come from 'ladder' transitions, where the pump laser excites molecules by $v=1 \leftarrow 0$, and the probe laser excites molecules by $v=3 \leftarrow 1$ such that the upper vibrational state of the pump transition is the lower state of the second transition. As these probe transitions have negligible lower state population even with the increased vibrational temperature produced by the pump, these typically do not have Doppler broadened features underneath these transitions.

We tentatively assign the Doppler broadened, positive going features as starting from rotational levels of the lowest bending state, which is metastable given the slow rate of V -> RT relaxation. These features are more prominent in the case of CH_4 over that of CH_3D. The lowest excited vibrational state of CH_3D (1166.1 cm^{-1}) is lower than that of CH_4 (1367.4 cm^{-1}), and thus a significantly faster V -> RT rate is expected for CH_3D by the exponential gap law. In the case of CH_4, the lowest bending state is the F2 symmetry v_4 fundamental level. Electric dipole selection rules allow this lower vibrational state to be driven to states of A1, E, F1, and F2 symmetry, while such transitions from the A1 ground state only are allowed to the F2 vibrational levels. Based upon our assignment, we expect to find combination differences to ground state absorption features of methane near 7400 cm^{-1}, as well as within the observed transitions from the v_4 state. Note that unlike for transitions from the ground state, upper states will typically share multiple transitions from different lower states that are fully allowed even neglecting rovibrational interactions. Due to the expected

strong rovibratonal interactions of the rovibrational states near 7400 cm^{-1}, we anticipate that there should be a significant number of combination difference transitions observed between the 1.6 and 1.35 μm Spectra. High sensitivity and high resolution spectra near 1.35 μm has been obtained at both 80 and 300 K by a group from Grenoble [50]. Our next experimental step is to repeat the double resonance measurements in the liquid nitrogen cooled cell, which should give us estimates for the rotational excitation of the lower states of these hot band transitions and then combine our spectra with those of Grenoble to do a combination difference search which we hope will give us sufficient number of assigned lines to bootstrap an assignments for both spectra and allow fitting the observed term values to an effective molecular ro-vibrational Hamiltonian.

It is also worth mentioning that the broad negative features and sharp negative features do not always have same phase shifts difference. By phase shifts it means to get the highest peak-to-peak, the phase settings on lock-in amplifier are not the same for these two features. Also, the phase shifts between these features do not have a fixed difference.

It's also necessary to pay attention to is the choice of pressure within the double resonance single pass cell. We ran several measurements using different methane pressure, and it has been found that the optimum pressure for detecting sharp negative and positive features is ~300 mtorr for CH_4 and CH_3D for the 1 m long cell. For broad negative or positive features, their peak values all seem to increase with higher pressure or number density of target molecules.

4.5 Conclusion

This chapter is intended to help identifying transitions from previous CRDS spectrum of CH_3D from previous chapter. Firstly we introduce the fundamentals of theoretical spectrum analysis, including group theory, rotational spectra of symmetric top molecules, vibrational transition types, Herzberg's character table, irreducible representation, selection rules, etc. Then we list four different methods that we used, which are software simulation, combination differences, temperature dependence, and double resonance. Symmetric top molecules' Hamiltonian diagonal terms for the ground state, perpendicular state and parallel state are simulated by software called Pgopher. Combination differences are used to find possible pairs of transitions starting from adjacent ground state and ending in same excited states. Then our temperature controlled spectrum provides evidence for ground state energy and rotational quanta prediction from temperature dependence, which works well especially for lower J levels. At last, our double resonance system uses two lasers to excite transitions from the same ground state, to provide strong proof for the lower state quanta. All these results can be found listed in appendix.

Bibliography

[1] L. J. Fry, Practical building of methane power plants for rural energy independence (1974)

[2] C. Breyer, S. Rieke, M. Sterner, and J. Schmid, Hybrid PV-Wind-Renewable Methane power plants - a potential cornerstone of global energy supply, 26th European Photovoltaic Solar Energy Conference (2011)

[3] H. Knight, Wonderfuel: Welcome to the age of unconventional gas, New Scientist (2010).

[4] Electricity Net Generation, U.S. Energy Information Administration (2014)

[5] M. Ishida, D. Zheng, T. Akehata, Energy, Vol. 12, Issue 2 (1987).

[6] K. Tomishigea, S. Kanazawab, K. Suzukib, M. Asadullaha, M. Satoc, K. Ikushimad, and K. Kunimoria, Applied Catalysis A: General, Vol. 233, Issues 1–2 (2002).

[7] G. Brennera, K. Pickenäckera, O. Pickenäckera, D. Trimisa, K. Wawrzineka, and T. Webera, Combustion and Flame, Vol. 123, Issues 1–2 (2000).

[8] D. A. Pittam and G. Pilcher, Measurements of heats of combustion by flame calorimetry. Part 8.—Methane, ethane, propane, n-butane and 2-methylpropane, J. Chem. Soc., Faraday Trans. 1 (1972).

[9] W.M. Thornton D.Sc.D.Eng.a, XV. The relation of oxygen to the heat of combustion of organic compounds, Vol. 33, Issue 194 (1917).

[10] Energy Academy, Heriot-Watt University, BP Statistical Review of World Energy (2014).

[11] U.S. Energy Information Administration, Short-Term Energy Outlook (2014).

[12] K. A. Kvenvolden, Methane hydrates and global climate, Global Biogeochemical Cycles, Volume 2, Issue 3, pp. 221-229 (1988).

[13] J. Lelieveld, S. Lechtenböhmer, S. S. Assonov, C. A. M. Brenninkmeijer, C. Dienst, M. Fischedick and T. Hanke, Nature 434, 841-842 (2005).

[14] Pavlov, A. A., J. F. Kasting, L. L. Brown, K. A. Rages, and R. Freedman (2000), J. Geophys. Res., 105(E5), 11981–11990 (2000).

[15] W. D. Gunter, T. Gentzis, B. A. Rottenfusser, and R. J. H. Richardson, Energy Conversion and Management, Volume 38 (1997).

[16] U. H. Wiechert, Earth's Early Atmosphere, Perspectives: Geology, Science, VOL 298 (2002).

[17] R. E. Kopp, J. L. Kirschvink, I. A. Hilburn, and C. Z. Nash, Proceeding of the National Academy of Sci., vol. 102 no. 32, 11131-11136 (2005).

[18] R. W. Howarth, R. Santoro, and A. Ingraffea, Methane and the greenhouse-gas footprint of natural gas from shale formations, Climatic Change, Volume 106, Issue 4, pp 679-690 (2011).

[19] J. D. Haqq-Misra, S. D. Domagal-Goldman, P. J. Kasting, and J. F. Kasting, Astrobiology, Volume 8, Issue 6 (2009).

[20] S. M. Millera, S. C. Wofsya, etc, Proceeding of the National Academy of Sci., Vol. 110, No. 50 (2013).

[21] K. Johnson , M. Huyler , H. Westberg , B. Lamb , and P. Zimmerman, Environ. Sci. Technol., 28 (2), pp 359–362 (1994).

[22] Z. Cai, G. Xing, X. Yan, H. Xu, H. Tsuruta, K. Yagi, and K. Minami, Methane and nitrous oxide emissions from rice paddy fields as affected by nitrogen fertilisers and water management, Plant and Soil, Volume 196, Issue 1, pp 7-14 (1997).

[23] G. J. WHITING, and J. P. CHANTON, Primary production control of methane emission from wetlands, Nature 364, 794 - 795 (1993).

[24] P. Boeckx, , O. van Cleemput, and I. Villaralvo, Soil Biology and Biochemistry, Volume 28, Issues 10–11 (1996).

[25] S. Husted, J. of Environmental Quality, Vol. 23 No. 3, p. 585-592 (1993).

[26] R. L. Sass, F. M. Fisher, F. T. Turner, and M. F. Jund, Global Biogeochemical Cycles, Vol 5 Issue 4 (2012).

[27] M. J. Whiticar, Chemical Geology, Volume 161, Issues 1–3 (1999).

[28] P. Quay, J. Stutsman, D. Wilbur, A. Snover, E. Dlugokencky, and T. Brown, Global Biogeochemical Cycles, Vol 13 Issue 2 (1999).

[29] P. P. Tans, A note on isotopic ratios and the global atmospheric methane budget, Global Biogeochemical Cycles, Vol 11 Issue 1 (2012).

[30] C. M. Stevens, and A. Engelkemeir, Journal of Geophysical Research: Atmospheres, Vol 93 Issue D1 (2012).

[31] J.H. van't Hoff, Vorlesungen u¨ber theoretische undphysikalische Chemie, (1898).

[32] L. Pauling, The Nature of the Chemical Bond, 2nd ed. (1940).

[33] R. N. Zare, Angular Momentum: Understanding Spatial Aspects in Chemistry and Physics (1988).

[34] H. Hollenstein, R. Marquardt, M. Quack and M.A. Suhm, J. Chem. Phys. 101 (5), 3588 (1994).

[35] H. Hollenstein, R. Marquardt, M. Quack and M.A. Suhm, Ber. Bunsenges. Phys. Chem. 99 (3), 275 (1995).

[36] R. Marquardt and M. Quack, J. Chem. Phys. 109 (24), 10628 (1998).

[37] S. D. Peyerimhoff, M. Lewerenz and M. Quack, Chem. Phys. Lett. 109 (6), 563 (1984).

[38] D.W. Schwenke, Spectrochim. Acta A 58 (4), 849 (2002).

[39] R. Marquardt and M. Quack, J. Phys. Chem. A 108 (15), 3166 (2004).

[40] O. N. Ulenikovab, E. S. Bekhterevaab, S. Albertа, S. Bauereckerac, H. Hollensteina and M. Quack, Molecular Physics, Vol. 108, Nos. 7–9 (2010).

[41] Y. Tang, S. L. Yang, and K. K. Lehmann, Journal of Molecular Spectroscopy 291 (2013).

[42] K. Deng, X. Wang, H. Lin, D. Wang and Q. Zhu, Molecular Physics, VOL. 97, NO. 6 (1999).

[43] P. F. Bernath, Spectra of atoms and molecules, Oxford University Press, second edition (2005).

[44] T. Shimanouchi, Tables of molecular vibrational frequencies consolidated Vol I, National Bureau of Standards (1972).

[45] G. Herzberg, Electronic Spectra and Electronic Structure of Polyatomic Molecules (1966).

[46] C. J. H. Schute, J. B. Bertie, P. R. Bunker, J. T. Hougen, I. M. Mills, J. K. G. Watson, and B. P. Winnewisser, Pure Appl. Chem. 69, 1663, 1641, 1651 (1997).

[47] I. M. Mills, Molecular Spectroscopy: Modern Research, p.115 (1972).

[48] http://pgopher.chm.bris.ac.uk

[49] G. Tarrago, M. Delaveau, L. Fusina, and g. Guelachvili, J. Molec. Spectrosc., 126, 149 (1987).

[50] D. Mondelain, S. Kassi, L. Wang and A. Campargue, Phys. Chem. Chem. Phys., 13, 7985-7996 (2011).

[51] F. Menard-Bourcin, J. Menard and C. Boursier, J. Molec. Spectrosc. 242, 55–63 (2007).

[52] J. J. Klaassen, S. L. Coy, J. I. Steinfeld, and B. Abel, J. of Chem. Phys. 101, 10533 (1994).

[53] F. Menard-Bourcin, L. Doyennette, J. Menard, and C. Boursier, J. Phys. Chem. A 104, 5444-5450 (2000)

[54] O. N. Ulenikov, E. S. Bekhtereva, S. Albert, S. Bauerecker, H. Hollenstein, and M. Quack, Molecular Physics, 108(7-9), 1209-1240 (2010).

Chapter 5 A rigid, monolithic but still scannable cavity ring-down spectroscopy cell

A novel cell for continuous wave cavity ring-down spectroscopy (cw-CRDS) is described and tested. The cell is monolithic and maintains a rigid alignment of the two cavity mirrors. Two high-resolution and high-force piezoelectric transducers (PZT's) are used to sweep the length of the cell by elastic deformation of the 2.86 cm outer diameter stainless steel tube that makes up the body of the cell. The cavity length is scanned more than 1/2 wavelength of the near-IR light used, which ensures that at least one TEM_{00} mode of the cavity will pass through resonance with the laser. This allows the use of a frequency-locked-laser cw-CRDS technique, which increases the precision of the measurements compared to the alternative of sweeping the laser more than one free spectral range (FSR) of the cavity. The performance of the cell is demonstrated by using it to detect the absorption spectrum of methane (CH_4) at the wavenumber regions of around 6051.8 – 6057.7 cm^{-1}.

5.1 Introduction

Detection of trace species continues to be an important application of optical spectroscopic techniques [1-4]. Cavity ring-down spectroscopy (CRDS) has been extensively used for the detection of those species in recent decades because of its long effective path-length and high sensitivity [2-5]. Among the other advantages is its immunity to the fluctuation of the laser intensity[5] because CRDS measures the decay rate of the laser power in the cavity. Compared with pulsed-laser CRDS, continuous-wave (cw) CRDS provides narrow bandwidth, *i.e.* high resolution [6-20]. More importantly, stable excitation of only the TEM_{00} modes of the cavity, which is

Yongxin Tang, Shaoyue L. Yang, and Kevin K. Lehmann
Published in Review of Scientific Instruments
Volume 83, April 2012, Pages 043115 1-7

only possible when the excitation laser has a bandwidth much narrower than the free spectral range (FSR) of the cavity, leads to more stable cavity decay rates and thus higher sensitivity of the method [6-11]. In the IR region, particularly at low pressure, the width of individual ro-vibrational transitions are comparable to the free spectral range (FSR) of cavities of convenient length, and then cw excitation of the cavity is important for the accuracy of the experimentally determined spectrum and the molecular concentrations deduced from it.

When using a spectrally narrow laser, with linewidth, $\Delta\nu_L$, less than the FSR of the cavity, the cavity and/or the laser must be tuned into resonance to allow efficient cavity excitation of one TEM_{00} mode of the cavity. This is usually done by sweeping either the cavity length or the laser frequency. A scan amplitude of the laser of at least one FSR, or of the cavity length of at least $\lambda/2$, will insure that at least one TEM_{00} mode will come into resonance with the laser on each sweep [6-7].

For diode lasers, and many other single mode lasers as well, it is possible to electronically sweep the laser the few hundred MHz, which is typically required to ensure resonance. The disadvantage of this is that, without additional measurement, the optical frequency at which the sample absorption is measured is uncertain by the laser scan amplitude and thus at least one FSR of the cavity. As an example, for the cell described below (FSR = 380 MHz), and a Doppler full width at half maximum (FWHM) of 500 MHz (typical small molecule value in the Telecom Laser spectral window), the absorption of the sample will change from 67 – 100 % of its peak value as the cavity mode moves from half a FSR off resonance to on resonance. With a Doppler width of 250 MHz, the absorption varies from 20 – 100 % as the mode drifts.

It is possible to measure the laser scan ramp voltage when the cavity ring-down event is initiated by sufficient cavity transmission, and thereby make a correction for the laser frequency modulation, but this often introduces unacceptable error. One cause of this error is phase shifts in the transducer that produces the laser frequency modulation (FM). For very precise measurements, we would like to lock the laser frequency, say to an absorption line or optical comb tooth, and for that we would likely want no FM or a different one than used to ramp around the cavity mode.

The most common way to realize this required sweep is to mount at least one of the mirrors that make up the CRDS cavity with one or more piezoelectric transducers (PZT) actuators, allowing for electronic control of the mirror position. This has the advantage that each cavity decay occurs with light inside the cavity initially within the bandwidth of the laser. As the cavity scans, the Doppler shift of the light off of the moving mirror will keep the intracavity light in resonance with the scanning mode. For experiments with Doppler or broader lines, this shift in intracavity frequency during a couple cavity lifetimes is negligible, since the scan rate per cavity lifetime must be less than the laser linewidth in order to not suppress the cavity excitation.[4] To allow the maintenance of vacuum integrity of the cell while having a moving mirror, one has traditionally either had the PZTs exposed to the gas sample or had externally mounted PZTs but used a bellows or oversized O-ring to allow for length adjustment. The disadvantage of the former is that it can introduce contamination, the gas could contain components that chemically attack the PZT transducer, or one can get electrical breakdown, particularly when working in the desired pressure range where pressure broadening about matches Doppler broadening, which is desired to simultaneously maximize signal to noise and effective spectral resolution. The use of

a bellows and external PZT mounted to a cavity has been used for many years in our laboratory [8-11]. The studies on the noise and stability of the setup have been reported [8-9]. While highly suitable for an instrument permanently mounted on an optical table, the spring loaded mirror mounts lead to misalignment when the cell is subjected to even modest acceleration or significant vibration. We have also observed the cell needs small changes in mirror alignment when the cell's internal pressure cycles from low to ambient pressure and back, and even a drift in the cell's empty cavity decay rate that correlates with changes in ambient pressure [8], likely due to very slight changes in mirror alignment which changes where on the mirrors the TEM_{00} mode is centered. Given the growing importance of portable cw-CRDS instruments with long-term stability, scientists want a cell that will maintain a rigid alignment of the mirrors relative to one another.

In this paper, we describe the design of a stainless steel cell that allows for improved mechanical stability. When used with a frequency locked laser (which we are currently working on) this cell should allow for increased precision in the determination of molecular density using cw-CRDS. The Allan variance is used to present the long-term stability of the ring-down decay time [8]. In the final section, we show the measurements of methane (CH_4) absorption by using the new design we have made. The eventual goal is to precisely measure $^{12}C/^{13}C$ and H/D ratios of environmental methane without requiring pre-concentration of the gas. The isotope values of CH_4 provide additional information that is useful for resolving the relative importance of individual sources and sinks, and they differ for biotic and abiotic origins [21-25].

5.2 Experimental

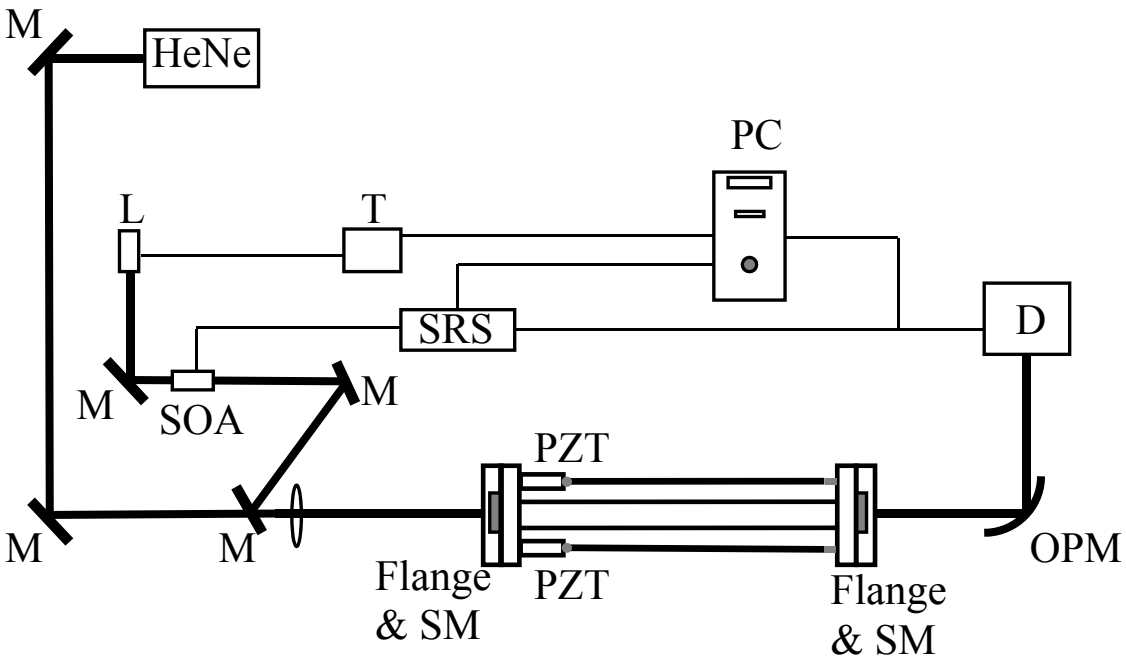

FIG. 1. The experimental setup. SOA: semiconductor optical amplifier. L: near-IR distribution feedback (DFB) laser. T: temperature controller. SRS: digital delay/pulse generator (Stanford Research System). D: InGaAs detector. SM: super mirrors. OPM: off-axis parabolic mirror. PZT: piezoelectric transducers.

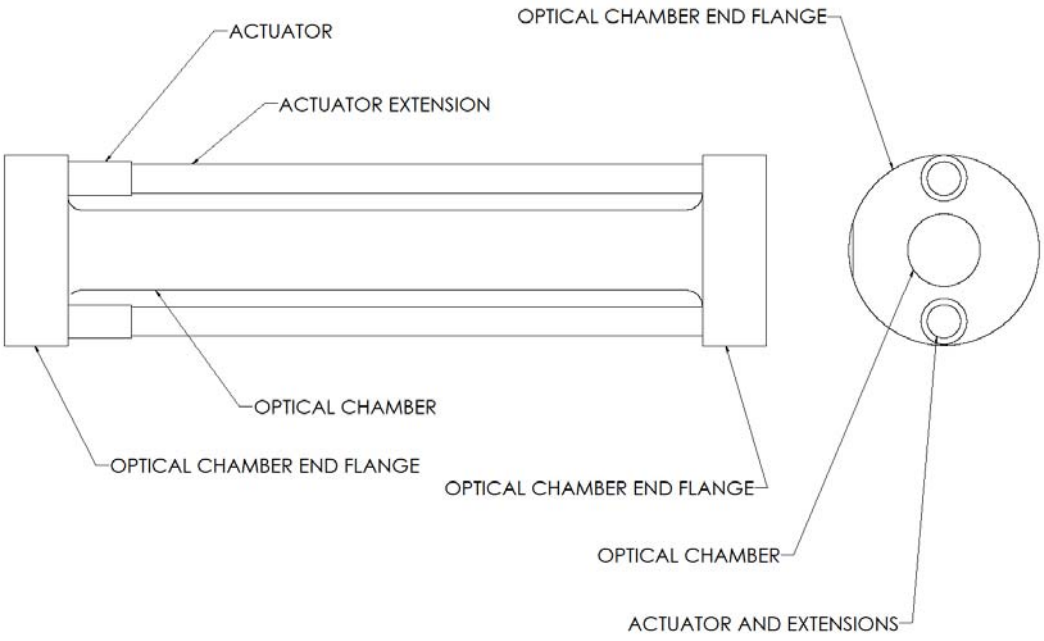

FIG. 2. A diagram of the stainless steel cavity whose length can be swept by using a pair of PZT's.

Figure 1 shows the experimental schematic containing our new cell design, and Figure 2 shows a diagram of the stainless steel cavity. The stainless steel cell has a mirror-to-mirror length of about 40 cm which gives a FSR of 380 MHz. The outer diameter of the center tube is ~ 2.86 cm and the inner diameter is ~ 1.27 cm. The mirrors are held inside the gas sample, i.e. are not simultaneously used as vacuum windows. The ending 'view port' conflat flanges have an outer diameter of 7.5 cm. Two PZTs (Physik Instrumente, model P844.20W) were mounted perpendicular to the end flanges of the stainless steel cell and were used to sweep the length of the cavity. The PZT length was 6.5 cm. Two stainless steel rods (with a diameter of 1.8 cm and a length of 33 cm) were attached to the other flange of the cell by ¼-20 threaded rods and were used to transfer force. In order to minimize compression of the threaded

rods, *C*-shaped spacers were machined with a thickness selected so they would produce a snug fit between the end of the rods and the end flange and these were press fit after the rods and PZT's were mounted. In order to minimize torque on the PZT when tightening the rod, a sapphire ball was used between them. The manufacturer specifies that the maximum open-loop travel distance of the PZT is 30 μm (with a resolution of 0.3 nm) when a voltage of 0 – 100 V is applied to it. In this work, the applied voltage was swept between 1 – 19 V, which would generate a PZT extension of 4.8 μm against no resistance. The observed travel distance of the mirrors was less than this, a little larger than 1 FSR (~ 0.88 μm). The PZT's were driven by a 20 Hz triangular wave, generated by a function generator (Agilent, model 33220A) and amplified by a PZT driver (Physik Instrument, model P863). The triangular modulation signal has a 50 % symmetry, so the maximum total trigger rate was 40 Hz. The PZT manufacturer also specifies that the response time of the PZT's is sub-millisecond.

The displacement of the mirrors produced by the force against the end flanges is given by $\Delta L = (L \times F) / (A \times E)$, where L is the distance between the end flanges, F is the total force applied, A is the cross sectional area of the stainless steel cell, and E is the Young's modulus for stainless steel. Assuming L = 0.4 m, A = 5.15 cm^2, and E = 207 GPa, a total force of F = 267 N is calculated to produce 1 μm of displacement. Each of the PZTs we have used are specified as being able to apply 3 kN of force, and a travel of 30 μm, well more than what is needed to sweep the cavity by the required λ/2 even at relatively long IR wavelengths. We used a pair of symmetrically placed PZT actuators so as not to cause a warping of the cell that would move the optical axis of the cell as the cavity length is scanned. Note that the stainless rods used to

transmit the force between the ends of the cell will themselves compress while the central cell body expands. If each rod has area *A'*, and length *L'*, and assuming the same Young's modulus, each PZT will expand by a factor of $\left(1+\frac{L'}{L}\times\frac{A}{2A'}\right)$ times the increase in distance between the mirrors. This factor is ~ 2.0 for our cell.

The input mirror of the cavity is flat and the output one has a radius of curvature of 1 m (Advanced Thin Films). Both mirrors have the back side wedged by 0.55° to prevent the laser feedback into the cavity, which could modify the cavity decay rate. The mirrors are pressed against the cell and held rigidly in place. The TEM_{00} mode of the cavity has a focus on the flat mirror and a calculated beam waist of ω_0 = 0.5 mm and a divergence of ~1 mrad upon leaving the cell. On the output mirror, the TEM_{00} mode has a beam waist of ω_1 = 0.7 mm. Light transmitted by the cavity was focused onto a 300 μm diameter Indium Gallium Arsenide (InGaAs) detector/amplifier (Tiger Optics) using a focus lens with a 2.5-cm focal length, producing a calculated 30 μm diameter spot size at the focus on the detector. The detector and lens are tilted to minimize feedback to the cavity TEM_{00} mode, which can disturb the cavity decay rate.

The stainless steel cell based upon this design approach (but without PZT's) has been demonstrated in instruments that have been shipped throughout the world and have not required any realignment when they arrive onsite, nor after years of use. The input laser radiation can be adjusted to lie on the optical axis and thus mirror angle adjustment is not required. Because this is somewhat more challenging than when the mirror angles can be adjusted, in the Appendix of this paper we give an explicit procedure to align the input beam. The obvious mechanical advantage of monolithic

cavity was previously believed offset by the apparent inability to scan the length between the mirrors and thus the resonance wavelength of the cavity, but the presently reported cell demonstrates this is not in fact true.

Our experimental setup, shown in Figure 1, is similar to other cw-CRDS instrumental and has been presented in our previous reports [8-11]. Briefly, a distribution feedback (DFB) laser (NTT Electronics Corporation, model NLK1U5EAAA) was used to measure the cavity ring-down spectrum in this work. The laser module was driven by an ultra-low noise current sources (ILX Lightwave, model 3620). The short term spectral linewidth of the laser was given as 2 MHz by the manufacturer, which we previously confirmed by a self heterodyne measurement. The laser is observed to have a frequency jitter of 20 MHz peak-to-peak, measured over a few seconds. The laser temperature was stabilized by using a Wavelength electronics temperature controller, and was adjusted by using the output of a 16-bit or 12-bit D/A board which determined the set voltage of the controller. By changing the laser temperature, the laser wavelength/wavenumber can be tuned. The laser beam passed through a two lens telescope and was mode-matched into the stainless steel cavity. A pulse/delay generator (Stanford Research System, model DG535) was used to turn off a semiconductor optical amplifier, SOA, (COVEGA, model BOA-5690) and to trigger a 12-bit PCI A/D board when the laser intensity on the detector exceeded a preset threshold, typically 2.5 V, which is approximately the mean peak transmission of the TEM_{00} mode. Each ring-down decay transient was fit to a single-exponential decay using a nonlinear fitting algorithm with equal weights of the points. The resulting cavity decay rate is the sum of the loss rate due to the mirrors, $2\times(1-R)\times FSR$, where R is the power reflectivity of the mirrors, and the loss due to sample extinction, $c\times\alpha(\nu)$,

where c is the light speed and $\alpha(\nu)$ is the extinction coefficient of the gas between the mirrors.

A gas cylinder with 5.01 ppm CH_4 in N_2 was purchased from Praxair (GTS-Welco). The flow was adjusted by using a mass flow controller (Brooks Instrument, Model 5850E). The temperature inside the cavity were the same as the ambient, 294(2) K.

5.3 Results and Discussion

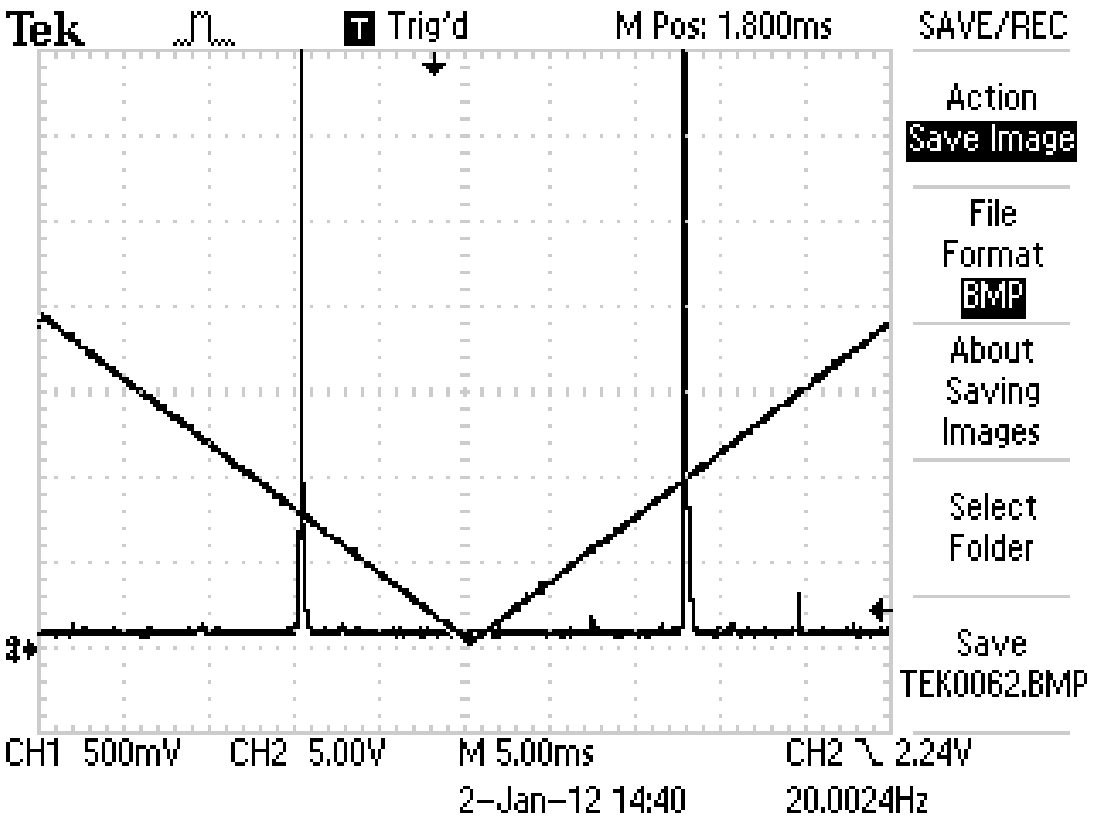

FIG. 3. Mode structure of the CRDS cavity. The length of the cavity was scanned by PZT at intracavity pressure 1 atmosphere. The calculated FSR is 380 MHz. All high order transverse modes were very weak.

By careful alignment, we can significantly reduce the transmission of higher order modes. Figure 3 shows a typical example of the CRDS cavity transmission for a single recorded by an oscilloscope (Tektronix, model TDS1012), revealing the cavity mode structure. The triangular signal (channel 2) was the output from Agilent function generator, which was also applied to the PZT's through the piezo driver (× 10 gain). The voltage shown on the oscilloscope is the output from Agilent function generator before being amplified. Channel 1 of the oscilloscope is the intensity of light transmitted by the ring-down cavity. It can be seen that the TEM_{00} transmission dominates over the higher order modes. Examining 30 captured cavity sweeps, we find that the average peak transmission of the TEM_{00} mode was > 2.1 V (about 1/5 were off scale at 3.5 V), while for the highest transverse mode (TEM_{01}), the mean peak transmission was 0.15 V. This is essentially equivalent to previous work reported from our laboratory using our traditional adjustable mirror cavity [9], where the transmission of higher order modes was reduced to around 6 % of that of the TEM_{00} with careful alignment. The probability on each sweep of triggering on a mode during each sweep [4] is exp(-I), where I is the ratio of the trigger voltage divided by the mean peak transmission of the mode. For the TEM_{01} mode with mean transmission of 6% of the 2.5V trigger threshold, the calculated probability of triggering the detection system is 6×10^{-8}, compared to 0.30 for the TEM_{00} mode.

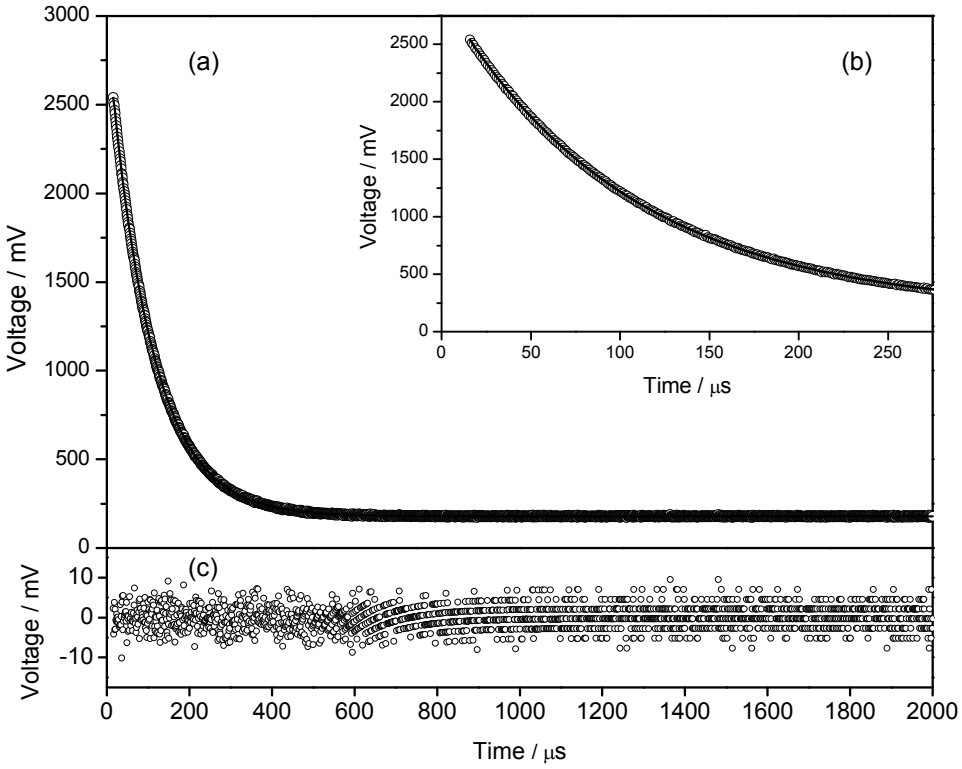

FIG. 4. (a) One example of the ring-down decay curves, along with the first-order exponential fitting. The first 15 point was skipped in the fitting. The ring-down time constant from the fitting was 102.69(4) μs with the Chi-square of 1.070. (b) The inset shows the ring-down decay curve before 275 μs. (c) The residual between the measured data and the fitting result.

Figure 4 (a) shows one example of the ring-down decay curves, along with the first-order exponential fitting, which gave a ring-down decay time constant of 102.69(4) μs with a reduced Chi-square, χ^2, of 1.07, *i.e.* the root mean square (rms) residuals of the fit are only ~ 3.5 % higher than the measured rms noise on the detector when the input laser was blocked. The detector signal was digitized for 2 ms, at a rate of 1 MHz. The first 15 points of each decay transient were not used in the fit to allow turn off

transients to die away. The inset in Figure 4 (b) shows the ring-down decay curve before 275 μs. Also shown in Figure 4 (c) is the residual between the measured data and the fitting result. Most of the residuals are smaller than 10 mV. The residual plot shows the first-order exponential decay fitting was acceptable in this work, and there is no intermode beating. It should be noted that the residuals after ~ 550 μs reflect the intrinsic noise of the detector/amplifier.

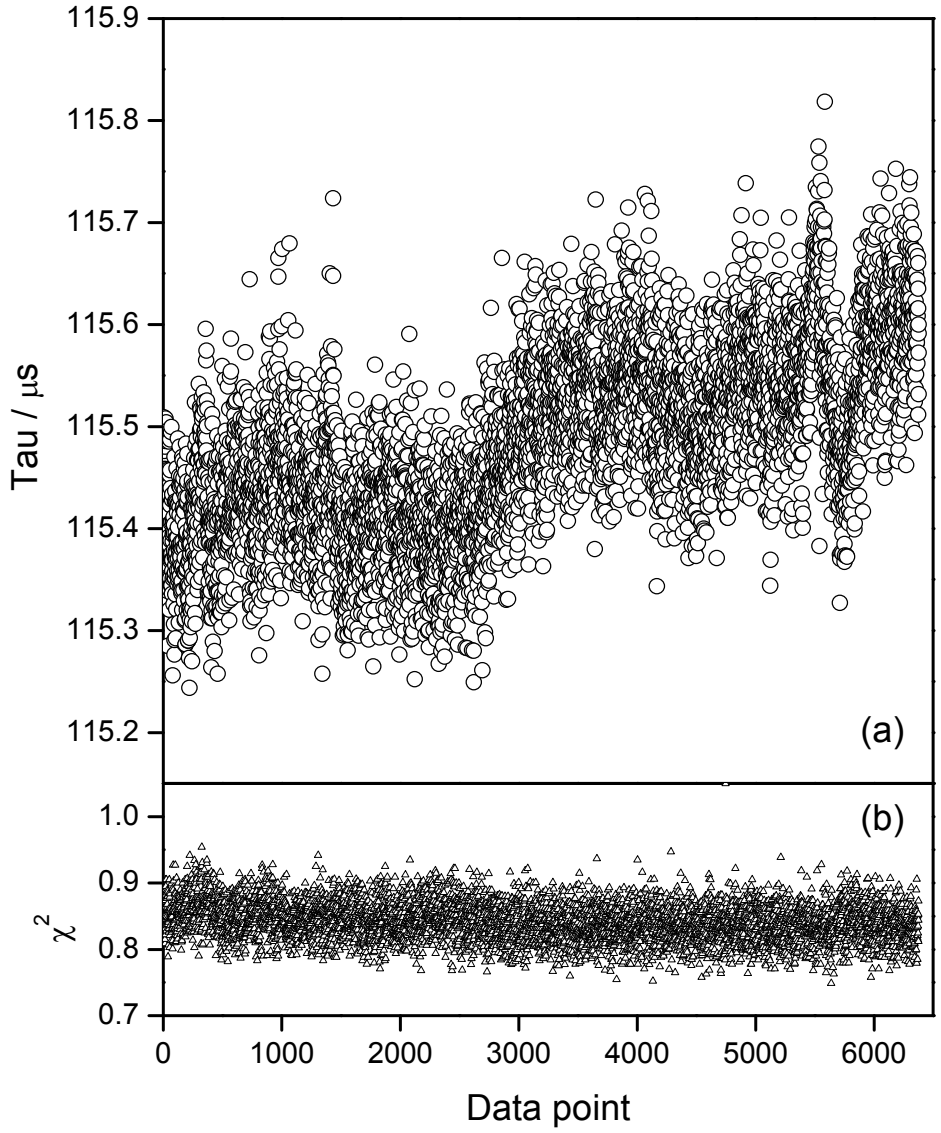

FIG. 5. 16-hour measurement of CRDS when the length of the stainless steel cavity was swept. Filled in the cavity was 180 sccm CH_4/N_2 flow (5.01 ppm). The laser temperature was selected such that the laser wavelength was off the CH_4 absorption. (a) The ring-down time constant. (b) Chi-square of exponential decay fit of each ring-down event.

Figure 5 (a) presents a 16-hour CRDS measurement without intentionally changing any experimental parameters. A gas flow of 180 sccm CH_4/N_2, vented into the room, was used. The fluctuation of decay time (τ) was less than 0.5 % in 16 hours as shown. A portion of the fluctuation could be attributed to the change of the ambient temperature and pressure [8]. Figure 5 (b) presents the χ^2 of each ring-down decay. The χ^2 (reduced chi-square value) is determined from the fit of each decay to a single exponential decay model. In this calculation, each data point is given a standard deviation equal to that of a measurement of the detector signal with the excitation laser turned off, which was conducted before the ring-down measurement. Based upon the difference in sequential decay times (to eliminate the effect of drift) a shot-to-shot standard deviation of τ of 0.052 μs (0.04 % of τ) is calculated, which can be compared to a standard error value of ~ 0.034 μs predicted from the individual fits. The observed value corresponds to a single shot fluctuations (1σ) in the sample absorbance of 1.5×10^{-11} cm^{-1}.

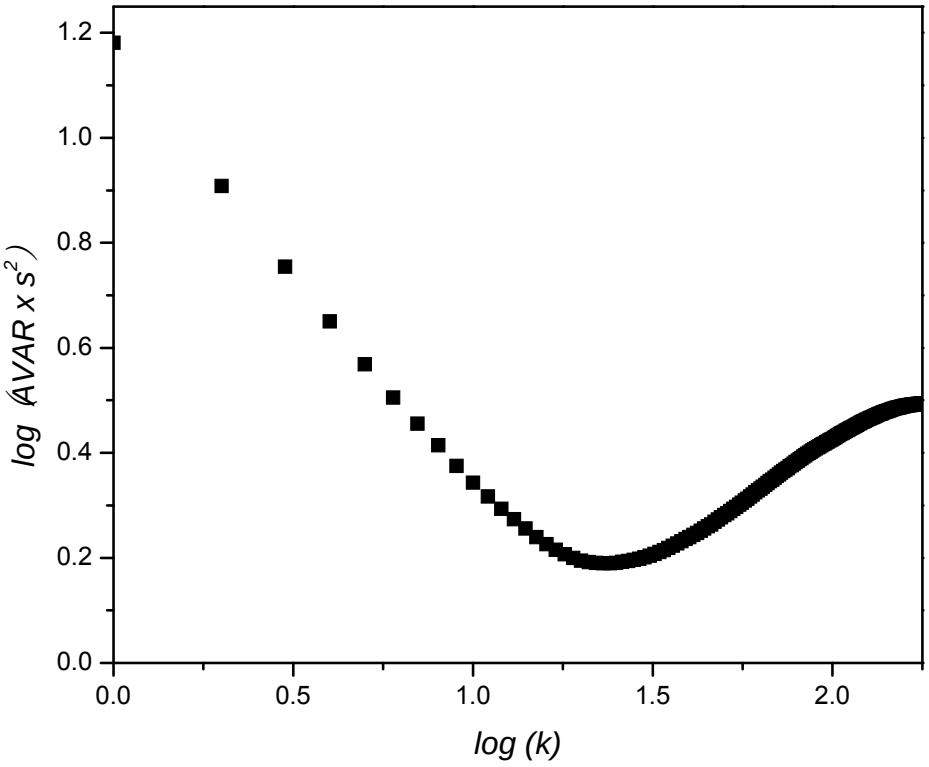

FIG. 6. Allan Variance plot of the measured ring-down decays as shown in FIG. 5.

We calculate the Allan variance [8], shown in Figure 6, of the cavity decay rate to analyze the slow drift of the ring-down decays. The Allan variance gives the observed mean squared fluctuations when the samples of different length are averaged. If the only noise in the system is uncorrelated shot-to-shot, the slope of the log-log plot of Allan variance will be -1. If the system displays a linear drift in time of the cavity loss, a log-log plot will have a minimum and increase with slope +2; for diffusive drift it will have slope +1. The position of the minimum in the Allan variance plot gives the optimum integration time, and its value gives the minimum variance one can reach by averaging the data. As shown in Figure 6, the optimum averaging is 23 decays

($10^{1.36}$), corresponding to integration time of 3.46 minutes. For details of Allan variance, please refer to the references [8, 26-27]. This sensitivity could be improved by comparing the difference between the loss at two closely spaced wavelengths to correct for common mode drift in cavity loss [8].

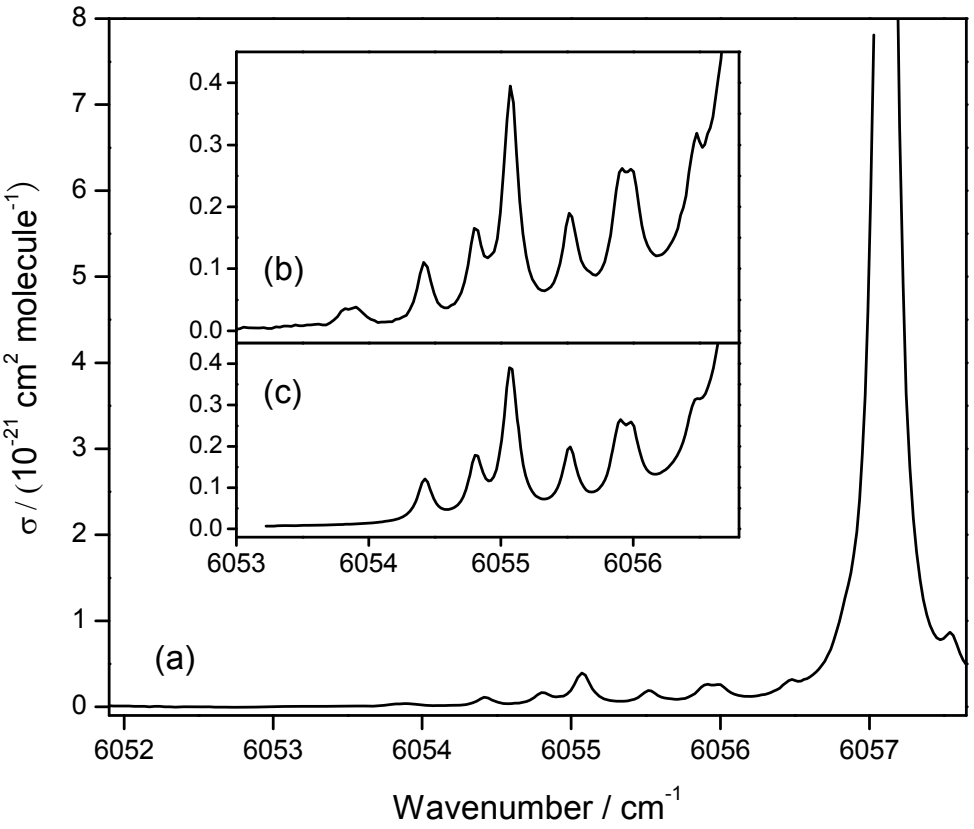

FIG. 7. (a) Absorption cross sections of 1 atmosphere and 5.01 ppm CH_4 in N_2 at the wavenumber region of 6051.8 – 6057.7 cm^{-1} measured using the PZT-driven length-scanned stainless steel cavity. The strong band at ~ 6057.08 cm^{-1} was skipped. (b) The absorption cross sections of weak CH_4 bands between 6053.0 and 6056.8 cm^{-1}. (c) The calculated CH_4 absorption cross sections by using the Voigt function, and line strengths, pressure-broadening and pressure-shift coefficients from HITRAN [28].

The absorption band at ~ 6053.85 cm^{-1} shown in Figure 7 (b) could be assigned to CH_3D according to our previous measurements [30].

Figure 7 shows a typical absorption spectrum of CH_4 measured using the length-sweeping stainless steel cavity. Since the number density of CH_4 in this work was relatively large (around 1.24×10^{14} molecule/cm^3), the ring-down decay time constants are too short near the strong absorption peak to be detected using our experimental setup (without reducing the trigger threshold), we had to skip over it. The wavenumber was calculated from the laser temperature. The temperature tuning coefficient of the DFB laser frequency is around - 12.5 GHz/^{o}C. This number changes slightly for different lasers. The wavenumber of each laser we use was separately calibrated by using several strong absorption peaks from CH_4, CO_2 and H_2O, which have been well studied and are listed in the HITRAN database [28]. We also assumed that the wavenumber changed linearly with the laser temperature. In this work, the step size of the laser temperature scan was between 0.04 and 0.08 ^{o}C, which corresponded to the wavenumber step size of ~ 0.017 and 0.034 cm^{-1}, respectively. This was good enough to resolve the absorption structure at the ambient pressure. At each laser temperature/wavenumber, 80 ring-down events were repeated. The average of these decay rates was used to calculate the corresponding absorption cross section by using equation 1:

$$\sigma(\nu)=\frac{\Delta k(\nu)}{N\times c} \qquad (1)$$

Where $\sigma(\nu)$ is the absorption cross section at the wavenumber studied (ν), N is number density of the molecules studied, and Δk is calculated using equation 2:

$$\Delta k(\nu)=\frac{1}{\tau(\nu)}-\frac{1}{\tau_0} \qquad (2)$$

Where $\tau(\nu)$ and τ_0 are the averaged ring-down decay constant with and without the absorbance, respectively. In principle, τ_0 might shift slightly with wavenumber and time, but it was assumed to be constant in this work. Since the number density of CH_4 in this work was larger than those typically employed in our group, it is possible for us to quantitatively examine the weak tail between 6053.0 and 6056.8 cm^{-1}, as shown in Figure 7 (b). Figure 7 (c) presents the calculated absorption cross sections by using the Voigt function and the line strength, along with the pressure-broadening and pressure-shift coefficients, reported in HITRAN in the same wavenumber region [28] as Figure 7 (b). The program used for the calculation was written using Mathematica (version 5.2). The step size of the wavenumber during the calculation was 0.02 cm^{-1}, similar to the step size used in the experiments. As shown in Figure 7 (b) and (c), both the positions and the intensities are very similar between the calculation and the measurement. Figure 7 indicates that sweeping the length of a stainless steel cell to obtain the laser-cavity resonance in CW cavity ring-down spectroscopy is feasible. It should be noted that the absorption band at ~ 6053.85 cm^{-1} could be attributed to CH_3D according to the literature [29] and our previous measurements [30]. In the buffer gas of N_2, CH_3D has two absorption bands at 6053.652 and 6053.935 cm^{-1} with the absorption cross sections of 7.10×10^{-27} and 7.91×10^{-27} cm^2 cm^{-1} $molecule^{-1}$ respectively [30]. If we included the contribution from CH_3D, the total apparent absorption cross sections of CH_4 and CH_3D at these wavenumbers were expected to be around 7×10^{-23} and 8×10^{-23} cm^2/molecule, respectively, which are very close the measured values. The abundance of CH_3D from the commercial CH_4 cylinder is very close to the nominal natural abundance (~ 0.0616 %) value. The small difference between the calculated and measured values might come from the baseline subtraction.

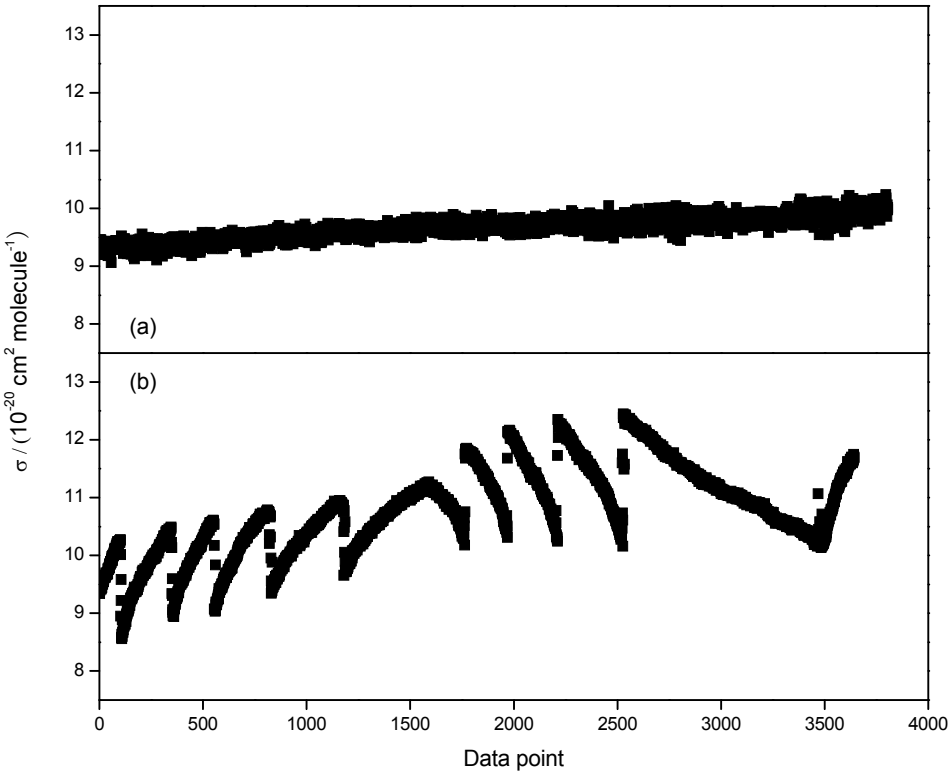

FIG. 8. CRDS absorption at ~ 13 Torr CH_4/N_2. The laser wavenumber was sitting on the absorption peak of CH_4 at ~ 6057.08 cm^{-1}. (a) The cavity length was swept. Δk drifted slightly because of both the drift of baseline (τ_0) and the drift of the laser wavenumber. (b) The laser current was swept. Each data point in the figure is the average of 80 cavity decays.

The advantage of using cavity mode modulation over laser frequency modulation is dramatic at low pressure, near the Doppler Limited regime. Figure 8 compares two measurements of the cell, the upper one with cavity length modulation and the second with diode laser current modulation, with a depth slightly more than one FSR of the cavity. The cell contained a total pressure of 13 Torr N_2 with 5.01 ppm of CH_4 and the laser was initially manually tuned to the peak of the methane absorption at ~

6057.08 cm^{-1}. Each data point shown in Figure 8 is the average of 80 cavity decays. The upper, cavity length scan, shows a slow drift, while the lower, frequency modulated curve, shows the thermal drift of the cavity modes of the cell, which shift the frequency at which ring-down events are recorded relative to the peak of the absorption line. Assuming a thermal expansion coefficient of stainless steel of 16 ppm/K, one can calculate that the modes of the cavity will shift by 1 FSR for a cell temperature change of 0.13 K. It is technically difficult to tune by varying the temperature of the entire cell considering the potential mobility of this setup and thus we did not attempt to change the temperature.

5.4 Conclusions

The feasibility of sweeping the length of a monolithic stainless steel cell by elastic deformation to reach laser-cavity resonance in CW cavity ring-down spectroscopic measurements has been demonstrated. Methane with a number density of 5.01 ppm in N_2 was used to test the stability at the total pressure of 1 atmosphere. The shot-to-shot fluctuation of the ring-down time was less than 0.5 % in 16 hours. The measured CH_4 absorption spectra were very similar to the calculation by using the Voigt function and literature values from HITRAN. Further work will be conducted in future. In particular, when moving to low pressure measurements with a frequency stabilized laser, the increase in precision of the extracted analyte concentration will be substantial because we will substantially reduce the uncertainty in where on the absorption profile the absorption coefficient is measured.

5.5 Appendix: Mode matching into a Cavity with fixed mirrors

For a cell with two curved mirrors, the optic axis is defined by the line that passes through the center of curvature of each mirror. If one mirror is a flat, as in our cell, the optic axis is defined as the normal to the flat mirror that passes through the center of curvature of the curved mirror. As long as the cavity is not close to the concentric limit of stability, the precision of the fixed mounting does not present a challenge of machining; a mrad error in the normal will move the optic axis by ~ 1 mm. Bringing the input laser beam onto the optic axis requires four adjustments. To mode match the cavity further requires placement of the position and size of the incoming beam to match that of the TEM_{00} mode of the cavity. The later can be calculated using standard resonator theory, though one is cautioned to not neglect that a curved concave mirror will act as a defocusing lens when used in transmission.

To adjust the input beam, one needs a pair of mirrors, with one ideally close to the cell input. Better is to be able to independently change to position of the input beam without changing its angle. One way to do this is to use a four axis mount for the fiber to free space coupler but doing so does not allow a fixed, external telescope. An alternative is to use a prism, such as a Amici Roof prism or a pair of 45° prisms rotated 90° to one another, that allows x, y translation of a beam without changing beam direction. When entering a flat-curved mirror cavity on the flat mirror, the direction of the input beam is correct if it is normal to the high reflector side of the input mirror, i.e. the input beam retro-reflects back to its source. The minimum spot size of the TEM_{00} mode, ω_0, sets the scale for how accurately the beam must be positioned, and its far field divergence angle, $\lambda/\pi\omega_0$, set the scale for the angle

tolerance. Lehmann and Romanini give expressions that allow the overlap of all modes to be calculated as a function of the errors in the input alignment and beam parameters.[31]

We now describe an explicit alignment procedure. First, the position and mirror separation of the telescope are adjusted so that the input near-IR radiation has the proper beam size and focal point to match the calculated TEM_{00} mode of the cavity. Use of a commercial beam profiler makes this an easy task. This need not be done to very high precision – an error of 30% will only reduce the maximum energy coupling into the TEM_{00} mode 10 %. The position of the focus is even more forgiving, and error in the focus position by $\pm z_0$ (the confocal length for the cavity TEM_{00} mode) will only reduce the TEM_{00} mode power coupling by 5% [31-32]. The crude alignment of the input beam is done by first aligning a He-Ne beam so that the reflected spots overlap and then forcing the IR beam to pass through irises aligned with the red beam. This is not precise due to the wedge in the input mirror combined with the dispersion of the mirror material. One can calculate this deviation and move the input beam accordingly. Next, an aperture the size of the calculated TEM_{00} mode leaving the cell is mounted on an x, y adjustable mount and the time averaged cavity transmission is measured as the cavity is swept back and forth more than 1 FSR. The aperture is moved to center it in the region with cavity transmission. Since each excited cavity mode is symmetric around the optic axis of the cavity, this should place the iris close to the optic axis of the cavity modes. Then the input beam position and direction is adjusted to produce maximum time averaged intensity on the detector. Given that the spatial filtering by the aperture has substantially higher transmission for the TEM_{00} than higher modes, this should maximize overlap with that mode. The

cavity transmission *vs.* aperture position can be used to estimate how close to align the cavity optic axis the input beam is. As this improves, the position of the aperture can be adjusted to more precisely align it with the optic axis. When this optimization is completed (and assuming the input beam has close to the correct size and focal position), the strongest overlap should be with the TEM_{00} mode of the cavity. One can then look at the cavity transmission as a function of sweep and make final input beam angle and position adjustments to minimize the intensity in higher transverse modes. This is made challenging by the fact that there is 100 % intensity noise of each mode's transmission for the usual case that the laser linewidth is much greater than the width of the cavity mode. It is useful to know the expected displacement (in terms of ramp voltage) of the TEM_{10} and TEM_{20} modes from the TEM_{00} mode. If the input beam is perfectly aligned with the axes, the overlap with odd order modes should be zero, so one should concentrate on reducing these. If there remains significantly more intensity in the TEM_{20} mode after input beam alignment is optimized, then either the input beam focal position or size is needs to be improved, or the input beam does not have sufficiently low M^2 value. Our experience is that many of the fiber to air couplers introduce significant spherical aberration in the beam, and this ultimately limits the degree to which the beam can be mode-matched.

It is important not to have the detection electronics trigger on a higher transverse mode, as these invariably have different mirror loss than the TEM_{00} mode, thereby introducing noise in the calculated sample loss. If a full FSR of the cavity is scanned, then the detection threshold must be set high enough to prevent triggering on these modes. An alternative is to only make small cell length scans around the position of the TEM_{00} mode, such that one does not scan over the higher order modes with

significant excitation. This further improves the rate that cavity decays are observed since one spends a higher fraction of the time resonantly exciting the cavity. By capturing the scan voltage when the detection system is triggered, one can apply slow feedback to the average voltage applied to the PZTs to correct for drift of the cavity relative to the laser.

Bibliography

[1] A. A. Kosterev, F. K. Tittel, IEEE J Quantum Electron. **38**, 582 (2002).

[2] W. Denzer, G. Hancock, M. Islam, C. E. Langley, R. Peverall, G. A. D. Ritchie, D. Taylor, Analyst **136**, 801 (2011).

[3] S. S. Brown, Chem. Rev. **103**, 5219 (2003).

[4] bJ. B. Dudek, P. B. Tarsa, A. Velasquez, M. Wladyslawski, P. Rabinowitz, K. K. Lehmann, Anal. Chem. **75**, 4599 (2003).

[5] A. O'Keefe, D. A. G. Deacon, Rev. Sci. Instru. **59**, 2544 (1988).

[6] D. Romanini, A. A. Kachanov, F. Stoeckel, Chem. Phys. Lett. **270**, 538 (1997).

[7] D. Romanini, A. A. Kachanov, N. Sadeghi, F. Stoeckel, Chem. Phys. Lett. **264**, 316 (1997).

[8] H. F. Huang, K. K. Lehmann, Appl. Opt. **49**, 1378 (2010).

[9] H. F. Huang, K. K. Lehmann, Opt. Express **15**, 8745 (2007).

[10] H. F. Huang, K. K. Lehmann, Appl. Opt. **47**, 3817 (2008).

[11] H. F. Huang, K. K. Lehmann, Chem. Phys. Lett. **463**, 246 (2008).

[12] W. Denzer, G. Hancock, M. Islam, C. E. Langley, R. Peverall, G. A. D. Ritchie, R. A. Washenfelder, N. L. Wagner, W. P. Dube, S. S. Brown, Environ. Sci. Technol. **45**, 2938 (2011).

[13] D. Taylor, Analyst **136**, 801 (2011).

[14] F. Ye, B. Qi, L. Qian, Opt. Lett. **36**, 2080 (2011).

[15] R. Wada, A. J. Orr-Ewing, Analyst **130**, 1595 (2005).

[16] D. B. Atkinson, Analyst **128**, 117 (2003).

[17] M. D. Wheeler, S. M. Newman, A. J. Orr-Ewing, M. N. R. Ashfold, J. Chem. Soc. Faraday Trans. **94**, 337 (1998).

[18] A. M. Parkes, B. L. Fawcett, R. E. Austin, S. Nakamichi, D. E. Shallcross, A.J. Orr-Ewing, Analyst **128**, 960-965 (2003).

[19] B. L. Fawcett, A. M. Parkes, D. E. Shallcross, A. J. Orr-Ewing, Phys. Chem. Chem. Phys. **4**, 5960 (2002).

[20] J. Domysławska, S. Wójtewicz, D. Lisak, A. Cygan, F. Ozimek, K. Stec, Cz. Radzewicz, R. S. Trawiński, R. Ciuryło, J. Chem. Phys. **136**, 024201 (2012).

[21] M. J. Mumma, G. L. Villanueva, R. E. Novak, T. Hewagama, B. P. Bonev, M. A. DiSanti, Avi M. Mandell, M. D. Smith, Science **323**, 1041 (2009).

[22] J. P. Pinto, J. I. Lunine, S. J. Kim, Y. L. Yung, Nature **319** 388 (1986).

[23] C. R. Webster, P. R. Mahaffy**,** Planetary and Space Sci. **59**, 271 (2011).

[24] C. A. Nixon, R. K. Achterberg, S. Vinatier, B. Bézard, A. Coustenis, P. G. J. Irwin, N. A. Teanby, R. de Kok, P. N. Romani, D. E. Jennings, G. L. Bjoraker, F. M. Flasar, Icarus **195**, 778 (2008).

[25] Q. Ma, S. Wu, Y. Tang, Geochimica Cosmochimica Acta **72**, 5446 (2008).

[26] D. W. Allan, Proc. IEEE **54**, 221 (1966).

[27] P. Werle, R. Mucke, F. Slemr, Appl. Phys. B **57**, 131 (1993).

[28] L. S. Rothman, I. E. Gordon, A. Barbe, D. C. Benner, P. F. Bernath, M. Birk, V. Boudon, L. R. Brown, A. Campargue, J. P. Champion, K. Chance, L. H. Coudert, V. Dana, V. M. Devi, S. Fally, J. M. Flaud, R. R. Gamache, A. Goldman, D. Jacquemart, I. Kleiner, N. Lacome, W. J. Lafferty, J. Y. Mandin, S. T. Massie, S. N. Mikhailenko, C. E. Miller, N. Moazzen-Ahmadi, O. V. Naumenko, A. V. Nikitin, J. Orphal, V. I. Perevalov, A. Perrin, A. Predoi-Cross, C. P. Rinsland, M. Rotger, M. Simeckova, M. A. H. Smith, K. Sung, S. A. Tashkun, J. Tennyson, R. A. Toth, A. C. Vandaele, J. Vander Auwera, J. Quan. Spec. Radiative Transfer **110**, 533 (2009).

[29] K. Deng, X. G. Wang, H. Lin, D. Wang, Q. S. Zhu, Mole. Phys. **97**, 787 (1999).

[30] Y. X. Tang, S. L. Yang, K. K. Lehmann, D. C. Benner, Measurements of CH_3D Line Strengths, Foreign Pressure-Broadening and Pressure-Shift Coefficients at Near-IR Region Using Continuous-Wave Cavity Ring-Down Spectroscopy (In preparation. To be submitted to the Journal of Molecular Spectroscopy).

[31] K. K. Lehmann, D. Romanini, J. Chem. Phys. **105**, 10263 (1996).

[32] A. E. Siegman, *Lasers*. University Science Books; 1986.

Chapter 6 Summary and future plans

6.1 Summary

Chapter 1 gave a brief introduction about fundamentals of CRDS. We described two of the most common CRDS schemes, P-CRDS and CW-CRDS, as well as brief introduction of several other CRDS developments. CRDS has developed significantly during the past three decades. Because of its immunity to intensity fluctuation, high sensitivity and high repetition rate, CRDS have developed greatly during the past three decades and they are practiced in various fields.

Chapter 2 discussed two different ways to tune DFB semiconductor diode lasers, temperature as course tuning and current as fine tuning. A new design of temperature controller was introduced using almost the same thermistor and analog voltage controller while having a more even wavenumber tuning coefficient throughout the entire temperature region. We also designed a feedback loop using frequency modulation and digitized PID controller which greatly improved the short term frequency jitter of the DFB lasers.

Chapter 3 introduced the measurement of the line strengths of CH_3D ro-vibrational transitions ($2\nu_4$) in the wavenumber regions of 6017.5 – 6031.5 cm^{-1} and 6046.5 – 6070.0 cm^{-1} by CW-CRDS. We also measured the foreign pressure-broadening and the pressure-shift effects of N_2, O_2 and CO_2 on CH_3D absorption lines. These coefficients are needed for the precise determination of the concentration of CH_3D and thus methane isotopic ratio when present as a trace component in these gases.

Chapter 4 explained our approaches to the analysis of the CH_3D near-IR spectrum. As one of the most important hydrocarbon prototype molecules, CH_3D's overtone band in the near infrared region was not been well studied. We used the Pgopher [4,5] software package to simulate two rovibrational overtone bands of CH_3D and combination differences were used to find possible pairs of transitions starting from adjacent ground state rotational levels and ending in same excited states. We also designed a single pass cell for measuring methane absorption spectrum under different temperatures for estimating lower state energy and rotational quanta, which proved to be working well for lower J levels. An IR-IR double resonance system was used to provide strong proof for the lower state quanta.

Chapter 5 described and tested a novel cell for CW-CRDS. The cell is monolithic and maintains a rigid alignment of the two cavity mirrors. Two high-resolution and high-force PZTs are used to sweep the length of the cell by elastic deformation of the 2.86 cm outer diameter stainless steel tube that makes up the body of the cell. The performance of the cell was demonstrated by using it to detect the absorption spectrum of methane (CH_4) near 6050 cm^{-1}.

6.2 Recent progress

The hypotheses about Martian methane origins remain to be proved by more experimental methods, including analyzing the isotopic consumption of methane emissions on Mars' surface. Our collaborators Onstott *et al*. developed a near infra-red CW-CRDS device with the goal of measuring seasonal changes in the isotopic composition of atmospheric $^{12}CH_4$ and $^{13}CH_4$ on Earth and eventually on Mars. Their reported 1σ detection limit was 1.9×10^{-12} cm^{-1}, corresponding to 10 pptv of CH_4 at

100 Torr, while the Earth's global methane level is around 1800 ppb. The same group later made direct measurements of methane emissions from abandoned oil and gas wells in Pennsylvania [2]. They also developed a compact near-IR CW-CRDS [3], which has titanium optical cavity with rugged quartz windows as protections to survive the harsh environmental changes during space flight and a Martian surface mission.

6.3 Future plans

6.3.1 CH_3D linestrength measurement at intermedia temperature

We used the linestrength temperature dependence for estimating the ground state energy and rotational quantum number in chapter 4. The two temperatures we chose were room temperature 293K and liquid nitrogen boiling temperature 77K. For higher J levels' absorption peaks, the intensities dropped significantly at 77K, resulting in much worse signal to noise ratio. We are planning to measure the absorption spectrum at other intermedia temperatures, which might provide better estimation for ground state energies especially for transitions with lower state J >6.

6.3.2 Assignment of double resonance peaks

We tentatively assign the Doppler broadened, positive going features as starting from rotational levels of the lowest bending state, which is metastable given the slow rate of V -> RT relaxation. These features are more prominent in the case of CH_4 over that of CH_3D. Based upon our assignment, we expect to find combination differences to ground state absorption features of methane near 7400 cm^{-1}, as well as within the observed transitions from the ν_4 state. Due to the expected strong rovibratonal interactions of the rovibrational states near 7400 cm^{-1}, we anticipate that there should

be a significant number of combination difference transitions observed between the 1.6 and 1.35 μm Spectra.

6.3.3 Liquid nitrogen cooled double resonance

We also plan to repeat the double resonance measurements in the liquid nitrogen cooled cell, which should give us estimates for the rotational excitation of the lower states of these hot band transitions and then combine our spectra with those of Grenoble to do a combination difference search which we hope will give us sufficient number of assigned lines to bootstrap an assignments for both spectra and allow fitting the observed term values to an effective molecular ro-vibrational Hamiltonian.

6.3.4 Double resonance in CRDS

Previously, temperature dependence and double resonance experiments were carried out using single pass cell filled with pure methane, which only has a path length of less than 1m. We plan to incorporate the pump laser beam used in double resonance experiment into our CRDS setup, turning on or off the pump laser beam in the middle of each ring-down event. The normal CRDS spectrum would be obtained by fitting the curve free of pump laser, while double resonance information can be collected from the other part of the curve. This setup will enable measuring both CRDS and double resonance at the same time. We expect the Doppler effect will show up since the pump laser beam will not always counter-propogate with the probe laser beam, which is also the laser beam for CRDS which travels back and forth between the two super mirrors.

Bibliography

[1] Y. Chen, K. K. Lehmann, J. Kessler, B. S. Lollar, G. L. Couloume, and T. C. Onstott, Analytical chemistry 85, no. 23, 11250-11257 (2013).

[2] M. Kanga, C. M. Kanno, M. C. Reid, X. Zhang, D. L. Mauzerall, M. A. Celi, Y. Chen, and T. C. Onstott, Proceedings of the National Academy of Sciences, vol. 111, no. 51, 18173–18177 (2014).

[3] Y. Chen, P. Mahaffy, V. Holmes, J. Burris, P. Morey, K.K. Lehmann, B. Sherwood Lollar, G. Lacrampe-Couloume, T.C. Onstott, Planetary and Space Science
Vol 105, 117–122 (2015).

[4] PGOPHER, a Program for Simulating Rotational Structure, C. M. Western, University of Bristol, http://pgopher.chm.bris.ac.uk

[5] PGOPHER version 8.0, C M Western, 2014, University of Bristol Research Data Repository, doi:10.5523/bris.huflggvpcuc1zvliqed497r2

Appendix A

Table 1. Comparison of FTIR spectrum, CRDS spectrum, PGOPHER software simulation or combination differences calculation, double resonances, and transition assignments.

FTIR		CRDS		Pgopher or Comb. Diff (#) by lineposition			Double Resonance	Temperature Dependence		transition	Comment
freq.	line strength	freq.	line strength	freq.	line strength	Quanta		E	J		
5653.827	0.989	--	--	--	--	--		--	--	--	
5654.377	1.017	--	--	--	--	--		--	--	--	
5655.254	1.237	--	--	--	--	--		--	--	--	
5655.275	0.913	--	--	--	--	--		--	--	--	
5655.292	1.106	--	--	--	--	--		--	--	--	
5655.875	1.469	--	--	--	--	--		--	--	--	
5656.981	2.112	--	--	--	--	--		--	--	--	
5657.130	1.251	--	--	--	--	--		--	--	--	
5660.541	1.308	--	--	--	--	--		--	--	--	
5661.324	1.282	--	--	--	--	--		--	--	--	
5662.382	1.678	--	--	--	--	--		--	--	--	
5662.599	6.265	--	--	--	--	--		--	--	--	
5662.823	6.024	--	--	--	--	--		--	--	--	
5663.488	0.935	--	--	--	--	--		--	--	--	
5663.555	3.561	--	--	--	--	--		--	--	--	
5667.238	1.073	--	--	--	--	--		--	--	--	
5667.662	1.058	--	--	--	--	--		--	--	--	
5668.441	0.933	--	--	--	--	--		--	--	--	
5668.569	1.022	--	--	--	--	--		--	--	--	
5669.107	1.213	--	--	--	--	--		--	--	--	
5669.512	1.228	--	--	--	--	--		--	--	--	
5669.598	0.853	--	--	--	--	--		--	--	--	
5671.181	1.044	--	--	--	--	--		--	--	--	
5671.935	2.064	--	--	--	--	--		--	--	--	
5673.688	0.927	--	--	--	--	--		--	--	--	
5673.801	1.323	--	--	--	--	--		--	--	--	
5675.066	1.014	--	--	--	--	--		--	--	--	
5675.222	0.989	--	--	--	--	--		--	--	--	
5675.325	1.286	--	--	--	--	--		--	--	--	
5676.397	1.630	--	--	--	--	--		--	--	--	
5676.454	1.321	--	--	--	--	--		--	--	--	
5678.457	1.790	--	--	--	--	--		--	--	--	
5679.343	0.988	--	--	--	--	--		--	--	--	
5679.927	1.285	--	--	--	--	--		--	--	--	

5681.035	1.549	--	--	--	--	--		--	--	--	
5681.328	0.943	--	--	--	--	--		--	--	--	
5681.946	1.022	--	--	--	--	--		--	--	--	
5684.628	1.362	--	--	--	--	--		--	--	--	
5687.017	1.771	--	--	--	--	--		--	--	--	
5688.428	2.540	--	--	--	--	--		--	--	--	
5688.762	0.916	--	--	--	--	--		--	--	--	
5689.472	2.067	--	--	--	--	--		--	--	--	
5690.028	2.744	--	--	--	--	--		--	--	--	
5691.643	1.347	--	--	--	--	--		--	--	--	
5692.103	1.801	--	--	--	--	--		--	--	--	
5696.134	0.913	--	--	--	--	--		--	--	--	
5696.203	1.369	--	--	--	--	--		--	--	--	
5697.477	4.480	--	--	--	--	--		--	--	--	
5697.800	1.531	--	--	--	--	--		--	--	--	
5698.010	2.382	--	--	--	--	--		--	--	--	
5698.470	0.995	--	--	--	--	--		--	--	--	
5699.433	1.913	--	--	--	--	--		--	--	--	
5700.579	1.206	--	--	--	--	--		--	--	--	
5700.633	1.091	--	--	--	--	--		--	--	--	
5701.716	0.902	--	--	--	--	--		--	--	--	
5702.617	0.961	--	--	--	--	--		--	--	--	
5705.501	0.837	--	--	--	--	--		--	--	--	
5706.082	1.324	--	--	--	--	--		--	--	--	
5706.377	2.356	--	--	--	--	--		--	--	--	
5706.517	2.975	--	--	--	--	--		--	--	--	
5706.991	1.533	--	--	--	--	--		--	--	--	
5707.356	2.370	--	--	--	--	--		--	--	--	
5707.451	1.253	--	--	--	--	--		--	--	--	
5708.025	0.852	--	--	--	--	--		--	--	--	
5709.248	3.393	--	--	--	--	--		--	--	--	
5714.292	0.847	--	--	--	--	--		--	--	--	
5714.644	1.213	--	--	--	--	--		--	--	--	
5715.245	3.731	--	--	--	--	--		--	--	--	
5715.296	1.857	--	--	--	--	--		--	--	--	
5715.449	1.658	--	--	--	--	--		--	--	--	
5715.862	1.395	--	--	--	--	--		--	--	--	
5716.087	1.076	--	--	--	--	--		--	--	--	
5716.240	0.923	--	--	--	--	--		--	--	--	
5716.360	1.057	--	--	--	--	--		--	--	--	
5717.040	1.065	--	--	--	--	--		--	--	--	
5717.356	2.109	--	--	--	--	--		--	--	--	
5717.790	0.954	--	--	--	--	--		--	--	--	
5722.072	1.718	--	--	--	--	--		--	--	--	
5723.332	1.096	--	--	--	--	--		--	--	--	
5723.777	1.857	--	--	--	--	--		--	--	--	

5723.853	2.433	--	--	--	--	--		--	--	--	
5724.212	1.797	--	--	--	--	--		--	--	--	
5724.620	1.300	--	--	--	--	--		--	--	--	
5724.668	2.011	--	--	--	--	--		--	--	--	
5724.950	5.157	--	--	--	--	--		--	--	--	
5726.013	1.218	--	--	--	--	--		--	--	--	
5726.681	1.201	--	--	--	--	--		--	--	--	
5726.833	2.660	--	--	--	--	--		--	--	--	
5727.331	1.207	--	--	--	--	--		--	--	--	
5728.028	0.914	--	--	--	--	--		--	--	--	
5728.336	1.069	--	--	--	--	--		--	--	--	
5730.259	1.183	--	--	--	--	--		--	--	--	
5731.463	0.952	--	--	--	--	--		--	--	--	
5731.805	2.319	--	--	--	--	--		--	--	--	
5732.490	3.549	--	--	--	--	--		--	--	--	
5732.902	2.235	--	--	--	--	--		--	--	--	
5732.980	1.276	--	--	--	--	--		--	--	--	
5733.442	1.252	--	--	--	--	--		--	--	--	
5734.012	1.012	--	--	--	--	--		--	--	--	
5734.399	1.672	--	--	--	--	--		--	--	--	
5734.623	1.003	--	--	--	--	--		--	--	--	
5735.092	2.467	--	--	--	--	--		--	--	--	
5735.404	1.020	--	--	--	--	--		--	--	--	
5737.353	1.358	--	--	--	--	--		--	--	--	
5738.051	1.221	--	--	--	--	--		--	--	--	
5739.689	2.085	--	--	--	--	--		--	--	--	
5740.454	1.621	--	--	--	--	--		--	--	--	
5740.827	2.076	--	--	--	--	--		--	--	--	
5740.900	1.212	--	--	--	--	--		--	--	--	
5741.051	4.715	--	--	--	--	--		--	--	--	
5741.618	1.077	--	--	--	--	--		--	--	--	
5741.660	1.206	--	--	--	--	--		--	--	--	
5742.491	1.039	--	--	--	--	--		--	--	--	
5742.900	2.624	--	--	--	--	--		--	--	--	
5743.831	1.962	--	--	--	--	--		--	--	--	
5746.398	0.888	--	--	--	--	--		--	--	--	
5746.732	1.110	--	--	--	--	--		--	--	--	
5746.911	2.375	--	--	--	--	--		--	--	--	
5747.711	1.262	--	--	--	--	--		--	--	--	
5747.821	1.301	--	--	--	--	--		--	--	--	
5748.415	1.274	--	--	--	--	--		--	--	--	
5748.869	1.302	--	--	--	--	--		--	--	--	
5749.699	2.013	--	--	--	--	--		--	--	--	
5750.465	1.438	--	--	--	--	--		--	--	--	
5751.973	0.984	--	--	--	--	--		--	--	--	
5752.094	2.611	--	--	--	--	--		--	--	--	

5752.130	1.348	--	--	--	--	--		--	--	--	
5752.236	1.398	--	--	--	--	--		--	--	--	
5752.640	1.772	--	--	--	--	--		--	--	--	
5752.873	1.096	--	--	--	--	--		--	--	--	
5752.991	2.277	--	--	--	--	--		--	--	--	
5753.732	1.403	--	--	--	--	--		--	--	--	
5753.927	0.827	--	--	--	--	--		--	--	--	
5754.002	2.622	--	--	--	--	--		--	--	--	
5755.114	0.829	--	--	--	--	--		--	--	--	
5755.764	2.298	--	--	--	--	--		--	--	--	
5757.361	1.206	--	--	--	--	--		--	--	--	
5757.775	1.422	--	--	--	--	--		--	--	--	
5758.062	1.096	--	--	--	--	--		--	--	--	
5758.112	1.960	--	--	--	--	--		--	--	--	
5758.310	1.750	--	--	--	--	--		--	--	--	
5758.678	1.057	--	--	--	--	--		--	--	--	
5759.049	2.004	--	--	--	--	--		--	--	--	
5759.079	1.658	--	--	--	--	--		--	--	--	
5759.596	1.158	--	--	--	--	--		--	--	--	
5759.617	1.994	--	--	--	--	--		--	--	--	
5759.629	1.582	--	--	--	--	--		--	--	--	
5759.895	1.757	--	--	--	--	--		--	--	--	
5759.912	1.478	--	--	--	--	--		--	--	--	
5760.150	0.984	--	--	--	--	--		--	--	--	
5760.192	1.534	--	--	--	--	--		--	--	--	
5760.236	1.071	--	--	--	--	--		--	--	--	
5760.265	1.908	--	--	--	--	--		--	--	--	
5760.386	3.261	--	--	--	--	--		--	--	--	
5760.486	1.372	--	--	--	--	--		--	--	--	
5760.501	1.158	--	--	--	--	--		--	--	--	
5760.604	0.906	--	--	--	--	--		--	--	--	
5760.707	1.142	--	--	--	--	--		--	--	--	
5760.879	1.753	--	--	--	--	--		--	--	--	
5760.973	2.068	--	--	--	--	--		--	--	--	
5761.031	0.998	--	--	--	--	--		--	--	--	
5761.160	2.884	--	--	--	--	--		--	--	--	
5761.193	1.077	--	--	--	--	--		--	--	--	
5761.301	1.231	--	--	--	--	--		--	--	--	
5761.331	1.223	--	--	--	--	--		--	--	--	
5761.547	1.870	--	--	--	--	--		--	--	--	
5761.630	1.249	--	--	--	--	--		--	--	--	
5761.677	2.989	--	--	--	--	--		--	--	--	
5761.752	1.291	--	--	--	--	--		--	--	--	
5761.906	2.802	--	--	--	--	--		--	--	--	
5762.003	1.587	--	--	--	--	--		--	--	--	
5762.186	1.755	--	--	--	--	--		--	--	--	

5762.260	1.423	--	--	--	--	--		--	--	--	
5762.354	1.297	--	--	--	--	--		--	--	--	
5762.558	1.150	--	--	--	--	--		--	--	--	
5762.606	1.602	--	--	--	--	--		--	--	--	
5762.744	1.465	--	--	--	--	--		--	--	--	
5762.840	1.919	--	--	--	--	--		--	--	--	
5762.864	1.740	--	--	--	--	--		--	--	--	
5762.937	0.865	--	--	--	--	--		--	--	--	
5763.246	1.442	--	--	--	--	--		--	--	--	
5763.304	1.578	--	--	--	--	--		--	--	--	
5763.317	0.995	--	--	--	--	--		--	--	--	
5763.384	1.458	--	--	--	--	--		--	--	--	
5763.435	1.436	--	--	--	--	--		--	--	--	
5763.549	1.842	--	--	--	--	--		--	--	--	
5763.592	2.789	--	--	--	--	--		--	--	--	
5763.819	1.088	--	--	--	--	--		--	--	--	
5763.938	1.928	--	--	--	--	--		--	--	--	
5764.472	4.392	--	--	--	--	--		--	--	--	
5764.631	4.400	--	--	--	--	--		--	--	--	
5764.950	1.329	--	--	--	--	--		--	--	--	
5765.023	1.296	--	--	--	--	--		--	--	--	
5765.082	1.237	--	--	--	--	--		--	--	--	
5765.321	0.877	--	--	--	--	--		--	--	--	
5765.361	2.162	--	--	--	--	--		--	--	--	
5765.401	2.401	--	--	--	--	--		--	--	--	
5765.720	1.823	--	--	--	--	--		--	--	--	
5765.836	1.345	--	--	--	--	--		--	--	--	
5765.935	1.273	--	--	--	--	--		--	--	--	
5765.982	2.451	--	--	--	--	--		--	--	--	
5766.033	1.806	--	--	--	--	--		--	--	--	
5766.176	1.631	--	--	--	--	--		--	--	--	
5766.228	1.149	--	--	--	--	--		--	--	--	
5766.283	1.360	--	--	--	--	--		--	--	--	
5766.299	1.358	--	--	--	--	--		--	--	--	
5766.351	1.111	--	--	--	--	--		--	--	--	
5766.413	0.943	--	--	--	--	--		--	--	--	
5766.579	1.039	--	--	--	--	--		--	--	--	
5766.775	0.949	--	--	--	--	--		--	--	--	
5766.848	1.367	--	--	--	--	--		--	--	--	
5767.111	1.095	--	--	--	--	--		--	--	--	
5767.138	1.516	--	--	--	--	--		--	--	--	
5767.178	1.287	--	--	--	--	--		--	--	--	
5767.412	0.917	--	--	--	--	--		--	--	--	
5767.543	1.008	--	--	--	--	--		--	--	--	
5767.774	1.099	--	--	--	--	--		--	--	--	
5768.164	1.281	--	--	--	--	--		--	--	--	

5768.311	6.108	--	--	--	--	--		--	--	--	
5768.562	1.330	--	--	--	--	--		--	--	--	
5769.312	1.665	--	--	--	--	--		--	--	--	
5769.341	2.064	--	--	--	--	--		--	--	--	
5769.588	1.022	--	--	--	--	--		--	--	--	
5770.140	1.355	--	--	--	--	--		--	--	--	
5770.698	1.239	--	--	--	--	--		--	--	--	
5771.156	1.236	--	--	--	--	--		--	--	--	
5772.142	1.067	--	--	--	--	--		--	--	--	
5772.378	2.644	--	--	--	--	--		--	--	--	
5773.038	1.223	--	--	--	--	--		--	--	--	
5773.169	1.752	--	--	--	--	--		--	--	--	
5773.419	2.336	--	--	--	--	--		--	--	--	
5773.614	2.303	--	--	--	--	--		--	--	--	
5773.835	2.235	--	--	--	--	--		--	--	--	
5773.933	1.466	--	--	--	--	--		--	--	--	
5773.993	1.354	--	--	--	--	--		--	--	--	
5774.674	0.998	--	--	--	--	--		--	--	--	
5775.419	0.866	--	--	--	--	--		--	--	--	
5775.431	0.913	--	--	--	--	--		--	--	--	
5775.495	0.804	--	--	--	--	--		--	--	--	
5776.244	2.071	--	--	--	--	--		--	--	--	
5776.280	1.179	--	--	--	--	--		--	--	--	
5777.154	1.999	--	--	--	--	--		--	--	--	
5777.206	1.098	--	--	--	--	--		--	--	--	
5777.378	3.447	--	--	--	--	--		--	--	--	
5777.453	2.067	--	--	--	--	--		--	--	--	
5778.155	2.622	--	--	--	--	--		--	--	--	
5778.272	4.369	--	--	--	--	--		--	--	--	
5778.722	1.112	--	--	--	--	--		--	--	--	
5778.881	1.820	--	--	--	--	--		--	--	--	
5779.434	1.002	--	--	--	--	--		--	--	--	
5779.575	1.419	--	--	--	--	--		--	--	--	
5780.499	0.970	--	--	--	--	--		--	--	--	
5780.686	4.101	--	--	--	--	--		--	--	--	
5781.109	1.110	--	--	--	--	--		--	--	--	
5781.502	1.381	--	--	--	--	--		--	--	--	
5781.890	1.001	--	--	--	--	--		--	--	--	
5782.365	1.301	--	--	--	--	--		--	--	--	
5782.594	3.249	--	--	--	--	--		--	--	--	
5782.812	1.939	--	--	--	--	--		--	--	--	
5783.018	1.881	--	--	--	--	--		--	--	--	
5783.350	2.743	--	--	--	--	--		--	--	--	
5784.183	1.621	--	--	--	--	--		--	--	--	
5784.298	0.983	--	--	--	--	--		--	--	--	
5784.944	1.141	--	--	--	--	--		--	--	--	

5785.237	3.103	--	--	--	--	--		--	--	--	
5785.270	2.977	--	--	--	--	--		--	--	--	
5785.471	1.524	--	--	--	--	--		--	--	--	
5785.816	3.329	--	--	--	--	--		--	--	--	
5785.883	0.931	--	--	--	--	--		--	--	--	
5786.045	6.112	--	--	--	--	--		--	--	--	
5786.432	0.974	--	--	--	--	--		--	--	--	
5786.797	1.262	--	--	--	--	--		--	--	--	
5786.966	1.272	--	--	--	--	--		--	--	--	
5787.031	1.154	--	--	--	--	--		--	--	--	
5787.789	0.890	--	--	--	--	--		--	--	--	
5788.102	0.909	--	--	--	--	--		--	--	--	
5788.244	1.660	--	--	--	--	--		--	--	--	
5788.306	7.680	--	--	--	--	--		--	--	--	
5788.354	1.121	--	--	--	--	--		--	--	--	
5788.923	4.791	--	--	--	--	--		--	--	--	
5789.061	1.311	--	--	--	--	--		--	--	--	
5789.201	2.633	--	--	--	--	--		--	--	--	
5789.854	1.570	--	--	--	--	--		--	--	--	
5790.278	3.731	--	--	--	--	--		--	--	--	
5790.386	2.287	--	--	--	--	--		--	--	--	
5790.444	1.284	--	--	--	--	--		--	--	--	
5790.548	2.059	--	--	--	--	--		--	--	--	
5790.773	2.464	--	--	--	--	--		--	--	--	
5790.819	2.656	--	--	--	--	--		--	--	--	
5791.121	1.100	--	--	--	--	--		--	--	--	
5791.474	1.251	--	--	--	--	--		--	--	--	
5791.525	2.563	--	--	--	--	--		--	--	--	
5792.008	8.996	--	--	--	--	--		--	--	--	
5792.898	1.766	--	--	--	--	--		--	--	--	
5793.128	1.516	--	--	--	--	--		--	--	--	
5793.151	1.227	--	--	--	--	--		--	--	--	
5793.640	3.265	--	--	--	--	--		--	--	--	
5793.878	1.063	--	--	--	--	--		--	--	--	
5793.943	0.933	--	--	--	--	--		--	--	--	
5794.236	2.620	--	--	--	--	--		--	--	--	
5795.093	4.365	--	--	--	--	--		--	--	--	
5795.146	1.167	--	--	--	--	--		--	--	--	
5795.555	2.444	--	--	--	--	--		--	--	--	
5795.733	1.087	--	--	--	--	--		--	--	--	
5795.945	1.374	--	--	--	--	--		--	--	--	
5796.004	1.492	--	--	--	--	--		--	--	--	
5796.238	2.965	--	--	--	--	--		--	--	--	
5796.273	2.197	--	--	--	--	--		--	--	--	
5797.168	2.224	--	--	--	--	--		--	--	--	
5797.222	2.589	--	--	--	--	--		--	--	--	

5797.253	1.611	--	--	--	--	--		--	--	--	
5797.673	1.089	--	--	--	--	--		--	--	--	
5797.861	3.391	--	--	--	--	--		--	--	--	
5797.902	1.508	--	--	--	--	--		--	--	--	
5798.147	1.120	--	--	--	--	--		--	--	--	
5798.206	2.244	--	--	--	--	--		--	--	--	
5798.358	13.026	--	--	--	--	--		--	--	--	
5799.148	0.958	--	--	--	--	--		--	--	--	
5799.396	1.151	--	--	--	--	--		--	--	--	
5799.582	4.250	--	--	--	--	--		--	--	--	
5799.919	1.748	--	--	--	--	--		--	--	--	
5800.600	3.835	--	--	--	--	--		--	--	--	
5800.831	2.033	--	--	--	--	--		--	--	--	
5800.992	1.639	--	--	--	--	--		--	--	--	
5801.098	3.110	--	--	--	--	--		--	--	--	
5801.208	1.585	--	--	--	--	--		--	--	--	
5801.329	2.235	--	--	--	--	--		--	--	--	
5801.636	7.201	--	--	--	--	--		--	--	--	
5801.680	0.807	--	--	--	--	--		--	--	--	
5801.834	2.207	--	--	--	--	--		--	--	--	
5801.931	1.433	--	--	--	--	--		--	--	--	
5802.499	1.247	--	--	--	--	--		--	--	--	
5802.615	1.691	--	--	--	--	--		--	--	--	
5802.636	1.115	--	--	--	--	--		--	--	--	
5802.746	0.942	--	--	--	--	--		--	--	--	
5802.877	2.232	--	--	--	--	--		--	--	--	
5803.473	3.071	--	--	--	--	--		--	--	--	
5804.327	3.588	--	--	--	--	--		--	--	--	
5804.381	1.144	--	--	--	--	--		--	--	--	
5804.489	1.168	--	--	--	--	--		--	--	--	
5804.532	5.482	--	--	--	--	--		--	--	--	
5804.609	1.702	--	--	--	--	--		--	--	--	
5804.965	4.230	--	--	--	--	--		--	--	--	
5805.547	2.186	--	--	--	--	--		--	--	--	
5806.119	4.329	--	--	--	--	--		--	--	--	
5806.404	0.959	--	--	--	--	--		--	--	--	
5806.451	1.350	--	--	--	--	--		--	--	--	
5806.472	2.027	--	--	--	--	--		--	--	--	
5806.926	4.878	--	--	--	--	--		--	--	--	
5806.977	4.059	--	--	--	--	--		--	--	--	
5807.548	3.326	--	--	--	--	--		--	--	--	
5807.665	3.264	--	--	--	--	--		--	--	--	
5807.901	1.621	--	--	--	--	--		--	--	--	
5808.164	1.112	--	--	--	--	--		--	--	--	
5808.435	9.685	--	--	--	--	--		--	--	--	
5808.549	1.152	--	--	--	--	--		--	--	--	

5808.871	2.163	--	--	--	--	--		--	--	--	
5808.941	1.988	--	--	--	--	--		--	--	--	
5809.034	1.118	--	--	--	--	--		--	--	--	
5809.717	1.510	--	--	--	--	--		--	--	--	
5809.776	3.380	--	--	--	--	--		--	--	--	
5810.632	2.270	--	--	--	--	--		--	--	--	
5811.455	7.025	--	--	--	--	--		--	--	--	
5811.533	3.178	--	--	--	--	--		--	--	--	
5811.700	1.230	--	--	--	--	--		--	--	--	
5811.922	1.127	--	--	--	--	--		--	--	--	
5812.212	1.793	--	--	--	--	--		--	--	--	
5812.641	1.007	--	--	--	--	--		--	--	--	
5812.859	1.980	--	--	--	--	--		--	--	--	
5813.193	2.539	--	--	--	--	--		--	--	--	
5813.490	1.258	--	--	--	--	--		--	--	--	
5813.799	1.668	--	--	--	--	--		--	--	--	
5814.273	6.261	--	--	--	--	--		--	--	--	
5814.431	5.774	--	--	--	--	--		--	--	--	
5814.477	4.281	--	--	--	--	--		--	--	--	
5815.034	1.568	--	--	--	--	--		--	--	--	
5815.411	1.432	--	--	--	--	--		--	--	--	
5816.311	1.772	--	--	--	--	--		--	--	--	
5816.746	3.554	--	--	--	--	--		--	--	--	
5816.797	4.704	--	--	--	--	--		--	--	--	
5817.738	4.354	--	--	--	--	--		--	--	--	
5818.557	6.366	--	--	--	--	--		--	--	--	
5818.766	4.674	--	--	--	--	--		--	--	--	
5818.912	1.039	--	--	--	--	--		--	--	--	
5819.199	1.788	--	--	--	--	--		--	--	--	
5819.302	2.100	--	--	--	--	--		--	--	--	
5819.734	2.153	--	--	--	--	--		--	--	--	
5820.171	1.999	--	--	--	--	--		--	--	--	
5820.700	1.110	--	--	--	--	--		--	--	--	
5821.553	8.349	--	--	--	--	--		--	--	--	
5821.646	3.009	--	--	--	--	--		--	--	--	
5822.169	1.257	--	--	--	--	--		--	--	--	
5822.197	2.226	--	--	--	--	--		--	--	--	
5822.613	1.030	--	--	--	--	--		--	--	--	
5822.791	1.272	--	--	--	--	--		--	--	--	
5823.505	1.317	--	--	--	--	--		--	--	--	
5823.779	2.952	--	--	--	--	--		--	--	--	
5823.839	1.185	--	--	--	--	--		--	--	--	
5823.888	2.788	--	--	--	--	--		--	--	--	
5824.087	1.809	--	--	--	--	--		--	--	--	
5824.793	2.743	--	--	--	--	--		--	--	--	
5825.056	1.805	--	--	--	--	--		--	--	--	

5825.572	2.075	--	--	--	--	--		--	--	--	
5825.938	2.477	--	--	--	--	--		--	--	--	
5826.103	4.120	--	--	--	--	--		--	--	--	
5826.457	1.757	--	--	--	--	--		--	--	--	
5826.898	1.123	--	--	--	--	--		--	--	--	
5827.087	1.223	--	--	--	--	--		--	--	--	
5827.443	1.010	--	--	--	--	--		--	--	--	
5827.510	1.300	--	--	--	--	--		--	--	--	
5828.020	1.041	--	--	--	--	--		--	--	--	
5828.834	12.703	--	--	--	--	--		--	--	--	
5828.894	1.169	--	--	--	--	--		--	--	--	
5829.065	2.898	--	--	--	--	--		--	--	--	
5829.371	0.948	--	--	--	--	--		--	--	--	
5829.865	4.246	--	--	--	--	--		--	--	--	
5830.143	1.318	--	--	--	--	--		--	--	--	
5830.886	2.199	--	--	--	--	--		--	--	--	
5831.073	2.355	--	--	--	--	--		--	--	--	
5831.293	1.757	--	--	--	--	--		--	--	--	
5831.572	1.234	--	--	--	--	--		--	--	--	
5831.818	1.790	--	--	--	--	--		--	--	--	
5832.243	2.019	--	--	--	--	--		--	--	--	
5832.753	2.615	--	--	--	--	--		--	--	--	
5833.006	1.293	--	--	--	--	--		--	--	--	
5833.242	1.093	--	--	--	--	--		--	--	--	
5833.522	2.449	--	--	--	--	--		--	--	--	
5833.658	1.089	--	--	--	--	--		--	--	--	
5834.098	0.884	--	--	--	--	--		--	--	--	
5834.239	1.915	--	--	--	--	--		--	--	--	
5834.728	0.979	--	--	--	--	--		--	--	--	
5835.122	1.107	--	--	--	--	--		--	--	--	
5835.306	1.347	--	--	--	--	--		--	--	--	
5835.431	0.860	--	--	--	--	--		--	--	--	
5836.576	2.143	--	--	--	--	--		--	--	--	
5836.904	0.929	--	--	--	--	--		--	--	--	
5837.115	1.213	--	--	--	--	--		--	--	--	
5837.990	1.004	--	--	--	--	--		--	--	--	
5838.110	1.330	--	--	--	--	--		--	--	--	
5838.124	1.111	--	--	--	--	--		--	--	--	
5838.402	2.045	--	--	--	--	--		--	--	--	
5838.588	0.921	--	--	--	--	--		--	--	--	
5838.934	1.225	--	--	--	--	--		--	--	--	
5838.963	1.103	--	--	--	--	--		--	--	--	
5839.237	1.457	--	--	--	--	--		--	--	--	
5839.799	1.224	--	--	--	--	--		--	--	--	
5839.971	2.974	--	--	--	--	--		--	--	--	
5840.270	2.091	--	--	--	--	--		--	--	--	

5840.586	2.194	--	--	--	--	--		--	--	--	
5840.753	1.957	--	--	--	--	--		--	--	--	
5841.038	1.807	--	--	--	--	--		--	--	--	
5842.251	1.371	--	--	--	--	--		--	--	--	
5843.314	1.133	--	--	--	--	--		--	--	--	
5843.978	1.386	--	--	--	--	--		--	--	--	
5844.223	1.462	--	--	--	--	--		--	--	--	
5845.351	1.081	--	--	--	--	--		--	--	--	
5845.697	3.131	--	--	--	--	--		--	--	--	
5845.929	2.114	--	--	--	--	--		--	--	--	
5846.198	3.427	--	--	--	--	--		--	--	--	
5846.306	1.381	--	--	5846.304	0.17	pP15(15)		--	--	pP15(15)	
5846.373	3.337	--	--	--	--	--		--	--	--	
5847.494	1.465	--	--	--	--	--		--	--	--	
5847.580	1.699	--	--	--	--	--		--	--	--	
5847.780	1.605	--	--	--	--	--		--	--	--	
5847.948	2.229	--	--	--	--	--		--	--	--	
5848.112	1.604	--	--	--	--	--		--	--	--	
5848.844	0.984	--	--	--	--	--		--	--	--	
5849.026	0.907	--	--	--	--	--		--	--	--	
5849.298	1.993	--	--	--	--	--		--	--	--	
5849.400	3.644	--	--	--	--	--		--	--	--	
5849.783	1.914	--	--	--	--	--		--	--	--	
5850.210	1.800	--	--	--	--	--		--	--	--	
5850.296	2.997	--	--	--	--	--		--	--	--	
5850.325	1.945	--	--	--	--	--		--	--	--	
5850.443	1.268	--	--	--	--	--		--	--	--	
5850.481	1.706	--	--	--	--	--		--	--	--	
5850.488	1.715	--	--	--	--	--		--	--	--	
5850.846	1.869	--	--	--	--	--		--	--	--	
5851.025	2.120	--	--	--	--	--		--	--	--	
5851.674	1.061	--	--	--	--	--		--	--	--	
5851.721	1.260	--	--	--	--	--		--	--	--	
5851.811	1.524	--	--	--	--	--		--	--	--	
5851.964	3.030	--	--	--	--	--		--	--	--	
5852.080	2.889	--	--	--	--	--		--	--	--	
5852.508	5.263	--	--	--	--	--		--	--	--	
5852.571	3.231	--	--	--	--	--		--	--	--	
5852.745	1.496	--	--	--	--	--		--	--	--	
5852.985	2.033	--	--	--	--	--		--	--	--	
5853.080	2.455	--	--	--	--	--		--	--	--	
5853.195	2.959	--	--	--	--	--		--	--	--	
5853.245	3.397	--	--	--	--	--		--	--	--	
5853.486	5.007	--	--	--	--	--		--	--	--	
5853.546	1.718	--	--	--	--	--		--	--	--	
5853.921	2.069	--	--	--	--	--		--	--	--	

5854.052	2.818	--	--	--	--	--		--	--	--	
5854.167	3.968	--	--	--	--	--		--	--	--	
5854.269	1.153	--	--	--	--	--		--	--	--	
5854.349	4.076	--	--	--	--	--		--	--	--	
5854.437	2.968	--	--	--	--	--		--	--	--	
5854.668	0.956	--	--	--	--	--		--	--	--	
5854.754	1.097	--	--	--	--	--		--	--	--	
5854.844	3.323	--	--	--	--	--		--	--	--	
5854.917	5.819	--	--	--	--	--		--	--	--	
5855.195	2.159	--	--	--	--	--		--	--	--	
5855.333	1.939	--	--	5855.305	0.13	pP12(16)		--	--	--	
5855.398	1.658	--	--	--	--	--		--	--	--	
5855.444	1.585	--	--	--	--	--		--	--	--	
5855.461	1.808	--	--	--	--	--		--	--	--	
5855.503	0.973	--	--	--	--	--		--	--	--	
5855.568	6.135	--	--	--	--	--		--	--	--	
5855.913	0.953	--	--	--	--	--		--	--	--	
5856.025	2.245	--	--	--	--	--		--	--	--	
5856.056	2.074	--	--	--	--	--		--	--	--	
5856.201	2.399	--	--	--	--	--		--	--	--	
5856.292	4.276	--	--	--	--	--		--	--	--	
5856.590	5.618	--	--	--	--	--		--	--	--	
5856.702	1.984	--	--	--	--	--		--	--	--	
5856.815	0.918	--	--	--	--	--		--	--	--	
5856.900	6.842	--	--	--	--	--		--	--	--	
5856.952	3.522	--	--	--	--	--		--	--	--	
5857.046	1.484	--	--	--	--	--		--	--	--	
5857.125	4.248	--	--	--	--	--		--	--	--	
5857.215	1.946	--	--	--	--	--		--	--	--	
5857.340	9.232	--	--	--	--	--		--	--	--	
5857.477	1.585	--	--	--	--	--		--	--	--	
5857.739	2.745	--	--	--	--	--		--	--	--	
5857.893	11.399	--	--	--	--	--		--	--	--	
5858.248	3.328	--	--	5858.266	0.16	pP14(14)		--	--	--	
5858.509	0.895	--	--	--	--	--		--	--	--	
5858.575	13.253	--	--	--	--	--		--	--	--	
5858.708	3.118	--	--	--	--	--		--	--	--	
5858.805	2.019	--	--	--	--	--		--	--	--	
5858.930	1.672	--	--	--	--	--		--	--	--	
5858.981	3.105	--	--	--	--	--		--	--	--	
5859.045	5.218	--	--	--	--	--		--	--	--	
5859.229	8.959	--	--	--	--	--		--	--	--	
5859.303	2.088	--	--	--	--	--		--	--	--	
5859.472	5.220	--	--	--	--	--		--	--	--	
5859.739	1.371	--	--	5859.796	0.13	qP0(17)		--	--	--	

5859.938	1.384	--	--	--	--	--		--	--	--	
5860.005	4.822	--	--	--	--	--		--	--	--	
5860.171	7.166	--	--	--	--	--		--	--	--	
5860.224	1.198	--	--	--	--	--		--	--	--	
5860.249	1.257	--	--	--	--	--		--	--	--	
5860.287	2.782	--	--	--	--	--		--	--	--	
5860.452	0.980	--	--	--	--	--		--	--	--	
5860.486	1.381	--	--	--	--	--		--	--	--	
5860.561	2.407	--	--	--	--	--		--	--	--	
5860.694	4.850	--	--	5860.652	0.10	pP13(15)		--	--	--	
5860.765	1.111	--	--	--	--	--		--	--	--	
5861.008	4.926	--	--	--	--	--		--	--	--	
5861.064	0.954	--	--	--	--	--		--	--	--	
5861.107	1.275	--	--	--	--	--		--	--	--	
5861.214	7.184	--	--	--	--	--		--	--	--	
5861.371	3.100	--	--	--	--	--		--	--	--	
5861.635	1.994	--	--	--	--	--		--	--	--	
5861.808	3.998	--	--	--	--	--		--	--	--	
5861.850	3.936	--	--	--	--	--		--	--	--	
5862.204	3.525	--	--	--	--	--		--	--	--	
5862.312	1.827	--	--	--	--	--		--	--	--	
5862.380	1.241	--	--	--	--	--		--	--	--	
5862.550	2.207	--	--	--	--	--		--	--	--	
5862.712	6.375	--	--	--	--	--		--	--	--	
5862.750	2.269	--	--	--	--	--		--	--	--	
5862.808	1.806	--	--	--	--	--		--	--	--	
5862.860	3.322	--	--	--	--	--		--	--	--	
5862.897	0.988	--	--	--	--	--		--	--	--	
5863.033	3.277	--	--	--	--	--		--	--	--	
5863.172	1.895	--	--	--	--	--		--	--	--	
5863.223	8.510	--	--	--	--	--		--	--	--	
5863.548	2.033	--	--	5862.488	0.23	pP12(15)		--	--	--	
5863.677	2.947	--	--	5862.611	0.17	pP9(16)		--	--	--	
5863.792	7.224	--	--	5863.753	0.12	qP3(17)		--	--	--	
5863.994	1.013	--	--	--	--	--		--	--	--	
5864.024	1.961	--	--	--	--	--		--	--	--	
5864.078	6.303	--	--	--	--	--		--	--	--	
5864.281	4.827	--	--	5864.277	0.13	pP11(15)		--	--	pP11(15)	
5864.316	3.438	--	--	--	--	--		--	--	--	
5864.409	1.887	--	--	--	--	--		--	--	--	
5864.475	1.176	--	--	--	--	--		--	--	--	
5864.701	4.654	--	--	5864.607	0.23	qP0(16)		--	--	--	
5864.851	1.455	--	--	--	--	--		--	--	--	
5864.919	3.728	--	--	--	--	--		--	--	--	
5865.017	1.992	--	--	5865.020	0.11	qP1(16)		--	--	qP1(16)	

5865.389	2.035	--	--	--	--	--		--	--	--	
5865.589	1.009	--	--	--	--	--		--	--	--	
5865.654	0.807	--	--	--	--	--		--	--	--	
5865.714	2.274	--	--	--	--	--		--	--	--	
5865.879	2.255	--	--	5865.838	0.17	pP13(14)		--	--	--	
5865.982	1.454	--	--	--	--	--		--	--	--	
5866.098	0.894	--	--	--	--	--		--	--	--	
5866.204	2.117	--	--	5866.218	0.09	pP8(16)		--	--	--	
5866.234	1.588	--	--	5866.219	0.11	qP2(16)		--	--	--	
5866.727	1.627	--	--	5866.685	0.05	qP11(12)		--	--	--	
5866.769	1.586	--	--	5866.737	0.14	pP10(15)		--	--	--	
5866.832	1.915	--	--	--	--	--		--	--	--	
5867.181	3.045	--	--	--	--	--		--	--	--	
5867.231	1.244	--	--	--	--	--		--	--	--	
5867.303	0.947	--	--	--	--	--		--	--	--	
5867.640	1.289	--	--	--	--	--		--	--	--	
5867.664	1.405	--	--	--	--	--		--	--	--	
5867.713	2.234	--	--	--	--	--		--	--	--	
5867.852	1.745	--	--	--	--	--		--	--	--	
5868.038	1.097	--	--	5868.079	0.21	qP3(16)		--	--	--	
5868.142	1.374	--	--	--	--	--		--	--	--	
5868.265	0.978	--	--	--	--	--		--	--	--	
5868.382	0.995	--	--	--	--	--		--	--	--	
5868.428	1.587	--	--	--	--	--		--	--	--	
5868.772	1.201	--	--	--	--	--		--	--	--	
5869.074	0.834	--	--	--	--	--		--	--	--	
5869.182	1.607	--	--	--	--	--		--	--	--	
5869.652	1.180	--	--	5869.398	0.38	pP12(14)		--	--	--	
5869.865	0.996	--	--	5869.818	0.29	pP13(13)		--	--	--	
5869.963	0.845	--	--	5869.918	0.30	pP9(15)		--	--	--	
5870.154	1.350	--	--	--	--	--		--	--	--	
5870.263	1.532	--	--	--	--	--		--	--	--	
5871.105	0.949	--	--	--	--	--		--	--	--	
5871.269	1.165	--	--	--	--	--		--	--	--	
5872.317	4.209	--	--	5872.097	0.06	qP10(15)		--	--	--	
5872.548	1.026	--	--	--	--	--		--	--	--	
5872.615	1.741	--	--	5872.758	0.15	pP6(16)		--	--	--	
5872.824	4.805	--	--	5872.871	0.09	qP5(16)		--	--	--	
5873.141	1.852	--	--	5873.007	0.35	qP3(15)		--	--	--	
5873.502	1.312	--	--	5873.559	0.15	pP8(15)		--	--	--	
5874.104	1.220	--	--	--	--	--		--	--	--	
5874.129	0.997	--	--	--	--	--		--	--	--	
5874.226	5.004	--	--	--	--	--		--	--	--	
5875.105	1.130	--	--	5875.140	0.16	qP6(16)		--	--	--	
5875.223	2.140	--	--	5875.168	0.10	qP10(13)		--	--	--	

5876.020	0.963	--	--	5876.188	0.31	qP1(14)		--	--	--	
5878.188	1.920	--	--	--	--	--		--	--	--	
5878.468	0.849	--	--	--	--	--		--	--	--	
5878.928	0.976	--	--	--	--	--		--	--	--	
5878.987	1.115	--	--	--	--	--		--	--	--	
5879.105	1.875	--	--	5879.061	0.22	qP9(14)		--	--	--	
5879.420	0.929	--	--	--	--	--		--	--	--	
5879.800	3.113	--	--	5879.649	0.11	qP7(15)		--	--	--	
5880.407	5.189	--	--	--	--	--		--	--	--	
5881.242	1.243	--	--	5881.256	0.85	pP12(12)		--	--	--	
5881.939	1.600	--	--	--	--	--		--	--	--	
5882.317	7.288	--	--	5882.455	0.48	qP1(13)		--	--	--	
5882.645	1.910	--	--	5882.699	0.09	rP0(17)		--	--	--	
5882.951	1.046	--	--	5882.882	0.41	qP6(14)		--	--	--	
5883.389	1.162	--	--	5883.228	0.46	qP2(13)		--	--	--	
5883.834	6.711	--	--	5883.718	0.07	pP2(16)		--	--	--	
5886.596	1.663	--	--	5886.902	0.35	qP5(13)		--	--	--	
5888.437	0.949	--	--	--	--	--		--	--	--	
5888.570	5.287	--	--	--	--	--		--	--	--	
5888.610	0.991	--	--	5888.858	1.46	qP0(12)		--	--	--	
5889.010	1.522	--	--	5889.089	0.72	qP1(12)		--	--	--	
5890.501	4.477	--	--	5890.689	1.29	qP3(12)		--	--	--	
5890.874	1.609	--	--	--	--	--		--	--	--	
5891.063	5.076	--	--	--	--	--		--	--	--	
5891.339	1.666	--	--	--	--	--		--	--	--	
5891.374	2.527	--	--	--	--	--		--	--	--	
5891.453	5.215	--	--	--	--	--		--	--	--	
5891.496	1.721	--	--	--	--	--		--	--	--	
5891.579	1.493	--	--	--	--	--		--	--	--	
5891.612	1.876	--	--	--	--	--		--	--	--	
5891.639	1.774	--	--	--	--	--		--	--	--	
5891.746	1.698	--	--	5891.726	0.58	qP4(12)		--	--	--	
5891.792	3.773	--	--	--	--	--		--	--	--	
5892.032	5.049	--	--	5892.059	0.35	qP7(12)		--	--	--	
5892.261	1.144	--	--	--	--	--		--	--	--	
5893.224	17.133	--	--	--	--	--		--	--	--	
5893.272	1.799	--	--	5893.369	0.71	pP9(12)		--	--	--	
5893.836	1.278	--	--	5893.842	0.11	pP2(15)		--	--	pP2(15)	
5893.910	1.367	--	--	--	--	--		--	--	--	
5894.070	1.289	--	--	5894.055	0.58	pP11(11)		--	--	--	
5895.067	2.009	--	--	5895.837	2.09	qP0(11)		--	--	--	
5896.754	0.949	--	--	--	--	--		--	--	--	
5896.826	4.972	--	--	--	--	--		--	--	--	
5898.070	1.187	--	--	5898.110	0.82	qP4(11)		--	--	--	
5898.779	4.690	--	--	5898.611	0.70	qP5(11)		--	--	--	

5898.991	1.126	--	--	--	--	--		--	--	--	
5899.546	1.478	--	--	5899.661	0.44	pP3(14)		--	--	--	
5900.312	2.058	--	--	--	--	--		--	--	--	
5900.454	1.600	--	--	--	--	--		--	--	--	
5900.502	0.874	--	--	--	--	--		--	--	--	
5900.621	3.527	--	--	--	--	--		--	--	--	
5900.896	1.252	--	--	--	--	--		--	--	--	
5900.955	1.401	--	--	5900.874	0.40	pP5(13)		--	--	--	
5900.981	1.226	--	--	--	--	--		--	--	--	
5901.293	0.926	--	--	--	--	--		--	--	--	
5901.360	1.933	--	--	5901.302	0.49	pP7(12)		--	--	--	
5901.478	10.944	--	--	--	--	--		--	--	--	
5901.587	1.852	--	--	--	--	--		--	--	--	
5902.067	1.624	--	--	5902.168	1.62	pP9(11)		--	--	--	
5902.360	0.831	--	--	--	--	--		--	--	--	
5902.427	6.891	--	--	--	--	--		--	--	--	
5902.790	1.151	--	--	5902.782	0.53	qP7(10)		--	--	qP7(10)	
5902.952	4.775	--	--	5903.066	2.85	qP0(10)		--	--	--	
5903.107	2.038	--	--	5903.066	2.85	qP0(10)		--	--	--	
5903.163	4.913	--	--	5903.130	0.19	pP2(14)		--	--	--	
5903.283	4.068	--	--	5903.226	1.40	qP1(10)		--	--	--	
5903.339	3.249	--	--	--	--	--		--	--	--	
5903.378	5.886	--	--	--	--	--		--	--	--	
5903.640	1.949	--	--	5903.664	1.33	qP2(10)		--	--	--	
5904.228	1.306	--	--	5904.257	2.45	qP3(10)		--	--	--	
5904.438	0.844	--	--	5904.473	1.44	qP6(10)		--	--	--	
5905.023	1.148	--	--	5904.992	0.91	qP5(10)		--	--	--	
5905.097	4.929	--	--	--	--	--		--	--	--	
5905.196	1.494	--	--	5905.110	1.28	pP6(12)		--	--	--	
5905.498	1.208	--	--	5905.629	1.26	pP10(10)		--	--	--	
5905.850	1.055	--	--	5905.737	0.86	pP8(11)		--	--	--	
5907.210	2.630	--	--	--	--	--		--	--	--	
5907.723	2.537	--	--	--	--	--		--	--	--	
5907.916	1.070	--	--	--	--	--		--	--	--	
5908.637	2.015	--	--	5908.713	0.53	qP7(9)		--	--	--	
5908.911	2.634	--	--	--	--	--		--	--	--	
5909.007	1.359	--	--	5909.021	0.63	pP5(12)		--	--	--	
5909.219	1.862	--	--	--	--	--		--	--	--	
5909.418	3.026	--	--	5909.436	0.92	pP7(11)		--	--	--	
5909.726	8.802	--	--	--	--	--		--	--	--	
5909.846	1.653	--	--	5909.962	2.65	pP9(10)		--	--	--	
5910.121	2.451	--	--	--	--	--		--	--	--	
5910.388	2.666	--	--	5910.493	3.72	qP0(9)		--	--	--	
5910.446	1.326	--	--	5910.622	1.83	qP1(9)		--	--	--	
5910.773	6.110	--	--	5910.801	1.63	qP6(9)		--	--	--	
5910.856	1.017	--	--	5910.969	1.72	qP2(9)		--	--	--	

5911.427	8.848	--	--	5911.409	3.12	qP3(9)		--	--	--	
5911.681	1.112	--	--	5911.656	1.09	qP5(9)		--	--	--	
5912.196	1.382	--	--	5911.735	1.35	qP4(9)		--	--	--	
5912.499	1.381	--	--	5912.513	0.56	rP0(14)		--	--	--	
5912.836	1.264	--	--	5912.880	0.59	pP4(12)		--	--	--	
5913.352	1.989	--	--	5913.282	1.89	pP6(11)		--	--	--	
5913.446	3.995	--	--	--	--	--		--	--	--	
5913.511	1.484	--	--	--	--	--		--	--	--	
5913.901	1.311	--	--	5913.813	1.36	pP8(10)		--	--	--	
5914.754	7.812	--	--	--	--	--		--	--	--	
5914.914	3.485	--	--	--	--	--		--	--	--	
5914.997	4.294	--	--	5914.961	0.39	qP7(8)		--	--	--	
5915.054	6.616	--	--	--	--	--		--	--	--	
5915.619	1.935	--	--	5915.607	0.21	pP1(13)		--	--	--	
5916.052	3.571	--	--	--	--	--		--	--	--	
5916.367	2.464	--	--	5916.664	1.06	pP3(12)		--	--	--	
5917.227	1.639	--	--	5917.196	0.93	pP5(11)		--	--	--	
5917.248	1.468	--	--	--	--	--		--	--	--	
5917.378	4.741	--	--	5917.403	1.60	qP6(8)		--	--	--	
5917.536	2.126	--	--	5917.590	3.97	pP9(9)		--	--	--	
5917.699	1.752	--	--	5917.611	1.37	pP7(10)		--	--	--	
5917.970	3.217	--	--	--	--	--		--	--	--	
5918.028	7.161	--	--	5918.073	4.62	qP0(8)		--	--	--	
5918.137	1.295	--	--	--	--	--		--	--	--	
5918.167	2.485	--	--	5918.175	2.26	qP1(8)		--	--	qP1(8)	
5919.143	4.301	--	--	--	--	--		--	--	--	
5919.294	1.784	--	--	--	--	--		--	--	--	
5919.451	1.009	--	--	--	--	--		--	--	--	
5919.920	5.565	--	--	--	--	--		--	--	--	
5920.169	14.792	--	--	--	--	--		--	--	--	
5920.728	0.813	--	--	--	--	--		--	--	--	
5921.105	1.557	--	--	5921.095	0.87	pP4(11)		--	--	pP4(11)	
5921.499	4.291	--	--	5921.474	2.72	pP6(10)		--	--	--	
5921.583	1.804	--	--	--	--	--		--	--	--	
5922.440	3.665	--	--	--	--	--		--	--	--	
5923.510	2.158	--	--	--	--	--		--	--	--	
5923.524	1.471	--	--	--	--	--		--	--	--	
5923.563	2.158	--	--	--	--	--		--	--	--	
5923.583	1.646	--	--	--	--	--		--	--	--	
5923.597	1.734	--	--	--	--	--		--	--	--	
5923.635	1.473	--	--	--	--	--		--	--	--	
5923.675	2.667	--	--	--	--	--		--	--	--	
5923.724	2.093	--	--	--	--	--		--	--	--	
5923.792	2.128	--	--	--	--	--		--	--	--	
5923.823	2.070	--	--	--	--	--		--	--	--	
5923.845	2.136	--	--	--	--	--		--	--	--	

5923.871	2.085	--	--	--	--	--		--	--	--	
5923.928	2.998	--	--	--	--	--		--	--	--	
5923.962	5.660	--	--	--	--	--		--	--	--	
5924.048	1.653	--	--	--	--	--		--	--	--	
5924.062	1.324	--	--	--	--	--		--	--	--	
5924.073	1.321	--	--	--	--	--		--	--	--	
5924.085	1.270	--	--	--	--	--		--	--	--	
5924.097	1.478	--	--	--	--	--		--	--	--	
5924.116	1.444	--	--	--	--	--		--	--	--	
5924.130	1.291	--	--	--	--	--		--	--	--	
5924.142	1.335	--	--	--	--	--		--	--	--	
5924.154	1.609	--	--	5924.152	0.17	qQ14(14)		--	--	qQ14(14)	
5924.172	1.388	--	--	5924.171	0.33	pP1(12)		--	--	pP1(12)	
5924.185	1.613	--	--	--	--	--		--	--	--	
5924.197	1.458	--	--	--	--	--		--	--	--	
5924.210	1.966	--	--	5924.208	0.23	rP1(13)		--	--	rP1(13)	
5924.222	2.548	--	--	--	--	--		--	--	--	
5924.241	2.960	--	--	5924.239	1.14	qP6(7)		--	--	qP6(7)	
5924.251	2.757	--	--	--	--	--		--	--	--	
5924.271	1.266	--	--	--	--	--		--	--	--	
5924.281	1.123	--	--	--	--	--		--	--	--	
5924.292	1.165	--	--	--	--	--		--	--	--	
5924.303	1.206	--	--	--	--	--		--	--	--	
5924.313	1.434	--	--	--	--	--		--	--	--	
5924.327	1.471	--	--	--	--	--		--	--	--	
5924.334	1.462	--	--	--	--	--		--	--	--	
5924.347	1.542	--	--	--	--	--		--	--	--	
5924.372	1.566	--	--	--	--	--		--	--	--	
5924.383	1.726	--	--	--	--	--		--	--	--	
5924.402	2.103	--	--	--	--	--		--	--	--	
5924.447	1.754	--	--	--	--	--		--	--	--	
5924.482	2.092	--	--	--	--	--		--	--	--	
5924.519	3.487	--	--	--	--	--		--	--	--	
5924.564	1.422	--	--	--	--	--		--	--	--	
5924.584	2.031	--	--	--	--	--		--	--	--	
5924.610	2.543	--	--	--	--	--		--	--	--	
5924.649	1.335	--	--	--	--	--		--	--	--	
5924.673	1.388	--	--	--	--	--		--	--	--	
5924.683	1.444	--	--	--	--	--		--	--	--	
5924.699	1.304	--	--	--	--	--		--	--	--	
5924.710	1.245	--	--	--	--	--		--	--	--	
5924.725	1.239	--	--	--	--	--		--	--	--	
5924.736	1.258	--	--	--	--	--		--	--	--	
5924.751	1.264	--	--	--	--	--		--	--	--	
5924.770	1.258	--	--	--	--	--		--	--	--	
5924.790	1.531	--	--	--	--	--		--	--	--	

5924.804	1.361	--	--	--	--	--		--	--	--	
5924.815	1.354	--	--	--	--	--		--	--	--	
5924.834	1.340	--	--	--	--	--		--	--	--	
5924.851	2.042	--	--	--	--	--		--	--	--	
5924.872	1.423	--	--	--	--	--		--	--	--	
5924.889	2.156	--	--	--	--	--		--	--	--	
5924.941	4.332	--	--	5924.940	4.98	pP3(11)#		--	--	pP3(11)	
5925.001	2.587	--	--	--	--	--		--	--	--	
5925.205	1.663	--	--	5925.203	3.54	qP4(7)#		--	--	qP4(7)	
5925.413	1.572	--	--	5925.384	1.31	pP5(10)		--	--	--	
5925.656	2.883	--	--	5925.652	6.42	qP5(7)#		--	--	qP5(7)	
5925.708	3.073	--	--	5925.722	5.40	qP0(7)		--	--	--	
5925.807	3.245	--	--	5925.845	2.65	qP1(7)		--	--	--	
5925.999	1.232	--	--	5926.039	2.44	qP2(7)		--	--	--	
5926.275	3.517	--	--	5926.224	4.19	qP3(7)		--	--	--	
5926.470	8.018	--	--	--	--	--		--	--	--	
5926.571	8.169	--	--	--	--	--		--	--	--	
5926.629	8.483	--	--	--	--	--		--	--	--	
5926.657	8.837	--	--	--	--	--		--	--	--	
5927.493	2.723	--	--	--	--	--		--	--	--	
5927.823	4.033	--	--	--	--	--		--	--	--	
5928.819	5.191	--	--	5928.653	0.15	rP2(13)		--	--	--	
5928.971	1.901	--	--	5928.756	0.66	pP2(11)		--	--	--	
5929.103	3.020	--	--	--	--	--		--	--	--	
5929.301	1.396	--	--	5929.301	3.13	pP4(10)#		--	--	pP4(10)	
5929.343	1.210	--	--	5929.294	1.33	rP0(12)		--	--	--	
5929.410	1.048	--	--	--	--	--		--	--	--	
5929.446	1.480	--	--	--	--	--		--	--	--	
5929.655	6.369	--	--	5929.653	8.84	pP6(9)#		--	--	pP6(9)	
5929.714	2.013	--	--	5929.689	2.80	pP8(8)		--	--	--	
5929.785	1.393	--	--	--	--	--		--	--	--	
5929.805	1.293	--	--	--	--	--		--	--	--	
5931.183	1.989	--	--	--	--	--		--	--	--	
5932.029	1.960	--	--	--	--	--		365.4	7.9	--	
5932.353	2.424	--	--	5932.488	0.34	rP1(12)		356.2	7.8	--	
5932.624	1.625	--	--	--	--	--		194.1	5.6	--	
5932.661	0.842	--	--	5932.552	0.49	pP1(11)		--	--	--	
5932.854	1.676	--	--	5932.915	0.78	qP5(6)		343.4	7.6	--	
5933.159	2.847	--	--	5933.168	2.18	pP3(10)		243.2	6.3	--	
5933.242	2.101	--	--	--	--	--		291.7	7.0	--	
5933.521	5.091	--	--	5933.537	6.05	qP0(6)		227.6	6.1	qP0(6)	
5933.574	4.992	--	--	5933.595	2.92	qP1(6)		241.5	6.3	qP1(6)	
5933.642	1.335	--	--	5933.636	1.51	qP4(6)		252.7	6.5	qP4(6)	
5933.712	0.934	--	--	5933.727	2.62	qP2(6)		--	--	--	
5933.771	5.902	--	--	5933.829	2.70	pP7(8)		260.9	6.6	pP7(8)	

5934.671	2.201	--	--	--	--	--		358.7	7.8	--	
5934.803	3.718	--	--	5934.803	9.27	qP3(6)#		238.3	6.3	qP3(6)	
5935.748	1.675	--	--	--	--	--		351.8	7.7	--	
5935.871	3.388	--	--	--	--	--		403.3	8.3	--	
5936.270	0.146	--	--	--	--	--		128.4	4.5	--	
5936.450	0.146	--	--	--	--	--		88.7	3.6	--	
5936.654	1.024	--	--	--	--	--		355.2	7.7	--	
5936.792	2.880	--	--	5936.714	0.22	rP2(12)		395.3	8.2	--	
5936.844	2.510	--	--	--	--	--		427.4	8.5	--	
5936.893	4.426	--	--	--	--	--		476.7	9.0	--	
5937.012	1.279	--	--	5937.011	2.86	pP2(10)#		489.9	9.2	pP2(10)	
5937.106	0.146	--	--	--	--	--		16.4	1.3	--	
5937.254	3.381	--	--	--	--	--		432.6	8.6	--	
5937.491	2.087	--	--	5937.476	1.65	pP4(9)		--	--	--	
5937.636	1.733	--	--	--	--	--		373.6	7.9	--	
5937.786	5.951	--	--	5937.800	5.14	pP6(8)		363.3	7.8	--	
5938.061	11.804	--	--	--	--	--		--	--	--	
5938.089	10.428	--	--	--	--	--		--	--	--	
5938.200	16.690	--	--	--	--	--		61.3	3.0	--	
5938.352	0.960	--	--	--	--	--		281.5	6.8	--	
5939.026	0.146	--	--	--	--	--		88.0	3.6	--	
5940.047	0.146	--	--	5940.081	0.12	rP4(6)		167.7	5.2	--	
5940.136	1.393	--	--	--	--	--		356.0	7.7	--	
5940.402	0.146	--	--	5940.657	0.46	rP1(11)		127.0	4.4	--	
5940.853	1.302	--	--	5940.830	0.70	pP1(10)		--	--	--	
5941.050	1.315	--	--	--	--	--		--	--	--	
5941.134	1.364	--	--	5941.139	0.28	rP3(12)		--	--	rP3(12)	
5941.173	1.019	--	--	5941.180	1.02	qP4(5)		--	--	qP4(5)	
5941.365	7.653	--	--	5941.354	6.30	qP0(5)	J=5,K=0	183.2	5.4	qP0(5)	
5941.472	3.436	--	--	--	--	--		195.6	5.6	--	
5941.721	6.384	--	--	5941.473	3.80	qP3(5)	J=5,K=3	190.3	5.5	qP3(5)	
5941.849	3.928	--	--	5941.820	3.63	pP7(7)		384.5	8.1	--	
5942.480	1.122	--	--	--	--	--		135.9	4.6	--	
5942.592	1.373	--	--	--	--	--		--	--	--	
5942.655	0.146	--	--	--	--	--		172.6	5.3	--	
5943.030	0.146	--	--	--	--	--		120.7	4.3	--	
5943.558	1.275	--	--	--	--	--		421.8	8.5	--	
5944.165	2.460	--	--	--	--	--		290.2	7.0	--	
5945.017	4.385	--	--	5944.734	0.30	rP2(11)		468.2	9.0	--	
5945.158	3.507	--	--	--	--	--		521.5	9.5	--	
5945.210	1.954	--	--	5945.215	1.23	pP2(9)		--	--	pP2(9)	
5945.566	4.299	--	--	5945.620	0.06	rP4(12)		299.5	7.1	--	
5945.653	5.790	--	--	5945.653	2.12	pP4(8)#		420.0	8.5	pP4(8)	
5945.888	8.315	--	--	5945.888	6.78	pP6(7)#		352.8	7.7	pP6(7)	
5946.294	0.146	--	--	--	--	--		166.2	5.1	--	
5946.734	1.310	--	--	--	--	--		--	--	--	

5947.098	1.042	--	--	--	--	--		122.1	4.3	--	
5947.488	1.980	--	--	--	--	--		306.2	7.2	--	
5947.728	0.146	--	--	--	--	--		185.2	5.5	--	
5948.299	3.507	--	--	--	--	--		277.3	6.8	--	
5948.831	0.957	--	--	5948.780	0.59	rP1(10)		124.6	4.4	--	
5948.953	1.356	--	--	5948.942	0.37	rP3(11)		--	--	--	
5949.043	2.448	--	--	5949.046	3.19	pP1(9)#		400.8	8.3	pP1(9)	
5949.214	11.820	--	--	5949.192	6.07	qP0(4)	J=4,K=0	118.3	4.3	qP0(4)	
5949.388	0.920	--	--	5949.259	2.22	qP2(4)		--	--	--	
5949.453	1.323	--	--	--	--	--		--	--	--	
5949.528	12.974	--	--	5949.529	3.65	pP3(8)		--	--	pP3(8)	
5949.611	8.889	--	--	--	--	--		382.9	8.1	--	
5949.660	1.094	--	--	--	--	--		--	--	--	
5949.721	0.146	--	--	--	--	--		281.1	6.8	--	
5949.858	4.038	--	--	5949.852	3.10	pP5(7)		--	--	pP5(7)	
5950.443	2.408	--	--	--	--	--		450.1	8.8	--	
5950.443	2.408	--	--	--	--	--		--	--	--	
5950.517	2.443	--	--	--	--	--		385.7	8.1	--	
5950.936	1.254	--	--	--	--	--		--	--	--	
5951.290	0.146	--	--	--	--	--		100.6	3.9	--	
5952.191	2.298	--	--	--	--	--		--	--	--	
5952.656	1.253	--	--	--	--	--		--	--	--	
5952.757	1.345	--	--	5952.758	1.26	rP2(10)#		--	--	rP2(10)	
5952.805	1.603	--	--	--	--	--		--	--	--	
5953.025	3.274	--	--	--	--	--		298.8	7.1	--	
5953.126	1.905	--	--	--	--	--		294.4	7.0	--	
5953.286	4.293	--	--	5953.229	0.11	rP4(11)		469.4	9.0	--	
5953.378	2.712	--	--	5953.378	4.89	pP2(8)#		389.7	8.1	pP2(8)	
5953.533	3.653	--	--	5953.524	3.27	rP0(9)		--	--	rP0(9)	
5953.721	1.750	--	--	--	--	--		313.1	7.2	--	
5953.778	6.390	--	--	5953.767	2.76	pP4(7)		338.0	7.5	pP4(7)	
5953.950	8.848	--	--	5953.919	8.71	pP6(6)		273.9	6.7	pP6(6)	
5954.018	1.172	--	--	--	--	--		--	--	--	
5954.297	1.420	--	--	--	--	--		327.5	7.4	--	
5954.634	0.901	--	--	--	--	--		266.3	6.6	--	
5954.676	1.699	--	--	--	--	--		--	--	--	
5954.868	0.828	--	--	--	--	--		--	--	--	
5955.368	4.159	--	--	--	--	--		391.6	8.2	--	
5955.456	1.019	--	--	--	--	--		--	--	--	
5955.894	0.146	--	--	--	--	--		150.3	4.9	--	
5955.958	1.167	--	--	--	--	--		136.5	4.6	--	
5956.353	0.889	--	--	--	--	--		--	--	--	
5956.643	1.171	--	--	--	--	--		228.5	6.1	--	
5956.828	1.188	--	--	5956.832	0.48	rP3(10)		--	--	rP3(10)	
5956.900	1.732	--	--	5956.885	0.72	rP1(9)		332.5	7.5	rP1(9)	
5957.045	8.677	--	--	5957.055	1.43	qP2(3)	J=3,K=2	65.8	3.1	qP2(3)	

5957.186	1.169	--	--	--	--	--		--	--	--	
5957.212	2.081	--	--	5957.213	3.94	pP1(8)#		312.7	7.2	pP1(8)	
5957.363	1.217	--	--	--	--	--		--	--	--	
5957.656	5.777	--	--	5957.655	4.67	pP3(7)		--	--	pP3(7)	
5957.697	0.862	--	--	--	--	--		109.0	4.1	--	
5957.887	1.963	--	--	5957.803	0.63	qQ12(13)		244.0	6.3	--	
5957.931	4.116	--	--	5957.925	3.90	pP5(6)		262.9	6.6	pP5(6)	
5958.066	0.146	--	--	--	--	--		304.3	7.1	--	
5958.741	0.906	--	--	5959.089	0.91	qQ11(11)		362.9	7.8	--	
5959.550	0.146	--	--	--	--	--		216.1	5.9	--	
5960.660	0.146	--	--	--	--	--		195.3	5.6	--	
5960.870	17.784	--	--	5960.805	0.46	rP2(9)		--	--	--	
5960.928	7.660	--	--	5961.508	1.94	pP2(7)		362.1	7.8	pP2(7)	
5961.526	4.777	--	--	5961.517	3.87	rP0(8)		326.5	7.4	rP0(8)	
5961.856	4.198	--	--	5961.854	3.40	pP4(6)		256.1	6.5	pP4(6)	
5962.229	0.990	--	--	--	--	--		--	--	--	
5963.643	0.146	--	--	--	--	--		234.3	6.2	--	
5963.807	0.826	--	--	--	--	--		322.8	7.4	--	
5964.699	0.146	--	--	--	--	--		62.8	3.0	--	
5964.787	1.836	--	--	5964.786	2.16	rP3(9)#		--	--	rP3(9)	
5964.859	6.038	--	--	5964.862	8.37	qP1(2)#	J=2,K=1	17.5	1.4	qP1(2)	
5964.982	1.513	--	--	5964.977	0.83	rP1(8)	--	--	--	rP1(8)	
5965.342	2.563	--	--	5965.343	2.63	rP1(7)#	--	248.2	6.4	pP1(7)	
5965.401	1.388	--	--	--	--	--	--	202.7	5.7	--	
5965.741	9.747	--	--	5965.739	5.63	pP3(6)#	--	234.8	6.2	pP3(6)	
5965.958	5.179	--	--	5965.943	4.80	pP5(5)	J=5,K=5	203.7	5.7	pP5(5)	
5968.863	1.591	--	--	5968.864	1.69	rP2(8)#	--	226.6	6.1	rP2(8)	
5969.131	1.121	--	--	--	--	--	--	--	--	--	
5969.519	4.254	--	--	5969.516	4.57	rP0(7)	--	291.8	7.0	rP0(7)	
5969.594	3.902	--	--	5969.594	2.24	pP2(6)#	--	226.3	6.1	pP2(6)	
5969.890	5.026	--	--	5969.890	4.07	pP4(5)	--	184.2	5.4	pP4(5)	
5971.347	1.147	--	--	5970.839	4.16	qQ9(9)	--	317.3	7.3	--	
5972.126	11.736	--	--	--	--	--	--	--	--	--	
5972.649	2.383	--	--	5972.644	2.12	qP0(1)	J=1,K=0	26.7	1.8	qP0(1)	
5972.784	1.729	--	--	5972.783	0.60	rP3(8)	--	348.6	7.7	rP3(8)	
5973.053	1.603	--	--	5973.052	2.76	rP1(7)#	--	298.0	7.1	rP1(7)	
5973.427	2.984	--	--	5973.427	3.89	pP1(6)#	--	146.7	4.8	pP1(6)	
5973.778	9.269	--	--	5973.778	6.59	pP3(5)	J=5,K=3	190.4	5.5	pP3(5)	
5973.877	0.146	--	--	--	--	--	--	27.2	1.8	--	
5974.675	0.146	--	--	5974.400	2.87	qQ8(8)	--	114.6	4.2	--	
5976.906	1.122	--	--	5976.908	1.49	rP2(7)#	--	284.9	6.9	rP2(7)	
5977.491	3.975	--	--	5977.493	4.98	rP0(6)	J=6,K=0	222.1	6.0	rP0(6)	
5977.633	3.697	--	--	5977.634	2.57	pP2(5)	--	177.8	5.3	pP2(5)	
5977.684	1.244	--	--	5977.724	1.58	qQ9(11)	--	208.1	5.8	--	
5977.873	6.723	--	--	5977.873	4.74	pP4(4)	J=4,K=4	134.2	4.6	pP4(4)	

5978.197	1.747	--	--	5978.293	2.42	qQ7(8)	--	240.3	6.3	qQ7(8)	
5978.321	2.232	--	--	5978.426	8.88	qQ6(6)	--	341.6	7.6	qQ6(6)	
5978.884	1.678	--	--	--	--	--	--	400.7	8.2	--	
5979.193	1.732	--	--	5979.307	5.92	qQ6(7)	--	--	--	--	
5979.426	2.864	--	--	5979.427	7.97	qQ4(6)#	--	248.7	6.4	qQ4(6)	
5979.485	2.708	--	--	5979.394	4.90	qQ5(5)	--	--	--	--	
5979.633	3.722	--	--	--	--	--	--	335.4	7.5	--	
5979.733	5.986	--	--	--	--	--	--	187.1	5.5	--	
5979.857	5.704	--	--	5979.859	11.16	qQ5(6)#	--	276.4	6.8	qQ5(6)	
5979.972	5.012	--	--	5979.908	0.69	qQ2(8)	--	399.7	8.2	qQ2(8)	
5980.038	14.562	--	--	5979.862	3.31	qQ5(6)	--	365.4	7.9	qQ5(6)	
5980.126	10.389	--	--	5980.054	1.55	qQ7(9)	--	484.5	9.1	qQ7(9)	
5980.186	16.633	--	--	5979.394	4.90	qQ5(5)	J=5,K=5	169.8	5.2	qQ5(5)	
5980.231	17.907	--	--	5980.207	8.72	qQ3(3)	J=3,K=3	73.3	3.3	qQ3(3)	
overlapped	overlapped			5980.283	2.00	qQ2(3)	J=3,K=2	73.3	3.3	qQ2(3)	
5980.312	7.809	--	--	5980.327	3.20	qQ2(2)	J=2,K=2	55.0	2.8	qQ2(2)	
5980.381	12.044	--	--	5980.378	5.60	qQ1(1)#	J=1,K=1	138.2	4.7	qQ1(1)	
5980.483	10.647	--	--	5980.483	2.21	qQ5(7)	--	121.9	4.3	--	
5980.557	2.000	--	--	--	--	--	--	--	--	--	
5980.638	0.981	--	--	5980.651	0.27	qQ2(8)	--	295.0	7.0	qQ2(8)	
5980.736	4.493	--	--	5980.739	0.06	rP5(8)	--	455.5	8.8	rP5(8)	
5980.789	1.359	--	--	5980.790	1.84	rP3(7)#	--	278.8	6.8	rP3(7)	
5980.908	1.297	--	--	5980.824	1.50	qQ4(7)	--	219.1	6.0	qQ4(7)	
5980.967	2.179	--	--	5980.980	0.29	qQ10(13)	--	--	--	--	
5981.097	1.860	--	--	5981.097	0.88	rP1(6)	--	216.3	5.9	rP1(6)	
5981.195	5.611	--	--	--	--	--	--	553.3	9.8	--	
5981.263	1.863	--	--	--	--	--	--	--	--	--	
5981.270	1.867	--	--	5981.291	1.45	qQ5(8)	--	--	--	--	
5981.306	5.439	--	--	5981.306	2.12	qQ3(5)#	J=5,K=3	176.3	5.3	qQ3(5)	
5981.404	1.339	--	--	5981.389	0.98	qQ4(8)	--	--	--	--	
5981.456	3.277	--	--	5981.465	1.84	pP1(5)	--	181.9	5.4	pP1(5)	
5981.764	11.971	--	--	5981.769	7.49	pP3(4)	--	110.6	4.1	pP3(4)	
5981.892	1.998	--	--	5981.778	2.48	qQ6(9)	--	293.0	7.0	--	
5982.095	1.518	--	--	5982.151	0.63	qQ4(9)	--	--	--	--	
5982.241	1.156	--	--	5982.325	0.93	qQ5(9)	--	--	--	--	
5982.366	0.146	--	--	--	--	--	--	32.3	2.0	--	
5982.905	0.146	--	--	--	--	--	--	178.4	5.4	--	
5983.079	3.642	--	--	--	--	--	--	237.5	6.2	--	
5983.116	1.735	--	--	5983.152	0.39	qQ4(10)	--	265.9	6.6	--	
5983.186	7.051	--	--	--	--	--	--	106.1	4.0	--	
5983.551	1.009	--	--	5983.452	1.55	qQ6(10)	--	--	--	--	
5984.590	0.146	--	--	5984.700	0.12	rP4(7)	--	286.9	6.9	rP4(7)	
5984.933	1.075	--	--	5984.932	1.29	rP2(6)#	--	--	--	rP2(6)	
5985.439	4.544	--	--	5985.442	5.01	rP0(5)	--	168.2	5.2	rP0(5)	
5985.624	6.505	--	--	5985.624	2.74	pP2(4)#	--	135.0	4.6	pP2(4)	

5986.574	1.096	--	--	5986.577	0.25	rQ4(5)#	--	193.0	5.6	rQ4(5)	
5988.140	2.454	--	--	5988.130	2.20	qR0(0)	J=0,K=0	12.2	1.1	qR0(0)	
5988.635	1.763	--	--	5988.638	0.27	rP5(7)#	--	305.9	7.1	rP5(7)	
5988.785	1.340	--	--	5988.787	0.44	rP3(6)	--	234.4	6.2	rP3(6)	
5989.108	1.902	--	--	5989.108	1.67	rP1(5)#	--	148.8	4.8	rP1(5)	
5989.193	0.943	--	--	5989.137	0.14	pQ8(13)	--	229.7	6.1	--	
5989.450	2.631	--	--	5989.450	3.83	pP1(4)#	J=4,K=1	110.9	4.1	pP1(4)	
5989.696	14.092	--	--	5989.702	8.29	pP3(3)	J=3,K=3	78.1	3.4	pP3(3)	
5989.954	0.146	--	--	5990.001	0.24	qQ8(13)	--	201.0	5.7	--	
5990.749	1.341	--	--	--	--	--	J=2,K=2	63.5	3.0	--	
5991.686	0.938	--	--	5991.359	0.35	pQ8(8)	--	50.0	2.6	--	
5992.167	1.161	--	--	--	--	--	--	--	--	--	
5992.433	0.146	--	--	--	--	--	--	101.0	3.9	--	
5992.497	0.945	--	--	5992.415	0.30	qQ9(14)	--	--	--	--	
5992.565	1.572	--	--	5992.658	0.06	rP4(6)	--	166.7	5.2	rP4(6)	
5992.972	1.190	--	--	5992.929	0.37	rP2(5)	--	204.8	5.8	rP2(5)	
5993.098	0.908	--	--	5993.021	0.18	pQ7(13)	--	--	--	--	
5993.357	4.962	--	--	5993.358	4.54	rP0(4)	--	120.2	4.3	rP0(4)	
5993.553	4.813	--	--	5993.556	2.86	pP2(3)	J=3,K=2	72.1	3.2	pP2(3)	
5993.636	0.146	--	--	--	--	--	--	54.3	2.8	--	
5994.139	2.438	--	--	--	--	--	--	103.4	4.0	--	
5994.523	1.392	--	--	5994.388	0.51	pQ7(10)	--	--	--	--	
5994.569	1.761	--	--	--	--	--	--	--	--	--	
5994.729	0.844	--	--	5994.760	0.13	qQ8(14)	--	--	--	--	
5994.808	0.945	--	--	5994.884	0.65	pQ7(9)	--	317.4	7.3	pQ7(9)	
5995.493	1.881	--	--	5995.334	0.68	pQ7(8)	--	--	--	--	
5995.840	5.711	--	--	5995.839	1.58	qR1(1)	J=1,K=1	11.7	1.1	qR1(1)	
5996.756	0.146	--	--	5996.753	0.71	rP3(5)#	--	177.3	5.3	rP3(5)	
5996.818	0.146	--	--	5996.848	0.38	pQ6(13)	--	206.1	5.8	--	
5997.084	1.417	--	--	5997.075	0.58	rP1(4)	--	147.4	4.8	rP1(4)	
5997.272	0.929	--	--	5997.321	0.59	pQ6(12)	--	--	--	--	
5997.380	3.524	--	--	5997.382	1.74	pP1(3)#	--	81.9	3.5	pP1(3)	
5997.435	1.408	--	--	--	--	--	--	--	--	--	
5997.493	1.498	--	--	--	--	--	--	--	--	--	
5997.523	1.241	--	--	--	--	--	--	--	--	--	
5997.548	1.905	--	--	--	--	--	--	--	--	--	
5997.852	1.048	--	--	5997.766	0.99	pQ6(11)	--	--	--	--	
5998.227	5.057	--	--	--	--	--	--	--	--	--	
5998.276	5.153	--	--	5998.269	1.37	pQ6(10)	--	--	--	--	
5998.326	4.570	--	--	--	--	--	--	--	--	--	
5998.437	6.719	--	--	--	--	--	--	312.8	7.2	--	
5998.803	2.357	--	--	5998.778	1.75	pQ6(9)	--	--	--	--	
5999.263	2.690	--	--	5999.265	2.03	pQ6(8)	--	380.6	8.0	pQ6(8)	
5999.481	12.528	--	--	--	--	--	--	--	--	--	
5999.519	12.096	--	--	--	--	--	--	--	--	--	
5999.626	5.838	--	--	--	--	--	--	--	--	--	

5999.690	1.918	--	--	5999.704	2.02	pQ6(7)	--	343.7	7.6	pQ6(7)	
6000.004	1.371	--	--	--	--	--	--	55.9	2.8	--	
6000.075	1.222	--	--	6000.075	1.07	pQ6(6)#	--	260.0	6.6	pQ6(6)	
6000.642	13.207	--	--	--	--	--	--	--	--	--	
6000.657	12.521	--	--	--	--	--	--	--	--	--	
6000.744	16.670	--	--	--	--	--	--	--	--	--	
6000.887	0.146	--	--	6000.884	0.18	rP2(4)#	--	165.0	5.1	rP2(4)	
6000.969	0.146	--	--	--	--	--	--	328.3	7.4	--	
6001.239	2.729	--	--	6001.239	3.52	rP0(3)	--	83.0	3.5	rP0(3)	
6001.385	1.233	--	--	--	--	--	--	58.0	2.9	--	
6001.429	4.430	--	--	6001.433	2.88	pP2(2)	J=2,K=2	45.7	2.5	pP2(2)	
6001.669	20.471	--	--	--	--	--	--	--	--	--	
6001.736	11.179	--	--	6001.710	0.62	pQ5(11)	--	--	--	--	
6002.240	1.086	--	--	6002.213	0.86	pQ5(10)	--	286.6	6.9	--	
6002.521	28.673	--	--	--	--	--	--	--	--	--	
6002.587	21.104	--	--	--	--	--	--	--	--	--	
6002.745	1.352	--	--	6002.716	1.11	pQ5(9)	--	--	--	--	
6003.248	21.167	--	--	6003.202	1.35	pQ5(8)	--	--	--	--	
6003.300	19.238	--	--	--	--	--	--	--	--	--	
6003.518	9.595	--	--	6003.495	5.91	qR0(2)	J=2,K=0	25.7	1.8	qR0(2)	
overlapped	overlapped			6003.556	1.60	qR2(2)	J=2,K=2	--	--	qR2(2)	
6003.668	1.658	--	--	6003.654	1.48	pQ5(7)	--	--	--	--	
6003.835	15.204	--	--				--	356.9	7.8		
6003.880	26.174	--	--	--	--	--	--	217.3	6.0	--	
6004.063	2.109	--	--	6004.058	1.40	pQ5(6)	--	294.5	7.0	pQ5(7)	
6004.294	17.773	--	--	6004.281	0.31	pQ4(13)	--	288.8	6.9	--	
6004.408	1.478	--	--	6004.410	0.66	pQ5(5)#	--	135.7	4.6	pQ5(5)	
6004.643	10.967	--	--	--	--	--	--	213.0	5.9	--	
6004.784	1.489	--	--	--	--	--	--	164.6	5.1	--	
6004.859	4.863	--	--	--	--	--	--	--	--	--	
6004.999	1.435	--	--	6004.997	0.64	rP1(3)#	--	141.5	4.7	rP1(3)	
6005.259	2.514	--	--	6005.258	1.47	pP1(2)#	J=2,K=1	28.2	1.9	pP1(2)	
6005.479	0.853	--	--	--	--	--	--	--	--	--	
6005.554	1.197	--	--	6005.596	0.74	pQ4(11)	--	211.7	5.9	--	
6006.146	1.829	--	--	6006.137	1.03	pQ4(10)	--	324.5	7.4	--	
6006.655	1.950	--	--	6006.656	0.87	pQ4(9)#	--	397.6	8.2	pQ4(9)	
6007.145	2.037	--	--	6007.131	1.68	pQ4(8)	--	380.5	8.0	pQ4(8)	
6007.363	1.078	--	--	--	--	--	--	--	--	--	
6007.597	2.567	--	--	6007.581	1.93	pQ4(7)	--	289.9	6.9	pQ4(7)	
6007.644	5.932	--	--	--	--	--	J=3,K=3	80.1	3.4	--	
6007.997	3.004	--	--	6007.989	2.02	pQ4(6)	--	237.7	6.2	pQ4(6)	
6008.350	1.939	--	--	6008.347	1.83	pQ4(5)#	--	202.4	5.7	pQ4(5)	
6008.645	1.671	--	--	6008.646	1.23	pQ4(4)#	--	132.2	4.5	pQ4(4)	
6008.957	1.184	--	--	6008.670	1.21	pQ3(12)	--	--	--	--	
6009.008	1.039	--	--	6008.962	0.47	rQ0(16)	--	--	--	--	
6009.083	1.697	--	--	6009.080	1.97	rP0(2)	--	42.9	2.4	rP0(2)	

6009.443	1.775	--	--	--	--	--	--	380.7	8.0	--	
6009.475	1.739	--	--	6009.401	1.76	pQ3(11)	--	360.4	7.8	--	
6009.583	2.541	--	--	--	--	--	--	125.5	4.4	--	
6010.001	3.970	--	--	6010.005	2.44	pQ3(10)	--	--	--	pQ3(10)	
6010.530	4.051	--	--	6010.540	3.21	pQ3(9)	--	440.4	8.7	pQ3(9)	
6011.033	5.424	--	--	6011.035	4.38	pQ3(8)#	--	487.4	9.1	pQ3(8)	
6011.173	10.499	--	--	6011.175	6.98	qR0(3)	J=3,K=0	80.7	3.5	qR0(3)	
overlapped	overlapped			6011.162	13.95	qR1(3)	J=3,K=1	--	--	qR1(3)	
6011.267	5.412	--	--	6011.154	10.94	qR2(3)	J=3,K=2	61.9	3.0	qR2(3)	
6011.413	1.637	--	--	--	--	--	--	162.4	5.1	--	
6011.487	6.829	--	--	6011.480	5.02	pQ3(7)	--	174.3	5.3	pQ3(7)	
overlapped	overlapped			6012.788	2.90	qR3(3)	J=3,K=3	--	--	qR3(3)	
6011.891	6.619	--	--	6011.891	5.36	pQ3(6)#	--	241.2	6.3	pQ3(6)	
6012.244	6.495	--	--	6012.244	5.26	pQ3(5)#	J=5,K=3	183.0	5.4	pQ3(5)	
6012.353	0.965	--	--	6012.329	0.72	pQ2(12)	--	--	--	--	
6012.542	5.150	--	--	6012.542	4.50	pQ3(4)#	--	123.4	4.4	pQ3(4)	
6012.783	4.320	--	--	6012.783	2.88	pQ3(3)#	J=3,K=3	103.1	4.0	pQ3(3)	
6013.078	1.904	--	--	6013.077	1.05	pP1(1)	J=1,K=1	0.6	0.1	pP1(1)	
6013.319	1.913	--	--	6013.166	1.04	pQ2(11)	--	--	--	--	
6013.866	3.030	--	--	6013.831	1.43	pQ2(10)	--	463.9	8.9	--	
6014.396	2.778	--	--	6014.397	2.00	pQ2(9)#	--	456.0	8.8	pQ2(9)	
6014.891	5.773	--	--	6014.888	2.46	pQ2(8)#	--	397.2	8.2	pQ2(8)	
6015.345	4.669	--	--	6015.343	2.86	pQ2(7)#	--	288.4	6.9	pQ2(7)	
6015.660	8.659	--	--	--	--	--	--	183.5	5.4	--	
6015.753	5.510	--	--	6015.751	3.13	pQ2(6)#	J=6,K=2	224.8	6.1	pQ2(6)	
6015.850	0.146	--	--	--	--	--	--	136.3	4.6	--	
6015.968	1.312	--	--	6016.030	0.91	pQ1(12)	--	293.0	7.0	--	
6016.105	4.102	--	--	6016.107	3.21	pQ2(5)#	J=5,K=2	167.4	5.2	pQ2(5)	
6016.183	1.338	--	--	--	--	--	--	379.4	8.0	--	
6016.404	5.030	--	--	6016.404	3.01	pQ2(4)#	J=4,K=2	100.7	3.9	pQ2(4)	
6016.450	9.425	--	--	--	--	--	--	99.2	3.9	--	
6016.641	4.265	--	--	6016.641	2.50	pQ2(3)#	J=3,K=2	89.7	3.7	pQ2(3)	
6016.825	2.343	--	--	6016.826	2.15	pQ2(2)#	J=2,K=2	52.4	2.7	pQ2(2)	
6017.163	1.956	--	--	6016.931	1.28	pQ1(11)	--	--	--	--	
--	--	6017.590	0.506	6017.635	1.72	pQ1(10)	--	--	--	--	
6017.709	2.414	6017.706	2.74	6017.648	2.02	rQ0(13)	--	440.2	8.7	--	
6017.944	1.002	6017.941	0.887	6017.940	1.29	RQ0(14)	J=4,K=4	--	--	--	
--	--	6018.098	0.553	--	--	--	--	--	--	--	
6018.239	4.817	6018.235	3.4	6018.235	2.28	pQ1(9)#	--	432.5	8.6	pQ1(9)	
--	--	6018.279	0.644	--	--	--	--	--	--	--	
--	--	6018.322	0.541	--	--	--	--	--	--	--	
6018.492	4.459	6018.488	3.87	6018.884	1.23	qR4(4)	J=4,K=4	181.5	5.4	qR4(4)	
6018.734	3.879	6018.731	4.24	6018.734	2.68	pQ1(8)#	--	334.3	7.5	pQ1(8)	
6018.814	7.906	6018.811	6.98	6018.830	7.59	qR0(4)	J=4,K=0	104.1	4.0	qR0(4)	
6018.862	6.228	6018.858	6.34	6018.885	3.62	qR1(4)	J=4,K=1	100.3	3.9	qR1(4)	

6019.016	1.530	--	--	--	--	--	--	--	--	--	not CH3D peak
6019.057	5.124	6019.053	4.85	6019.009	3.11	qR2(4)	J=4,K=2	122.9	4.4	qR2(4)	
6019.187	4.870	6019.184	5.02	6019.188	3.11	pQ1(7)	J=7,K=1	289.4	6.9	pQ1(7)	
6019.380	3.521	6019.376	2.69	--	--	--	J=5,K=2	164.2	5.1	--	
--	--	6019.537	0.559	--	--	--	--	--	--	--	
6019.592	5.852	6019.588	5.26	6019.592	3.43	pQ1(6)	J=6,K=1	217.3	6.0	pQ1(6)	
6019.798	2.204	6019.795	1.8	--	--	--	--	--	--	--	
6019.943	4.888	6019.939	5.48	6019.943	3.57	pQ1(5)	J=5,K=1	161.0	5.1	pQ1(5)	
6020.071	1.709	6020.067	1.87	--	--	--	--	123.4	4.4	--	
6020.149	3.559	6020.146	3.3	--	--	--	--	--	--	--	
6020.239	6.738	6020.236	5.29	6020.239	3.47	pQ1(4)	J=4,K=1	120.6	4.3	pQ1(4)	
6020.477	4.619	6020.474	4.74	6020.478	3.10	pQ1(3)	J=3,K=1	63.3	3.0	pQ1(3)	
6020.657	4.778	6020.654	3.75	6020.660	2.44	pQ1(2)#	J=2,K=1	33.7	2.1	pQ1(2)	
6020.782	3.146	6020.779	2.51	6020.780	1.57	pQ1(1)#	J=1,K=1	26.7	1.8	pQ1(1)	
6020.808	5.549	6020.811	4.67	--	--	--	--	--	--	--	
6021.459	8.087	6021.456	6.34	6021.464	7.86	rQ0(9)	--	467.6	9.0	rQ0(9)	
6021.714	1.323	6021.711	1.37	--	--	--	--	264.6	6.6	--	
6022.068	6.941	6022.065	8.18	6022.077	9.81	rQ0(8)	J=8,K=0	366.5	7.9	rQ0(8)	
--	--	6022.253	0.555	6022.494	0.21	rQ1(14)	--	--	--	--	
6022.623	11.374	6022.619	9.62	6022.628	11.64	rQ0(7)	J=7,K=0	287.1	6.9	rQ0(7)	
6023.015	1.701	6023.011	1.11	--	--	--	--	--	--	--	
6023.118	9.184	6023.115	11.2	6023.118	13.07	rQ0(6)	J=6,K=0	224.9	6.1	rQ0(6)	
--	--	6023.381	0.597	--	--	--	--	--	--	--	
6023.456	1.268	6023.452	0.87	--	--	--	--	272.9	6.7	--	
6023.549	11.808	6023.546	11.4	6023.547	13.82	rQ0(5)	J=5,K=0	157.3	5.0	rQ0(5)	
6023.912	10.998	6023.909	11.5	6023.909	13.63	rQ0(4)	J=4,K=0	106.9	4.0	rQ0(4)	
--	--	6024.138	0.563	6024.118	0.09	rQ2(16)	--	--	--	rQ2(16)	
6024.205	12.202	6024.201	10.5	6024.201	12.31	rQ0(3)	J=3,K=0	64.5	3.0	rQ0(3)	
--	--	6024.318	0.611	--	--	--	--	--	--	--	
6024.425	7.181	6024.422	8.46	6024.421	9.84	rQ0(2)	J=2,K=0	31.3	2.0	rQ0(2)	
6024.473	1.416	6024.470	0.799	6024.436	0.32	rQ1(13)	--	--	--	RQ1(13)	
--	--	6024.490	0.463	--	--	--	--	--	--	--	
6024.573	5.570	6024.570	5.44	6024.569	6.37	rQ0(1)	J=1,K=0	12.9	1.1	rQ0(1)	
6024.701	10.647	6024.697	12.4	--	--	--	J=5,K=3	170.8	5.2	--	
6025.333	1.015	6025.329	0.983	6025.330	4.47	rR4(4)#	--	114.3	4.2	rR4(4)	
6025.359	0.850	6025.356	0.699	6025.248	0.87	rQ1(11)	--	--	--	--	
6025.423	1.129	6025.419	1.2	--	--	--	--	--	--	--	
6025.920	4.292	6025.917	4.75	--	--	--	J=5,K=4	196.6	5.6	--	
--	--	6025.943	2.2	6025.739	1.23	rQ1(10)	--	--	--	--	
6026.224	14.087	--	--	6026.172	1.65	rQ1(9)	--	337.9	7.5	--	
6026.338	2.115	--	--	6026.341	0.98	qR5(5)	J=5,K=5	204.4	5.8	qR5(5)	
6026.477	7.978	6026.473	7.23	6026.534	7.57	qR0(5)	J=5,K=0	166.4	5.2	qR0(5)	
6026.576	7.098	6026.572	7.28	--	--	--	--	182.0	5.4	--	
6026.693	1.156	6026.689	1.15	6026.573	2.10	rQ1(8)	--	--	--	rQ1(8)	

6026.956	3.907	6026.953	4.71	6026.951	2.54	rQ1(7)#	--	293.7	7.0	rQ1(7)	
6027.030	5.520	6027.026	4.72	6026.793	3.28	qR2(5)	J=5,K=2	176.3	5.3	qR2(5)	
--	--	6027.129	0.504	--	--	--	--	--	--	--	
--	--	6027.170	0.537	--	--	--	--	--	--	--	
6027.301	6.148	6027.298	5.22	6027.300	2.89	rQ1(6)	J=6,K=1	227.1	6.1	rQ1(6)	
6027.437	1.995	6027.433	1.61	--	--	--	--	290.8	7.0	--	
6027.613	5.258	6027.610	5.52	6027.613	3.05	rQ1(5)	J=5,K=1	160.8	5.1	rQ1(5)	
6027.882	4.684	6027.879	5.37	6027.882	2.95	rQ1(4)	J=4,K=1	111.7	4.1	rQ1(4)	
6028.103	5.166	6028.100	4.82	6028.102	2.50	rQ1(3)	J=3,K=1	70.4	3.2	rQ1(3)	
6028.272	2.865	6028.269	2.99	6028.269	1.62	rQ1(2)	J=2,K=1	21.8	1.6	rQ1(2)	
--	--	6028.497	0.703	6028.504	0.41	rQ2(13)	--	--	--	rQ2(13)	
6029.137	3.600	6029.134	4.32	--	--	--	J=6,K=2	221.4	6.0	--	
6029.583	0.146	6029.581	0.448	6029.465	1.02	rQ2(11)	--	322.7	7.4	--	
6029.655	2.164	6029.652	1.72	--	--	--	--	337.5	7.5	--	
--	--	6029.788	0.624	6029.808	1.38	rQ2(10)	--	--	--	rQ2(10)	
6029.853	2.049	6029.849	2.27	--	--	--	--	477.3	9.0	--	
--	--	6029.873	0.631	--	--	--	--	--	--	--	
--	--	6030.052	0.548	--	--	--	--	--	--	--	
6030.142	2.752	6030.139	3.08	6030.145	1.78	rQ2(9)	--	427.6	8.5	rQ2(9)	
--	--	6030.235	0.694	--	--	--	--	--	--	--	
6030.279	1.257	6030.275	1.51	--	--	--	--	335.7	7.5	--	
--	--	6030.489	0.486	6030.487	2.18	rQ2(8)	--	--	--	rQ2(8)	
--	--	6030.581	0.712	--	--	--	--	--	--	--	
6030.637	1.967	6030.634	1.93	--	--	--	--	392.5	8.2	--	
6030.831	4.492	6030.828	4.97	6030.826	2.52	rQ2(7)	J=7,K=2	302.8	7.1	rQ2(7)	
6031.097	0.981	6031.093	0.733	--	--	--	--	--	--	--	
6031.152	4.468	6031.148	5.14	6031.155	2.60	rQ2(6)#	J=6,K=2	216.4	5.9	rQ2(6)	
6031.443	4.545	--	--	6031.443	2.60	rQ2(5)#	J=5,K=2	158.1	5.0	rQ2(5)	
6031.489	1.698	--	--	--	--	--	--	--	--	--	
6031.698	3.704	--	--	6031.698	2.26	rQ2(4)#	J=4,K=2	120.9	4.3	rQ2(4)	
6031.908	2.958	--	--	6031.908	1.50	rQ2(3)	J=3,K=2	77.2	3.4	rQ2(3)	
6032.226	1.299	--	--	--	--	--	--	306.8	7.2	--	
6032.363	4.399	--	--	6032.360	4.41	rR0(0)	J=0,K=0	3.0	0.4	rR0(0)	
6032.560	13.441	--	--	--	--	--	--	235.7	6.2	--	
6033.416	4.396	--	--	6033.494	1.48	qR6(6)	--	224.4	6.1	qR6(6)	
6033.839	3.418	--	--	6033.876	2.04	rQ3(11)	--	274.9	6.8	--	
6033.978	2.951	--	--	--	--	--	--	472.5	9.0	--	
6034.013	6.156	--	--	6034.013	12.42	rQ3(10)#	--	--	--	rQ3(10)	
6034.198	12.606	--	--	6034.202	17.57	rQ3(9)#	--	270.4	6.7	qR0(6)	
6034.227	0.146	--	--	--	--	--	--	299.9	7.1	--	
6034.281	2.153	--	--	6034.300	7.06	qR0(6)	--	--	--	qR0(6)	
6034.390	5.890	--	--	6034.398	3.44	qR1(6)	--	217.8	6.0	qR1(6)	
6034.456	6.578	--	--	6034.459	4.02	rQ3(8)#	--	358.5	7.8	rQ3(8)	
6034.742	7.137	--	--	6034.740	4.45	rQ3(7)#	--	310.7	7.2	rQ3(7)	
6035.025	7.679	--	--	6035.025	4.52	rQ3(6)#	--	245.4	6.4	rQ3(6)	

6035.188	1.448	--	--	6035.047	2.14	qR4(6)	--	--	--	--	
6035.278	0.146	--	--	--	--	--	--	67.7	3.1	--	
6035.289	6.682	--	--	6035.289	3.83	rQ3(5)#	J=5,K=3	174.2	5.3	rQ3(5)	
6035.517	5.321	--	--	6035.517	2.54	rQ3(4)#	--	148.7	4.8	rQ3(4)	
6035.685	0.146	--	--	--	--	--	--	176.6	5.3	--	
6036.177	0.831	--	--	6036.176	0.52	qR1(1)#	J=1,K=1	24.4	1.7	qR1(1)	
6036.585	1.111	--	--	--	--	--	--	--	--	--	
6036.653	19.474	--	--	--	--	--	--	--	--	--	
6038.231	1.209	--	--	6038.271	1.19	rQ4(10)	--	--	--	--	
6038.282	2.121	--	--	6038.324	1.49	rQ4(9)	--	--	--	--	
6038.332	4.136	--	--	6038.336	0.74	rQ4(11)	--	295.2	7.0	--	
6038.429	2.555	--	--	--	--	--	--	301.7	7.1	--	
6038.474	3.027	--	--	6038.478	1.70	rQ4(8)#	--	412.0	8.4	rQ4(8)	
6038.690	2.865	--	--	6038.689	1.78	rQ4(7)#	--	346.1	7.6	rQ4(7)	
6038.921	3.300	--	--	6038.923	1.61	rQ4(6)#	--	237.5	6.2	rQ4(6)	
6039.113	0.146	--	--	--	--	--	--	207.0	5.8	--	
6039.156	3.235	--	--	6039.151	1.07	rQ4(5)	J=5,K=4	203.4	5.7	rQ4(5)	
6039.744	1.178	--	--	6039.965	0.33	rQ4(14)	--	--	--	--	
6040.034	4.438	--	--	6040.033	6.36	rR0(1)#	J=1,K=0	15.9	1.3	rR0(1)	
6040.265	11.951	--	--	6040.171	0.53	qR7(7)	--	287.1	6.9	qR7(7)	
6040.419	1.632	--	--	--	--	--	--	295.7	7.0	--	
6040.833	3.810	--	--	--	--	--	--	97.7	3.8	--	
6040.943	1.659	--	--	6040.800	0.21	rQ4(15)	--	--	--	--	
6041.411	3.649	--	--	--	--	--	--	319.5	7.3	--	
6041.504	1.749	--	--	6041.567	0.12	rQ4(16)	--	--	--	--	
6041.875	4.081	--	--	6041.947	0.07	rQ4(17)	--	344.2	7.6	--	
6041.927	2.971	--	--	--	--	--	J=5,K=5	225.8	6.1	--	
6042.056	5.627	--	--	6042.159	6.22	qR0(7)	--	302.7	7.1	qR0(7)	
6042.274	1.110	--	--	6042.284	3.04	qR1(7)	--	357.5	7.8	qR1(7)	
6042.434	2.365	--	--	6042.314	2.15	qR6(7)	--	292.8	7.0	qR6(7)	
6042.467	0.146	--	--	6042.495	1.21	rQ5(9)	--	249.8	6.4	--	
6042.522	4.914	--	--	6042.537	1.31	rQ5(8)	--	334.5	7.5	rQ5(8)	
6042.633	2.314	--	--	6042.618	2.84	qR2(7)	--	438.7	8.7	qR2(7)	
6042.661	3.405	--	--	6042.663	4.27	rQ5(7)#	--	320.9	7.3	rQ5(7)	
6042.845	2.664	--	--	6042.842	17.66	rQ5(6)#	--	283.8	6.9	rQ5(6)	
6043.069	1.175	--	--	6043.037	5.04	qR3(7)	--	--	--	--	
6043.565	0.146	--	--	6043.564	0.43	pR3(3)#		198.5	5.7	pR3(3)	
6043.756	1.790	--	--	6043.752	1.18	pR1(2)#	J=2,K=1	64.3	3.0	pR1(2)	
6043.791	6.614	--	--	6043.787	3.17	rR1(1)	J=1,K=1	31.0	2.0	rR1(1)	
6044.180	0.146	--	--	--	--	--	--	257.9	6.5	--	
6044.696	1.217	--	--	--	--	--	--	335.0	7.5	--	
6045.084	1.100	--	--	6044.879	0.48	rQ5(13)	--	315.5	7.3	--	
6046.133	0.967	--	--	6046.162	0.36	qR8(8)	--	--	--	--	
6046.609	3.603	6046.606	2.99	6046.609	6.46	rQ6(8)#	--	396.0	8.2	rQ6(8)	
6046.644	2.522	6046.641	2.33	6046.646	3.95	rQ6(7)#	--	333.6	7.5	rQ6(7)	
6046.713	3.082	6046.709	2.96	6046.712	5.66	rQ6(9)#	--	526.8	9.5	rQ6(9)	

6046.888	6.819	6046.884	4.67	--	--	--	--	375.0	8.0	--	
6046.952	41.113	--	--	--	--	--	--	--	--	--	not CH3D peak
6047.066	2.681	6047.076	2.35	6046.949	1.49	rQ6(10)	--	--	--	--	
6047.428	0.146	6047.434	0.824	6047.429	0.64	pR2(3)#	--	43.9	2.4	pR2(3)	
6047.544	4.631	6047.540	4.47	--	--	--	--	373.6	8.0	--	
6047.660	5.937	6047.657	6.42	6047.662	7.85	rR0(2)	J=2,K=0	39.5	2.3	rR0(2)	
6047.853	1.672	6047.850	1.6	--	--	--		245.2	6.4	--	
6048.336	5.394	6048.333	4.9	6048.348	0.83	rQ6(11)		390.1	8.1	--	
6048.534	4.838	6048.530	4.11	--	--	--		379.4	8.0	--	
6049.034	3.330	6049.031	2.57	6049.048	1.10	rQ6(12)		405.1	8.3	--	
6049.351	1.090	6049.348	0.987	--	--	--		--	--	--	
--	--	6049.403	0.617	--	--	--		--	--	--	
6049.649	4.844	6049.645	4.63	6049.635	0.75	qR7(8)		405.8	8.3	qR7(8)	
6050.139	1.477	6050.136	1.45	6050.151	5.20	qR0(8)		--	--	qR0(8)	
6050.245	3.293	6050.241	3.64	6050.306	2.55	qR1(8)		343.9	7.6	qR1(8)	
--	--	6050.510	0.612	6050.538	0.12	pR5(5)		--	--	pR5(5)	
--	--	6050.663	0.855	6050.669	0.44	rQ7(8)		--	--	rQ7(8)	
6050.702	2.577	6050.694	2.51	6050.730	2.41	qR2(8)		421.0	8.5	qR2(8)	
6050.886	1.006	6050.882	1.05	6050.876	0.56	rQ7(9)		--	--	rQ7(9)	
6051.008	1.130	6051.005	1.01	6051.007	1.63	pR3(4)#		151.8	4.9	pR3(4)	
6051.265	2.913	6051.262	2.93	6051.266	1.25	pR1(3)		124.4	4.4	pR1(3)	
6051.307	2.111	6051.304	2.14	6051.321	0.52	rQ7(10)		--	--	--	
6051.378	5.367	6051.375	6.17	6051.377	3.28	rR1(2)	J=2,K=1	34.8	2.1	rR1(2)	
6051.526	0.877	6051.523	0.845	6051.387	2.28	qR6(8)		--	--	--	
--	--	6051.882	0.501	6051.805	1.88	qR4(8)		--	--	--	
6052.480	0.146	6052.479	0.631	--	--	--		290.5	7.0	--	
6052.631	2.011	6052.628	1.41	--	--	--		252.7	6.5	--	
--	--	6052.760	0.723	6052.937	0.59	rQ6(14)		--	--	--	
6053.227	3.241	--	--	--	--	--		--	--	--	not CH3D peak
--	--	6053.666	0.703	--	--	--		--	--	--	
--	--	6053.947	0.783	6053.891	0.18	pR6(6)		--	--	--	
--	--	6054.362	0.646	6054.362	0.43	rQ7(12)		--	--	--	
6054.698	1.704	6054.695	1.33	6054.482	0.33	pR4(5)		--	--	--	
6054.876	1.247	6054.873	1.16	6054.876	0.89	pR2(4)		123.5	4.4	pR2(4)	
6055.024	3.605	6055.021	3.63	6055.008	0.29	rQ8(9)		483.5	9.1	rQ8(9)	
6055.079	1.723	--	--	6055.062	0.14	qR10(10)		--	--	--	not CH3D peak
6055.181	11.388	6055.178	9.31	6055.181	4.80	rR2(2)	J=2,K=2	35.9	2.2	rR2(2)	
6055.242	7.200	6055.239	7.44	6055.245	8.75	rR0(3)	J=3,K=0	38.2	2.2	rR0(3)	
--	--	6055.274	0.543	--	--	--		--	--	--	
6055.597	3.884	6055.594	4.17	6055.459	0.26	rQ8(10)		438.8	8.7	--	
6055.629	5.129	6055.626	4.12	--	--	--		443.3	8.7	--	
6056.296	4.671	6056.293	3.65	6056.398	0.36	rQ7(13)		443.1	8.7	--	

6056.973	3.174	6056.969	2.86	--	--	--		466.4	8.9	--	
6057.083	46.902	--	--	--	--	--		--	--	--	not CH3 D peak
--	--	6057.118	0.726	--	--	--		--	--	--	
--	--	6057.443	0.627	6057.212	0.07	pR7(7)		--	--	--	
6057.525	1.450	--	--	6057.364	0.08	qR11(11)		--	--	--	
6057.619	3.702	6057.616	4.25	6057.767	0.09	qR12(12)		476.4	9.0	--	
--	--	6058.212	1.48	6057.861	0.25	pR5(6)		--	--	--	
6058.249	4.576	6058.245	5.2	6058.317	4.14	qR0(9)		331.9	7.5	qR0(9)	
6058.394	1.522	6058.390	1.35	6058.388	1.29	pR3(5)		194.7	5.6	pR3(5)	
6058.638	1.539	6058.634	1.41	6058.506	2.03	qR1(9)		--	--	--	
6058.717	2.028	6058.713	2.14	6058.724	1.37	pR1(4)		103.4	4.0	pR1(4)	
6058.910	6.794	6058.906	6.3	6058.913	3.33	rR1(3)#	J=3,K=1	71.1	3.2	rR1(3)	
6059.233	1.753	6059.229	1.91	6059.030	1.93	qR2(9)		379.6	8.0	qR2(9)	
6060.896	0.888	6060.893	0.896	6060.747	0.79	rQ9(11)		--	--	rQ9(11)	
--	--	6061.166	0.691	6061.168	0.38	pR6(7)		--	--	pR6(7)	
6061.284	1.354	6061.280	1.26	--	--	--		--	--	--	
--	--	6061.516	0.822	--	--	--		--	--	--	
6061.555	2.689	6061.552	2.57	--	--	--		523.7	9.5	--	
6062.261	1.319	6062.257	1.36	6062.263	1.02	pR2(5)		168.5	5.2	pR2(5)	
6062.722	8.867	6062.719	8.39	6062.723	4.49	rR2(3)#	J=3,K=2	71.0	3.2	rR2(3)	
6062.783	6.624	6062.780	7.36	6062.785	9.00	rR0(4)	J=4,K=0	109.0	4.1	rR0(4)	
6062.843	1.235	6062.840	0.61	--	--	--		--	--	--	
--	--	6062.865	0.552	--	--	--		--	--	--	
6062.953	2.831	6062.950	3.1	--	--	--		--	--	--	
6063.067	1.842	6063.064	1.78	--	--	--		--	--	--	
--	--	6063.351	0.656	--	--	--		--	--	--	
6063.538	3.284	6063.535	3.14	--	--	--		451.7	8.8	--	
--	--	6063.558	0.908	--	--	--		--	--	--	
6063.655	3.304	6063.652	3.03	--	--	--		474.1	9.0	--	
6064.289	2.844	6064.286	2.45	6064.225	0.07	pR9(9)		364.5	7.8	pR9(9)	
--	--	6064.536	0.521	6064.464	0.14	pR7(8)		--	--	--	
--	--	6064.692	0.501	6064.841	0.41	rQ9(12)		--	--	--	
6065.090	2.137	--	--	6065.127	0.35	pR5(7)		--	--	--	
6065.721	1.626	6065.717	1.34	6065.722	1.44	pR3(6)#		244.2	6.3	pR3(6)	
6065.885	2.870	6065.882	2.2	--	--	--		--	--	--	
--	--	6065.908	0.795	--	--	--		--	--	--	
6065.994	1.138	6065.991	0.806	6065.976	0.21	rQ8(14)		--	--	--	
6066.107	2.145	6066.103	1.97	6066.107	1.43	pR1(5)#		137.2	4.6	pR1(5)	
6066.387	7.397	6066.384	6.11	6066.387	3.24	rR1(4)	J=4,K=1	172.7	5.3	rR1(4)	
6066.541	23.648	6066.538	22.7	6066.543	11.61	rR3(3)#	J=3,K=3	106.5	4.0	rR3(3)	
--	--	6066.583	1.19	--	--	--		--	--	--	
6066.705	1.004	--	--	6066.707	3.14	qR0(10)		--	--	--	not CH3 D peak
6066.754	0.835	6066.751	0.76	--	--	--		--	--	--	

6067.001	1.458	6066.998	0.74	6067.004	3.45	qR6(10)		--	--	qR6(10)	
6067.086	22.466	--	--	--	--	--		--	--	--	not CH3D peak
6067.148	21.692	--	--	6067.209	0.49	qR8(10)		--	--	--	not CH3D peak
6068.154	0.146	--	--	6068.388	0.53	pR6(8)		237.6	6.2	pR6(8)	not CH3D peak
--	--	6068.762	0.49	6068.487	2.74	qR3(10)		--	--	--	
--	--	6069.092	0.492	6069.100	0.40	pR4(7)#		--	--	pR4(7)	
6069.266	3.429	6069.263	3.94	--	--	--		350.3	7.7	--	
--	--	6069.429	0.507	6069.484	1.23	qR4(10)		--	--	--	
6069.590	1.056	6069.587	1.18	6069.589	1.07	pR2(6)#		299.6	7.1	pR2(6)	
6070.214	8.381	--	--	6070.214	4.17	rR2(4)#	J=4,K=2	107.2	4.0	rR2(4)	
6070.287	6.068	--	--	6070.284	8.64	rR0(5)		81.0	3.5	rR0(5)	
6070.673	1.544	--	--	--	--	--		--	--	--	
6070.973	1.761	--	--	6070.811	0.07	rQ11(12)		--	--	--	
6071.087	2.194	--	--	6071.210	0.14	rQ8(15)		--	--	--	
6071.785	1.960	--	--	6071.660	0.19	pR7(9)		422.3	8.5	--	
6072.369	2.049	--	--	6072.418	0.33	rQ9(14)		--	--	--	
6072.703	2.132	--	--	--	--	--		--	--	--	
6072.991	1.036	--	--	6072.990	0.97	pR3(7)#		--	--	pR3(7)	
6073.298	0.146	--	--	6073.250	0.14	rQ10(13)		232.8	6.2	--	
6073.436	1.659	--	--	6073.436	1.50	pR1(6)#		--	--	pR1(6)	
6073.647	1.408	--	--	--	--	--		--	--	--	
6073.817	5.331	--	--	6073.815	3.03	rR1(5)#		160.3	5.0	rR1(5)	
6074.053	17.041	--	--	6074.055	10.19	rR3(4)		125.1	4.4	rR3(4)	
6074.100	4.440	--	--	--	--	--		--	--	--	
6074.615	1.638	--	--	6074.503	0.59	qR9(11)		--	--	--	
6075.114	1.226	--	--	--	--	--		--	--	--	
6075.360	0.834	--	--	6075.372	2.28	qR0(11)		--	--	--	
6076.861	2.003	--	--	6076.859	1.36	pR2(7)#		--	--	pR2(7)	
6076.943	24.957	--	--	--	--	--		--	--	--	
6077.052	23.597	--	--	6077.513	2.01	qR3(11)		--	--	--	
6077.662	6.400	--	--	6077.662	3.73	rR2(5)#		--	--	rR2(5)	
6077.757	6.970	--	--	6077.743	7.73	rR0(6)		--	--	rR0(6)	
6077.904	13.526	--	--	6077.908	6.11	rR4(4)#		--	--	rR4(4)	
6080.028	1.149	--	--	6079.938	0.80	qR5(11)		--	--	--	
6080.201	1.215	--	--	6080.201	0.76	pR3(8)#		--	--	pR3(8)	
6080.245	0.912	--	--	6080.260	0.55	qR7(11)		--	--	--	
6080.606	3.257	--	--	6080.579	1.35	qR6(11)		--	--	--	
6080.708	1.372	--	--	6080.708	1.19	pR1(7)#		--	--	pR1(7)	
6080.834	1.192	--	--	6081.086	0.17	qR10(12)		--	--	--	
6081.206	4.751	--	--	6081.205	2.78	rR1(6)		--	--	rR1(6)	
6081.528	21.404	--	--	6081.527	8.91	rR3(5)#		--	--	rR3(5)	

6081.843	1.229	--	--	--	--	--		--	--	--	
6082.863	0.848	--	--	6082.754	0.59	pR6(10)		--	--	--	
6083.864	1.061	--	--	6083.830	0.08	rQ11(14)		--	--	--	
6084.076	0.868	--	--	6084.077	0.67	pR2(8)#		--	--	pR2(8)	
6085.075	5.825	--	--	6085.072	3.23	rR2(6)#		--	--	rR2(6)	
6085.200	5.497	--	--	6085.162	5.88	rR0(7)		--	--	rR0(7)	
6085.250	1.057	--	--	6085.241	0.05	pR12(13)		--	--	--	
6085.351	3.314	--	--	--	--	--		--	--	--	
6085.414	10.764	--	--	6085.414	7.11	rR4(5)#		--	--	rR4(5)	
6086.625	19.045	--	--	6086.684	0.09	qR11(13)		--	--	--	
6086.742	16.721	--	--	6086.727	0.38	pR5(10)		--	--	--	
6086.780	12.454	--	--	6086.765	0.15	rQ9(16)		--	--	--	
6086.824	11.288	--	--	6086.902	1.41	qR3(12)		--	--	--	
6087.375	0.985	--	--	6087.373	0.77	pR3(9)#		--	--	pR3(9)	
6087.926	1.306	--	--	6087.927	1.45	pR1(8)#		--	--	pR1(8)	
6088.562	3.494	--	--	6088.547	2.33	rR1(7)		--	--	rR1(7)	
6088.977	12.461	--	--	6088.975	7.22	rR3(6)		--	--	rR3(6)	
6089.314	14.071	--	--	6089.314	5.86	rR5(5)		--	--	rR5(5)	
6089.355	4.778	--	--	6089.359	0.15	pR8(12)		--	--	pR8(12)	
6092.187	3.518	--	--	--	--	--		--	--	--	
6092.246	1.722	--	--	6092.203	0.06	rQ11(15)		--	--	--	
6092.551	0.993	--	--	6092.575	5.43	rR0(8)		--	--	--	
6092.603	2.165	--	--	6092.605	1.29	rR2(7)#		--	--	rR2(7)	
6092.655	4.623	--	--	--	--	--		--	--	--	
6092.912	7.347	--	--	6092.912	4.12	rR4(6)#		--	--	rR4(6)	
6095.911	3.038	--	--	6095.860	1.93	rR1(8)		--	--	--	
6096.168	25.173	--	--	--	--	--		--	--	--	
6096.251	2.136	--	--	--	--	--		--	--	--	
6096.369	8.275	--	--	--	--	--		--	--	--	
6096.416	17.716	--	--	6096.416	5.77	rR3(7)#		--	--	rR3(7)	
6096.490	9.769	--	--	--	--	--		--	--	--	
6096.812	2.666	--	--	6096.718	0.95	qR3(13)		--	--	--	
6096.870	10.527	--	--	6096.868	8.40	rR5(6)#		--	--	rR5(6)	
6098.452	0.973	--	--	6098.241	0.57	pR2(10)		--	--	--	
6098.713	0.863	--	--	6098.628	0.44	qR4(13)		--	--	--	
6099.823	3.708	--	--	6099.827	2.04	rR2(8)#		--	--	rR2(8)	
6100.116	3.830	--	--	6100.210	0.36	qR9(13)		--	--	--	
6100.420	7.292	--	--	6100.421	3.21	rR4(7)#		--	--	rR4(7)	
6100.687	2.386	--	--	6100.744	0.15	pR7(13)		--	--	--	
6100.833	21.123	--	--	6100.833	10.29	rR6(6)		--	--	rR6(6)	
6103.339	2.555	--	--	6103.131	1.53	rR1(9)		--	--	--	
6103.873	13.231	--	--	6103.875	4.44	rR3(8)		--	--	rR3(8)	
6104.002	2.612	--	--	6104.027	0.33	qR1(14)		--	--	--	
6104.460	7.058	--	--	6104.463	3.52	rR5(7)#		--	--	rR5(7)	
6105.622	11.725	--	--	--	--	--		--	--	--	

6106.042	14.911	--	--	--	--	--		--	--	--	
6106.219	5.301	--	--	--	--	--		--	--	--	
6106.247	6.844	--	--	--	--	--		--	--	--	
6106.279	8.992	--	--	--	--	--		--	--	--	
6107.164	0.889	--	--	6107.142	3.41	rR0(10)		--	--	--	
6107.236	2.605	--	--	6107.193	1.56	rR2(9)		--	--	--	
6107.655	2.259	--	--	--	--	--		--	--	--	
6107.974	5.003	--	--	6107.979	2.40	rR4(8)		--	--	rR4(8)	
6108.339	1.986	--	--	6108.370	0.11	pR7(14)		--	--	--	
6108.512	17.778	--	--	6108.517	7.60	rR6(7)		--	--	rR6(7)	
6110.032	1.473	--	--	6110.037	0.10	qR10(14)		--	--	qR10(14)	
6110.505	1.613	--	--	6110.331	1.16	rR1(10)		--	--	--	
6110.787	0.923	--	--	--	--	--		--	--	--	
6111.385	8.332	--	--	6111.385	4.13	rR3(9)#		--	--	rR3(9)	
6112.044	2.486	--	--	--	--	--		--	--	--	
6112.134	5.315	--	--	6112.130	2.56	rR5(8)		--	--	rR5(8)	
6112.546	11.127	--	--	6112.541	5.04	rR7(7)#		--	--	rR7(7)	
6114.485	12.776	--	--	6114.473	0.20	qR1(15)		--	--	--	
6114.550	4.067	--	--	6114.540	1.15	rR2(10)		--	--	--	
6114.607	3.695	--	--	--	--	--		--	--	--	
6114.665	13.039	--	--	--	--	--		--	--	--	
6114.729	2.479	--	--	6114.810	2.44	rR0(11)		--	--	--	
6115.103	5.926	--	--	6115.218	0.26	pR1(12)		--	--	--	
6115.452	1.728	--	--	6115.392	0.19	qR7(14)		--	--	--	
6115.636	3.507	--	--	6115.626	1.69	rR4(9)		--	--	--	
6115.669	2.576	--	--	6115.681	0.16	qR8(14)		--	--	--	
6116.322	10.665	--	--	6116.322	5.80	rR6(8)#		--	--	rR6(8)	
6117.562	3.186	--	--	6117.588	0.20	pR2(13)		--	--	--	
6118.120	1.328	--	--	6118.307	0.11	pR6(15)		--	--	--	
6119.037	4.414	--	--	6118.937	2.36	rR3(10)		--	--	--	
6119.791	1.537	--	--	6119.753	0.25	pR3(14)		--	--	--	
6119.966	4.456	--	--	6119.918	1.71	rR5(9)		--	--	--	
6120.466	6.252	--	--	6120.466	3.03	rR7(8)#		--	--	rR7(8)	
6122.418	1.250	--	--	6122.573	0.08	pR4(15)		--	--	--	
6122.999	1.594	--	--	6122.703	0.13	pR2(14)		--	--	--	
6123.102	0.927	--	--	--	--	--		--	--	--	
6123.219	1.849	--	--	--	--	--		--	--	--	
6123.410	1.280	--	--	--	--	--		--	--	--	
6123.493	2.542	--	--	6123.378	0.95	rR4(10)		--	--	--	
6123.583	2.460	--	--	6123.427	0.16	qR5(15)		--	--	--	
6123.736	1.818	--	--	--	--	--		--	--	--	
6124.057	3.236	--	--	6123.963	0.14	pR3(15)		--	--	--	
6124.154	2.271	--	--	6124.196	0.55	rR1(12)		--	--	--	
6124.257	0.987	--	--	6124.254	3.47	rR6(9)#		--	--	rR6(9)	
6124.371	6.990	--	--	--	--	--		--	--	--	
6124.555	6.474	--	--	6124.555	3.20	rR8(8)		--	--	rR8(8)	

6126.126	3.494	--	--	6126.536	1.42	rR3(11)		--	--	--	
6127.011	3.538	--	--	6127.297	1.07	rR0(13)		--	--	--	
6128.084	1.794	--	--	6128.462	0.72	rR5(10)		--	--	--	
6128.512	2.292	--	--	6128.593	1.74	rR7(9)		--	--	--	
6128.799	3.443	--	--	6128.857	0.17	qR9(15)		--	--	--	
6130.389	2.201	--	--	--	--	--		--	--	--	
6130.468	0.842	--	--	6130.563	0.35	rR1(13)		--	--	--	
6130.759	1.148	--	--	--	--	--		--	--	--	
6131.846	1.476	--	--	--	--	--		--	--	--	
6132.358	6.759	--	--	--	--	--		--	--	--	
6132.593	1.241	--	--	--	--	--		--	--	--	
6132.787	2.206	--	--	--	--	--		--	--	--	
6132.841	5.671	--	--	6132.694	1.45	rR8(9)		--	--	--	
6132.955	2.661	--	--	6132.756	0.64	rR0(14)		--	--	--	
6133.048	3.361	--	--	6133.336	1.58	rR6(10)		--	--	--	
6133.120	3.882	--	--	--	--	--		--	--		
6133.983	1.417	--	--	6134.241	0.95	rR3(12)		--	--	--	
6135.495	1.261	--	--	--	--	--		--	--	--	
6135.525	1.251	--	--	6135.706	0.27	rR2(13)		--	--	--	
6136.747	2.723	--	--	6136.532	0.87	rR5(11)		--	--	--	
6136.870	1.984	--	--	--	--	--		--	--	--	
6136.970	8.614	--	--	6136.960	4.57	rR9(9)		--	--	--	
6137.433	2.271	--	--	6137.277	0.11	rR0(17)		--	--	--	
6137.738	1.294	--	--	6138.337	0.75	rR7(10)		--	--	--	
6139.076	1.621	--	--	6139.253	0.17	qR6(16)		--	--	--	
6140.976	2.077	--	--	6139.624	0.55	rR4(12)		--	--	--	
6141.203	0.875	--	--	--	--	--		--	--	--	
6141.866	2.201	--	--	6141.705	1.76	rR6(11)		--	--	--	
6141.914	0.976	--	--	6141.867	0.60	rR3(13)		--	--	--	
6141.976	1.680	--	--	--	--	--		--	--	--	
6142.007	3.640	--	--	6141.994	0.17	rR2(14)		--	--	--	
6142.150	1.120	--	--	6142.194	0.07	qR7(16)		--	--	--	
6142.248	2.207	--	--	--	--	--		--	--	--	
6142.423	3.508	--	--	6143.163	0.80	rR8(10)		--	--	--	
6144.272	1.286	--	--	--	--	--		--	--	--	
6145.634	1.187	--	--	6145.225	0.57	rR5(12)		--	--	--	
6146.036	4.818	--	--	--	--	--		--	--	--	
6146.758	1.252	--	--	6146.980	0.87	rR7(11)		--	--	--	
6146.904	2.546	--	--	6147.101	2.39	rR9(10)		--	--	--	
6149.191	1.287	--	--	6149.841	1.53	rR10(10)		--	--	--	
6149.866	3.002	--	--	6150.921	1.16	rR6(12)		--	--	--	
6151.114	1.043	--	--	--	--	--		--	--	--	
6151.521	1.687	--	--	6151.372	0.07	rR2(16)		--	--	--	
6152.207	1.700	--	--	6152.311	0.82	rR8(11)		--	--	--	
6152.655	2.388	--	--	--	--	--		--	--	--	
6153.778	1.409	--	--	--	--	--		--	--	--	

6155.880	2.641	--	--	--	--	--		--	--	--	
6156.577	1.124	--	--	6156.668	0.59	rR7(12)		--	--	--	
6159.801	1.677	--	--	6160.887	0.71	rR6(13)		--	--	--	
6162.523	1.469	--	--	6162.447	0.59	rR8(12)		--	--	--	
6163.249	1.426	--	--	6163.215	0.97	rR11(11)		--	--	--	
6166.809	1.413	--	--	6168.162	1.15	rR9(12)		--	--	--	
6174.959	0.867	--	--	6173.356	0.57	rR10(12)		--	--	--	
6177.032	2.124	--	--	6176.983	1.16	rR12(12)		--	--	--	